Sequentially linear analysis with equivalent frame method to simulate unreinforced masonry structures

Sequentially linear analysis with equivalent frame method to simulate unreinforced masonry structures

Master of Science Thesis

For the degree of Master of Science in Structural Engineering
at Delft University of Technology

By
Max Alphons Emerie Ferket

May, 2018

Supervisor:	MSc.	M. Pari	SE-SM
Thesis Committee:	Dr.	M.A.N. Hendriks (chair)	SE-SM
	Prof.	J.G. Rots	SE-SM
	MSc.	M. Pari (supervisor)	SE-SM
	Dr.	G.J.P. Ravenshorst	SE-SBE

TU Delft
Delft University of Technology

Preface

This thesis is a final assignment to achieve the degree Master of Science in Civil Engineering. It is about combining a sequentially linear analysis and the equivalent frame method to model an unreinforced masonry façade. The main part of this thesis is on approaching the results of the experiment with a full-scale, two-story masonry building at the University of Pavia in Italy.
The idea of this subject arose when I had a discussion with Max Hendriks last September.
During my academic education, I was most interested in the courses on the finite element method, its applications and the mathematical background. I was therefore glad that I could start this project.
The months flew by as I was working on this project.
I want to thank my thesis committee, consisting of Prof. Rots, Dr. Hendriks, Dr. Ravenshorst and MSc. Pari, for the feedback and new insights I had during our meetings. I want to thank Manimaran Pari in particular as he invested a lot of time in giving me counsel and developing new software.
Secondly, I want to thank the company Diana FEA for using a version of their software, before it is released.
I also want to thank my family and friends for the possibilities to clear my mind in the past few months and most importantly Marieke who has always been there for me.
I hope you will enjoy reading this thesis.

Max Ferket

Breda, April 2018

Abstract

There is great demand for an analysis method which can accurately describe the behaviour of unreinforced masonry structures subjected to a lateral load as there are many regions vulnerable to earthquakes in countries around the world, that have old unreinforced masonry buildings.
The province of Groningen in the Netherlands is a good example of such an area.
This behaviour is difficult to describe because of the composition of masonry with the interaction between the bricks and the mortar, and the brittle properties of the material resulting in convergence errors in common finite element analyses.
This research investigates how the equivalent frame method in combination with a sequentially linear analysis can be used to model the behaviour of a façade of an unreinforced masonry structure, subjected to a lateral pushover load. The experimental data of the two-story building experiment at the University of Pavia is used to compare the results.
Two different types of models are made, a continuum element model and a beam element model, with each two different modeling approaches, the three-zoned approach for the piers and spandrels and a uniform model. The three-zoned approach uses the bed joint tensile strength at the ends of the piers and spandrels, and the maximum tensile strength at the center of those element to simulate rocking and shear failure respectively. The most important results are listed below:

i. The three-zoned approach in combination with a continuum model was able to accurately describe the failure mechanism of the façade and perform the analysis stable, with a maximum tensile strength adjusted to $f_{tu} = 0.08\ \mathrm{MPa}$. Shear failure in the piers was the dominant failure mode. As a lateral push-over load was used and not a cyclic load as in the experiment, the maximum load of the structure was for most displacements somewhat higher than in the experiment, but the maximum load was $150\ \mathrm{kN}$ in both cases. The displacement of $22\ \mathrm{mm}$ in the experiment was not reached, but a displacement of $10\ \mathrm{mm}$.
ii. The beam model analysis aborted early as a result of a reduction of the initial load factor. It was found that the fixed crack approach in combination with high shear forces in the structure resulted in a fixed crack coordinate system that was rotated from the beam axis. Principal stresses could exceed the strength of the material and wrong integration points were damaged reducing their strength severely. At this stage a maximum displacement of $5\ \mathrm{mm}$ is reached while the force is $165\ \mathrm{kN}$, higher than in the experiment. The structure responds very brittle.
iii. Shear stresses in the beam element model exceeded the strength of the material. Adding shear interfaces in an SLA will result in a more correct failure pattern.
iv. For the beam model, a sensitivity check was done for the mesh size, fracture energy, number of saw-teeth and number of integration points. All values were accurate enough.
v. A relation exists between an initial load factor reduction and the opening of a crack in the corresponding integration point that damages at an initial load factor reduction. This behaviour should be investigated further as this is not fully understood.
vi. Crack closure errors were found in both models and resulted in some non-secant branches. This had no big influence on the result before the maximum load.

In conclusion, the results of this thesis confirm the potential of the SLA to accurately approximate the behaviour of an unreinforced masonry structure as it was possible to run a stable analysis with accurate results for the continuum model. The beam model gave similar results in terms of forces and bending moments compared with an incremental iterative approach, but the analysis was aborted early. New developments like a rotating crack approach and shear interfaces will result in a more stable analysis as the right failure behaviour will be followed resulting in a more accurate load-displacement relation.

Contents

List of Figures

List of Tables

1. Introduction

1.1 General introduction

There are many old unreinforced masonry buildings in areas sensitive to earthquakes across Europe. Examples are Italy with its building heritage where recently an earthquake struck in central Italy during the summer of 2016. Closer to home is the province of Groningen in the Netherlands. Here, also many unreinforced buildings have been built and the danger of earthquakes still lingers.
Even though the Dutch government recently declared that it will abort the gas extraction in Groningen before the year 2030, this will not stop the risks of earthquakes as the soil is already disturbed enough. During previous earthquakes, buildings have been damaged and cracks have developed.
Currently, many engineers are busy modelling unreinforced masonry structures to investigate the strength damaged buildings have left and what forces they can withstand. As this concerns, very brittle materials and structures that have already been damaged, classical strength calculations are not applicable. Finite element calculations are often used to model the plastic post-peak behaviour, however these models have their own difficulties. Very brittle material behaviour is difficult to model in an incremental iterative approach as snap-back and snap-through behaviour often occur as a result of crack openings and material softening. A proposed solution to model this behaviour is a sequentially linear analysis. Generally speaking, this method loads a model with a load case that is proportionally scaled until the strength criterion is violated in an integration point. In this integration point, the stiffness is reduced a little bit with a stepwise degrading material law and the process is repeated until in theory all integration points are damaged. With this approach all analysis steps are linear elastic which evades convergence problems that occur in an incremental iterative approach.
Different approaches can be used to model an unreinforced masonry structure dependent on the level of detail, calculation time and cost. In the second part of this research, the equivalent frame approach is used. This method simplifies the structure as a frame with flexible piers and spandrels and infinitely stiff corners. The idea behind this approach is that it simplifies the structure, reduces the calculation time while maintaining a certain level of accuracy. In this report, a smeared continuum model is used first in combination with a sequentially linear analysis and later a beam element model, following the equivalent frame approach, together with a sequentially linear analysis. For both analyses a two-dimensional façade of an unreinforced masonry building is modelled. The goal of this research is to investigate the quality of the equivalent frame approach in combination with a sequentially linear analysis and compare the results with experimental data and the results of the continuum model in combination with a sequentially linear analysis.

1.2 Structure of the report

At the start of this thesis, a literature study was done to acquire the knowledge requested to do this investigation. The literature study focused on five subjects. First, more knowledge on masonry structures was needed. This included general characteristics, types of failure behaviour and different approaches to make a finite element model of a masonry structure. The second part focused on the finite element method. This to get more knowledge on element behaviour and the mathematics behind them. Concerning solution methods, this part explained nonlinear finite element solution methods. A distinction was made in geometric nonlinearity and material nonlinearity and a standard incremental iterative approach was explained together with the benefits and difficulties. This to explain the desire for a method which evades some of these difficulties. This is where the sequentially linear analysis comes into play, which is the third topic of the literature research. The basics behind

propagating damage and stepwise secant material laws is explained together with the algorithm behind the method. The current state of the art of the method is explained which includes new procedures by van de Graaf [1].
The next topic is about the equivalent frame method which will be used in this thesis. Also, the experiment at the University of Pavia which concerns a cyclic test on a two-story unreinforced masonry structure is discussed. The important results of the master thesis of Nobel [2], which can be seen as a prequel of this report, are shown. A final chapter explains the theory behind a Mindlin Beam element with fiber-section, using the research of Ferreira [3]. These elements will be implemented in Diana FEA by Pari amongst others to be applicable for an SLA.
After the literature study, the model method of this research is explained. Here, the different models are shortly introduced and explained. Several models are used in this report and this short chapter can be seen as a reference.
Later, the results of the research will be shown. This part is divided in the first part in which a model with continuum elements is investigated and a second part which focuses on a model with beam elements. For both models, first an introduction on a small structure is done to validate the element and method. Later, the full façade is modelled. For both the case with the continuum elements as for the beam elements an in-depth analysis is done on integration point level.
Later, some improvements are implemented to achieve better results.

1.3 Research question

The question that this investigation tries to answer is formulated as:

How can a sequentially linear analysis be used together with the equivalent frame approach to model a façade of an unreinforced masonry structure?

To answer this question, several sub questions have to be investigated regarding masonry behavior, the equivalent frame method and the sequential linear analysis.
After these questions has been answered, the following questions will be answered:

How can a sequentially linear analysis be used in combination with a continuum model to model a façade of an unreinforced masonry structure?

What are the differences between the results of the continuum model approach and the equivalent frame approach?

First a continuum model is used as the results of this analysis are important to compare with the results of the equivalent frame approach. For both models, a sequentially linear analysis will be used and therefore differences between the two approaches can be related to the chosen model.
For both models, an important question to answer is:

How stable and accurate are the results of the model?

The stability of the model can be qualified by the initial load factor of the sequentially linear analysis. The more this factor stays equal to one, the more the method is stable. The accuracy of the model will be judged by comparing the load-displacement diagram with the experimental data, by looking at the failure mode and the stresses and strains in the structure.

2. Literature Review

This literature review contains five parts. Those four parts cover the essential knowledge to successfully do this research. The first part is a brief introduction on masonry buildings. The second part an explanation of the finite element method. The third part is about the sequential linear analysis. The fourth part is about the equivalent frame method and previous research in this area, especially the master thesis of W.L. Nobel. The fifth part is about the Mindlin beam elements used in the beam element model.

2.1 Masonry buildings

The invention of masonry was thousands of years ago. Mud was used as mortar and the bricks were just stones found in the area. In time this developed with the invention of burned bricks and cement to more sophisticated structures. In the Netherlands, many buildings are built out of masonry.
The province Groningen in the Netherlands suffers from earthquakes these days because of gas extraction. In Groningen, a giant gas field was found around 50 years ago. While this gas field gave the Netherlands wealth, around 248,5 billion euros in profits, it also resulted in 854 earthquakes from 1991 till 2015 [4]. In 2016, the University of Groningen researched the consequences of the earthquakes and concluded that between 90.000 and 100.000 people have acknowledged damage to their houses, of which 25.000 people more than once [5].
This situation gives questions about the stability of the buildings in the province. With normal linear-elastic calculations, many buildings will definitively fail according to those standards. However, nonlinear behavior of the structures gives them extra capacity to bear higher loads. This research focuses on masonry buildings, because there are many in that region. Another reason is that the difficult brittle and softening behavior with cracking and crushing of the wall is difficult to model with ordinary methods. To understand how the force distribution in a masonry wall works, the properties of the wall are examined in the next parts.

2.1.1 General characteristics

Although the building material is used for thousands of years, it is still used often nowadays because the technique is relatively simple. Important parameters that make masonry popular are: "its aesthetics, solidity, durability and low maintenance, versatility, sound absorption and fire protection" [6]. A major difference between masonry and other building materials is the homogeneity. For example, steel is a very homogeneous material and therefore relatively easy to model, especially because the isotropic and tensile behavior of steel is very similar to the compressive behavior. For concrete, there is a big difference in compressive behavior and tensile behavior. On structural scale it can be assumed isotropic and homogeneous.
For masonry, the differences in strength of mortar and stone and the stone orientation make it heterogeneous an anisotropic (although in a macro model, it is assumed to be homogeneous).
In general, masonry is modelled orthotropic with elastic properties. It can be split in the stones and the mortar. The interface between the mortar and the stones holds the parts together. Because stone and mortar both have relatively strong compressive strengths compared to tensile strengths, the material is strong in compression, but weak in tension. Therefore, masonry is often applied in walls, piers and in arcs. The brittle cracking behavior compared to the stiff elastic behavior make the failure occur without large deformations, which would occur using steel.

The differences in tensile and compressive strength make the material similar to concrete for uniaxial loading conditions. From experiments, the relation between the stresses and strains in the material is examined. It appears from experiments that the material relation between stress and strain in masonry can be modelled with a linear tensile curve and a parabolic compression curve.

Figure 2.1 shows this behaviour for the relation between the stress in a material and the displacement in an axial test. The descending after the yield load shows the softening behaviour of the material. Because of the cracks that occur when the material yields, the material becomes damaged and therefore less stiff and less strong. This is the opposite behaviour one examines in structural steels where the branch ascends after the yield point resulting in hardening of the material, i.e. it becomes stronger.

The crack energy is made visible with G_f, it is the surface below the stress-displacement curve. In other words, the energy needed to crack the material is far less than the energy needed to crush the masonry. In compression, after crushing, a higher force and strain can be taken by the masonry. In tensile failure, the strength rapidly decreases.

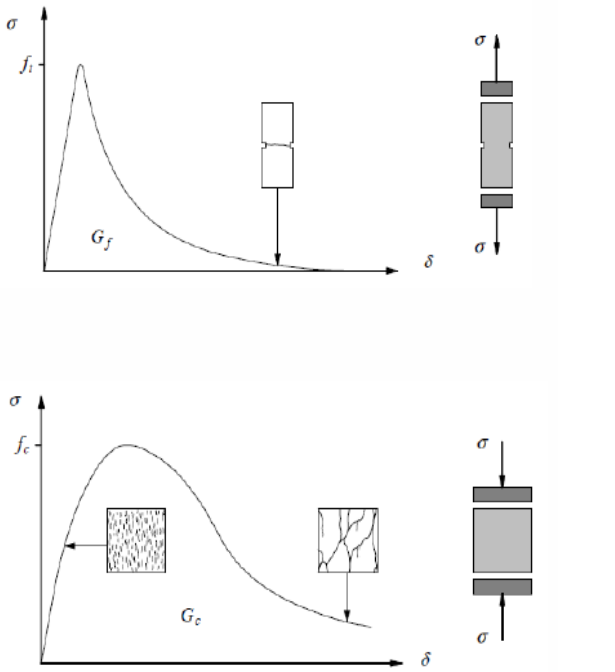

Figure 2.1; Tensile and Compressive uniaxial material model [28]

In this research, walls are loaded in plane, therefore, no forces perpendicular on the wall are taken into account. The only forces on the wall are horizontal and vertical. In the case of a two-dimensional model subjected to an earthquake, this is a good assumption, because all the forces are also in plane.

2.1.2 Mortar and Brick mortar bond

The mortar is the paste between the bricks that holds them together. It gives the masonry wall strength and stability. It is a mixture of sand, water and in most cases Portland cement.

There are many studies done on the brick-mortar bond. The behavior of the interface between brick and mortar is a result of the hydration products deposited on the brick surface and in the brick pores [7]. The initial moisture that is present in the bricks before the mortar is applied has an influence on the penetration of hydration products in the brick pores. It is a mechanical bond. Another influence is the increase of the bond strength when the compressive strength of mortar is increased, although the highest value is reached for a moisture saturation value around 80% [7].

The bond between the bricks and the mortar is very important in a structure, because it transfers the loads through the structure.

2.1.3 Modelling of masonry

Different models can be made to model the behavior of masonry piers or walls. The modelling of masonry for computer simulations is important because it accurately describe the behavior of a masonry structure in loading conditions. This helps to understand the failure mechanisms that can occur and is needed to verify the designs that are made by engineers. Especially if the loading conditions become very complex or the structure, an appropriate model is essential. Another case in

which accurate models and simulations are needed is the case presented in this thesis. Old structures are validated if they can still bear the load. This is the case when safety demands are changed in time and there is serious doubt if these old buildings, that maybe do not reach the demands that are required nowadays, are still strong enough. Hidden strength reserves can be found with the help of these types of models. The same holds for buildings that are damaged. For these buildings there can also be doubt whether they fulfill the requirements or not. Numerical analysis can also help in the serviceability limit state [6].

There are three most common ways to model masonry. The first one is micro-modeling. In this model, the units, mortar and interfaces are modelled by discontinuous elements, with other material parameters. The different types of materials in the model are modelled as different materials. The interfaces between the bricks and the mortar have properties to accurately describe the crack/slip behavior between the mortar and the bricks. This type of modeling is very detailed and therefore accurate. It also has a downside. Because of the large number of elements and degrees of freedom, a lot of memory has to be stored to make calculations with this model. This increases the calculation time. A simplification of this model is simplified micro-modeling. The dimensions of the bricks are somewhat expended to make them adjacent. They are modelled with continuum elements. The mortar and interfaces are merged in interfaces between the expanded bricks. Average parameters are used for the interfaces, which reduces the accuracy of this model. Also, the dimensions of the bricks are larger and the dimensions of the mortar are different compared to reality. The bricks are expanded to keep the total geometry of the structure the same. The interfaces still have the same crack/slip behavior. The Poisson's effect of the mortar is neglected. A third way to model the structure is with macro-modelling. In this model, all the bricks and mortar are merged into one continuum. The continuum is regarded anisotropic. A difficulty occurs when material parameters of the composite are assigned. Because the composite is made out of different materials with different behavior, the material parameters have to be found in experiments. The result is an orthotropic continuum with different material strength and elasticity in different directions. This model can be applied, because the interaction between the bricks and mortar is negligible when global failure is the scope [6].

Important to notice is that the type of model is dependent on the type of research. For detailed microscale failure, micro-modelling is probably more applicable, while for global failure macro-modeling is probably the best choice.

A different model called the equivalent frame method is applied in this research. This model will be discussed in later chapters.

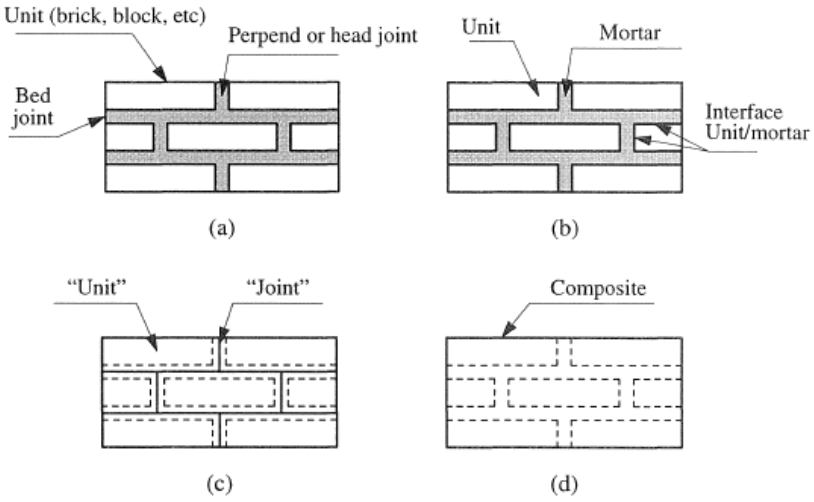

Figure 2.2; Different models for masonry. masonry (a), detailed micro-modeling (b); simplified micro-modelling (c); macro-modelling (d). [6]

2.1.4 Failure mechanisms of masonry

As told before, the focus will lay on a two-dimensional model of a wall. Only in-plane forces are taken into account. Also, the out-of-plane deformations and bending because of eccentric loads or instabilities are neglected. As this research is on earthquake damages in masonry, the load condition can be represented as a wall which has a compressive dead load in vertical direction and is subjected to a horizontal lateral load at the top. The dead load represents the self-weight of the wall and the weight of the structure above the wall, the lateral load represents the monotonical load of the earthquake on the building.
The stress state in the wall can be represented by Figure 2.3. There are shear stresses along and axial stresses on the masonry part. Many different failure types are possible because of the stone mortar pattern in masonry.

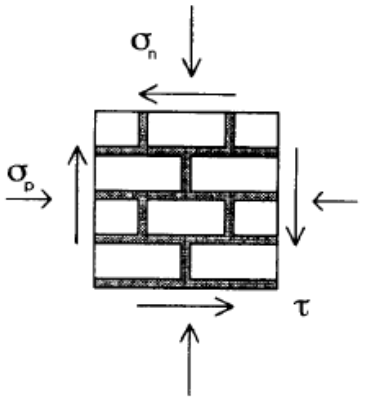

Figure 2.3; Stress state in masonry [8]

On a small scale, there are three proposed failure criteria: a shear criterion, a tensile strain criterion and a compressive stress criterion. [8]
The shear criterion is based on a Mohr-Coulomb frictional law. Slipping takes place when somewhere in the structure a critical shear strength τ_{crit} is reached. In general, the law is given by:

$$\tau_{crit} = -\sigma_n tan\phi + c \tag{2.1.1}$$

With c a cohesion term $[\mathrm{MPa}]$, σ_n the normal force $[\mathrm{MPa}]$ and ϕ the friction angle $[°]$.

The tensile criterion can be described according to [8] as an ultimate strain. First the orthotropic linear elastic relations can be described:

$$\epsilon_t = \frac{\sigma_{tt}}{E_t} - \nu_{nt}\frac{\sigma_{nn}}{E_n} \;\; ; \;\; \epsilon_{nn} = \frac{\sigma_{nn}}{E_n} - \nu_{tn}\frac{\sigma_{tt}}{E_t} \;\; ; \;\; \gamma_{tn} = \frac{\tau_{nt}}{G} \tag{2.1.2}$$

In which a crack-oriented coordinate system is applied. In this coordinate system, the direction t is tangential to the crack and the direction n normal to the crack. The shear modulus G can be described in different ways. It is common to describe the shear modulus as a constant factor β times the initial shear modulus:

$$G = \beta G_0 = \beta \frac{E_0}{2(1+\nu_0)} \tag{2.1.3}$$

According to [1], this can result in excessive stress-locking. This results in large stresses that are transferred through a crack that is open, which is not realistic. For small values of β another proposal by [9] can be used to avoid this. This concerns a shear modulus based on the minima of the elastic moduli:

$$G_{red} = \frac{E_{min}}{2\left(1+\nu_0\frac{E_{min}}{E_0}\right)} \tag{2.1.4}$$

With $E_{min} = \min(E_n, E_t)$

The reduced Poisson's ratios are described by:

$$\nu_{tn} = \nu_0 \frac{E_n}{E_0} \tag{2.1.5}$$

$$\nu_{tn} = \nu_0 \frac{E_t}{E_0} \tag{2.1.6}$$

This reduction is necessary to prevent that a large strain in one direction results in a large strain in the orthogonal direction because of the Poisson's ratio.

The tensile crack can be found in the direction of the principal strain in the wall. The principal strain can be found by the general equation for plane stress cases:

$$\epsilon_1 = \frac{\epsilon_{nn} + \epsilon_{tt}}{2} + \frac{1}{2}\sqrt{(\epsilon_{nn} - \epsilon_{tt})^2 + \gamma_{tn}^2} \tag{2.1.7a}$$

$$\tan(2\theta) = \frac{\gamma_{tn}}{\epsilon_{tt} - \epsilon_{nn}} \tag{2.1.7b}$$

Cracking occurs when somewhere in the material, the principal strain reaches the value ϵ_u.

Crushing occurs when the maximum compressive stress (the second principal stress), reaches the compressive strength.

$$\sigma_2 = \frac{\sigma_{nn} + \sigma_{tt}}{2} - \sqrt{\left(\frac{\sigma_t - \sigma_n}{2}\right)^2 + \tau^2} \leq f_c' \tag{2.1.8}$$

On a large scale, the common failure mechanisms of piers are the following: Rocking failure, shear sliding, diagonal cracking. [10]

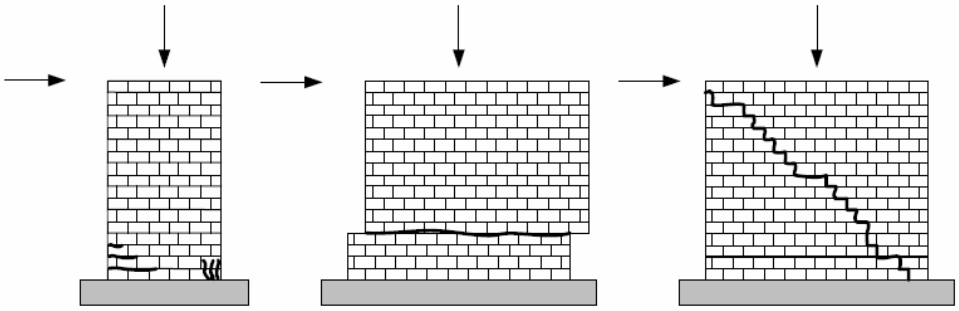

Figure 2.4; Failure mechanisms with lateral force; rocking (left), shear sliding (middle) and diagonal cracking (right) [2]

Rocking: The bed joint cracks. Therefore, the force has to be carried by the compressive part. This compressive part crushes as the compressive stress increases and the wall overturns.
Shear sliding: A sliding plane develops because the horizontal shear resistance cannot withstand the lateral force. A horizontal tensile crack occurs in the bed joints. Sliding occurs for low vertical loads.
Shear cracking: A diagonal zigzag pattern occurs between the bricks or through the bricks. This is dependent on the strength of the mortar, mortar-brick interface and the strength of the bricks.

The rocking strength can be described with the help of Figure 2.5. The horizontal force for which rocking occurs can be described as:

$$V_r = \frac{D^2 t}{H_0}\frac{p}{2}\left(1 - \frac{p}{\kappa f_u}\right) \tag{2.1.9}$$

This relation comes from the equillibrium of moments. $p = \frac{P}{Dt}$. The effective height H_0 can be calculated from the boundary conditions of the wall:

$$\alpha_v = \frac{M}{VD} = \frac{H_0}{D} = \frac{\psi' H}{D}3 \tag{2.1.10}$$

κ simplifies the stress distribution at the toe as an equivalent rectangular distribution with.
From $Pe = VH_0$ the relation can be written as: $V_r = \frac{Pe}{H_0}$. With $e = \frac{D}{2}$ and $P = pDt$.

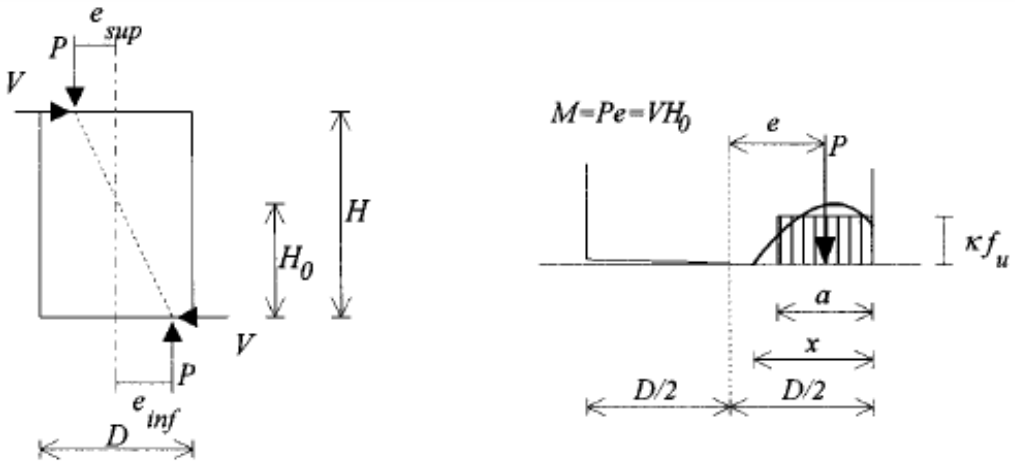

Figure 2.5; Rocking strength of a masonry wall load and dimension representation [10]

Because the diagonal cracking failure mechanism can be through mortar and stones, this is hard to describe. Especially because the parameters in vertical and horizontal direction are different.
One approach from [10] is to assume that diagonal shear failure is attained when the principal stress at the center of the pier attains a critical value. This lead to the following relation:

$$V_d = \frac{f_{tu} D t}{b}\sqrt{1 + \frac{p}{f_{tu}}} \tag{2.1.11}$$

The strength f_{tu} is the conventional (maximum) tensile strength of masonry belonging to diagonal shear failure. This strength has to be determined by shear tests. b is a parameter determined with the aspect ratio H/D. This is however only applicable on walls that are fixed in both ends. Another approach is with a Mohr-Coulomb criterion:

$$\tau_u = c + \mu\sigma_v \tag{2.1.12}$$

This lead to the following equation for the horizontal force:

$$V_d = Dt\tau_u = Dt(c + \mu p) = Dt\left(c + \mu\,\frac{P}{Dt}\right) \tag{2.1.13}$$

Where c and μ are global strength parameters.

The easiest way to describe the sliding mechanism is just the equation:

$$V_s = \mu P \tag{2.1.14}$$

In which μ is the friction coefficient of the masonry. Cohesion is neglected in this case, because a crack already occurred.

2.2 The finite element method

The finite element method is a computational method invented more than 60 years ago. In this period the first computers were developed. The method is used to calculate partial differential equations, for example in structural mechanics. The pioneers of the finite element method were structural engineers. The method is popular because it is a very good approximation of an analytical solution. The method divides the structure in a mesh of small elements. Different element types (linear, parabolic, cubic etc.) are available to accurately describe the displacements of the structure. In general, smaller elements result in convergence of the numerical solution to the analytical solution. In the finite element method, the displacements and the forces are related with a stiffness matrix in the following equation:

$$\boldsymbol{Ka} = \boldsymbol{f} \tag{2.2.1}$$

An important step in a finite element analysis is to transform the governing equation into a weak form. The strong form of the equation is multiplied with a weight function and integrated over the volume. After the weak form is derived, the equation is discretized with a Galerkin method. An example is given in the derivation of the Timoshenko beam element:

2.2.1 Timoshenko beam element

The Timoshenko beam theory differs from the Euler-Bernoulli beam theory by taking the shear deformation into account. It is therefore also applicable for high beams in which shear deformation is dominant. With the help of Figure 2.6, the relation between the deformations and strains can be described. The derivation from [11] is followed. Cross-sections remain planar but not perpendicular to the deformed axis.

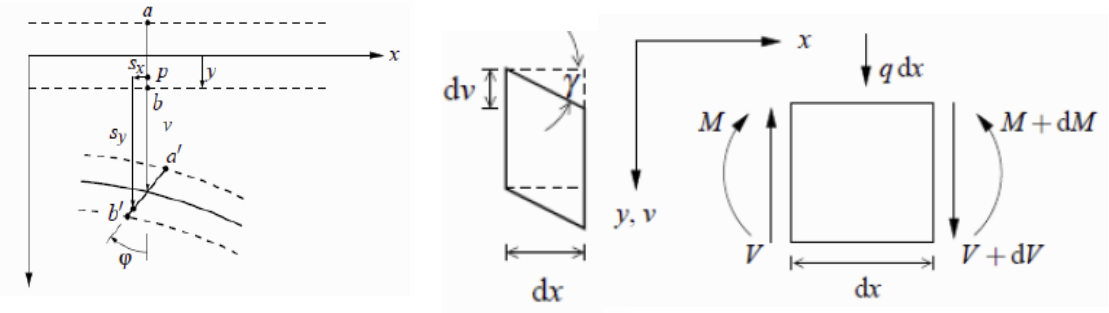

Figure 2.6; Timoshenko beam model [11] (left). Shear deformation in beam element and equilibrium [11] (right)

The deformation of a point in the beam in x-direction s_x and in y-direction s_y can be described by:

$$s_x(x,y) = -y\phi(x) \quad ; \quad s_y(x,y) = v(x) \tag{2.2.2}$$

The strain in the axial direction and the shear strain can be described by:

$$\epsilon_{xx} = \frac{ds_x}{dx} = -y\frac{d\phi}{dx} \quad ; \quad \gamma_{xy} = \frac{ds_x}{dy} + \frac{ds_y}{dx} = -\phi + \frac{dv}{dx} \tag{2.2.3}$$

From Figure 2.6 can be concluded that:

$$\frac{dv}{dx} = \tan(\gamma_{xy}) \approx \gamma_{xy}\ ; \quad \frac{dV}{dx} = -q\ ; \quad \frac{dM}{dx} = V \tag{2.2.4}$$

This is true for small angles γ. The second equation follows from vertical equilibrium. The third equation neglects quadratic terms, because they are relatively small. By using the relation between the shear force and the shear strain and the second equation from (2.2.3):

$$V = GA_s\gamma_{xy} = GA_s\left(\frac{dv}{dx} - \phi\right) \tag{2.2.5}$$

By applying Hooke's law:

$$\sigma_{xx} = E\epsilon_{xx} = -Ey\frac{d\phi}{dx} \tag{2.2.6}$$

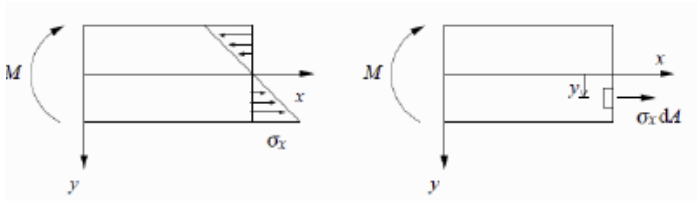

Figure 2.7; Relation stress and bending moment [11]

From Figure 2.7, the moment M on the cross section can be described by the axial stress:

$$M = \int dM = \int \sigma_{xx} y dA = -\int Ey^2\frac{d\phi}{dx}\,dA = -EI\frac{d\phi}{dx} \quad with\ I = \int y^2 dA \tag{2.2.7}$$

Now all the equations can be combined to derive the final two equations. Combining the last equation of (2.2.4), (2.2.5) and (2.2.7):

$$-EI\frac{d^2\phi}{dx^2} - GA_s\left(\frac{dv}{dx} - \phi\right) = 0 \tag{2.2.8}$$

Combining the second equation of (2.2.4) and (2.2.5):

$$GA_s\left(\frac{d^2v}{dx^2} - \frac{d\phi}{dx}\right) = -q \tag{2.2.9}$$

To transform these equations in a weak form, the governing equations (2.2.8) and (2.2.9) are multiplied with a weight function and integrated over the volume. The distributed force q is from here on written as f_y. To make the equations shorter, the derivations to x are written in subscript: $\frac{dv}{dx} = v_{,x}$. The derivation from [12] is followed.

$$-\int_\Omega \bar{\theta}EI\theta_{,xx}d\Omega - \int_\Omega \bar{\theta}GA_s(v_{,x} - \theta)d\Omega = 0 \tag{2.2.10}$$

$$\int_{\Omega} \bar{v} G A_s \left(v_{,xx} - \theta_{,x}\right) d\Omega + \int_{\Omega} \bar{v} f_y d\Omega = 0 \tag{2.2.11}$$

After integration by parts:

$$\int_{\Omega} \bar{\theta}_{,x}\, EI \theta_{,x} d\Omega - \int_{\Gamma} \bar{\theta}\, EI \theta_{,x} n\, d\Gamma - \int_{\Omega} \bar{\theta} G A_s \left(v_{,x} - \theta\right) d\Omega = 0 \tag{2.2.12}$$

$$-\int_{\Omega} \bar{v}_{,x}\, G A_s \left(v_{,x} - \theta\right) d\Omega + \int_{\Gamma} \bar{v}\, G A_s \left(v_{,x} - \theta\right) n_x d\Gamma + \int_{\Omega} \bar{v} f_y d\Omega = 0 \tag{2.2.13}$$

The boundary conditions are given as:

$$v = g_v \;\; ; \;\; \theta n = g_\theta \;\; ; \;\; m\, n = T \;\; ; \;\; q\, n = F_y \tag{2.2.14}$$

With T a bending moment and F_y a vertical force. The natural boundary conditions appeared in the weak form equation and can now be filled in:

$$\int_{\Omega} \bar{\theta}_{,x}\, EI \theta_{,x} d\Omega - \int_{\Omega} \bar{\theta} G A_s \left(v_{,x} - \theta\right) d\Omega + \int_{\Gamma_M} \bar{\theta}\, T\, d\Gamma = 0 \tag{2.2.15}$$

$$-\int_{\Omega} \bar{v}_{,x}\, G A_s \left(v_{,x} - \theta\right) d\Omega + \int_{\Gamma_Q} \bar{v}\, G F_y\, d\Gamma + \int_{\Omega} \bar{v} f_y d\Omega = 0 \tag{2.2.16}$$

Because the derivatives are of the first order, linear shape functions can be used. The variable displacements and rotations of (2.2.15) and (2.2.16) are discretized by a vector of shape functions and a vector which describes the nodal displacements. These nodal displacements are the displacements that are sought in a finite element scheme.

$$v = \boldsymbol{N}^v \boldsymbol{a}_e^v \;\; ; \;\; \theta = \boldsymbol{N}^\theta \boldsymbol{a}_e^\theta \;\; ; \;\; \bar{v} = \boldsymbol{N}^v \boldsymbol{b}_e^v \;\; ; \;\; \bar{\theta} = \boldsymbol{N}^\theta \boldsymbol{b}_e^\theta \tag{2.2.17}$$

The relation $\boldsymbol{N}_{,x} = \boldsymbol{B}$ is used**.** By filling in these shape functions:

$$\int_{\Omega_e} \boldsymbol{B}^{\theta^T} EI \boldsymbol{B}^\theta d\Omega\, \mathbf{a}_e^\theta + \int_{\Omega_e} \boldsymbol{N}^{\theta^T} G A_s \boldsymbol{N}^\theta d\Omega\, \mathbf{a}_e^\theta - \int_{\Omega_e} \boldsymbol{N}^{\theta^T} G A_s \boldsymbol{B}^v d\Omega\, \mathbf{a}_e^v = -\int_{\Gamma_{e_M}} \boldsymbol{N}^{\theta^T} T\, d\Gamma \tag{2.2.18}$$

$$\int_{\Omega_e} \boldsymbol{B}^{v^T} G A_s \boldsymbol{B}^v d\Omega\, \mathbf{a}_e^v - \int_{\Omega_e} \boldsymbol{B}^{v^T} G A_s \boldsymbol{N}^\theta d\Omega\, \mathbf{a}_e^\theta = \int_{\Gamma_{e,Q}} \boldsymbol{N}^{v^T} F_y\, d\Gamma + \int_{\Omega_e} \boldsymbol{N}^{v^T} f_y d\Omega \tag{2.2.19}$$

Now this can be assembled in a matrix-vector representation:

$$\begin{bmatrix} \boldsymbol{k}^{\theta\theta} & \boldsymbol{k}^{\theta v} \\ \boldsymbol{k}^{v\theta} & \boldsymbol{k}^{vv} \end{bmatrix} \begin{bmatrix} \boldsymbol{a}^\theta \\ \boldsymbol{a}^v \end{bmatrix} = \begin{bmatrix} \boldsymbol{f}_\theta \\ \boldsymbol{f}_v \end{bmatrix} \tag{2.2.20}$$

With:

$$\boldsymbol{k}^{\theta\theta} = \int_{\Omega_e} \boldsymbol{B}^{\theta^T} EI \boldsymbol{B}^\theta d\Omega + \int_{\Omega_e} \boldsymbol{N}^{\theta^T} G A_s \boldsymbol{N}^\theta d\Omega \tag{2.2.21a}$$

$$\boldsymbol{k}^{\theta v} = -\int_{\Omega_e} \boldsymbol{N}^{\theta^T} GA_s \boldsymbol{B}^v d\Omega \tag{2.2.21b}$$

$$\boldsymbol{k}^{v\theta} = -\int_{\Omega_e} \boldsymbol{B}^{v^T} GA_s \boldsymbol{N}^{\theta} d\Omega \tag{2.2.21c}$$

$$\boldsymbol{k}^{vv} = \int_{\Omega_e} \boldsymbol{B}^{v^T} GA_s \boldsymbol{B}^v d\Omega \tag{2.2.21d}$$

$$\boldsymbol{f}_\theta = -\int_{\Gamma_{e_M}} \boldsymbol{N}^{\theta^T} T \, d\Gamma \tag{2.2.21e}$$

$$\boldsymbol{f}_v = \int_{\Gamma_{e,Q}} \boldsymbol{N}^{v^T} F_y \, d\Gamma + \int_{\Omega_e} \boldsymbol{N}^{v^T} f_y d\Omega \tag{2.2.21f}$$

As an example, with one-point numerical integration, the stiffness matrix looks like:

$$\boldsymbol{K} = \begin{bmatrix} \frac{EI}{L} + \frac{GA_sL}{4} & -\frac{EI}{L} + \frac{GA_sL}{4} & \frac{GA_s}{2} & -\frac{GA_s}{2} \\ -\frac{EI}{L} + \frac{GA_sL}{4} & \frac{EI}{L} + \frac{GA_sL}{4} & \frac{GA_s}{2} & -\frac{GA_s}{2} \\ \frac{GA_s}{2} & \frac{GA_s}{2} & \frac{GA_s}{L} & -\frac{GA_s}{L} \\ -\frac{GA_s}{2} & -\frac{GA_s}{2} & -\frac{GA_s}{L} & \frac{GA_s}{L} \end{bmatrix} \tag{2.2.22}$$

2.2.2 Nonlinear finite element method

Structural behavior can roughly be divided in two categories: linear behavior and nonlinear behavior. Linear behavior is a simplified model of material behavior and a good approximation in the case of small deformations and rotations or infinitesimal strains, i.e. cases in which the relations between the stresses and the strains are linear. This also implies that on material level, no yielding may occur. In the case of linear elastic behavior, the stiffness matrix $\boldsymbol{K}$, which describes the relation between the forces and the displacements, is constant. The result is that for every load in the linear elastic region, the corresponding displacement can be found instantly. Because of the latter, linear finite element analyses have very fast calculation times. Also, the principal of superposition can be used.
In contrast to the linear relations in the linear finite element equations, the nonlinear finite element method is far more challenging. Nonlinearities have different causes. In structural mechanics, the most common ones are geometric nonlinearities and material nonlinearities.

2.2.2.1 Geometric nonlinearity

In the most common cases, the changes in geometry as a result of deformations are not taken into account in the relation between the deformations and the strains. This is often a valid approximation, because for most problems in civil engineering, the strains are small and therefore the use of complex relations between displacements and strains have almost no added accuracy, while they make the calculations far more difficult. There are often many examples for which this approximation does not hold. A well-known example is a cable structure, the geometry changes for different loading conditions. Also buckling of a column is a well-known example of nonlinear behaviour, where the deformations result in higher order forces, which change the force-displacement relations.
Measurements to take these problems into account are different formulations of stresses and strains and to update these relations during loading. Commonly, the Green-Lagrange strain tensor is used

instead of the engineering strain. Also, stresses can be represented by the second Piola-Kirchhoff stress tensor which plots the stresses in the fibre direction instead of the Cauchy stress tensor.

2.2.2.2 Material nonlinearity

A material nonlinearity occurs when a material is loaded by its yield strength for some time. When this occurs, depending on the material, cracks and permanent deformations or rotations can occur.
Material nonlinearities occur in the constitutive equations, which describe the behavior of the material, the stress-strain relations.
Material behavior can be described by yield functions. Well-known yield functions are the Mohr-Coulomb yield function for soils and the Von Mises yield function (Figure 2.8) for steel. A yield function gives a combination of principal stresses for which plasticity will occur. These combinations are bounded by the yield surface. Hardening and softening (cracking) of materials can be described by expanding and shrinking yield functions.
Because the relation between stresses and strains changes in the case of plasticity, the stiffness matrix $\boldsymbol{K}$ has to be updated during the calculation. The calculations are therefore done with an incremental approach. The load or displacement is added in small steps.
The incremental approach is explained in the next section.

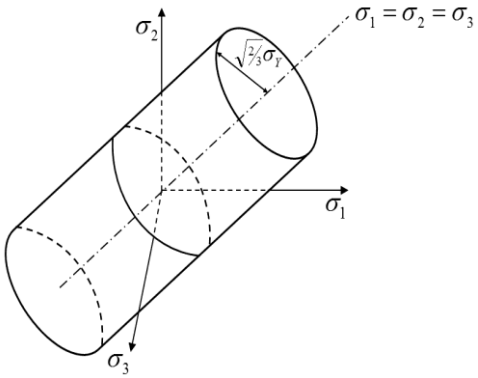

Figure 2.8; Von Mises Yield surface [27]

2.2.2.3 Incremental iterative approach

The easiest way to do an incremental procedure is to split the force of equation 2.2.1 in an internal part and an external part. In an equilibrium point the external load equals the internal load:

$$\boldsymbol{f}_{int}^{t} = \boldsymbol{f}_{ext}^{t} \tag{2.2.23}$$

A load increment is applied:

$$\boldsymbol{f}_{ext}^{t+\Delta t} - \boldsymbol{f}_{e}^{t} = \Delta \boldsymbol{f}_{e} \tag{2.2.24}$$

The current stiffness matrix, which is derived by linearizing the stress-strain relations in the equilibrium point, is used to calculate the corresponding displacement increment:

$$\Delta \boldsymbol{a} = \boldsymbol{K}^{-1}\left(\boldsymbol{f}_{ext}^{t+\Delta t} - \boldsymbol{f}_{i}^{t}\right) \tag{2.2.25}$$

After the load step, the new tangent stiffness matrix is calculated and the procedure continues.
Unfortunately, this method has a downside that there is no control mechanism. Because the nonlinear stress-strain and displacement-strain relations are linearized, the solution with this algorithm, drifts away from the real solution (Figure 2.9).

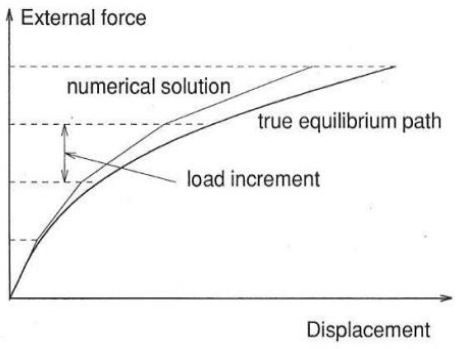

Figure 2.9; Drifting tendency of a purely incremental approach [13]

This can be overcome by adding iterations in the calculation procedure. A common way to do this is by using a Newton-Raphson procedure. The procedure is visible in Figure 2.10.
In this way the error is calculated after every load step and a better estimation is made until the error is sufficiently small. This results in an accurate estimation of the load-displacement relation.

The procedure starts with the displacement and force at the beginning from which the stress and strain are derived. The relation between the stress and the strain determines the tangent stiffness operator $\boldsymbol{K}$. A force increment is added from which the displacement increment is calculated:

$$\Delta \boldsymbol{a}^{\mathbf{1}} = (\boldsymbol{K}^0)^{-1}\left(\boldsymbol{f}_{ext}^{t} + \Delta \boldsymbol{f}_{ext} - \boldsymbol{f}_{int}^{0}\right) \tag{2.2.26}$$

With the kinematic and constitutive relations, the strains and stresses are calculated from the displacement increments.
The new stress is given as:

$$\boldsymbol{\sigma}^{\mathbf{1}} = \boldsymbol{\sigma}^0 + \Delta \boldsymbol{\sigma}^1 \tag{2.2.27}$$

With this stress, the new internal force in this load step is calculated.

$$\boldsymbol{f}_{int}^{1} = \int_V \boldsymbol{B}^T \boldsymbol{\sigma}^{\mathbf{1}} dV \tag{2.2.28}$$

With the new found internal force, an equilibrium check can be done by calculating the difference between the internal force and the external force:

$$\boldsymbol{r}_{\mathbf{1}} = \boldsymbol{f}_{ext}^{t} + \Delta \boldsymbol{f}_{ext} - \boldsymbol{f}_{i}^{1} \tag{2.2.29}$$

First the new tangent stiffness operator is calculated with the new stresses and strains. After this, the new variation of the displacement is calculated:

$$\boldsymbol{da}^2 = (\boldsymbol{K}^1)^{-1}\boldsymbol{r}^1 \tag{2.2.30}$$

The displacement increment is updated. From this increment the new strains and stresses are calculated:

$$\Delta \boldsymbol{a}^2 = \Delta \boldsymbol{a}^1 + \boldsymbol{da}^2 \tag{2.2.31}$$
$$\boldsymbol{\sigma}^2 = \boldsymbol{\sigma}^0 + \Delta \boldsymbol{\sigma}^2 \tag{2.2.32}$$

From the new stresses the new internal force and unbalance is calculated:

$$\boldsymbol{f}_{int}^{2} = \int_{V} \boldsymbol{B}^{T}\boldsymbol{\sigma}^{\boldsymbol{2}} dV \tag{2.2.33}$$

$$\boldsymbol{r}^{2} = \boldsymbol{f}_{ext}^{1} + \Delta\boldsymbol{f}_{ext} - \boldsymbol{f}_{int}^{2} \tag{2.2.34}$$

Now a convergence criterion is needed to determine if the solution is accurate enough. An often-used force convergence criterion is based on the L_2-norm of the force vectors.

$$\left\|\boldsymbol{f}_{ext} - \boldsymbol{f}_{int,j}\right\|_2 \leq \epsilon \times \left\|\boldsymbol{f}_{ext} - \boldsymbol{f}_{int,1}\right\|_2 \tag{2.2.35}$$

In words, convergence is reached when the difference between the L_2-norm of the external force minus the internal force of iteration j is smaller than a certain convergence tolerance ϵ times the L_2-norm of the external force minus the internal force of the first iteration. The convergence tolerance is commonly set on $\epsilon = 10^{-3}$. Important to notice is that the criterion is relative, as it is calculated on the unbalance of the first iteration. The accuracy of the first iteration is therefore important. Also, the value of the convergence tolerance is important. When the tolerance is too low, the solution is probably not accurate. A tolerance which is too high results in long calculation times with negligible increase in accuracy [13].

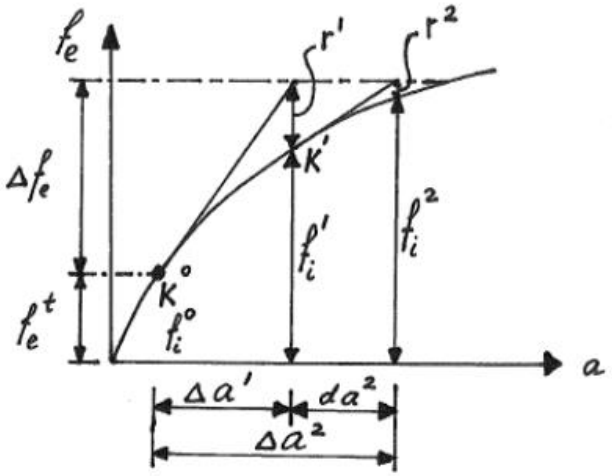

Figure 2.10; Newton-Raphson incremental iterative approach [13]

In the regular Newton-Raphson iterative approach. The tangent stiffness matrix is updated every iteration. This is not necessary. There are different schemes in which the tangent stiffness matrix is updated only at the beginning of a load increment (Modified Newton-Raphson), or a scheme where the linear elastic tangent stiffness matrix is used in every load step.
The advantage is that the tangent stiffness matrix does not have to be calculated every iteration, which saves calculation time at this point. A disadvantage is that the estimated displacement becomes worse which results in more iterations. Depending on the situation, it could reduce the calculation time.

2.2.2.4 Difficulties in the incremental iterative approach

While the incremental iterative approach seems robust, there are enough examples where issues occur and different solution techniques have to be used.

An example of a situation where difficulties occur is in the case of snap-through behavior (Figure 2.11). The procedure explained in the previous section is force controlled as a force increment is added every load step. This results in a singular stiffness matrix and therefore divergence when a peak load is reached, because no intersection with the external force is found. This is of course, because there is none. A solution for this problem is by using a displacement-controlled analysis. The displacement vector is split into two parts, one part with displacements that have to be calculated and a part with displacements that have been assigned with a certain displacement. The tangent stiffness matrix is therefore also composed in four parts. Therefore, a smaller part of the stiffness matrix is used to calculate the wanted displacements, which leads to a better conditioned stiffness matrix.

$$\begin{bmatrix} \boldsymbol{K}_{ff} & \boldsymbol{K}_{fp} \\ \boldsymbol{K}_{pf} & \boldsymbol{K}_{pp} \end{bmatrix} \begin{bmatrix} \Delta \boldsymbol{a}_f \\ \Delta \boldsymbol{a}_p \end{bmatrix} = -\boldsymbol{f}_{int,0} \tag{2.2.36}$$

$$\Delta \boldsymbol{a}_{f,1} = -\boldsymbol{K}_{ff}^{-1}\left(\boldsymbol{K}_{fp}\Delta \boldsymbol{a}_p + \boldsymbol{f}_{int,0}\right) \tag{2.2.37}$$

Although, the snap-through behavior can be calculated with this approach, the snap-back behavior of Figure 2.12 still results in a singular matrix and therefore divergence. This behavior can be calculated with the use of a path-following technique. The arc-length control technique is mostly used in this case.

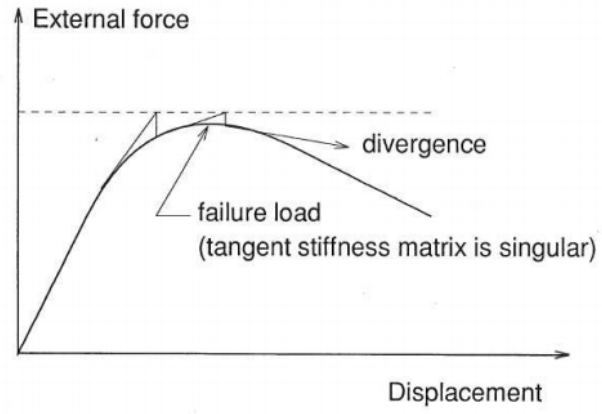

Figure 2.11; Divergence for snap-through behavior [13]

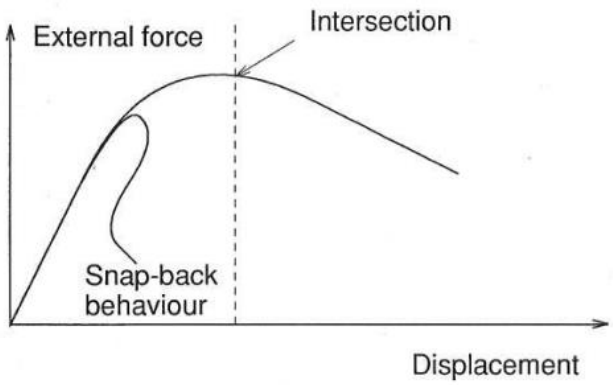

Figure 2.12; Divergence for snap-back behavior [13]

In an acr-length controlled analysis, instead of prescribing a force or a displacement, the norm of the increment in the load-displacement curve is prescribed (Figure 2.13). The size is chosen during the increment. The incremental external force is scaled with a load factor $\Delta\lambda_i$. Equation (2.2.25) can be written as:

$$\Delta \boldsymbol{a}^{j+1} = \boldsymbol{K}_i^{-1}(\Delta\lambda \hat{\boldsymbol{f}}_{ext} + \boldsymbol{f}_{ext}^{t} - \boldsymbol{f}_{int,j}) \tag{2.2.38}$$

The displacement is cut in two parts, one part which is calculated from the initial forces. The second part is from the external load component. The total displacement vector can be calculated with equation (2.2.40).

$$d\boldsymbol{a}_{\boldsymbol{j+1}}^{I} = \boldsymbol{K}^{-1}\left(\boldsymbol{f}_{ext}^{t} - \boldsymbol{f}_{int,j}\right) \tag{2.2.39}$$

$$d\boldsymbol{a}_{j+1}^{II} = \boldsymbol{K}^{-1}\hat{\boldsymbol{f}}_{ext} \tag{2.2.40}$$

$$d\boldsymbol{a}_{j+1} = d\boldsymbol{a}_{j+1}^{I} + \Delta\lambda_{j+1} d\boldsymbol{a}_{j+1}^{II} \tag{2.2.41}$$

In this analysis, the scalar load increment factor $\Delta\lambda$ is an extra variable. It is calculated by using the Euclidean norm, which stays constant during the load step:

$$\Delta\boldsymbol{a}_{j+1}^{T}\Delta\boldsymbol{a}_{j+1} + \beta^2\Delta\lambda_{j+1}^{2}\hat{\boldsymbol{f}}_{ext}^{T}\hat{\boldsymbol{f}}_{ext} = \Delta l^2 \tag{2.2.42}$$

In equation (2.2.42), the weight factor β and the length of the equilibrium path Δl are user-specified. In this case, the arc length method uses a circular method to calculate the next load step. This can be simplified by linearizing the incremental displacement and the load factor. This is made visible in Figure 2.13.

$$\Delta\boldsymbol{a}_{j+1}^{T}\Delta\boldsymbol{a}_{j+1} = \Delta\boldsymbol{a}_{j}^{T}\Delta\boldsymbol{a}_{j+1} \tag{2.2.43}$$

$$\Delta\lambda_{j+1}^{2} = \Delta\lambda_j\Delta\lambda_{j+1} \tag{2.2.44}$$

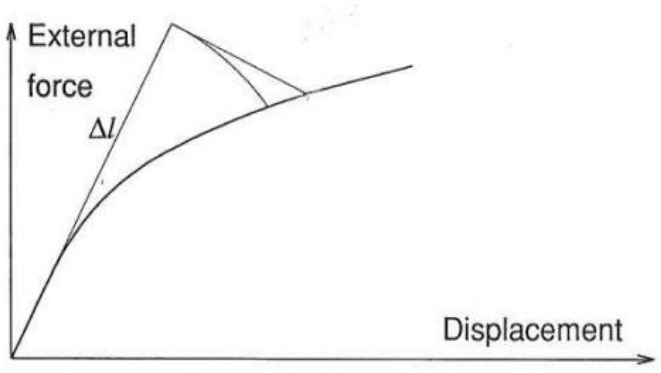

Figure 2.13; Circular and linearized constraint conditions [13]

Although the arc-length method can overcome snap-back behaviour. The incremental iterative approach is still very sensible for convergence errors. Great skills and practise are needed to find the correct results and validate that this is the case. Especially in the case of brittle materials, like masonry or concrete, several cracks can occur in a single increment. This can lead to drops in strength that even the arc-length method cannot calculate. The method is in those cases not very robust. Other proposals exist of different methods which are more robust. One example is the sequentially linear analysis which will be used in this research. In the next section, this method will be explained.

2.3 The sequentially linear Analysis

Nonlinear numerical computations to calculate the strength of structures are popular. Especially in the case where the ultimate strength of for example old structures, that possibly do not meet the requirements we demand of structures these days, is investigated. In those cases, a nonlinear finite element analysis can possibly proof that a building which does not meet the requirements of the design codes is still strong enough.
Naturally, a computational method must be reliable. The results should be correct and issues in the method must be avoided. A very popular method is an incremental iterative technique. In these methods, an increment is added to a parameter, for instance the load, and with the help of an iterative scheme, the corresponding displacements are found. Most of the times a Newton-Raphson scheme is used, like explained in the previous section. Although these methods can give good results, they often suffer from convergence issues especially in the case of very brittle materials like concrete or masonry. These convergence issues mainly occur due to snap-through and snap-back behavior where the numerical method cannot follow the path, because of convergence issues on element level. These issues are occurring because of ill-conditioned matrices in post-peak behavior. This can lead to results that cannot be trusted. Users have to be very skillful to obtain sound results and different advanced techniques like the path finding technique arc-length control are required.
A finite element technique that can avoid these convergence issues would be very helpful.
In 2001, Rots [14] proposed a new technique as a solution to this problem. This technique is called the sequentially linear analysis (SLA). The basis of this technique is a stepwise degradation of the material. Instead of load increments, damage increments are taken.
The load on the structure is scaled in a linear elastic calculation. In the first integration point were a limit point is reached, the stiffness is reduced with the help of a stepwise secant material law or saw-tooth law. This is repeated again and again until in theory all integration points are totally damaged, but in practice, often a maximum number of steps is defined.

2.3.1 Theory

As told before, although there are good iterative incremental approaches, there is no method that is unconditionally stable. The reasons for this are mostly convergence issues with crack opening in concrete or masonry structures.
The sequentially linear analysis procedure is based on the idea of reduced stiffness in the area where the material cracks. The reducing of the stiffness is automated in the procedure [1]. When an element reduces in stiffness due to a crack, the material has to redistribute the stresses, which results in a new situation. Only one element can be broken per cycle.

A characteristic of the sequentially linear analysis is the stepwise secant material law. This material law is a stepwise approximation of the nonlinear constitutive relation between the stresses and strains in a material.

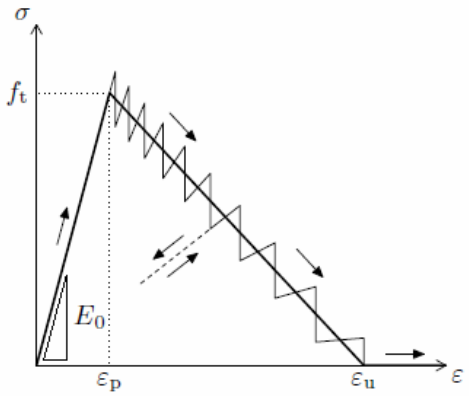

Figure 2.14; A stepwise secant material law [1]

In a linear elastic material, the relation between the principle stresses and principle strains can be described by Hook's law:

$$\sigma = E\epsilon \tag{2.3.1}$$

The reduced stiffness means that the elasticity of the material will decrease in a stepwise manner. This is visible in the figure above by the slopes of the saw teeth. The linear continous softening curve is approximated by the toothed material law. When the relation between the Young's modulus and the strain is plotted, a relation like in Figure 2.15 appears.
In this graph, it is visible that for certain strain levels, the Young's modulus drops in a stepwise manner. In this way, it approaches the nonlinear continious curve.
The secant stiffness can be written as a degrading function with a discrete damage parameter:

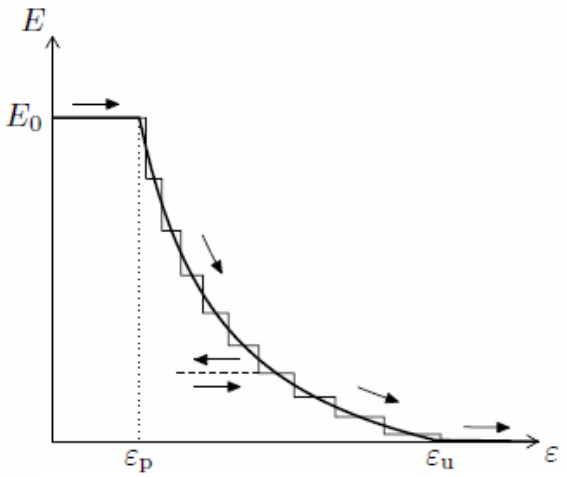

Figure 2.15;Relation Young's modulus and strain [1]

$$E = (1 - d)E_0 \tag{2.3.2}$$

With d the damage parameter between 0 and 1, E_0 the initial Young's modulus.
An important thing to notice is that the unloading is in a secant manner instead of in an elastic manner. According to Van de Graaf [1] this is not problematic for elasto-plastic materials in monotonic loading, because unloading occurs only locally.

The procedure works by the following steps [14]:
First the external load is added as a unit load, a critical element is found where the stress is closest to the yield strength. The critical global load is calculated by dividing the strength over the stress and multiplying that factor with the unit load. Calculate the displacement of this load.
Reduce the stiffness of the critical element to the next step in the stepwise material law.
Run the whole procedure again until a maximum number of steps has been passed. But other abort criterions are also possible, like a maximum deflection or when certain elements are cracked. Plot the results of the loads and displacements.
In other procedures, the critical multiplier λ is calculated for every integration point as:

$$\lambda_{crit;i} = \frac{f_i}{\sigma_i} \tag{2.3.3}$$

The smallest λ_{crit} leads to the smallest critical load for which a crack appears and is therefore the multiplier sought. At that location, the damage will occur first. By following this algorithm, the procedure has an event-by-event strategy.

2.3.2 Proportional and non-proportional loading

To successfully run an analysis, a difference has to be made between proportional and non-proportional loading. If loads are proportional, they increase and decrease with the same factor in every step. In a realistic situation, most loads are not proportional. For example, the self-weigh of a structure can often be regarded as constant, while the life load is variable. In a sequentially linear analysis, these load cases have to be held separate, because the load multiplier λ cannot be applied to all loads as this would result in proportional scaling. Several solutions of this problem are proposed in [1]. One of them will be explained here.

Every analysis step begins with considering the initial non-proportional load with load multiplier λ_{ini} only. First λ_{ini} is scaled until an integration point comes in a critical state. If this happens for $\lambda_{ini} < 1$, critical points occur before the full initial load is applied. In this case, the non-proportional load is applied in a proportional way until the full initial load is applied ($\lambda_{ini} = 1$), then the second part starts. When $\lambda_{ini} \geq 1$ after the first step, no damage is initiated and the second part starts i.e. the initial load stage has ended. In the next part, the non-proportional load and the proportional load are combined with two different load multipliers: λ_{ini} and λ_{ref}.

In general cases the following equation can be stated:

$$\boldsymbol{F}_{crit}^{j} = \lambda_{ini}^{j}\boldsymbol{F}_{ini} + \lambda_{ref}^{j}\boldsymbol{F}_{ref} \quad with\ \lambda_{ini}^{j} = 1\ and\ \lambda_{ref}^{j} = \lambda_{crit}^{j} \tag{2.3.4}$$

Speaking in the global stress relations, the global stresses are calculated as a sum of the stresses as a result of the constant initial load and the stresses by the proportional load [15]. In plane stress conditions, this is relatively easy as a direct solution method is available for the principal shear stress:

$$\sigma_{xx} = \sigma_{xx,c} + \lambda * \sigma_{xx,v} \tag{2.3.5a}$$

$$\sigma_{xx} = \sigma_{xx,c} + \lambda * \sigma_{xx,v} \tag{2.3.5b}$$

$$\sigma_{xy} = \sigma_{xy,c} + \lambda * \sigma_{xy,v} \tag{2.3.5c}$$

$$\sigma_{(1,2)}(\lambda) = \frac{1}{2}\left(\sigma_{xx} + \sigma_{yy}\right) \pm \sqrt{\frac{1}{4}\left(\sigma_{xx} - \sigma_{yy}\right)^2 + \sigma_{xy}^2} \tag{2.3.5d}$$

At a certain analysis step, a situation can occur that no critical load multiplier λ_{crit}^{j} can be found. This is the case when the initial load already violates the yield criterion in this step. Two strategies can be applied at this point. The first strategy (a) reduces the proportional part to 0, and searches for a critical load multiplier for the initial load only. The second strategy (b) works in a different manner. This strategy involves temporarily solving the following equation:

$$\boldsymbol{F}_{crit}^{j} = \bar{\lambda}_{crit}^{j}\boldsymbol{F}_{crit}^{j-1} + \bar{\lambda}_{ref}^{j}\boldsymbol{F}_{ref} \tag{2.3.6}$$

With:

$$\bar{\lambda}_{crit}^{j} = 1 \quad and \quad \bar{\lambda}_{ref}^{j} = \lambda_{crit}^{j} \tag{2.3.7}$$

In this case, the new reference load is not scaled from the initial load, but directly from the last iteration. This has the result that the same ratio between the initial load and the proportional load is kept before applying the new reference load. The advantage will be explained later.
When a failure point occurs without a fully applied initial load, the following conditions are adapted:

$$\bar{\lambda}^{j}_{crit} = \lambda^{j}_{crit} \quad and \quad \bar{\lambda}^{j}_{ref} = 0 \tag{2.3.8}$$

Now, the initial load and the reference load are scaled until a failure point occurs. Again, the difference in this method is that both the initial load and the proportional load are reduced with the same ratio as in the previous step. This is made visible in Figure 2.16.

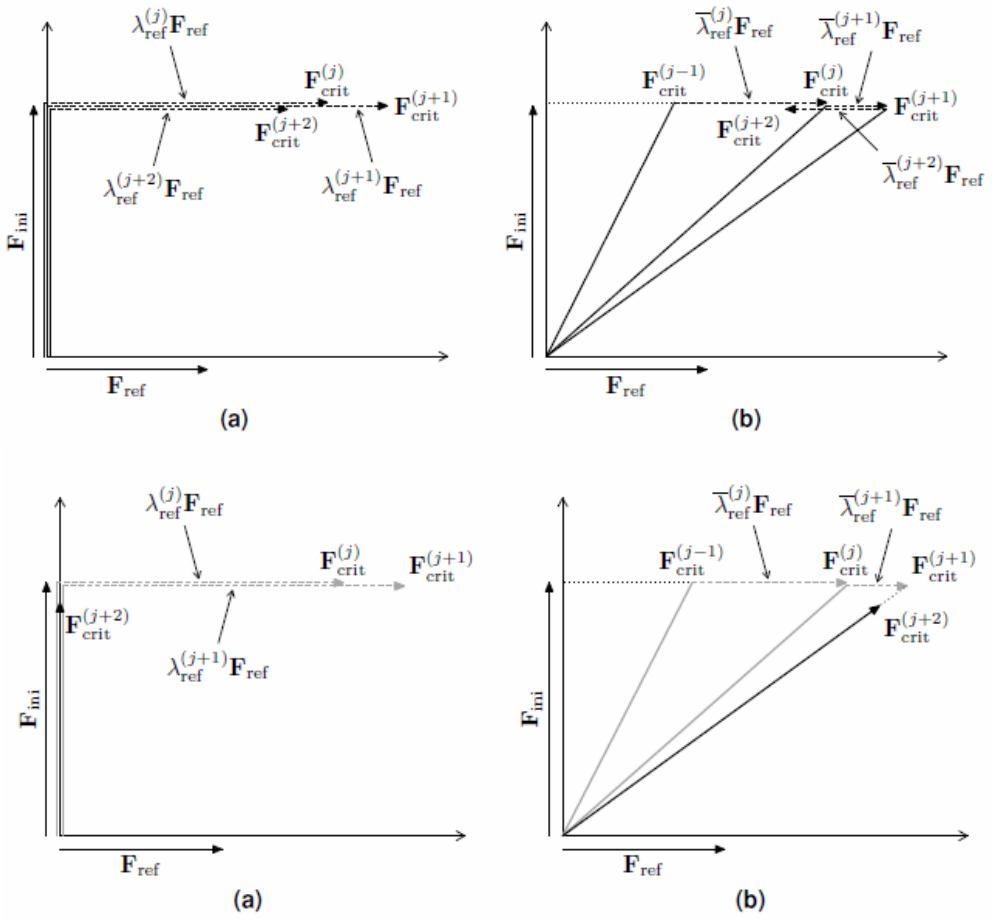

Figure 2.16; Visual explanation of the two double load multiplier strategies (a) and (b) for three analysis steps. Above are normal iterations, below iterations where the full initial load cannot be applied [1]

The big advantage of the second method is that the ratio between the initial load and the proportional load stays the same. The first method has as disadvantage that in the situation that the initial load is reduced, cracks will occur because of this load only. These cracks can therefore occur at places which are not correct. Therefore, the second method is preferred.

2.3.3 Stepwise secant material laws

The improved band width ripple concept as derived by Van de Graaf [1] will be explained. This method is chosen, because it is the recommended method. The original idea of the band width ripple concept was found by Rots. In the figure below, the continuous softening curve is banded by two dashed lines.

The band is shifted with pf_t to the positive and negative vertical direction. This band has therefore a width of $2pf_t$. The material law can be set up by switching from the uplifted curve to the curve which is lifted down and back. First, the current stiffness E is used to determine the intersection with the uplift curve. The corresponding strength and strain are calculated, $f_{t,k}^{+}$ and ϵ_k. From here, the lower bound is found:

$$f_{t,k}^{-} = f_{t,k}^{+} - 2pf_t \tag{2.3.9}$$

And from there the new stiffness is found:

$$E_{k+1} = \frac{f_{t,k}^{-}}{\epsilon_k} \tag{2.3.10}$$

This procedure is aborted when the stiffness E becomes negative. For difficult not explicit softening tails, the strain can be calculated in an iterative way.

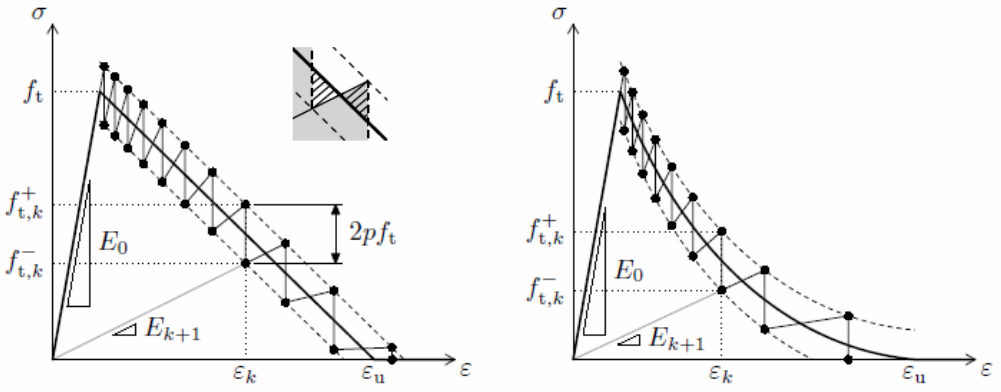

Figure 2.17; Band width ripple concept with linear (left) and nonlinear (right) softening [1]

This method is improved because there was still not a fracture energy invariant saw-tooth law.
Especially for nonlinear softening curves, the triangles of the overpredictions and underpredictions are not equal.

The improvement is in the fact that when the shifts are not equal but scaled, the net over and underprediction can be nil. In this approach, the upper curve is shifted with $p_1 f_t$ and the lower curve with $p_2 f_t$. Van de Graaf stated two requirements [1]:

1. The area enclosed by the saw-tooth law (which represents the amount of dissipated energy) should be equal to the area enclosed by the base material law.
2. The ultimate strain of the saw-tooth law should be equal to the ultimate strain of the base material law.

The iterative procedure is explained below:
First, the band width parameters p_1 and p_2 are estimated. After this, the teeth of the stepwise secant material law are calculated in the same manner as in the previous method.
In the next step, the energy dissipation and the ultimate strain are calculated:

$$\left(\frac{G_f^I}{h}\right)^* = \frac{1}{2}\epsilon_N p_1 f_t + \sum_{k=1}^{N-1} \frac{1}{2}\,\epsilon_k (p_1 + p_2) f_t \tag{2.3.11}$$

With the first term, the area of the last triangle and the second term, the area of the triangle couples.

$$\epsilon_u^* = \epsilon_N \tag{2.3.12}$$

Now there is a final check, whether the energy dissipation is small enough:

$$1 - \frac{\frac{G_f^I}{h^*}}{\frac{G_f^I}{h}} \;<\; \epsilon_{tol} \tag{2.3.13}$$

$$\left(1 - \frac{\epsilon_u^*}{\epsilon_u}\right)^2 + \left(\frac{\sigma_u^*}{f_t}\right)^2 < \epsilon_{tol} \tag{2.3.14}$$

The rest of the algorithm makes use of the smeared crack model. In the smeared crack model, cracks are smeared out over the area that belongs to an integration point. Smeared cracking has the advantage that cracks can occur everywhere in the material. With a discrete crack model, the cracks are predefined with interface elements. For a smeared crack model, the direction of the crack is free. The direction of the crack is perpendicular to the direction of the principal tensile stress.
A crack cooridnate system can be defined with crack axes n and t. n is the axis normal to the crack, while the t-axis is in the tangential direction. This coordinate system is fixed at that point, therefore this approach is called the fixed crack approach.
Now plane stress conditions are used to derive the constitutive relations between stresses and strains:

$$\begin{bmatrix}\sigma_{xx}\\ \sigma_{yy}\\ \sigma_{xy}\end{bmatrix} = \frac{E_0}{1-\nu_0^2}\begin{bmatrix}1 & \nu_0 & 0\\ \nu_0 & 1 & 0\\ 0 & 0 & \frac{1-\nu_0}{2}\end{bmatrix}\begin{bmatrix}\epsilon_{xx}\\ \epsilon_{yy}\\ \gamma_{xy}\end{bmatrix} \tag{2.3.15}$$

The smeared crack model which will be used, is now derived according to [1].
A crack occurs when somewhere in the material, the principal stress σ_1 equals the tensile strength f_t. When the material cracks, the constitutive relations are changed to implement the reduced stiffness. Two augmented Young's moduli tangential to the crack and perpendicular to the crack are introduced. Because the strains and stresses are also influenced by the Poisson's ratio, this quantity has to be reduced as well.

$$\nu_{tn} = \frac{\nu_0 E_n}{E_0} \quad ; \quad \nu_{nt} = \frac{\nu_0 E_t}{E_0} \tag{2.3.16}$$

The new constitutive relations become:

$$\begin{bmatrix}\sigma_{nn}\\ \sigma_{tt}\\ \sigma_{nt}\end{bmatrix} = \frac{1}{1-\nu_{tn}\nu_{nt}}\begin{bmatrix}E_n & \nu_{nt}E_n & 0\\ \nu_{tn}E_t & E_t & 0\\ 0 & 0 & (1-\nu_{tn}\nu_{nt})G\end{bmatrix}\begin{bmatrix}\epsilon_{nn}\\ \epsilon_{tt}\\ \gamma_{nt}\end{bmatrix} \tag{2.3.17}$$

Originally the shear modulus is represented as:

$$G = \beta G_0 = \beta \frac{E_0}{2(1+\nu_0)} \tag{2.3.18}$$

The shear modulus also has an augmented version. The reason is that in the fixed crack model, the principal directions can vary from the original direction at crack initiation. This can result in building shear stresses at the crack. The shear modulus is therefore represented as the result of the smallest Young's modulus and Poisson's ratio:

$$G = \frac{E_{min}}{2(1+\nu_{\min})} \tag{2.3.19}$$

$$E_{min} = \min(E_n, E_t) \quad and \quad \nu_{min} = \min(\nu_{tn}, \nu_{nt}) \tag{2.3.20}$$

A disadvantage of the smeared crack model is that the crack is a function of the element dimensions. The crack band width h is an important parameter used in those relations.

$$h = \sqrt{2A} \quad or \quad h = \sqrt{A} \tag{2.3.21}$$

This relation holds for linear and higher order elements respectively, with A the area of the element. Along with the crack opening w, the crack extensional strain ϵ_{cr} can be described as:

$$\epsilon_{cr} = \frac{w}{h} \tag{2.3.22}$$

The total strain can be described as the sum of the elastic strain and the crack strain:

$$\epsilon_k = \epsilon^{el} + \epsilon^{cr} \tag{2.3.23}$$

$$with \quad \epsilon^{el} = \frac{\sigma}{E_0} \tag{2.3.24}$$

Different relations between the crack stress and the crack strain can be set up. In [1], the linear, exponential and nonlinear relations are shown. Important points in those relations are the crack strain $\epsilon^{cr} = 0$ when $\sigma = f_t$ and $\sigma = 0$ when $\epsilon^{cr} = \epsilon_u^{cr}$.

Back to the improved band width model. The raised stress can be calculated with the strain from the equation above:

$$\underline{f_{t,k}^+} = E_k \epsilon_k \tag{2.3.25}$$

This limit is compared with the limit from the saw tooth diagram:

$$f_{t,k}^+ = \sigma_k + p_1 f_t \tag{2.3.26}$$

When the difference is smaller than a predefined tolerance, this strain is used to calculate the new stiffness:

$$E_{k+1} = \frac{f_{t,k}^{+} - \Delta\sigma_k}{\epsilon_k} \tag{2.3.27}$$

with

$$\Delta\sigma_k = \begin{cases} (p_1 + p_2) f_t & \text{if } 0 \leq k < N \\ p_1 f_t & \text{if } k = N \end{cases} \tag{2.3.28}$$

2.3.4 Current state of the art, simulating brittle failure

One of the last examples of studying the brittle failure of masonry walls and structures with a sequentially linear analysis is done by Anne van de Graaf in his PhD research in 2017 [1].
Among other numerical analyses, an analysis was performed on a masonry façade. The model is visible in Figure 2.18. A macro-modelling approach is applied with plane stress elements. The structure is subjected to self-weight, several nodal forces and a support settlement. The façade has a clamped support at the right corner and two vertical supports in the middle and at the left corner.
First the self-weight and nodal forces are applied as a non-proportional load. Next, a settlement is applied the left support as a proportional load.

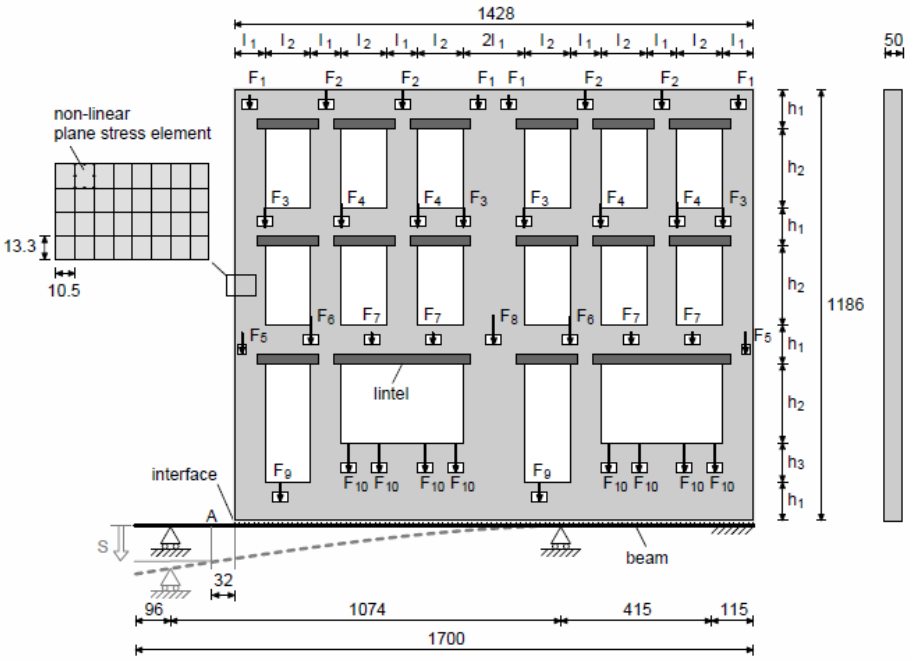

Dimension (mm)		Nodal forces (N)			
$l_1 =$	84	$F_1 =$	230	$F_6 =$	469
$l_2 =$	126	$F_2 =$	296	$F_7 =$	195
$h_1 =$	106	$F_3 =$	319	$F_8 =$	498
$h_2 =$	218	$F_4 =$	392	$F_9 =$	304
$h_3 =$	108	$F_5 =$	358	$F_{10} =$	467

Figure 2.18; Masonry facade model of Van de Graaf [1]

The first thing to mention is the importance of a criterion for the initial non-proportional load. In this example, there were 2478 steps needed before the non-proportional load was fully applied. This means that there were already many micro-cracks at the end of this load phase. The value of the load multiplier has to reach a value of 1 before the proportional load can be applied, because else the structure already failed because of the non-proportional load. In the case of proportional loading, the global load multiplier is of importance. Sometimes in the analysis, the program reduces the initial load because the structure is not able to bear the proportional load and the initial load at that time. With a reduction of the initial load, the next weakest integration point can still be found and after several

steps, the program can increase the initial load multiplier to a value of 1. However, this temporary reduction should not become too large and not for too many steps. For example, when the value of the global load multiplier $\lambda_{global} < 0.3$, the structure can be regarded as failed, because in the case of self-weight, the structure is not able to bear 0.3 of its own weight.
Also, the number of saw-teeth and the mesh size attributes to this behavior.

Another interesting type of behavior was found in the rightest pier of the lowest row. This pier behaved differently compared with other piers. In most piers, a crack opened and the crack width increased during the analysis. At this location, a crack opened, but closed after several analysis steps. The tension load that was previously in the pier, transformed into a compressive load. While this crack closure behavior is realistic in real life, it caused problems in the sequentially linear analysis procedure. The crack occurred because of the settlement of the support, the crack occurred because of a positive strain at that point in the cross-section. Several steps later, the positive strain is transformed into a negative strain which indicates compression and a crack closure. Because a crack occurred at this location, the damage variable was around the value of 1, which means that the stiffness is around 0. Therefore, the negative strain that occurred later, did not result in a compression stress, while that should be the case as a cracked cross-section can still transfer compressive stresses. Although the sequential linear analysis was able to give a robust simulation of the behavior of the structure, this crack closure problem has to be solved in order to make the behavior more accurate and realistic.

2.3.4.1 New developments for non-proportional loading

In section 2.3.3, an introduction was given to different types of non-proportional loading. As non-proportional loading in a sequentially linear analysis is still difficult to handle, new techniques to solve this problem are briefly mentioned here.
The techniques for SLA described early, all follow the classical load-unload (L-U) method. As explained before, in each analysis step, the structure is fully unloaded and reloaded. This is the case for the non-proportional load and the proportional load. This method is simple and robust as every analysis step is separate. A disadvantage is that it implies that the structure distributes the unbalanced forces as a result of the damage very fast over the whole structure, while the material neighboring the crack has an infinitely slow relaxation time [16]. In reality it is often visible that damage in a structure leads to damage in neighboring elements due to load increase as a result of the initial damage. This can be missed by applying the L-U method as the structure is immediately unloaded.
A different proposed solution for the use of non-proportional loading is suggested by Eliáš [17], which is called the force release (F-R) method. This is the opposing method of the L-U method as it forces the structure to redistribute the unbalanced forces ($\Delta\sigma^{(S)}$) as a result of the crack, in the neighboring elements or nodes.
Each time damage occurs, the unbalanced forces are added to the structure in the neighboring elements. It is possible that these elements are able to carry this extra force. Then the next step is initiated. If the neighboring elements are not able to carry the load, another element is damaged and the new unbalanced forces are added. This process will continue until all unbalanced forces have disappeared and new equilibrium is found. Neighboring elements can break sequentially as a result of this knock-on effect, which is often realistic. A downfall of this approach in that this method is unable to describe snap-back behaviour. It has been proven in by Eliáš et al. [17] that the solutions of the schemes L-U and F-R can be different even in the case of proportional loading.
The F-R method and the L-U method are the extreme cases of a newer method called the general method, developed by Eliáš [16]. The general method is introduced as a method which combines both approaches. It introduces a parameter ω which can be set to find a balance between the L-U method and the F-R method. It is possible to simulate snap-back behaviour with this approach.

The unbalanced forces from the F-R method ($\Delta\sigma$) are split up in two parts:

$$\Delta\sigma = \Delta\sigma^{(S)} + \omega\Delta\sigma^{(L)} \tag{2.3.29}$$

In which $\Delta\sigma$ is the external load, $\Delta\sigma^{(L)}$ is the external load increment and $\Delta\sigma^{(S)}$ are the unbalanced forces. When ω reaches high values for a positive or negative number, the redistribution is relatively slow compared to load changes [16].
Figure 2.19 shows graphically the effect of the parameter ω. When $\omega = 0$. This means that the external load is kept constant and everything is redistributed. This is similar to the F-R method as all the residual forces are distributed in the neighboring elements.
There exists a ratio for which the redistribution exactly finishes in the origin of the load-displacement coordinate system. This corresponds to point C. This is exactly the case in the L-U method, where the structure unloads every step.
Further damage is not possible in this direction as the stresses decrease to zero for all integration points. The direction in this case is $\omega^{(C)} = -\delta_A/\Delta\delta^{(L)}$. The ratio between the current point in the load-displacement graph and the current load.

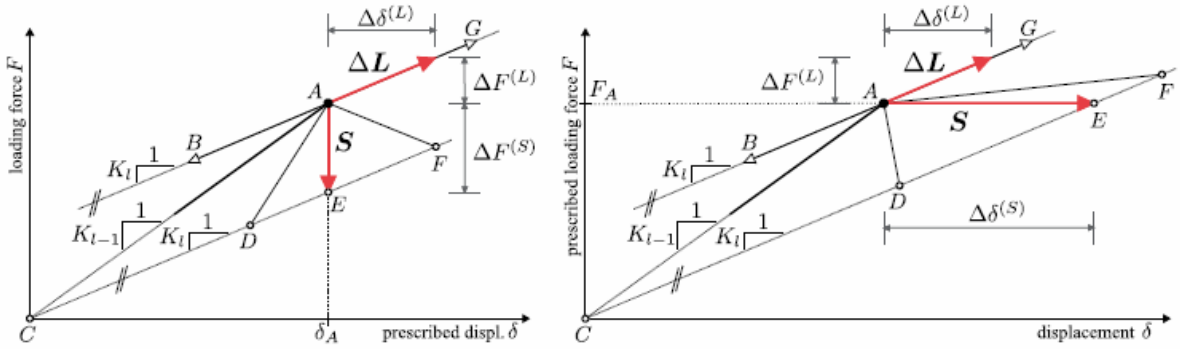

Figure 2.19; Possible directions of system response in force-deflection space during redistribution; Left: loading by a prescribed displacement, right: loading by a force. [16]

Currently, the research group of Pari, Rots and Hendriks developed a new method for non-proportional loading by reformulating the problem. The solution proposed should make it possible to do a non-proportional sequentially linear analysis for a three-dimensional stress situation. Currently, this is further investigated.

For plane stress situations it is easy to find the critical load multiplier as the global stresses can be constructed using relation $(2.3.5d)$. In a three-dimensional case, this is difficult as the eigenvalues of the stress tensor, with size $(3x3)$, are found using a cubic equation which cannot be solved directly.
To solve this, the problem was reformulated as an optimization problem in [15]. The two-dimensional variant will be briefly described here.
The normal stress on a plane is expressed as a function of the inclination of the plane to the reference axis with angle θ [15]. The load multiplier is a function of this angle $\left(\lambda = f(\theta)\right)$ as a relation can be derived for the load multiplier as a function of the stresses on the rotated plane.
When a minimum value of $\lambda(\theta)$ is found, the corresponding value for θ will give the rotation to the cracked coordinate system $(n, t$-coordinate system). As this function $\lambda(\theta)$ is periodical, only one maximum and minimum can be found in every period which are the load factors corresponding to the largest positive stress and the largest minimum stress. These factors are found with an optimization algorithm with linear convergence and guaranteed stability.
A single element test and a quasi-static pushover test on a masonry wall confirmed that this solution procedure is valid by comparing it with other non-proportional strategy tests.
To extend this method to a three-dimensional case, some difficulties have to be solved. The optimization method will be with two variables which requires an advanced technique. Also, the reduction to one period is not possible, so it has to be made sure that the found maximum is a global maximum and not a local maximum [15].

2.4 Equivalent Frame Method

The equivalent frame method is a model in which the computational time is reduced a lot compared to micro- and even macro-modelling. It is a simplification of structural components as an assemblage of numerically integrated beam elements.
According to [2], the entire pier or spandrel is modelled as an inelastic element in which the sectional response is evaluated via a fiber discretization in which each fiber may follow a material uniaxial nonlinear stress-strain relation. Different types of these models are: Fiber Flexural Model (FFM) with a linear shear response (purely flexural response) and the Fiber Flexure – Lumped Shear model (FF-LSM) in which the shear behavior is described as a nodal interface element placed between two nodes of adjacent elements. The shear behavior is modelled with an equivalent Coulomb-type criterion for a shear force limit. This chapter will mostly focus on the work done by Nobel [2] as this thesis will continue on his work.
Important are the failure mechanisms of masonry piers as discussed in section 2.1.4:

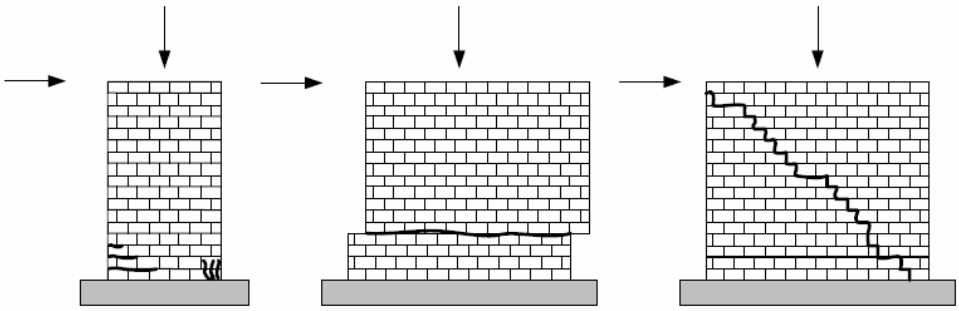

Figure 2.20; Failure mechanisms with lateral force; rocking (left), shear sliding (middle) and diagonal cracking (right) [2]

Rocking: Cracks start to propagate at the heel of the wall. Therefore, the force has to be carried by the compressive part, which is decreasing as cracks grow. This compressive part eventually crushes and the wall overturns.
Shear sliding: A sliding plane develops because the horizontal shear resistance cannot withstand the lateral force. A horizontal tensile crack occurs in the bed joints. Sliding occurs for low vertical loads.
Shear cracking: A diagonal zigzag pattern occurs between the bricks or through the bricks. This is dependent on the strength of the mortar, mortar-brick interface and the strength of the bricks.

2.4.1 Theory of the model

When a masonry building fails under seismic loading, a large part of the damage is situated in the piers and spandrels. The piers and spandrels are modelled as ideally elastic-plastic beam-column elements in which the chord rotation is limited. The joints are modelled infinitely stiff.
The original idea was given by Magenes and Della Fontana in 1998. They introduced a simple frame model for a non-linear static pushover analysis and found satisfying results, with relatively little calculation time [18].

With the total chord rotation θ as the sum of the flexural rotation ϕ and the shear deformation γ:

$$\theta = \phi + \gamma$$

Which is limited to 0.5% for shear failure and to 1% for flexural failure [18].

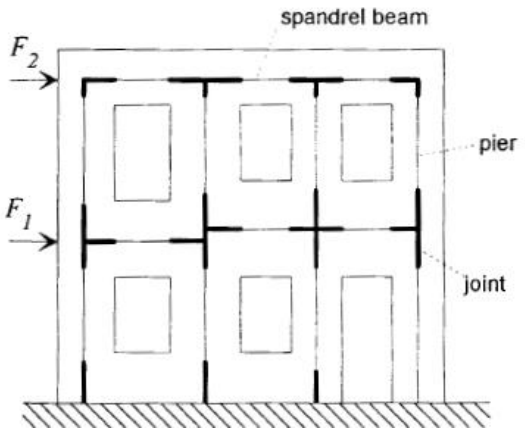

Figure 2.21; Equivalent frame idealization of a multistory wall with openings [18]

2.4.2 The different models

Nobel uses three model approaches for the façade in his thesis: One isotropic continuum model and 2 equivalent frame models. The continuum model is used to compare the results and calculation time of the two equivalent frame models. The continuum model has two categories. One of them with a three-zoned approach. In this way, cracking of the bed joint will probably take place in the top or bottom layer, while diagonal shear takes place diagonal over the element.

Important to notice is the fact that although masonry is anisotropic in material points, it can be seen as isotropic in diagonal cracking. For his single wall tests, he uses two different continuum models.

In the approach of Nobel, the two continuum models are the following:

The first model has all piers and spandrels represented by finite plane stress elements with the same material properties, the Continuum Model (CM). The joint tensile strength is used as the critical strength.

The second model has two extra layers with lower strength and lower fracture energy. This is done to approach the rocking failure of the piers and spandrels. In this model, the two extra layers are in the region where cracking along the bed joint probably will occur, and the original layer is in the region where diagonal cracking probably will occur. This model is called the Three Zoned – Continuum Model (TZ-CM). This continuum model is also used when modelling the façade.

The flexural parts are modelled with the bed joint tensile strength, the joint fracture energy and the compression strength of masonry.

In the continuum model, eight-node quadrilateral (CQ16M) plane stress elements are used.

Secondly, the fiber flexural model only considers the global response of the structure. It uses the DIANA Class III Mindlin beam elements, which include flexural and shear deformation. This element class will be discussed in section 2.5. In this method, the entire element is an inelastic element contrary to the continuum model, therefore inelasticity can also occur in the element. It is also dependent on material parameters and not on empirical strength domains.

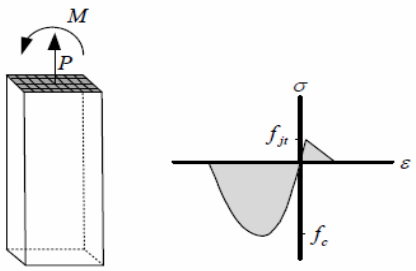

Figure 2.22; Stress strain relation of masonry bed joint [2]

However, the shear response is still linear elastic, therefore no diagonal cracking mode will take place [2]. The uniaxial behavior is governing for the flexural response. Therefore, the bed joints determine the material properties with a linear tension curve and a parabolic compression curve.

Third the Fibre Flexure – Lumped Shear model will be discussed.

In this model, the elements are modified to include shearing failure modes. In the previous elements, only linear elastic behavior was possible. A structural nodal interface is added to describe the relation

between normal and shear tractions and normal and shear relative displacements within the interface [2].
Two failure behaviors are added in the model. The tension model described earlier and the bilinear shear traction law. The model uses the interface element N4IF.

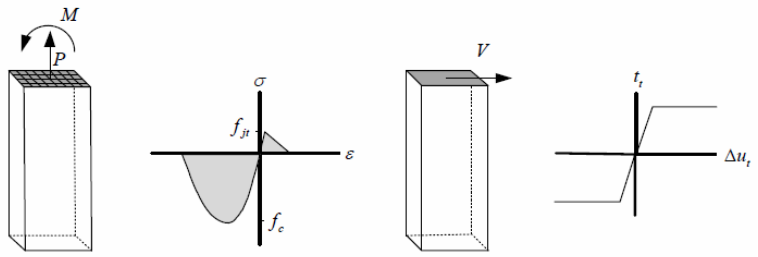

Figure 2.23; Flexural response (left) and shear response (right) [2]

Sliding shear failure is modelled with Coulomb friction (sliding of two surfaces), elastic perfectly plastic behavior. Because only one nodal interface describes the shear behavior of an element, the cohesion and friction angle are global strength parameters. This leads however to an overestimation because of weak head joints, a nonlinear shear stress distribution and a reduced section length because of tension cracks [2]. Corrections are: presence of weak head joints by Mann and Muller, include shear stress distribution effect by Magenes and Calvi, consider only the effective uncracked
section length by Abrams.

2.4.3 Two story masonry building

The two-story masonry building experiment from the University of Pavia is an experiment performed by Magenes, Calvi and Kingsley [19] on a full scale two story masonry building. The experiment set-up is simplified in [2] to make a two-dimensional model. The experiment will be explained here because this building will be used to perform a sequentially linear analysis.
The structure was built at the University of Pavia from typical building materials used in old Italian urban constructions like solid, fired clay bricks. The mortar is a mix of hydraulic lime and sand (1:3 volume). The building is loaded in plane with the door wall and the rear wall or windows wall (Figure 2.24). The building has two floors of steel I section beams. Two vertical loads of 248.4 kN and 236.8 kN are applied on the first and second floor respectively. The seismic load of an earthquake was simulated by four horizontal point loads on the floors of the building. Two on each side of the wall.

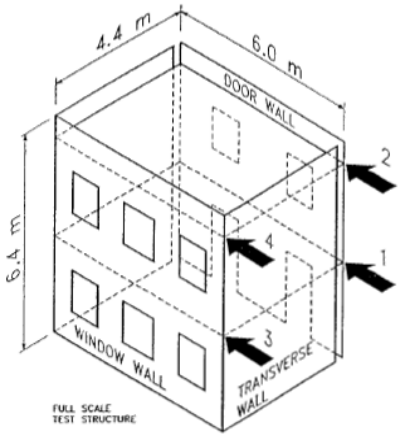

Figure 2.24; Two story full scale building [19]

It was found from tests with a shaking table that the four horizontal loads were almost equal for most experiments, because the behaviour of the structure was dominated by the flexible floors. The mass of the two floors and the peak acceleration were almost the same for the two floors which resulted in almost equal forces. The floors are pinned to the walls, therefore the loads on the walls are also almost equal [19].
In the experiment, the building was subjected to a cyclic load. Before cracking the pattern consists of a preliminary loading cycle followed by two cycles at the desired maximum displacement and one degradation cycle. After cracking, there will be two preliminary cycles, three maximum displacement cycles and two degradation cycles.

Found was, that the door wall was in practice an independent system from the windows wall and the two side walls. This was a result of the weak coupling of the flexible floor beams. The longitudinal force transfer through the floor was negligible [19].
The results were shown in a force-displacement relation, in which the force was the shear in the base of the designated wall and the displacement, the horizontal displacement of the second floor.
This relation is shown in Figure 2.25.

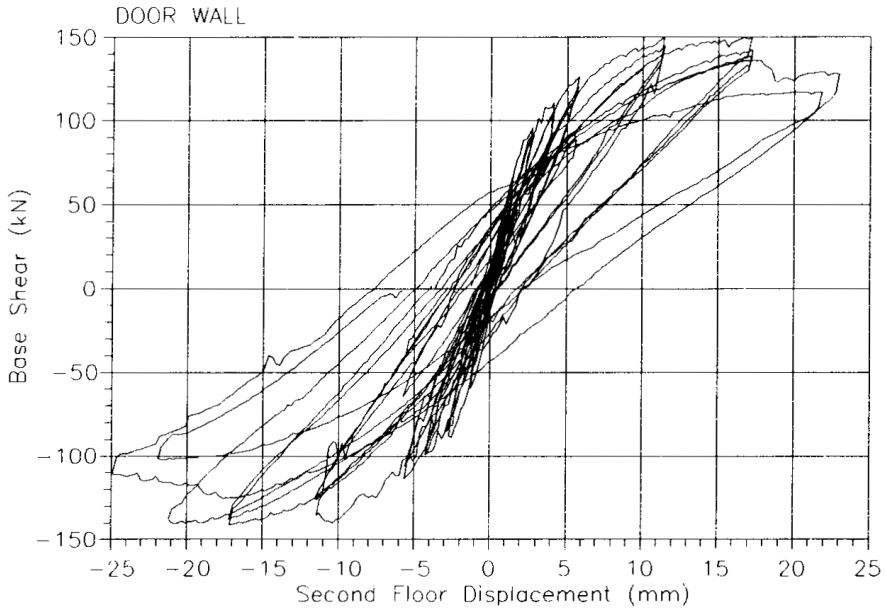

Figure 2.25; Base shear in relation to the second-floor displacement, door wall [19]

As noted in their report, it was remarkable that an unreinforced masonry structure did manage to achieve an ultimate displacement which was twice as large as the displacement at the peak load.
The damage pattern was difficult. First, cracking occurred in the spandrels, especially on the first floor. These cracks stopped propagating however and the dominating failure mechanism was shear cracking in the central pier. Further in the analysis, also the exterior piers failed in shear.
The shear failure in the central wall was in both diagonal directions while the shear failure in the exterior piers was in one direction, because of the overturning effect of the horizontal loads resulting in a combined rocking, shear dominated failure mode.

2.4.4 Results

Two tests are done in [2], a masonry wall is tested and a 2-story façade. The important results are summarized below. Because the focus lies on the equivalent frame approach, the continuum model results will not be discussed.

2.4.4.1 Masonry Panel

The first test is done on a single masonry pier. This to validate the model for one panel before applying it to a façade. In the test, a masonry pier is subjected to a constant vertical force. At the same time, a horizontal displacement is increased at the top. In real life this test was done at Delft University of Technology. The experimental data of that test is used to compare the results. The pier is discretized with two small beam elements, one at the top and one at the bottom, and five larger sized beam elements at the middle part of the beam. In the numerical simulation, the horizontal force is increased until failure occurs or an ultimate displacement is reached. A regular Newton-Raphson iteration scheme is used to solve the equations, with a combined force and displacement norm.

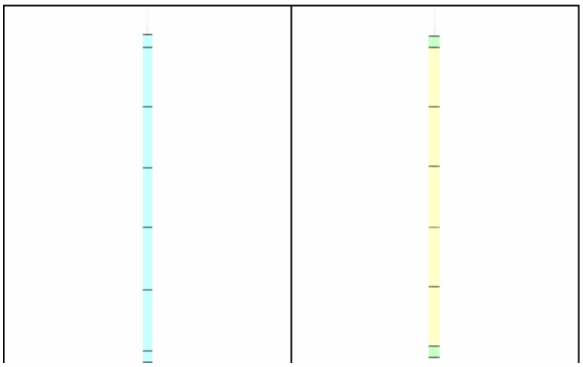

Figure 2.26; FFM model type a (left) and type b (right) [2]

In Figure 2.26, two alternatives are presented. The FFM model type a is the model described in the previous part. In FFM model type b, the bed joint fracture energy is slightly reduced in the top and bottom element, similar to the three-zoned continuum model.

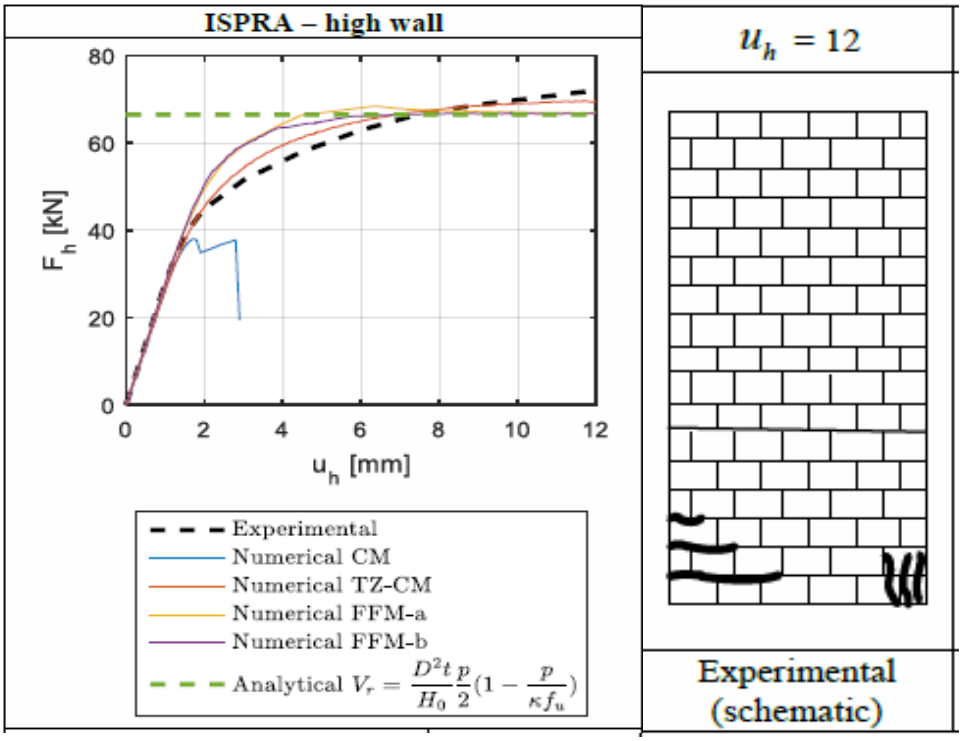

Figure 2.27; High wall model results [2]

For the high wall model (Figure 2.27) both FFM models are very similar to the experimental data. The high wall failed in rocking and therefore, the Fibre Flexural model is very capable of predicting the strength.

In Figure 2.28 the results for the low wall experiment are showed. These results overestimate the capacity of the wall. The failure branch is also not found. This is because the FFM model is not able to reproduce the diagonal crack pattern as shear failure is not included, while the wall definitely failed in shear. Now the same wall is simulated with the Fibre flexural lumped shear model to introduce the shear failure mechanism. Different Coulomb friction criteria are implemented to investigate which criterion perform the best.

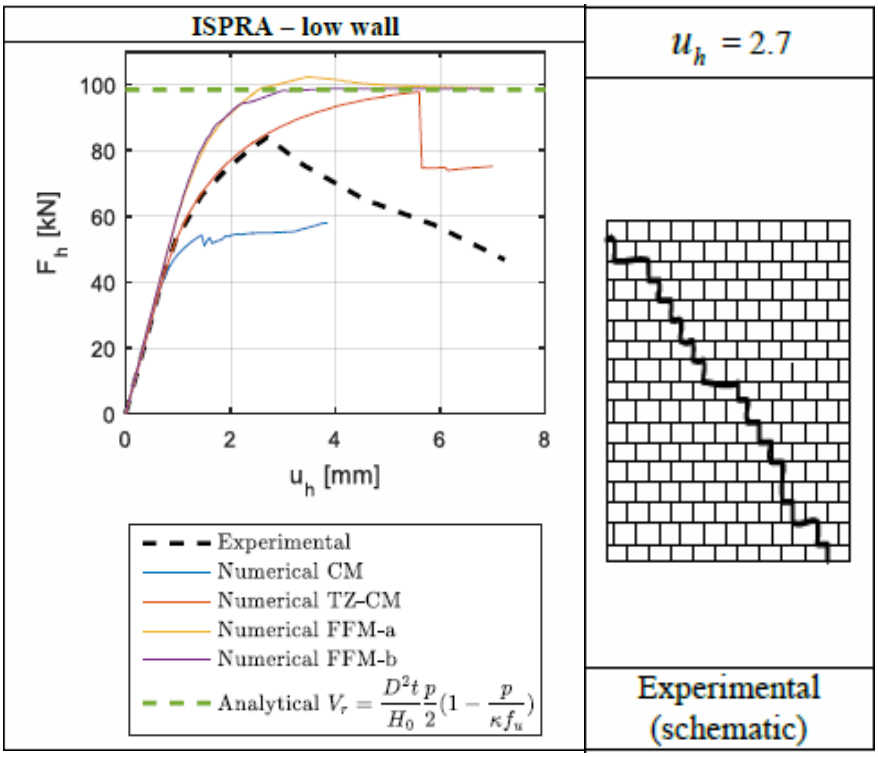

Figure 2.28; Force displacement results for the low wall experiment [2]

2.4.4.2 Two-story masonry façade results

This experiment is done on the building discussed in section Two story masonry building2.4.3. The results will be discussed here.

The FFM model is set up by using 82 beam elements in the piers and spandrels, the same way as in section 2.4.4.1 with model FFM type a. The two constant loads on the floors 1 and 2 are:

$p_1 = 20.7\ \mathrm{kN/m}$ and $p_2 = 19{,}8\ \mathrm{kN/m}$.

At the left two tyings are made in Diana to mount a steel beam to both floors. This beam is loaded with a prescribed monotonic displacement. The analysis is therefore displacement controlled.

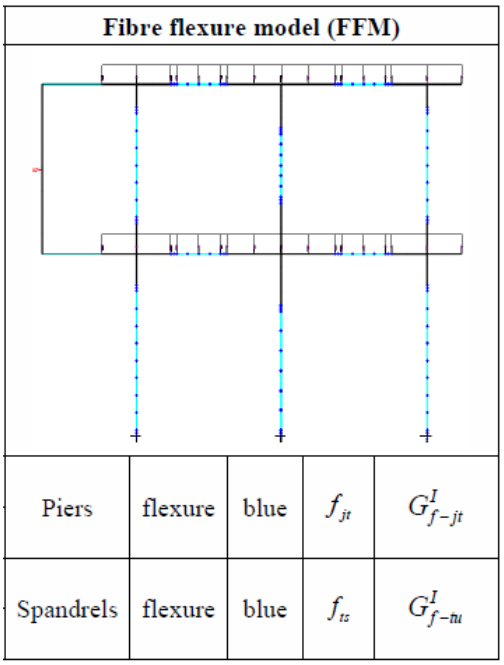

Figure 2.29; Fibre flexural model for the two-story building [2]

To make a good comparison with the experimental results, a nonlinear curve should be extracted from the cyclic loading curve of the experiment. This is done by creating a contour around the peak values of the load and the associated displacements.

First the analysis is performed with the FFM model. Here, the strength of the piers and spandrels are based on the joint tensile strength of the material. Not the maximum tensile strength. This results in a flexural response of the structure. Stiffness reductions and cracks occur in in the piers in this model. Almost no flexural damage was discovered in the spandrels. The peak strength was somewhat higher with FFM compared to the experimental results. An explanation can be that the material parameters and isotropic material model should be adjusted because it is not precise enough. A second explanation is the fact that a structure fails with a lower load in cyclic loading than in monotonic loading. In the experiment, cyclic loading is used which could give a lower peak load than in the FFM. The accuracy of the solution was nonetheless acceptable. The calculation time of FFM compared to the continuum model was less than one tenth.

At last, the FF-LSM is used to make a calculation that includes shear failure parameters. In this model, 66 beam elements are used and one interface element per pier or spandrel (10 in total). The boundary conditions are assumed as double fixed. Different shear failure criteria are used in different analyses. In general, the accuracy of the solution was increased, while maintaining the short calculation time. A negative effect was the occurrence of serious convergence problems. The conclusion drawn from this experiment was therefore that the fibre flexural model with lumped shear interfaces has many advantages in calculation time and simplicity while maintaining accuracy. However, the convergence problem that arose have to be solved to make this method more applicable.

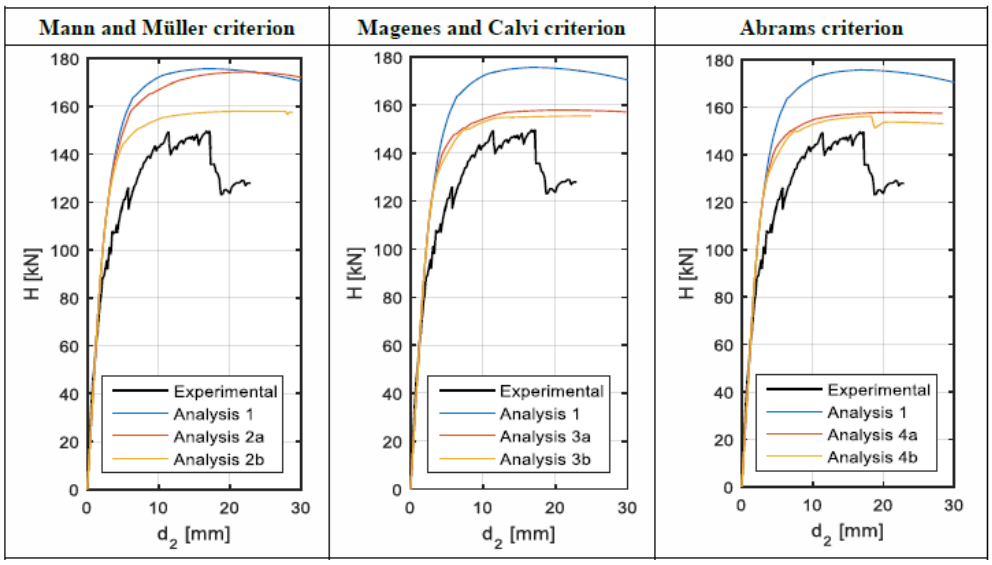

Figure 2.30; Results of various FFM-LSM analyses with different shear criteria [2]

In Figure 2.30 the results for the different shear criteria are shown. Analysis 1 is the FFM analysis. The shear failure was most correctly described by the Magenes and Calvi criterion because it found the experimentally observed failure modes (shear failure in pier P2, pier P3 and in both spandrels on the first floor). The Abrams criterion did not find the correct response in pier P3.

Table 2.1; Different shear criteria for the FF-LSM [2]

Analysis	Shear strength criterion			Softening	
	Pier	Shear span	Spandrel	Pier	Spandrel
1	-	-	-	-	-
2a	Mann and Müller	P	Mann and Müller	-	-
2b	Mann and Müller	P	Beyer	-	-
3a	Magenes and Calvi	P	Beyer	-	-
3b	Magenes and Calvi	PS	Beyer	-	-
3c	Magenes and Calvi	PS	Beyer	LS+DL	-
4a	Abrams	P	Beyer	-	-
4b	Abrams	PS	Beyer	-	-
LS+DL = Linear Softening + Drift Limitation; P = priori; PS = posteriori;					

The last analysis concerns analysis 3c (Figure 2.31) in which the Magenes and Calvi criterion is used with linear softening. By using this technique, the softening behavior was initiated, but the calculation could not continue because of convergence issues. The strength degradation started in pier P2.

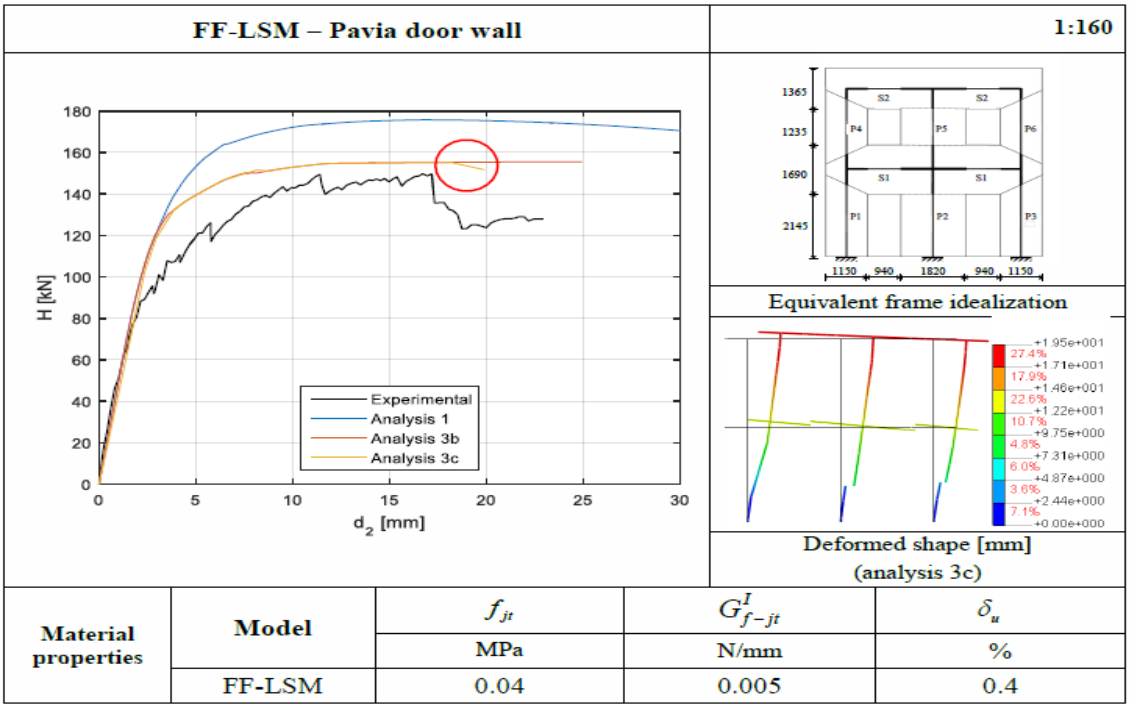

Material properties	Model	f_{jt}	G^{I}_{f-jt}	δ_u
		MPa	N/mm	%
	FF-LSM	0.04	0.005	0.4

Figure 2.31; Force-displacement curves for different analysis [2]

The most important conclusion drawn from this thesis is that the FF-LSM can accurately describe the rocking and shearing failure modes of a masonry wall, while reducing the calculation time with a tenth of the time of the continuum model. According to [2], the best way to use the beam model is by adding a small beam element at each and of each pier. This should be used next to an integration scheme with two Gaussian integration points along the bar axis and eleven fibre integration points over the area of the beam element. The choice of the failure criterion should be made carefully because not all criteria are even precise.

In this thesis, the two-story building model is used combined with a sequentially linear analysis to try to solve the convergence problems that arose in this thesis.

2.5 Mindlin Beam elements (fiber-section model)

To successfully apply the sequential linear analysis on the structure, the finite elements have to be applicable for this method. Common beam elements are not because the displacements and rotations are related directly to the moments and forces, while reduced stiffness has to be applied to the constitutive relations in a sequential linear analysis. Generally speaking, displacements are "assumed" in the nodes in finite element formulations. From these displacements, the strains in the integration points are calculated. With the constitutive relations, the stresses are calculated in the integration points. From these stresses the forces in the nodes are calculated. These forces are compared with the load on the structure. If the differences are sufficiently small, the displacements are accepted. When the solution is not precise enough, better displacements are proposed to fulfill the requirements.
In a fiber section model, everything is calculated from the stress-strain relationship. This relationship is based on the material parameters and is therefore a more accurate starting point.

2.5.1 Derivation of the fiber section model

The fiber section beam model used in this thesis is derived by Ferreira [3]. Small changes are made by Pari to make this model suitable for a sequential linear analysis. The model of Ferreira uses a smeared crack approach with rotating cracks for tensile behaviour. It assumes a constant shear stress along the cross-section. In the constitutive relations, the compressive behaviour is modelled using a parabola, the tensile behaviour is linear elastic with a linear descending branch after cracking. In a sequentially linear analysis, these relations will be approached with a saw-tooth law.

In a fiber section discretization, the cross-section of for instance a beam is divided in multiple fibers. The equilibrium, constitutive and compatibility equations of each fiber are derived and with it, the stresses and strains in the fibers are calculated. From these relations, the stiffness matrix is derived for incremental variations:

$$\begin{pmatrix} \Delta\sigma_{xx} \\ \Delta\sigma_{zz} \\ \Delta\tau_{xz} \end{pmatrix} = \begin{pmatrix} D_{11} & D_{12} & D_{13} \\ D_{21} & D_{22} & D_{23} \\ D_{31} & D_{32} & D_{33} \end{pmatrix} \begin{pmatrix} \Delta\epsilon_{xx} \\ \Delta\epsilon_{zz} \\ \Delta\gamma_{xz} \end{pmatrix} \tag{2.5.1}$$

Because the stress $\Delta\sigma_z$ should be equal to 0, the following equation must hold:

$$D_{21}\Delta\epsilon_{xx} + D_{22}\Delta\epsilon_{zz} + D_{23}\Delta\gamma_{xz} = 0 \tag{2.5.2}$$

Also, the increment of the shear stress $\Delta\tau_{xz}$ must be equal to the fixed shear stress given:

$$\Delta\tau_{xz} = \Delta\tau^* \tag{2.5.3}$$

From (2.5.1):

$$\Delta\tau_{xy} = D_{31}\Delta\epsilon_{xx} + D_{32}\Delta\epsilon_{zz} + D_{33}\Delta\gamma_{xz} = \Delta\tau^* \tag{2.5.4}$$

This leads to:

$$\Delta\gamma_{xz} = \frac{\Delta\tau^* - D_{31}\Delta\epsilon_{xx} - D_{32}\Delta\epsilon_{zz}}{D_{33}} \tag{2.5.5}$$

This can be substituted into equation (2.5.2) and rewritten:

$$D_{21}\Delta\epsilon_{xx} + D_{22}\Delta\epsilon_{zz} + \frac{D_{23}}{D_{33}}(\Delta\tau^* - D_{31}\Delta\epsilon_{xx} - D_{32}\Delta\epsilon_{zz}) \tag{2.5.6}$$

$$\left(D_{21} - \frac{D_{23}D_{31}}{D_{33}}\right)\Delta\epsilon_{xx} + \frac{D_{23}}{D_{33}}\Delta\tau^* + \left(D_{22} - \frac{D_{23}D_{32}}{D_{33}}\right)\Delta\epsilon_{zz} = 0 \tag{2.5.7}$$

$$(D_{33}D_{21} - D_{23}D_{31})\Delta\epsilon_{xx} + D_{23}\Delta\tau^* + (D_{33}D_{22} - D_{23}D_{32})\Delta\epsilon_{zz} = 0 \tag{2.5.8}$$

$$\Delta\epsilon_{zz} = \frac{(D_{23}D_{31} - D_{33}D_{21})\Delta\epsilon_{xx} - D_{23}\Delta\tau^*}{D_{33}D_{22} - D_{23}D_{32}} \tag{2.5.9}$$

Now this expression is used to rewrite equation (2.5.5):

$$\Delta\gamma_{xz} = \frac{\Delta\tau^*}{D_{33}} - \frac{D_{31}\Delta\epsilon_{xx}}{D_{33}} - \left(\frac{D_{32}}{D_{33}}\right)\frac{\left((D_{23}D_{31} - D_{33}D_{21})\Delta\epsilon_{xx} - D_{23}\Delta\tau^*\right)}{D_{33}D_{22} - D_{23}D_{32}} \tag{2.5.10}$$

$$D_{33}\Delta\gamma_{xz} = \frac{(D_{33}D_{22} - D_{23}D_{32})\Delta\tau^* - (D_{33}D_{22} - D_{23}D_{32})D_{31}\Delta\epsilon_{xx}}{D_{33}D_{22} - D_{23}D_{32}} - \frac{D_{32}\left((D_{23}D_{31} - D_{33}D_{21})\Delta\epsilon_{xx} - D_{23}\Delta\tau^*\right)}{D_{33}D_{22} - D_{23}D_{32}} \tag{2.5.11}$$

$$\Delta\gamma_{xz} = \frac{(D_{32}D_{21} - D_{31}D_{22})\Delta\epsilon_{xx} + D_{22}\Delta\tau^*}{D_{33}D_{22} - D_{23}D_{32}} \tag{2.5.12}$$

Now all functions can be expressed in the parameters $\Delta\epsilon_{xx}$ and $\Delta\tau^*$.
Next, two equilibrium conditions need to be fulfilled within the fiber. Namely, the unbalance in the vertical stress $\delta\sigma_{zz}$ should be 0 and the difference between shear stress $\Delta\tau_{xz}$ and the fixed value $\Delta\tau^*$, defined as $\delta\tau_{xz}$, should be equal to 0. These parameters can be expressed with:

$$\begin{pmatrix}\delta\sigma_{zz}\\ \delta\tau_{xz}\end{pmatrix} = \begin{pmatrix}D_{22} & D_{23}\\ D_{32} & D_{33}\end{pmatrix}\begin{pmatrix}\delta\epsilon_{zz}\\ \delta\gamma_{xz}\end{pmatrix} \tag{2.5.13}$$

This can be rewritten to express $\delta\epsilon_{zz}$ and $\delta\gamma_{xz}$ in terms of the other parameters:

$$\delta\epsilon_{zz} = \frac{\delta\sigma_{zz} - D_{23}\delta\gamma_{xz}}{D_{22}} \tag{2.5.14a}$$

$$\delta\gamma_{xz} = \frac{\delta\tau_{xz} - D_{32}\delta\epsilon_{zz}}{D_{33}} \tag{2.5.14b}$$

By combining these expressions:

$$\delta\epsilon_{zz} = \frac{D_{33}\delta\sigma_{zz} - D_{23}(\delta\tau_{xz} - D_{32}\delta\epsilon_{zz})}{D_{22}D_{33}} \tag{2.5.15}$$

Follows in:

$$\delta\epsilon_{zz} = \frac{D_{33}\delta\sigma_{zz} - D_{23}\delta\tau_{xz}}{D_{22}D_{33} - D_{23}D_{32}} \tag{2.5.16}$$

This can be used in equation $(2.5.14b)$ and rewritten:

$$D_{33}\delta\gamma_{xz} = \delta\tau_{xz} - D_{32}\frac{D_{33}\delta\sigma_{zz} - D_{23}\delta\tau_{xz}}{D_{22}D_{33} - D_{23}D_{32}} \tag{2.5.17}$$

$$D_{33}(D_{22}D_{33} - D_{23}D_{32})\delta\gamma_{xz} = \delta\tau_{xz}D_{22}D_{33} - \delta\tau_{xz}D_{23}D_{32} - D_{32}D_{33}\delta\sigma_{zz} + D_{32}D_{23}\delta\tau_{xz} \tag{2.5.18}$$

$$\delta\gamma_{xz} = \frac{\delta\tau_{xz}D_{22} - D_{32}\delta\sigma_z}{D_{22}D_{33} - D_{23}D_{32}} \tag{2.5.19}$$

Iteratively, convergence must be searched with the result: $\delta\epsilon_{zz} = 0$ and $\delta\tau_{xz} = 0$. This results in a stress σ_{zz} with a value of 0. Therefore, the model can be reduced to:

$$\begin{pmatrix}\sigma_{xx}\\0\\\tau_{xz}\end{pmatrix} = \begin{pmatrix}D_{11} & D_{12} & D_{13}\\D_{21} & D_{22} & D_{23}\\D_{31} & D_{32} & D_{33}\end{pmatrix}\begin{pmatrix}\epsilon_{xx}\\\epsilon_{zz}\\\gamma_{xz}\end{pmatrix} \tag{2.5.20}$$

Leads to:

$$\epsilon_{zz} = -\frac{D_{21}}{D_{22}}\epsilon_{xx} - \frac{D_{23}}{D_{22}}\gamma_{xz} \tag{2.5.21}$$

And finally:

$$\begin{pmatrix}\sigma_{xx}\\\tau_{xz}\end{pmatrix} = \begin{pmatrix}D_{11} - \frac{D_{12}D_{21}}{D_{22}} & D_{13} - \frac{D_{12}D_{23}}{D_{22}}\\D_{31} - \frac{D_{32}D_{21}}{D_{22}} & D_{33} - \frac{D_{32}D_{23}}{D_{22}}\end{pmatrix}\begin{pmatrix}\epsilon_{xx}\\\gamma_{xz}\end{pmatrix} \tag{2.5.22}$$

This matrix is also known as the fiber stiffness matrix $\boldsymbol{K}_{fibre}$.

In the element formulation, the strains have to be derived from the degrees of freedom. There are three nodal displacements possible. Two translations and one rotation, $a_i = [u_j \quad w_j \quad \theta_{y,j}]^T$. The relation between the strains and curvature in an integration point in the center of an element and the nodal displacements is:

$$\begin{bmatrix}\epsilon_0\\\gamma_0\\\chi_y\end{bmatrix} = [B_1 \quad B_2]\begin{bmatrix}a_1\\a_2\end{bmatrix}, \qquad [B_i] = \begin{bmatrix}\frac{\partial N_i}{\partial x} & 0 & 0\\0 & \frac{\partial N_i}{\partial x} & N_i\\0 & 0 & \frac{\partial N_i}{\partial x}\end{bmatrix} \tag{2.5.23}$$

In this equation, χ_y is the curvature of the cross-section and N_i are the shape functions.

The relation between the strains in the fibre and the strains and curvature in the center of an element is given by:

$$\begin{bmatrix}\epsilon_{xx}\\ \gamma_{xz}\end{bmatrix}_{fibre} = \boldsymbol{T}\begin{bmatrix}\epsilon_0\\ \gamma_0\\ \chi_y\end{bmatrix},\ \boldsymbol{T} = \begin{bmatrix}1 & 0 & z\\ 0 & 1 & 0\end{bmatrix} \tag{2.5.24}$$

The stiffness of the section is calculated by integrating the fibre stiffness over the cross-section:

$$\boldsymbol{K}_{sec} = \int \boldsymbol{T}^T \boldsymbol{K}_{fibre} \boldsymbol{T} dA \tag{2.5.25}$$

A careful look is needed for the compatibility of the shear strain in the Timoshenko beam element γ_0 and the shear strain on fibre level γ_{xz} [3].
The stiffness matrix of the element can be found by integrating the constitutive relation found in equation 2.5.4 over the length of the element while adding the finite shape function matrix $\boldsymbol{B}$.

$$\boldsymbol{K}_{elem} = \int \boldsymbol{B}\boldsymbol{K}_{sec}\boldsymbol{B} dx \tag{2.5.26}$$

Each element has one Gauss Point in the middle of the element.

3. Modelling strategies

Appendix C gives a tabular overview of the different models discussed here. Most importantly, the models can be distinguished in: 1. Continuum models or beam models, 2. Standard (uniform) models or three-zoned models. Combining these aspects give four categories.

3.1 Continuum element models

3.1.1 Pavia single wall

For the single wall, a continuum model with the three-zoned approach and mesh size $h = 0.1\ \mathrm{m}$ is used (Figure 4.3). This model is analysed three times with only the lateral load (4.3.2), the lateral load and the vertical floor load (4.3.3) and with all loads (4.3.4) (lateral, vertical floor load, self-weight). A mesh size study is done (4.3.5) in which the requested mesh size is doubled and halved (Figure 4.8)

3.1.2 Pavia façade

The continuum models of the full façade are divided in two categories, the three-zoned continuum model in Figure 4.38 (3ZCM) and the normal continuum model which uses the bed joint tensile strength of the material as the tensile failure strength for the full piers and spandrels (CM). The default 3ZCM with mesh size $h = 0.4\ \mathrm{m}$ is first analysed with only floor load and lateral load (4.4.2), then with all loads (4.4.3) (lateral, vertical floor load, self-weight). Then again, the mesh size is doubled and halved to do a mesh sensitivity study (4.4.3). Then for the continuum model (CM). A mesh sensitivity study is done with requested mesh sizes $h = 0.1\ \mathrm{m}$, $h = 0.2\ \mathrm{m}$ and $h = 0.4\ \mathrm{m}$ (4.4.4). The in-depth analysis of section 4.4.6 is done on the default CM with mesh size $0.25\ \mathrm{m}$.
In section 4.4.7.1, Both for the default 3ZCM with $h = 0.4\ \mathrm{m}$ and default CM with $h = 0.25\ \mathrm{m}$, the flexural parts with bed joint tensile strength are made of triangular elements to get a better aspect ratio. In section 4.4.7.2, four new models are made to do a parameter study on the reference tensile strength f_{tu}. Model a which is equal to the default 3ZCM with $h = 0.4\ \mathrm{m}$. Model b which is model a but with mesh size $h = 0.2\ \mathrm{m}$. Model c which is the default CM with $h = 0.25\ \mathrm{m}$ but f_{tu} of the midsections of the piers and spandrels changes. Model d which is the default CM, but the midsections of the piers f_{tu} is changed.

3.2 Beam element models

For the beam model (Figure 5.3), two approaches are used. First Nobel's FF model [2] which is a one zone beam model which uses the bed joint tensile strength as the tensile strength of the wall. Therefore, this model focusses on the rocking or flexural failure properties. Then, the three-zoned equivalent frame model (3ZEF) with three requested mesh sizes $h = 0.2\ \mathrm{m}$, $h = 0.1\ \mathrm{m}$ and $h = 0.05\ \mathrm{m}$. Then for the mesh size of $h = 0.1\ \mathrm{m}$, the number of integration points over the width is changed. The default mesh of $h = 0.1\ \mathrm{m}$ is used for the in-depth analysis of section 5.5. For the default beam model mesh, the applied mesh size is the size of the elements of the mid-sections. The flexural ends of the piers are divided in 8 elements, and the flexural ends of the spandrels in 6 elements. From this, the number of elements in the flexural parts for the different mesh sizes can be derived as they are scaled with the same ratio to the mesh size of the piers. Several improvements are suggested in section 5.6, where the default 3ZEF with mesh size $h = 0.1\ \mathrm{m}$ is used as a basis. The constitutive law is changed 5.6.1, a prestress with proportional loading is applied 5.6.2, the fracture energy is increased 5.6.3, the number of saw teeth is changed 5.6.4.

4. Continuum model with SLA

4.1 Introduction

This chapter is about the investigation with continuum elements. The chapter starts with general information on the Pavia building, the model and parameters (4.2). After this is explained, the analyses will be discussed. The first task is to get familiar with an SLA procedure and to identify if the procedure works in general. Several simulations are done, first a single wall will be tested under a lateral load (4.3). Three different approaches are used to investigate the robustness of the method, a model where only the lateral load is applied. A model with floor weight, but without self-weight and at last a model with all forces included, self-weight, floor load and lateral load. The size of the mesh is also tested and a closer look is taken to critical integration points and the stress-strain relations. An in-depth analysis is done on outstanding results, this includes for example initial non-proportional load reductions and strange branches that are not secant. Also, the model is tested again with the new Diana version released later during this research.
Later the full façade of the Pavia building is tested while subjected under a lateral pushover load (4.4). In this case, two models are used, a three-zoned model and a one zone-model. The different models are discussed and the results are compared with the results of the incremental iterative analysis using the equivalent frame method and the results of the Pavia experiment.
Later, possible improvements are suggested and tested. This is done to make the analysis more stable and therefore get better results.
Important to notice is that for all the damage plots given, the damage in this version of Diana can be tensile or compressive. No distinction is made in the plots. As the tensile strength of the material used is much lower as the compressive strength, almost all damage visible in the plots is tensile damage. The damage is defined as: $D = 1 - \frac{E_{current}}{E_{initial}}$.

4.2 General information

4.2.1 Properties and model considerations

The most important investigation is considering a continuum two-dimensional model of the Pavia house façade. The model is made with plane stress elements. The dimensions of the façade are given in Figure 4.1. For the continuum model, the dimensions of the piers and spandrels are shown in Table 4.1. The corners and center connections are also given. The following abbreviations are used: Corner floor 1 (CF1), Middle floor 1 (MF1), Corner floor 2 (CF2), Middle floor 2 (MF2). The equivalent frame idealization is the equivalent frame model used by Nobel [2].

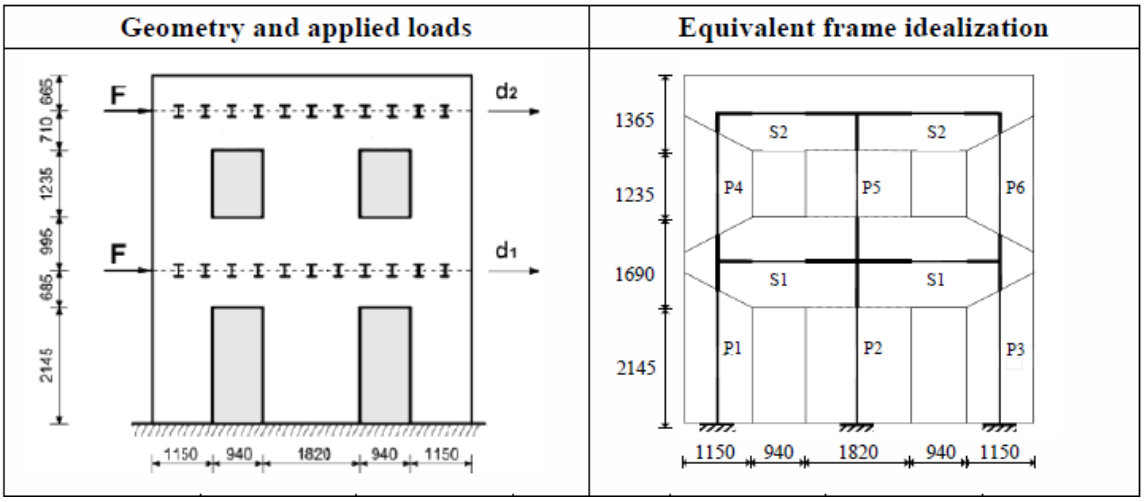

Figure 4.1; Geometry of the door façade [2]

Table 4.1; Geometry of the piers and corners in the continuum model

Pier Label	D	t	h
	[mm]	[mm]	[mm]
P1, P3	1150	250	2145
P2	1820	250	2145
P4, P6	1150	250	1235
P5	1820	250	1235
S1	940	250	1690
S2	940	250	1365
CF1	1150	250	1690
MF1	1820	250	1690
CF2	1150	250	1365
MF2	1820	250	1365

All the supports are modelled as clamped supports with a hinged support at the most left node in a pier and the other nodes attached with a tying to this one. This will result in a full clamped support for all the nodes at the bottom row. In this model, the three-zone approach will be used with a height of one twentieth of the pier or spandrel at both sides. This value is estimated from the model of Nobel. The constant load on the first and second floor is determined as: $f_1 = 20.7\ \mathrm{N/mm}$ and $f_2 = 19.8\ \mathrm{N/mm}$. The monotonic pushover load has a unit value, this load is scaled as the proportional load in the analysis.

After the geometry, the loads and the support, the material parameters are determined. Two model considerations are used for the façade: the "standard continuum model" (CM) or one zone continuum model and the "Three zoned continuum model" (3ZCM). In the standard continuum model, all elements in a pier or spandrel have the same properties based on the flexural failure behaviour. The bed joint tensile strength is used as the tensile strength of the material as this is assumed as the governing failure mechanism. In the three-zoned continuum model, the piers and spandrels are divided in a flexural part at the ends with the bed joint tensile strength and a shear part which uses the maximum tensile strength f_{tu} based on a diagonal shear test. Nobel [2] made this distinction of three zones which gave improved results in his analysis for the incremental iterative approach.
The different parts of the façade are: the midsection of the piers, the edges of the piers, the midsection of the spandrels, the edges of the spandrels and the connections. All elements are modelled as plane stress elements ($\sigma_{zz} = 0$).
In Table 4.2, the material parameters are given for the Pavia façade. The reference masonry tensile strength was not available in the original Pavia house test, it was determined in [2] as:
$f_{tu} = 0.14$ MPa by empirical testing.

Table 4.2; Material parameters Pavia house [2]

Property	Symbol	Unit	Case 3: University of Pavia tests
			Mean
Joint tensile strength	f_{jt}	MPa	0.04
Bed joint initial shear strength (cohesion)	c	MPa	0.23
Bed joint shear friction coefficient	μ	-	0.58
Reference masonry tensile strength (1)	f_{tu}	MPa	-
Compressive strength of mortar	f_m	MPa	3.0
Spandrel tensile strength (2)	f_{ts}	MPa	0.32/0.26
Young's modulus	E_2	MPa	1410
Poisson ratio	ν	-	0.2
Reference masonry fracture energy tensile mode-I (3)	G^I_{f-tu}	N/mm	0.02
Fracture energy tensile mode-I (4)	G^I_{f-jt}	N/mm	0.005
Fracture energy in compression for loading perpendicular to bed joints (5)	G_{f-m}	N/mm	10

Note:
(1) unknown for Pavia full scale test
(2) calculated being the cohesion and friction coefficient equal to 0.23 and 0.58 MPa, respectively; the interlocking parameter for the spandrels is equal to 0.86 and obtained from Cattari and Beyer (2015); the mean vertical stress is equal to 0.2 MPa at first floor and 0.1 MPa at second floor; the clamping stress is estimated to be 65 % of the mean vertical stress ($\gamma = 0.65$)
(3) estimation
(4) tensile bond behaviour of masonry: estimation based on Van der Pluijm (1992)
(5) evaluated 500 times larger than the tensile fracture energy G^I_{f-t}

Further, different strength properties are given to the elements for the 3ZCM. They are listed below in Table 4.3. In the standard model (CM), the flexure properties are adapted.

Table 4.3; Parameters for the different parts

Part	**Behavior**	**Strength** [Mpa]	**Fracture energy** [N/mm]
Pier midsection	Shear	f_{tu}	G_{f-tu}^{I}
Pier end section	Flexure	f_{jt}	G_{f-jt}^{I}
Spandrel midsection	Shear	f_{tu}	G_{f-tu}^{I}
Spandrel end section	Flexure	f_{ts}	G_{f-tu}^{I}

4.2.2 Element type and SLA parameters

In the continuum model analysis, a linear quadrilateral plane stress element will be used. The chosen element is called Q8MEM by Diana FEA. More detailed information can be found in the User's Manual of Diana FEA [20]. The linear element is chosen for its simplicity. It has four nodes and two degrees of freedom per node. The displacement polynomials can be expressed as:

$$u_i(\xi,\eta) = a_0 + a_1\xi + a_2\eta + a_3\,\xi\,\eta \tag{4.2.1}$$

The strains of the element are formulated as the derivatives of the displacements to the global x-coordinate or y-coordinate respectively. For example, the strain in x-direction ϵ_{xx} is written as:

$$\epsilon_{xx} = \frac{\partial u_x}{\partial x} = a_1 + a_3 y \tag{4.2.2}$$

In this equation, the isoparametric formulation (ξ,η)-coordinates are mapped to the (x,y)-coordinates. From this equation, it is visible that the strains in x-direction are constant in x-direction and vary linear in y-direction, vice versa for the strains in y-direction. By default, a constant shear strain over the element is used.

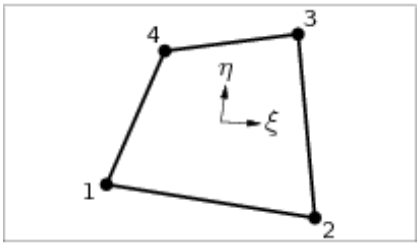

Figure 4.2; Q8MEM [20]

For the sequentially linear analysis the tensile and compressive strength parameters and fracture energy parameters are as given in Table 4.2 and Table 4.3. The β-factor used to calculate the shear modulus according to $(2.3.17)$. The reason this equation is used over $(2.3.18)$ is because the current version of Diana FEA only supports this equation. In this model: $\beta = 0.01$. The p-factor from $(2.3.8)$ is used. This has the risk of a difference in energy between the saw-tooth curve and the real curve like explained in 2.3.3. Also, the ultimate strain can be somewhat different. In this case, Diana does not yet support the new equation where the p_1-factor and p_2-factor are solved iteratively. In this model $p = 0.1$.
The maximum number of saw-teeth is limited by $N = 50$.

4.3 Continuum model introduction - Single wall test

4.3.1 Overview

First the program is tested for a single pier of the Pavia house, the left pier of the bottom row and the 3ZCM are chosen. The load will be applied in steps. First only the lateral load, later also the floor load and finally the full load will be applied including the floor load, self-weight and lateral load.
The results will be discussed and some interesting results will be examined.
In this part, the same three-zoned approach is used as in [2], i.e. the outer elements will have the bed joint tensile strength. The inner elements have the maximum tensile strength, dominant for shear, f_{tu} and G^{I}_{f-tu}. The pier will be subjected to its dead weight load and a distributed load q, because of the weight of the floors above. The factor $\frac{1620}{1150}$ is the part of the floor load that is taken by this pier.

$$q = \frac{(19.8 + 20.7) * 1620}{1150} = 57.05 \text{ N/mm} \tag{4.3.1}$$

The model is shown in Figure 4.3. A mesh size of $h = 0.1$ m is used.The top of the wall is fixed vertically with the left top corner, because it is attached to the first floor in the real structure. A proportional horizontal force acts on the left top corner of the wall. In the final analysis, the vertical load will be applied first. Next, the horizontal load will be scaled in a sequantially linear procedure. This is done in 7000 damage steps.
The mesh is scaled that the aspect ratio is equal to 1. This to get the best results for the continuum elements. When the displacements of the wall are mentioned, the horizontal displacement of the node in the top right corner is meant. When the force is mentioned, it refers to the total horizontal lateral load on the structure. This should be equal to the sum of the horizontal reaction forces following horizontal force equilibrium.

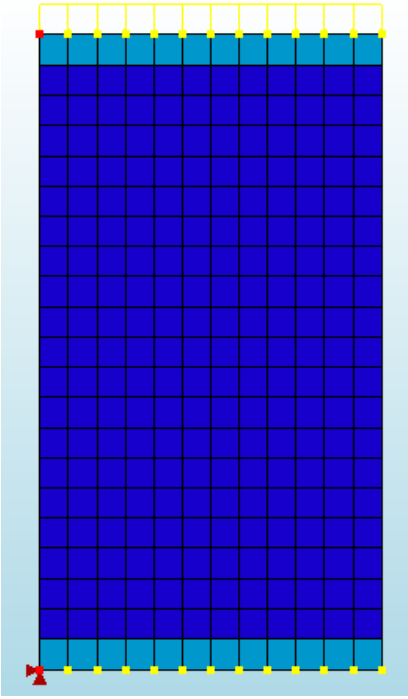

Figure 4.3; Single pier Pavia model, only flexural (left) and flexural and shear

4.3.2 Only lateral load

First, an analysis is done with only the lateral load. The resulting force-displacement diagram is shown in Figure 4.4. The force-displacement diagram shows the typical shivering contour familiar in an SLA. These local force reductions are the result of the method used in a sequentially linear analysis. Often, when there is a critical integration point found, other integration points are also very close to a critical stress as explained in [1]. When the damage is applied and the force is redistributed these points have almost no capacity left. The new critical integration point can only be found by reducing the load a little. This results in small unloading and reloading steps across the curve. At the end of the curve, the structure unloads with a big step. This is because the structure cannot bear the load for some steps and restores it later. A point of discussion should be made here. In reality, a structure cannot reduce the load for some steps to find equilibrium. Especially when this continues for some steps, one could say that the structure has failed, especially in a case where the vertical load only includes self-weight. Naturally, a structure should always be able to carry the full weight. In this case, only the first 4000 steps are shown in Figure 4.4. In the next steps, the load was recovered and reduced very often, similar to the last step. After this, the displacements grew rapidly, while the force was almost nil. Therefore, the conclusion was drawn that the structures had failed.

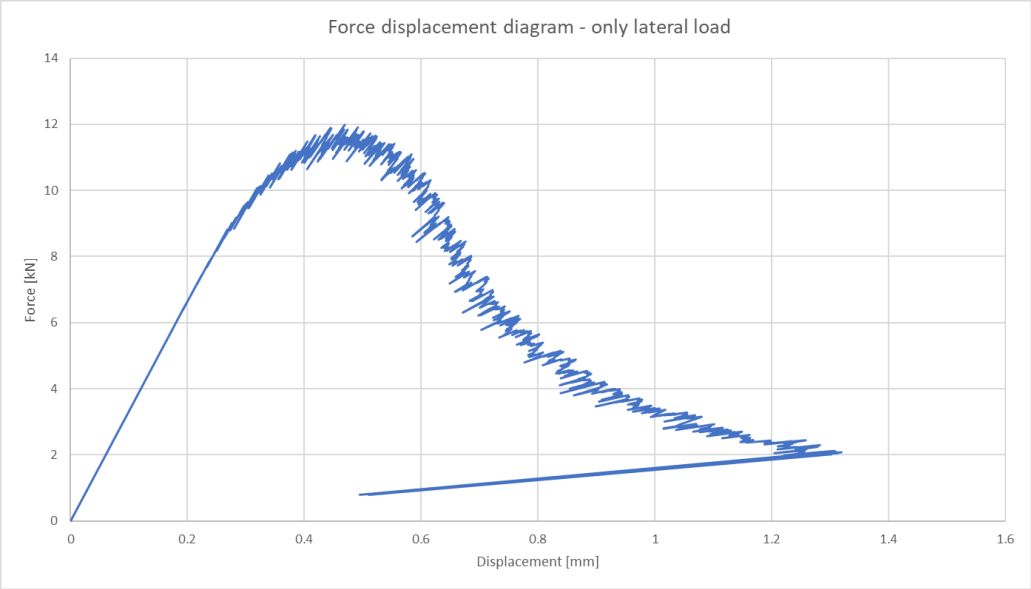

Figure 4.4; Force displacement diagram - only lateral load

4.3.3 Single wall without self-weight

The second model includes the vertical force at the top of the wall. This represents the load of the floors above the wall, in other words the q from equation $(4.3.1)$. Again, the three-zoned model with flexural parts and shear parts is used here. The analysis is done in 7000 steps.

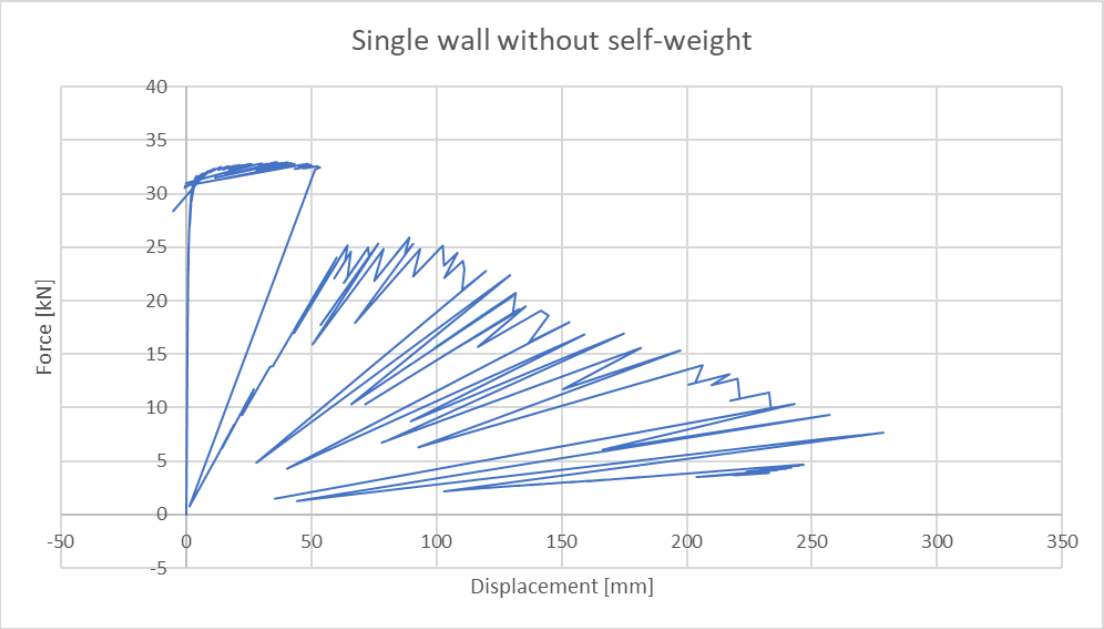

Figure 4.5; Load-displacement curve single wall without self-weight, first 4500 damage steps

For the first 2800 steps, only once in 25 steps the results are saved for post-processing to reduce the size of the output files, which can be quite big. The results are shown in Figure 4.5 and Figure 4.6. It is clear that this wall follows the rocking failure mode because the highest tensile stresses and therefore the damages start in the bottom left and top right corner. The other damage in the top left corner is caused by the load, which is applied over there. The combination of the vertical and horizontal force results in a higher total lateral load. For masonry, the tensile strength is lower than the compressive strength. Therefore, elements will fail earlier in tension than compression. The vertical weight on the wall acts as some kind of prestress, loading the wall in compression. This results in a higher lateral load for which the elements will fail in tension. Remarkable is the part after the maximum load. The displacements are reducing but not secant. There is even a negative displacement visible in some steps. This is of course not true in reality and these steps are investigated later in the analysis of the full house as it also occurs there. Please note that the part with displacements larger than $50\ \mathrm{mm}$ are analysis steps where the full vertical load cannot be applied. Therefore, these steps are not relevant as the structure should be regarded as failed. The principal strains show a similar view as the damage. Tensile cracks occur in the left toe of the wall and the top right corner.

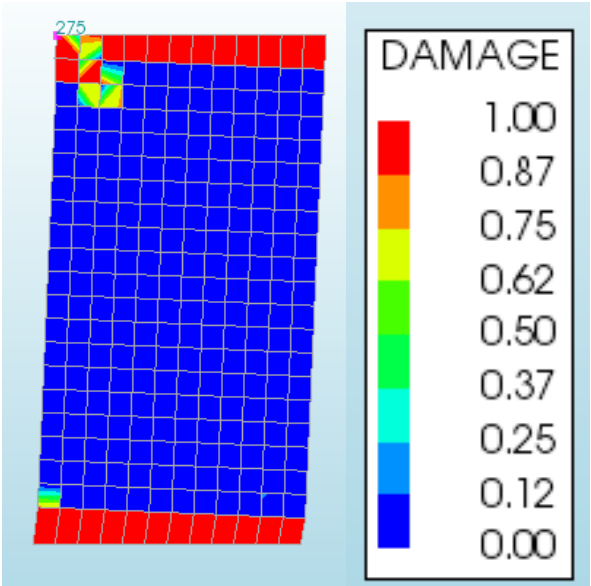

Figure 4.6; Damage to stiffness - Analysis step 3831

4.3.4 Single wall with self-weight

In this part, the single wall is tested and all loads are active, i.e. floor loading, self-weight and the lateral load. In this analysis, the results are not stable. In some stages the structure moves to the left, which is of course not realistic. The load-displacement diagram is shown in Figure 4.7. To make the method easier to apply in practice, not every analysis step should be selected in the results. If the results of every analysis step are saved, it decreases the workability because the analysis is much slower and the result files become very large. In Figure 4.7, two results files of the same structure are compared. The left figure is from an analysis which gives only output once in 25 damage steps. The right figure gives an output value for all steps:

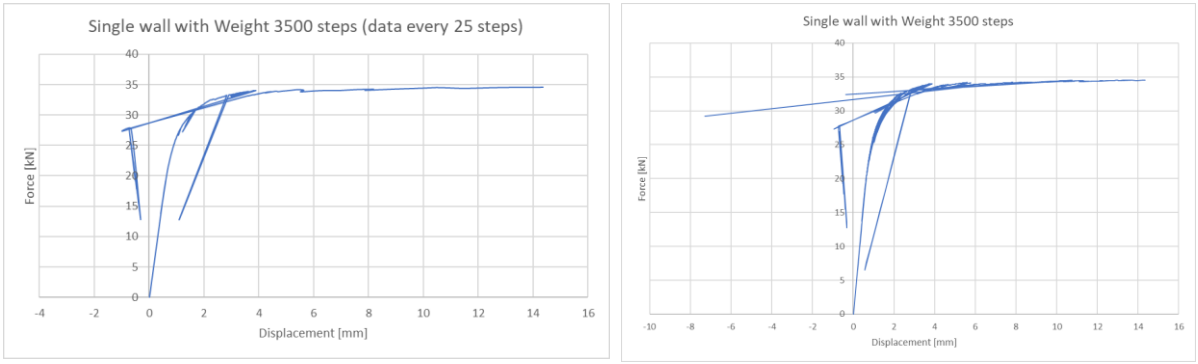

Figure 4.7; Load displacement single wall total load case; left results once in 25 steps, right all results

Comparing the two concludes that the most important global results are captured in the case with output once in 25 steps, but some outliners are missed or smaller. Although these results are important to examine, they are not important for the global result. This justifies the choice for reduced results to improve the speed of the analysis and post-processing.

The maximum load on the structure is significantly higher in this case than in the case without the self-weight and floor load. This is again because the compressive stress of the weight works as some kind of prestress on the structure. The structure is more likely to fail in tension over compression. Because of the material properties of masonry, the weight has a positive contribution to the resistance of the wall.

A careful look at the results is needed, because not everything is valid. For example, the analysis step where the displacements are in the opposite direction of the load. This is visible in the load-displacement graph by the part that is left of the y-axis.

4.3.5 Mesh size study

In this part, the wall is modelled with a coarse mesh and a fine mesh to investigate if differences occur.

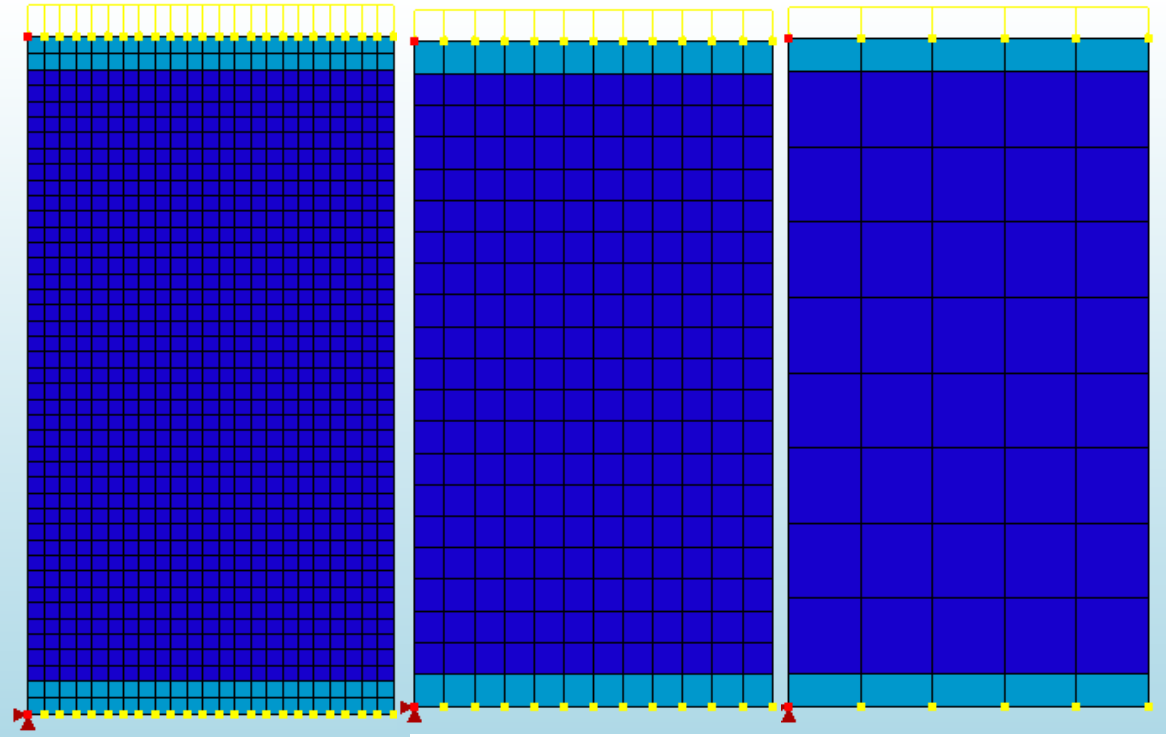

Figure 4.8; Three meshes, from left to right: fine, standard, coarse

The total result of the coarse mesh is shown in Figure 4.9. The result is quite good until the method becomes unstable. The structure unloads not secant to the origin and displaces negative. For the fine mesh, the structure does not reach the maximum value as in the previous examples. The element on which the lateral force acts is fully damaged early in the analysis and is seriously deformed. This damage results that between damage step 876 and 901 the structure cannot bear the initial load, visible in the reductions to the origin.

While in general cases in a finite element analysis the results improve if the mesh size is smaller, this does not seem the case here. The results for the coarse mesh and the fine mesh were both acceptable until the initial load factor reduced, ignoring the outliers. When some elements of the fine mesh were damaged, the structure was not able to carry the full vertical load and the force immediately dropped. This already happened for small loads and resulted in the structure failing for in the early stages of the analysis.

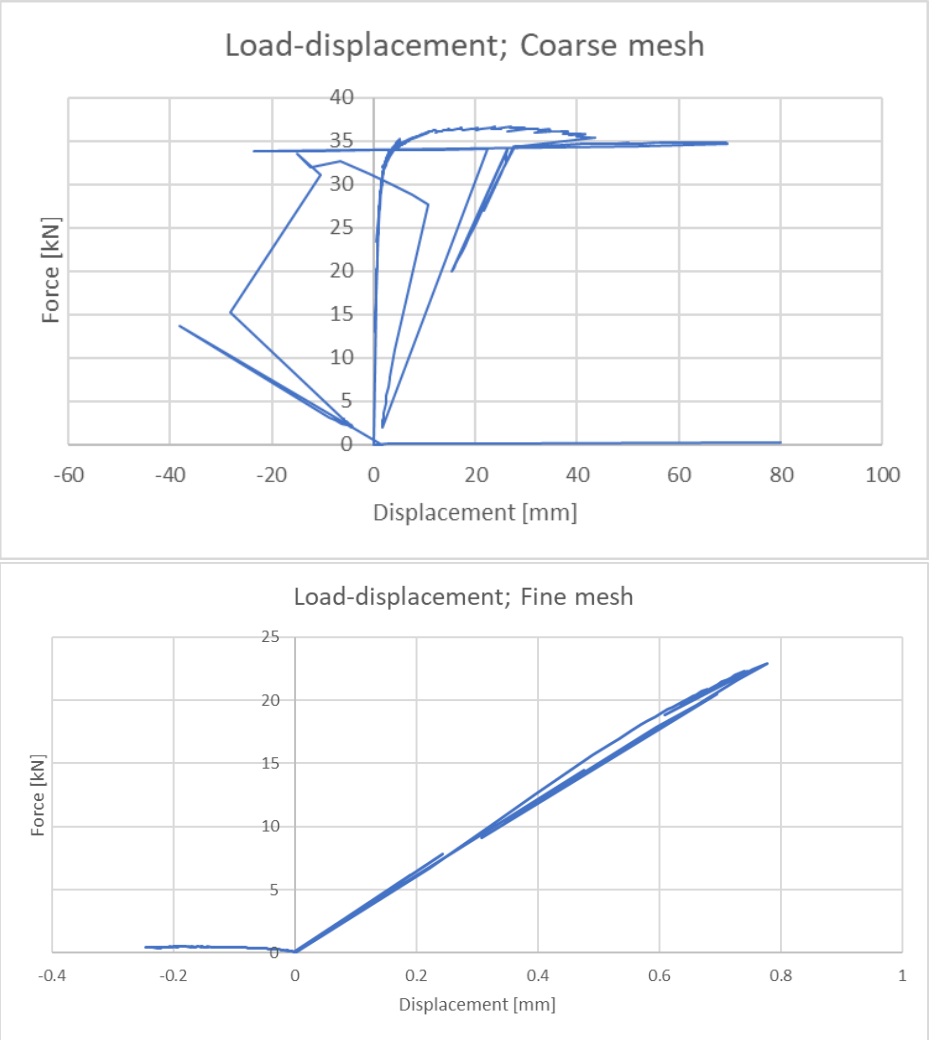

Figure 4.9; Load-displacement curves; Coarse mesh (up) and Fine mesh (down)

A graph is made (Figure 4.12) in which the initial load λ_{ini} is shown during the analysis for the fine mesh. Between damage step 876 and 901, the load factor is reduced to almost 0.4. The structure recovers itself in the next steps, only to drop the initial load again later. This part can be seen in the load-displacement relation as the reductions to the origin and back. In this case, some elements close to the point of load application misbehaved and failed, resulting in the end of the sequentially linear analysis. Extreme deformations for these elements were observed.

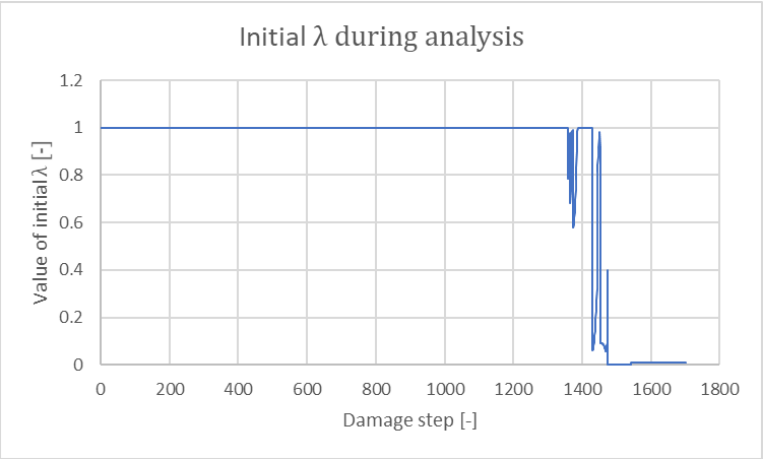

Figure 4.10; λ_{ini} during analysis; Coarse mesh

The big drop in the initial load graph corresponds with the step in which the proportional load reduces to a value of 2.031 kN (Figure 4.9). Every time the initial load factor drops, the load combination of the previous analysis step is scaled. This means that not only the lateral load reduces when the initial load factor reduces, but also the vertical load. The advantage is that ratio between the lateral load and the vertical load stays constant, the disadvantage is that the vertical force reduces and an unrealistic situation occurs as the vertical load from weight would never reduce in reality. If this is only for a few analysis steps it can be seen as a redistribution of the load.

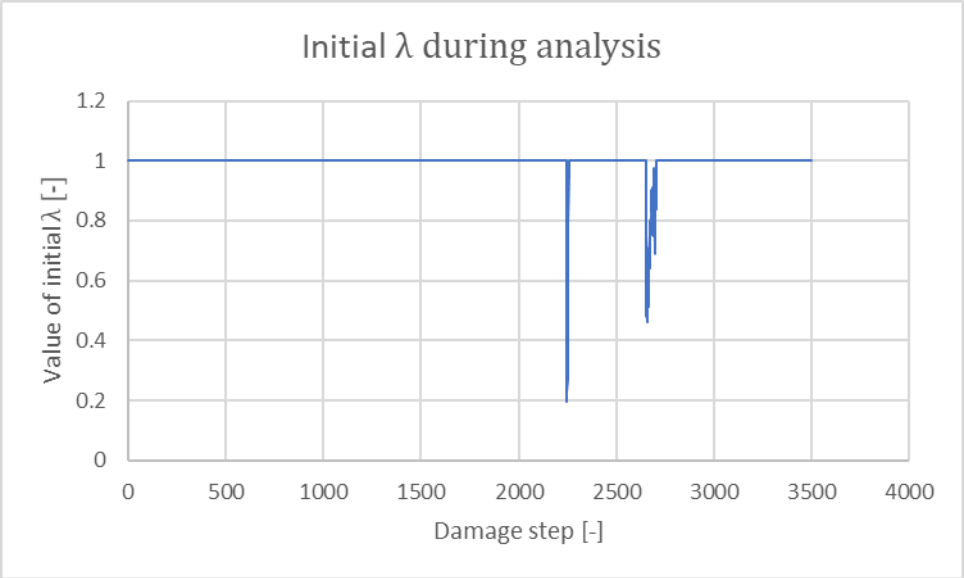

Figure 4.11; λ_{ini} during analysis; Standard mesh

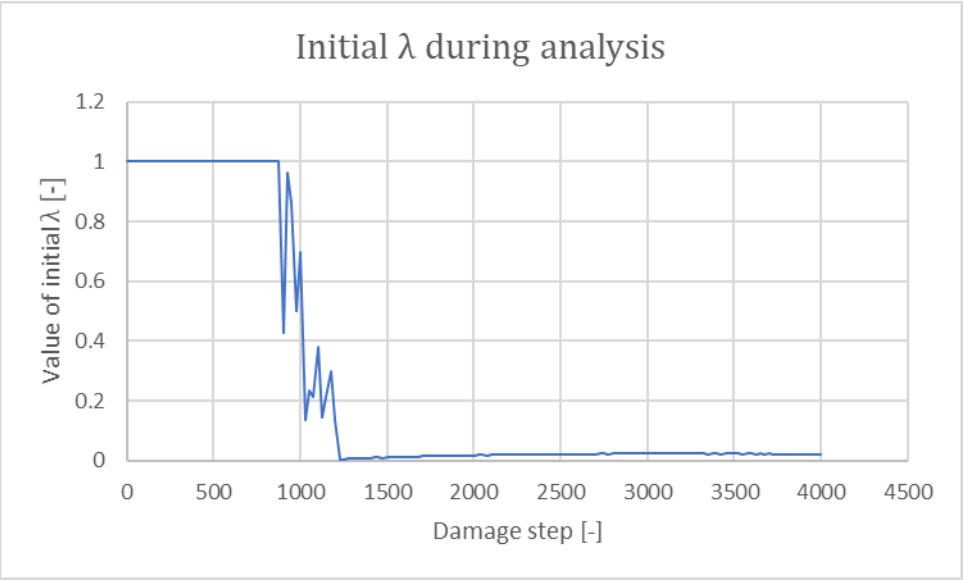

Figure 4.12; λ_{ini} during analysis; Fine mesh

The results of the previous three analyses are combined in one overview (Figure 4.13). The coarse mesh gave results which indicate that the structure can absorb relatively much energy before the analysis fails, while the fine mesh was only able to describe the elastic part. For the coarse mesh, a relatively large displacement was achieved, while the analysis was still stable.

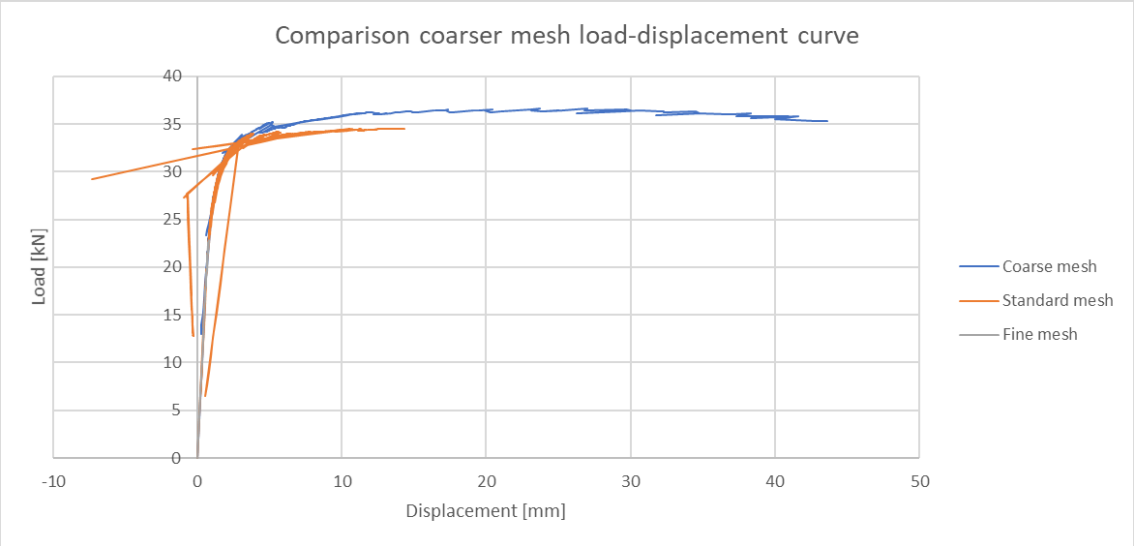

Figure 4.13; Load displacement comparison

4.3.6 Investigation on negative displacements and not secant branches

To get a better understanding, the standard mesh model is investigated around the unstable points to find the cause of this behavior. By taking a closer look at a small part of the graph (Figure 4.14) it is visible that the unloading is not secant to the origin. In all steps, the vertical reaction force of stays constant (76.499 kN), therefore there is no reduction of the initial load, which therefore cannot be the cause of this.

The real cause of this behaviour could be a crack closure problem as explained in section 2.3.4. To investigate this, parts of the structure should be examined in detail.

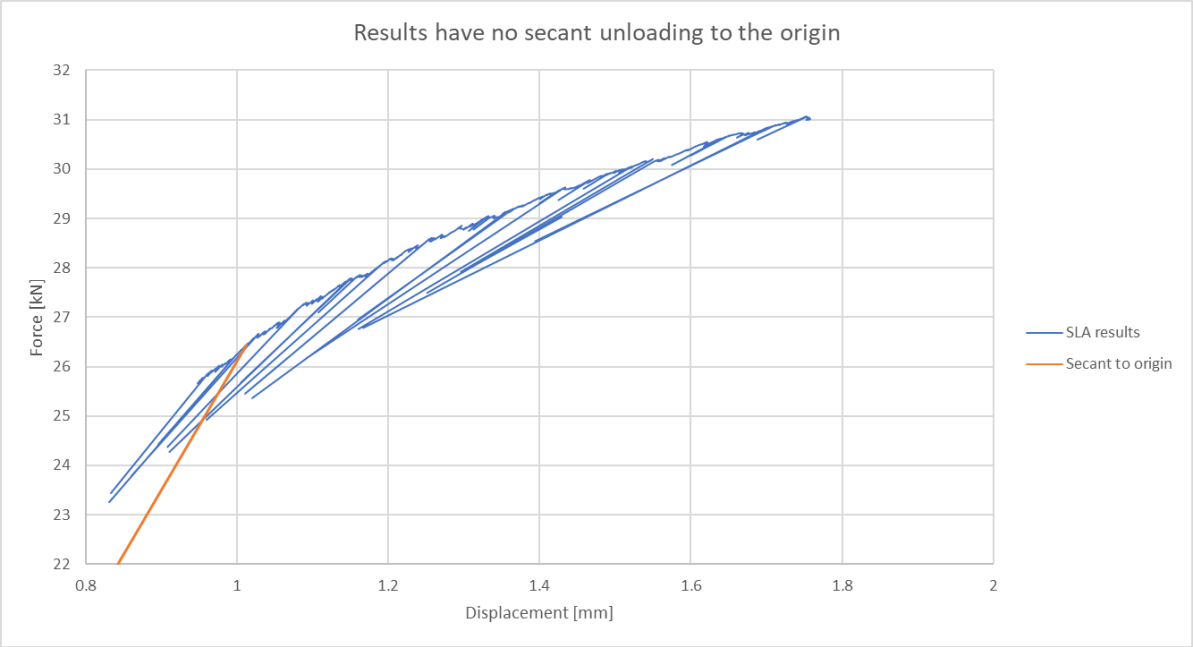

Figure 4.14; Closer look at a part of the curve without secant unloading to the origin

First, step 516 is investigated further. In this step, there is a large reduction of the load multiplier. In step 515, the load multiplier is 25790 N which reduces to 23440 N in step 516. The displacement reduces from 0.957 mm to 0.833 mm for those steps. These load reductions are visible in Figure 4.14 by the linear line segments branching from the load displacement curve. In the next three steps, the load increases to the level before the load decrease. The failure in steps 515 and 516 are tensile failures in element 7, integration point 2. This element is located in the lowest row of the structure, the sixth element from the left and has nodes 21, 10, 11, 20 (Figure 4.3).

Three plots are shown below, first two plots in which the stress states in the different analysis steps are shown (Figure 4.15 and Figure 4.16) and a third one with the damage levels (Figure 4.17). From the data, the boundaries for the principal stresses are found. The minimum principal stress $\sigma_{1,min} = -1.08 * 10^6$ N/mm^2, the maximum principal stress: $\sigma_{1,max} = 1.24 * 10^5$ N/mm^2. The change in sign of the principal stresses is important. Therefore, two diagrams are shown per damage step. The left diagram shows only the elements in compression and the right diagram shows only the elements in tension. In this way, the change from compression to tension or vice versa is clearly visible.

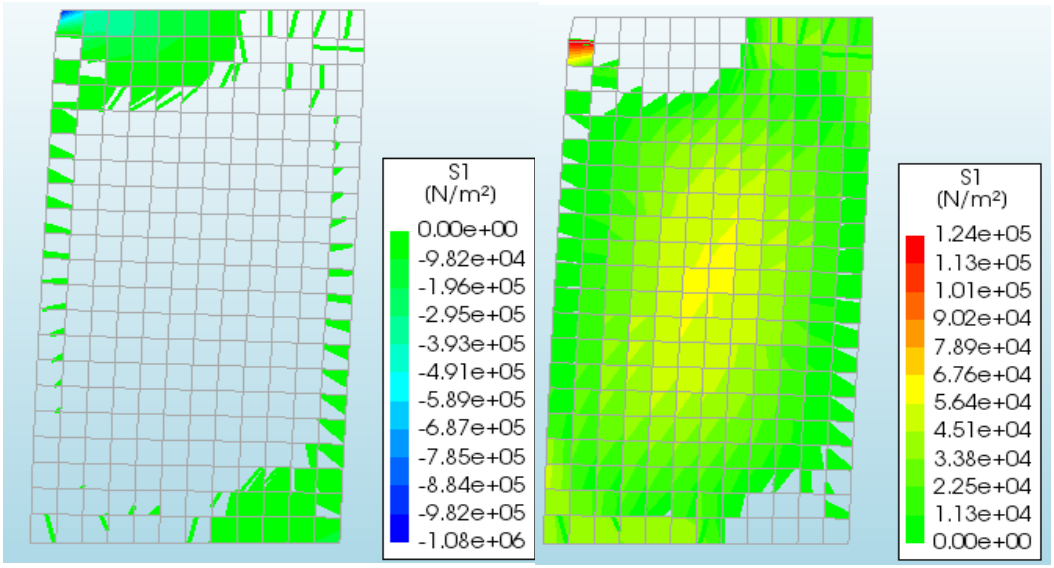

Figure 4.15; Step 515 Load 25789 N

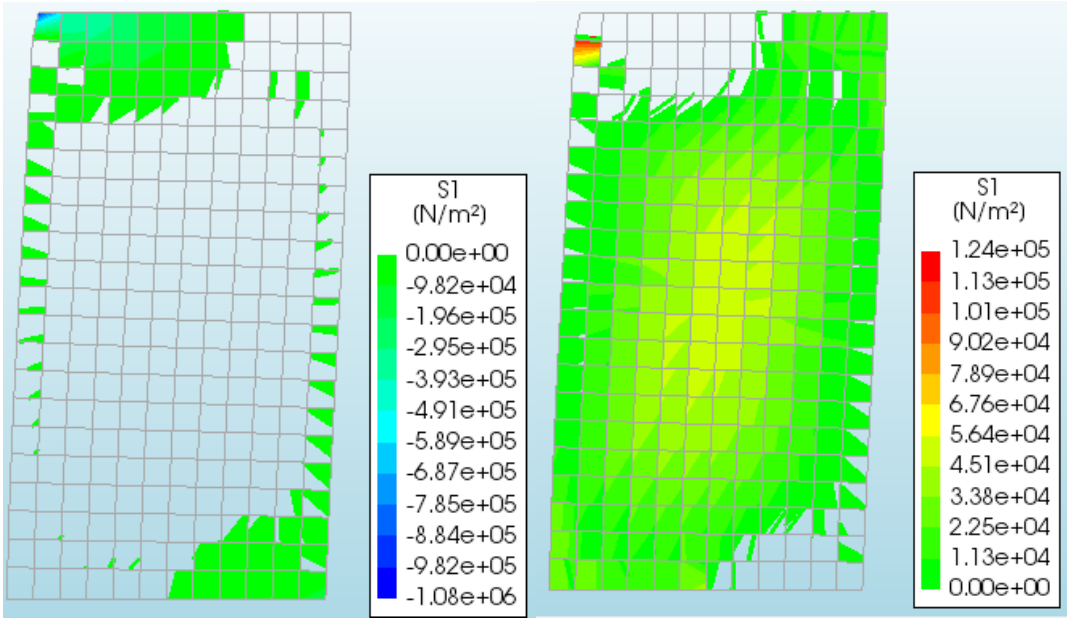

Figure 4.16; Step 516 Load 23444 N

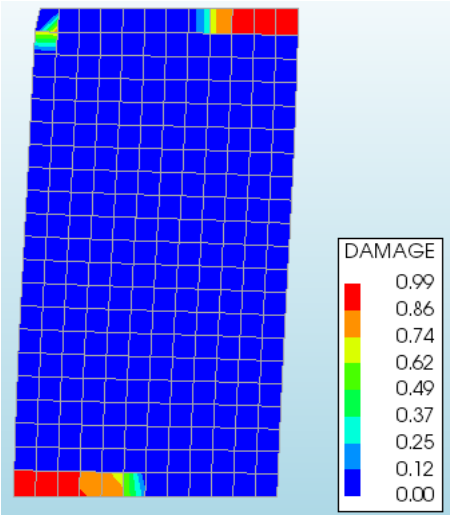

Figure 4.17; Damage level in damage step

A crack closure problem can only occur in an element that is cracked or damaged. Figure 4.17 shows those elements. Damage has only occurred in the first six elements counted from the left in the bottom row, the last five elements counted from the left in the top row and around the point where the force is applied. Comparing Figure 4.15 and Figure 4.16, only the fifth element counting from the right of the top row changes from tension to compression. This is element 245 in the finite element mesh.

Below in Figure 4.18, the stress state of the first principal stress is given for both elements, which confirms this more clearly.

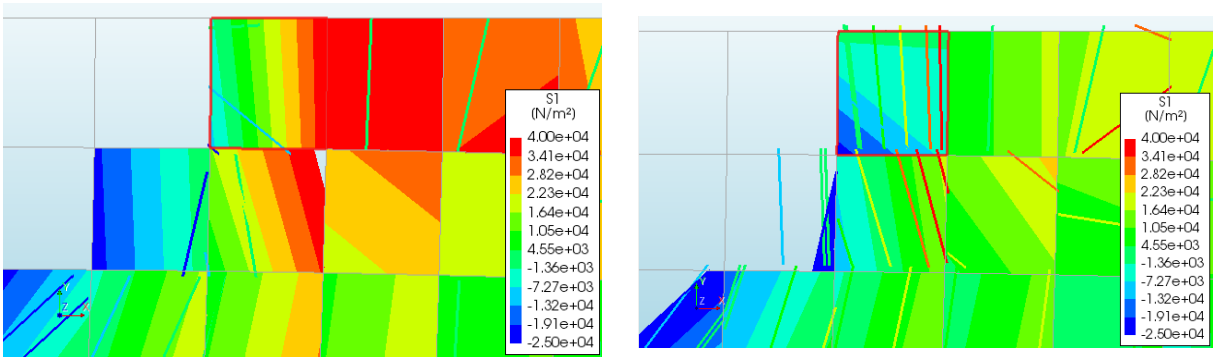

Figure 4.18; Stress state in element 245, step 515 (left) and step 516 (right)

Another step with a big reduction is step 577. In this step, the load reduces from 26244 N in step 576 to 23259 N in step 577. Also, the displacement reduces from 0.999 mm to 0.831 mm in those steps. The boundaries for the first principal stress are: $\sigma_{1,min} = -1.10 * 10^6$ N/mm^2 and $\sigma_{1,max} = 1.27 * 10^5$ N/mm^2.

Below in Figure 4.19 and Figure 4.20 are again the stress states, this time in step 576 and step 577 for the first principal stress σ_1:

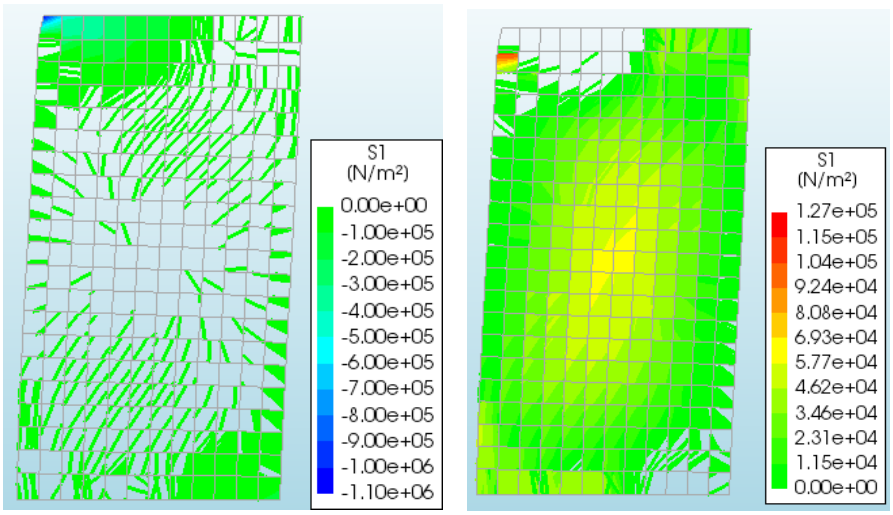

Figure 4.19; Stress state damage step 576

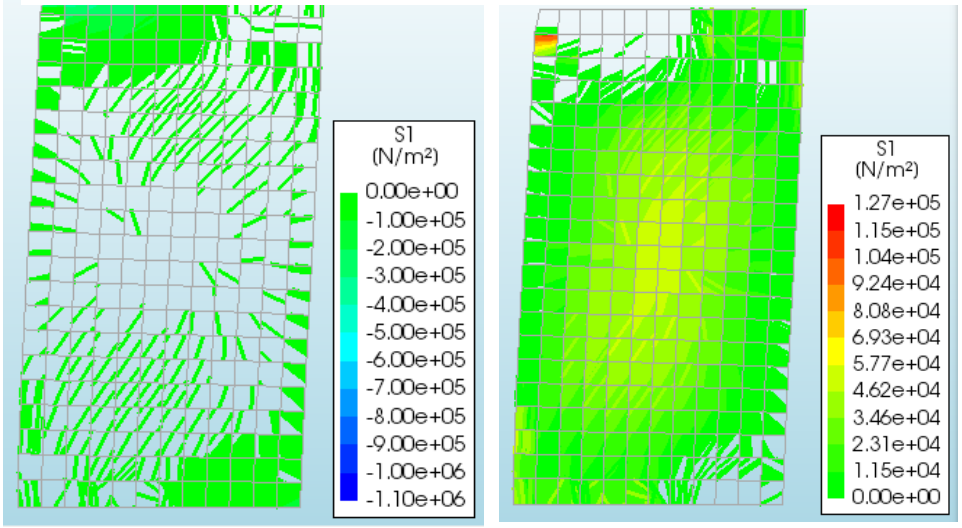

Figure 4.20; Stress state damage step 577

This time there are not many changes in the damaged elements for the first principal stress. The same figures are made for the second principal stress σ_2. The minimal value of the second principal stress: $\sigma_{2,min} = -2.30 * 10^6\ \mathrm{N/mm^2}$ and the maximum value of the second principal stress: $\sigma_{2,max} = 3.49 * 10^4\ \mathrm{N/mm^2}$.
In Figure 4.21 and Figure 4.22, the stress states are shown. In Figure 4.23, the damage of the structure is visible.

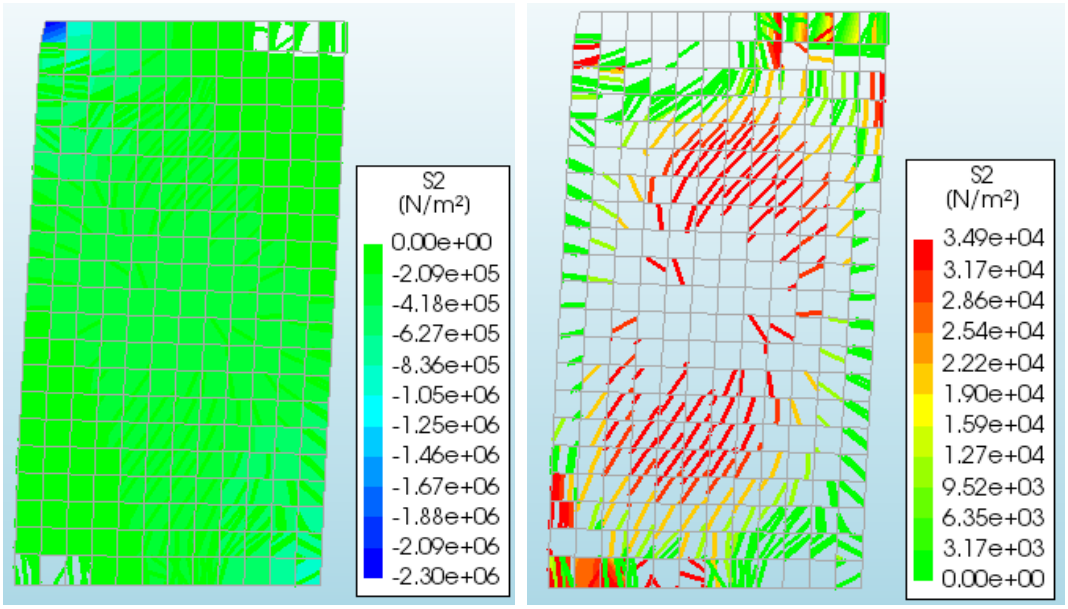

Figure 4.21; Stress state damage step 576

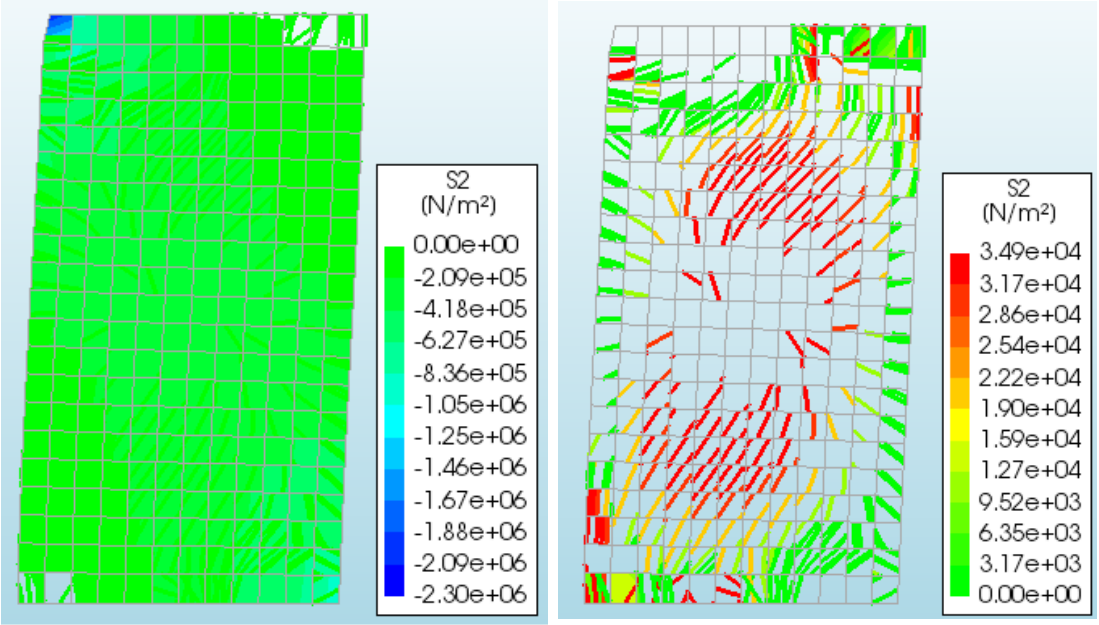

Figure 4.22; Stress state damage step 577

For the second principal stress σ_2, there are differences. The differences are in element 10 and element 244.

From Figure 4.21 and Figure 4.22 can be seen that two damaged elements go partly from tension to compression. The third element from the left in the bottom row (element 10) and the ninth element from left in the top row (element 244). Especially element 10 is severely damaged and has an almost zero stiffness.

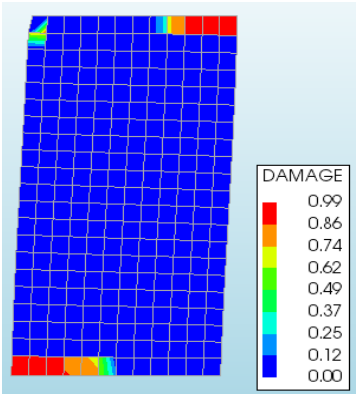

Figure 4.23; Damage in damage step 515

Below, element 10 is shown in Figure 4.24. In damage step 576, one step before the reduction. The element is fully loaded in tension. The highest value in the lower left corner ($3.50 * 10^{-2}$ N/mm^2). In the next damage step (step 577), the element is in compression in the right part of the element. This element is fully damaged (damage level $= 1.0$).

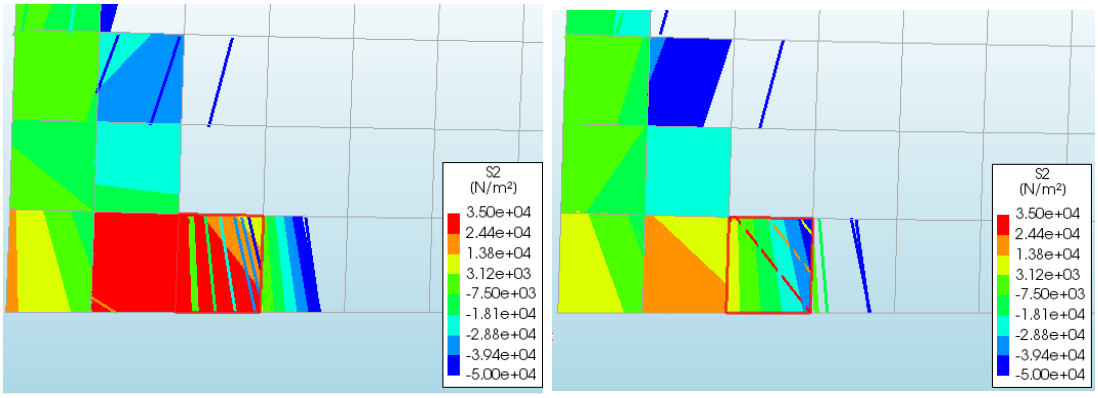

Figure 4.24; Stress state in element 10, step 576 (left) and step 577 (right)

In element 244, the stress state in step 576 shows an element which is half in compression and half in tension. In step 577, the stress has reduced which result in a different stress state with different parts in compression, and more severe. Only the top part is still in tension. This element is not fully damaged, but the damage is high (approximately 0.8).

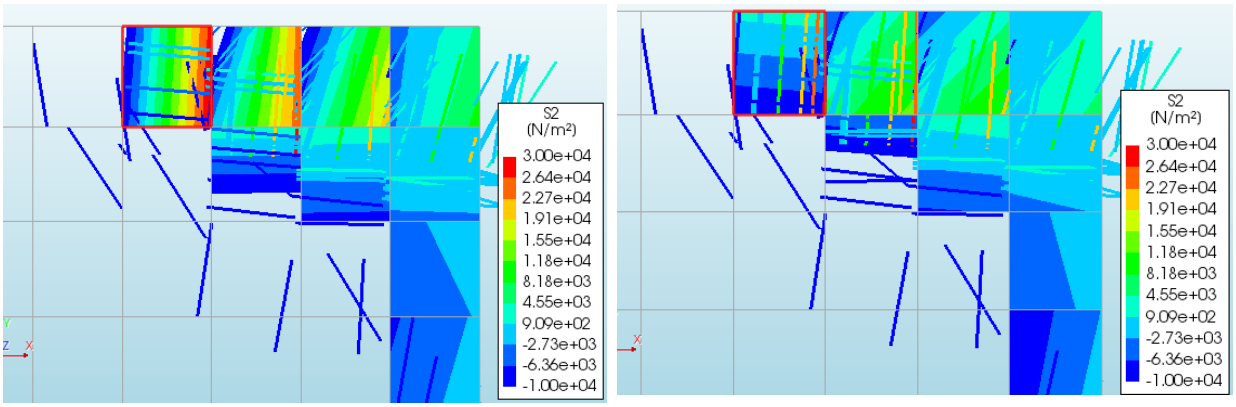

Figure 4.25; Stress state element 244, step 576 (left) and step 577 (right)

In both cases, step 516 and step 577, damaged elements changed from being in tension to compression. This combined with the fact that both elements were previously only damaged in tension results in the following line of reasoning: The elements were previously damaged because of tensile failures in the integration points. According to the sequentially linear analysis, the stiffness of those elements is reduced according to the saw-tooth law. However, when these elements change from tension to compression, the crack closes in reality because of the compressive stresses resulting in an adherent part which can transfer compressive stresses with the initial stiffness. In the sequential linear analysis procedure, this stiffness is reduced which results in a wrong stiffness and consequently strains which are too high, which leads to wrong displacements. Although a solid conclusion cannot be drawn yet, there is an indication this is the reason of the unstable unloading behavior which was encountered before. The conclusion is not solid yet, because crack closure behavior is detected at these unrealistic loading steps, but it has not been proved that this is also the cause, also the contour plot and stresses and strains in the nodes give a quick overview of the full structure but are not precise enough because the stresses and strains are calculated in the integration points of the elements and then extrapolated

to the nodes and over the element. The analysis is done again later with the new developed version of Diana FEA and a self-written MATLAB code is used to analyze the structure on crack-closure behaviour in the integration points. The values of the stresses and strains in the integration points are saved in a tabula file during the analysis and are examined later.

Now the negative displacements are examined. The negative displacements take place between damage steps 2652 and 2708. Again, the same method as before is used in which the change from tension to compression and vice versa is showed. At damage step 2651, one step before the negative displacement. The structure is damaged as shown in Figure 4.26. The damage has propagated further from the previous diagram. This is more than 5000 further and therefore, the structure is badly damaged. Almost the whole upper and lower row of elements is fully damaged.

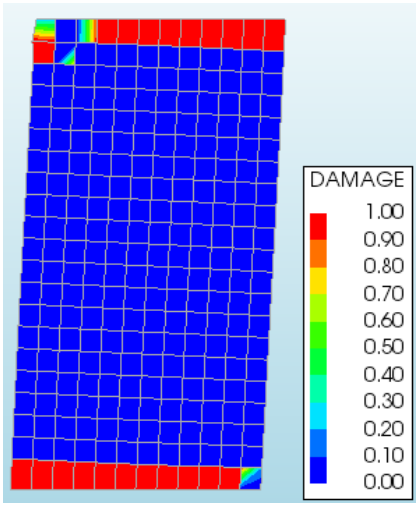

Figure 4.26; Damage step 5651, Damage level

First the first principal stress is examined, σ_1.
The maximum stress in the structure:
$\sigma_{1,max} = 3.61 * 10^5\ \mathrm{N/m^2}$, the minimum stress in the structure: $\sigma_{1,min} = -1.05 * 10^6\ \mathrm{N/m^2}$. These stresses are again the boundaries of the diagram.

Both stress states are shown in Figure 4.27 and Figure 4.28:

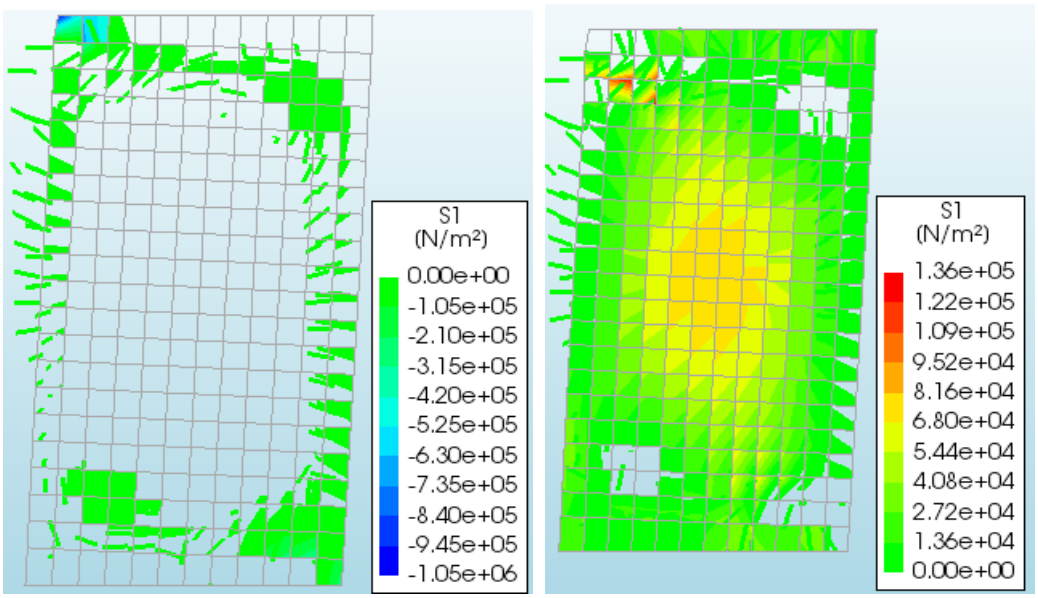

Figure 4.27; Damage step 2651 Load factor 33963

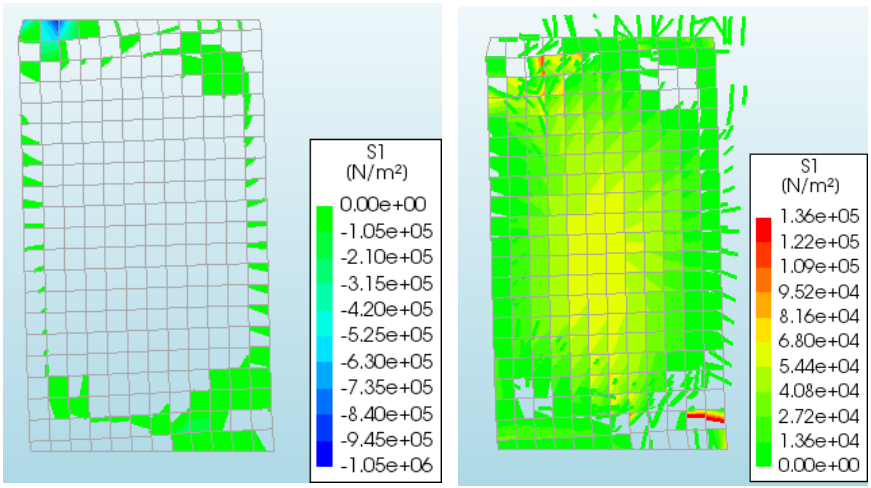

Figure 4.28; Damage step 2652, load 27321

Again, damaged material has almost no stiffness. When it is loaded in compression after damaged in tension, the damage to the stiffness stays the same, therefore large strains are occuring which result in false results. The stress state of the elements of the bottom row is showed in Figure 4.29.

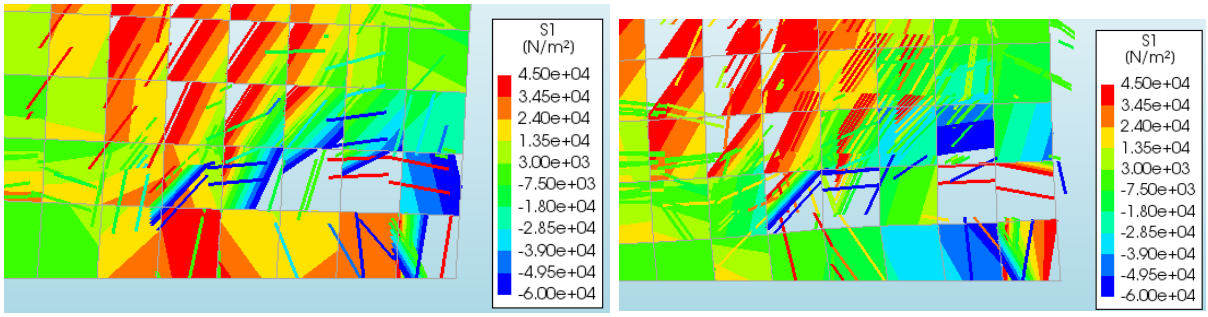

Figure 4.29; Analysis step 2651 left, and Analysis step 2652 right

In the previous cases, only one or two elements went from tension to compression. In this case, there are five fully damaged elements which go from tension in damage step 2651 to compression in damage step 2652. The same line of reasoning can be followed, in this case with that much damaged elements that the strains became so big that the displacement is reversed. This case shows even clearer that this behaviour is not realistic and results in wrong results.
The nodal stress and strain values of the principal stresses and strains are shown below extrapolated from an integration point in element 2. As expected, the strain decreases at step 2652. However, the principal stress changes from tensile to compressive, which is remarkable for the first principal stress, as this should always be the highest of the three. Given that the stress in the third direction $\sigma_{zz} = 0$ by definition in a plane stress approach, this should not be possible.

Table 4.4; Principal stress and strain in element 2 node 6

Stress and strain around step $2640 - 2660$		
step	Strain ϵ_1 $[-]$	Stress σ_1 $[\mathrm{N/m^2}]$
2640	0.000644	25684.09
2641	0.000644	25690.69
2642	0.000645	25727.24
2643	0.000649	25862.67
2644	0.00065	25871.37
2645	0.000651	25919.51
2646	0.000651	25900.98
2647	0.000652	25930.04
2648	0.000652	25933.43
2649	0.000655	26045.73
2650	0.000667	26400.47
2651	0.000664	26285.9
2652	0.000277	-36139.5
2653	0.000231	-32275.1
2654	0.000113	-15739.2
2655	0.000111	-15541
2656	0.00011	-15374.4
2657	0.000109	-15057.2
2658	0.000109	-15092.5
2659	0.000108	-14930.8
2660	0.000119	-16196.6

To show the error in stiffness when the curve switches from tension to compression (or vice versa), a stress-strain plot is made from the stress σ_{yy} and the strain ϵ_{yy} in a node nearby an integration point of element 12. This is the element in the corner left below. The stress σ_{yy} is chosen in stead of the principal stress because this stress does not change direction and the principal stress could because of redistribution and the initiation of a second crack. This as a result of the fixed crack approach. In this element, the crack should develop horizontally and therefore for the major part of the analysis, this could be regarded as the direction in which the damage occurs. Again these stresses and strains are extrapolated by Diana to the nodes. These are not the real stresses and strains in the integration points.

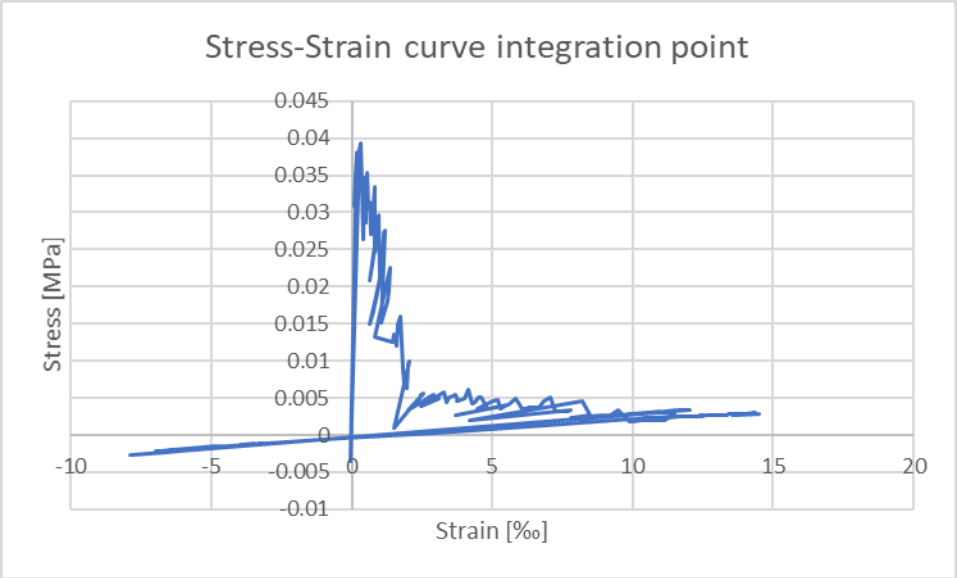

Figure 4.30; Stress (σ_{yy})- strain (ϵ_{yy}) curve extrapolated to node of element 12

The maximum strength reduces like expected when the material damages (Figure 4.30). The change from tension to compression occurs at analysis step 2652 when the structure moves to the left. Here this point is loaded in compression. In the compressive zone, the graph has the same tangent as where it left the tensile zone. In reality the stiffness in compression has not reduced and the stiffness should be the same it was initially.

From the results can be concluded that the necessary addition of the self-weight and vertical load results in unprecise output for some steps. The first reason for this is the added complexity caused by the initial compression because of the self-weight and floor load. This is of course essential because these loads should be present in the model. From literature follows that the non-proportional loading scheme is still difficult to apply.
Also, a first indication of a crack closure error appeared. Figure 4.31 shows this behaviour for an integration point. In this example damage occurs because the tensile strength is violated. This results in a reduction of the stiffness showed in diagram a. When the structure is reloaded in compression, the program uses the reduced stiffness to make the calculation. In diagram b, the compressive strength is reached, but the strain is too large. This leads to wrong displacements and incorrect results.

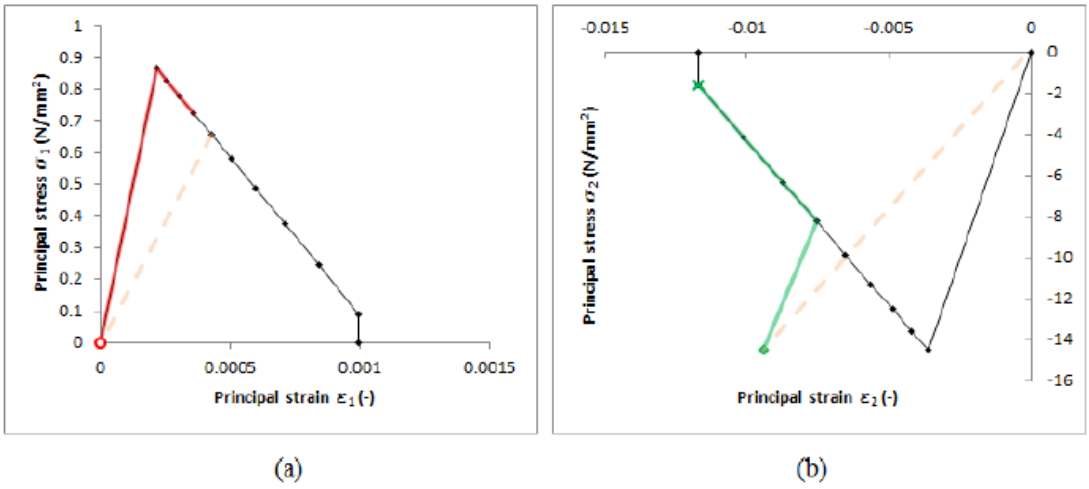

Figure 4.31; Crack closure error [25]

4.3.7 In-depth analysis

During the period of this research, new developments have been made and Diana version 10.2 was released. The analysis of the single wall (3ZCM) with self-weight and the floor load is repeated with the goal to compare the results of the new Diana version with the previous one and to give a more solid proof that crack-closure problems indeed occur during the analysis. The model used is the one with a mesh size of $h = 0.1$ m. This model had a good tradeoff between analysis time and accuracy. First the load-displacement relation is examined. Again, with the displacement of the top right corner of the wall and the proportional push-over load as the variables.

The result is shown in Figure 4.32. The previous result is not shown, because it was very similar to this one, which would make the figure less clear. Compared with the previous analysis, this one is far more stable. There are a few reductions visible, only the reduction around a displacement of $d \approx 2.5$ mm is the result of a reduction of the initial load factor (Figure 4.33). This reduction is secant to the origin. The other reduction at $d \approx 1.3$ mm is not the result of a reduction of the initial load factor, neither is it the result of successive failures in the same integration point. It is therefore

probably a redistribution of the forces in the structure. As this reduction is secant to the origin, no further attention is given to this.

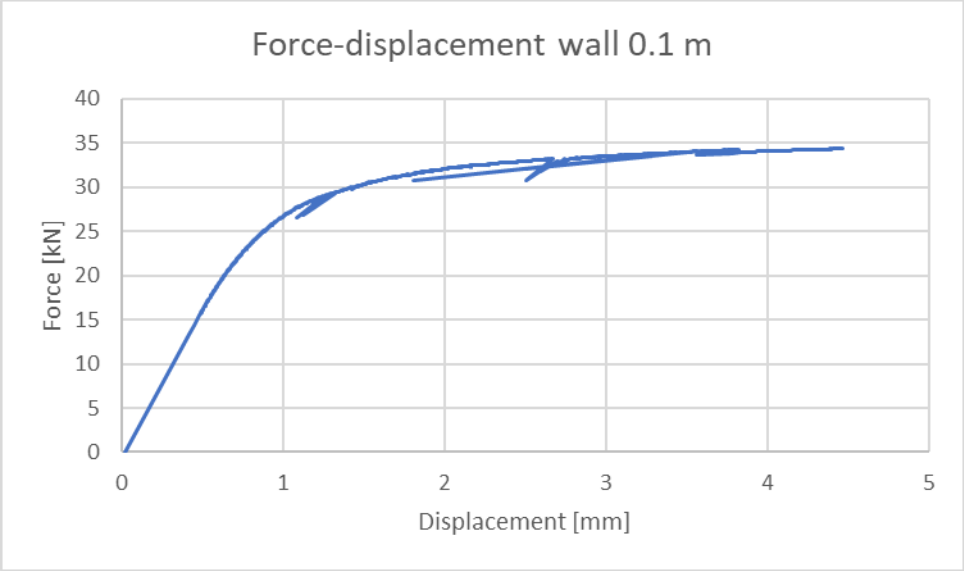

Figure 4.32; Force-displacement diagram Single wall push over, Diana 10.2 results

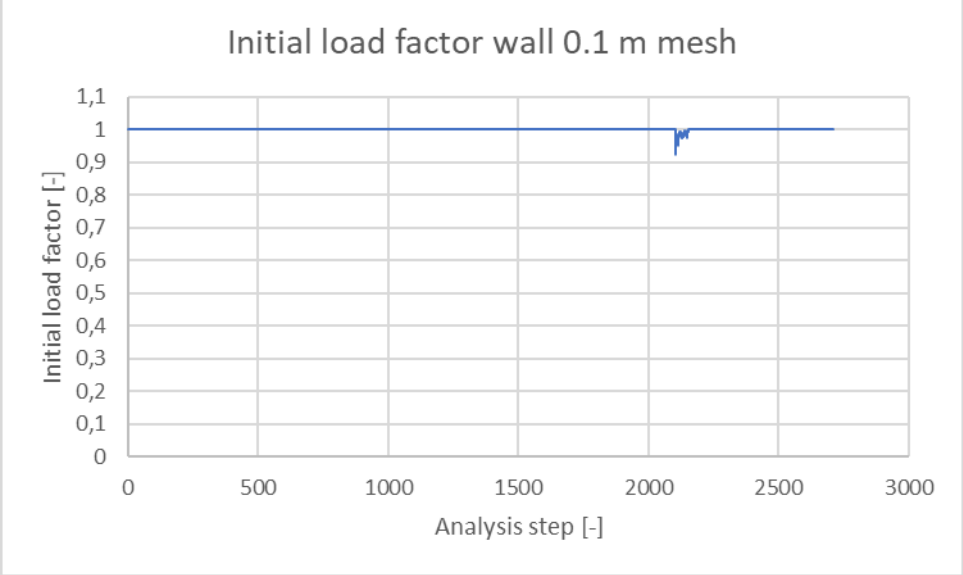

Figure 4.33; Initial load factor during Diana 10.2 analysis of single wall 0.1 m mesh

Something to highlight is the reduction at analysis step 2428. The force and displacement both reduce from $d = 3.44$ mm and $F = 33.928$ kN in analysis step 2427 to $d = 1.81$ mm and $F = 30.698$ kN in step 2428. In step 2429, the load and displacement increase back to $d = 3.01$ mm and $F = 33.073$ kN. This is not the result of a reduction of the initial load factor as $\lambda_{ini} = 1$ in all three steps. This result is important, because the unloading is not secant to the origin. To investigate this behaviour, an analysis is done which saves the strains, stresses and the damage of all integration points of all elements in analysis steps $2426, 2427, 2428$ and 2429 in a text file. A program is written with the use of MATLAB which stores this information (damage, strains and stresses) in one big matrix (Appendix A). Afterwards it can be searched for crack closure behaviour, i.e. integration points that are damaged in which the strains and simultaneously the stresses change sign between two analysis steps. Between analysis steps 2426 and 2427 the stresses and strains did not change sign. Between 2427 and 2428

the stresses and strains changed sign in many integration points and between analysis step 2428 and 2429 the elements with big reductions changed back. The elements and integration points in which important changes occurred were: Element 248 integration point 1 and integration point 3 and element 249 integration point 1. Changes also appeared in element 4, 7 and 245, but the stresses changed to relatively small values which have no big effect, because the strains will also be small.

The strains and stresses are viewed in the x, y-coordinate system, with strains ϵ_{xx} and ϵ_{yy} and stresses σ_{xx} and σ_{yy}. Later a plot is given for the principal direction. For this element the principal directions gave a clear view. For all diagrams shown below, the graph starts with the first analysis steps in the compressive region after which it moves to the tensile region.
The change of sign in stresses and strains in element 248 integration point 1 is visible in x-direction. The relation between the strain ϵ_{xx} and stress σ_{xx} during the analysis will be shown in Figure 4.34.
The crack closure error occurs when the strain jumps from $5.21 * 10^{-4}$ to $-2.7 * 10^{-4}$ and back. It crosses the origin and enters the compressive zone with the same stiffness.

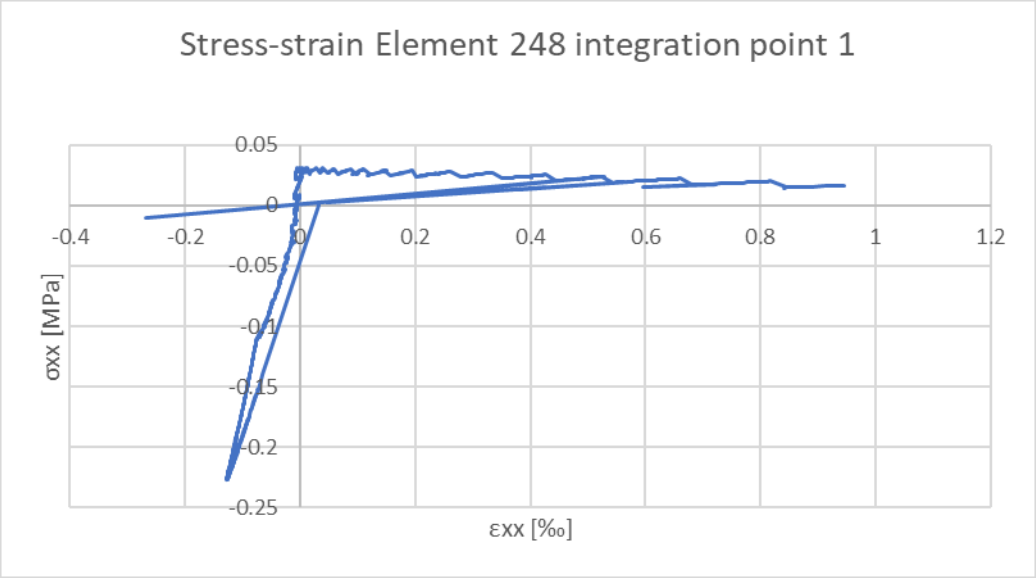

Figure 4.34; ϵ_{xx} and σ_{xx} during the analysis in element 248 integration point 1

In element 248 integration point 3, the reduction is visible in both the x-, and y-direction.

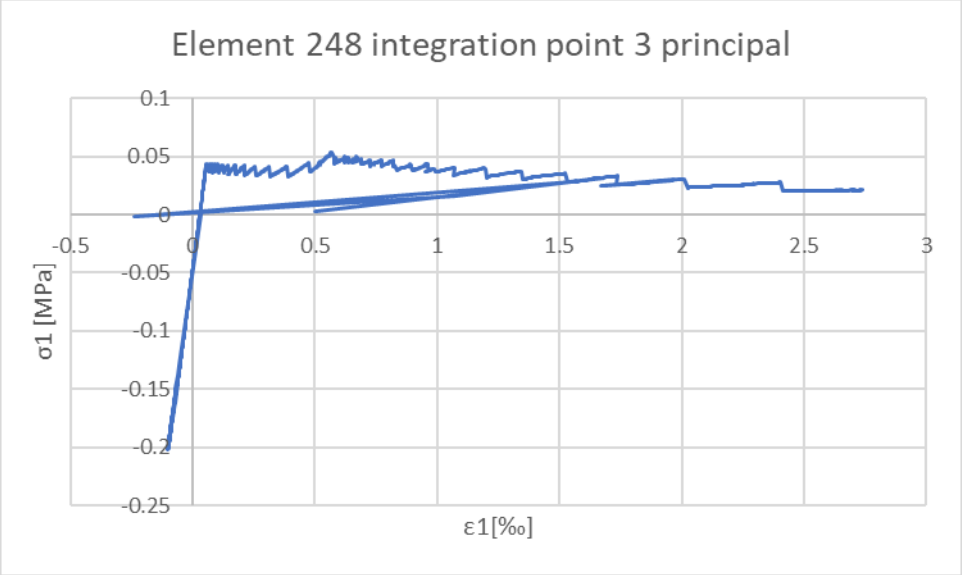

Figure 4.35; Principal stress and strain in element 248 integration point 3

In integration point 3, the crack closure error occurs in the same stage as in integration point 1.
Both integration points lay on the same horizontal distance.
The branch to the negative side is bigger when the stresses and strains are shown in the x-direction.

The last error occurs element 249 integration point 1, shown in Figure 4.36.
Again, the graph does not cross the origin.

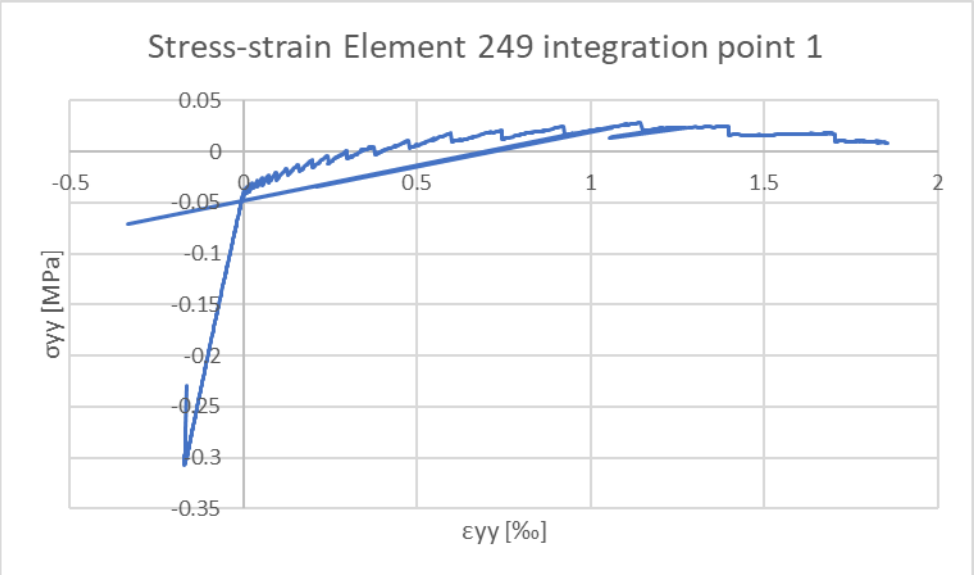

Figure 4.36; ϵ_{yy} and σ_{yy} during the analysis in element 249 integration point 1

As the stresses and strains in these steps are relatively high, the result of these wrong results is the reduction in Figure 4.32. For this integration point, the stresses and strains are shown for the global y-direction, because at some stage, the principal direction changes for this element disturbing the plot.

In Figure 4.37, the location of elements 248 and 249 is shown. These elements are in the top row of the wall and are damaged because of the flexural failure mode starting from the lower left and the top right corner.

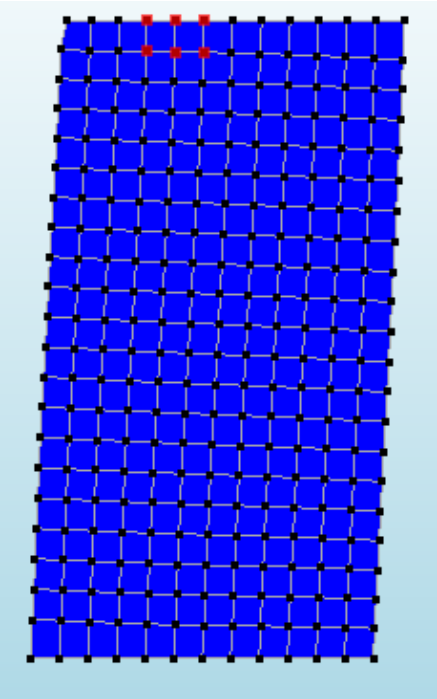

Figure 4.37; Location of element 248 (right) and 249 (left)

4.3.8 Conclusion

In this chapter, a single wall was tested to get familiar with the sequentially linear analysis and to verify if the method works. First an analysis with only a pushover load was performed. This analysis showed a load-displacement curve with softening after the peak load was reached. The analysis method was able to describe the snap-through behaviour without difficulties. At the end of the analysis, a major load decrease was observed. At that stage it was concluded that the wall had failed.

Next, an analysis was performed in which a constant floor load was added at the top of the wall. The maximum load increased much as a result of the weight acting as a prestress on the wall, making it possible to withstand a higher push-over load. This analysis had some difficulties. When the structure unloads, this was not secant to the origin in the first part of the post-peak behaviour. In some steps, the displacements were even negative. The failure pattern was flexural as tensile damage occurred in the bottom left and top right corner which propagated to the center. As the problems that occurred in this analysis were similar to the analysis with self-weight, the cause of this behaviour is investigated in there.

When self-weight was included, even more unstable analysis steps occurred. The global behaviour was almost perfect elastic-plastic behaviour (no hardening or softening), with a small elastoplastic part at the transition. The instability of some analysis steps is shown by an abrupt huge decrease in force, negative displacements and unloading not secant to the origin. First the mesh sensitivity is examined with a coarse mesh in which the mesh size is doubled and a fine mesh in which the mesh size is divided by two. Although the elements of the coarse mesh were quite large, the result was acceptable. After the peak, there is a small decrease in load. At some time, it is not possible to apply the full initial load factor and the structure can be regarded as failed. Before this happens, the structure has a displacement around $40\ \mathrm{mm}$. Therefore, the structure can be regarded as relatively ductile. The fine mesh showed the complete opposite behaviour. After the elastic branch, the structure immediately failed because of instability of some elements at the load application point and the load is decreased along the same branch. Remarkable was that the reduced mesh size did not improve the results but made them worse because of local instabilities.

Next, the unstable analysis steps in the standard mesh were investigated to find the cause of this behaviour. First, the structure was globally examined at these analysis steps by looking at the contour plot and some nodal approximations of the stresses and strains in the elements. This resulted in an indication that there could be crack closure errors in the analysis. In a later stage of the investigation, the analysis was repeated with the new Diana 10.2 version. In this analysis, the number of unstable steps was greatly reduced and also the negative displacements were not present anymore. There were however still some steps in which the initial load factor reduced and where the structure unloads not secant to the origin. A self-made MATLAB program was used, developed in the first place for the beam element analysis, which searched all the integration points of the structure for crack-closure errors around those critical analysis steps. In the case of the initial load factor reduction, no crack closure behaviour was found. However, in the analysis step where the structure did not unload secant to the origin, crack closure errors were found in many integration points. There were three significant errors; in element 248 integration point 1 and integration point 3 and element 249 integration point 3. These were significant because the strains and stresses were big in these integration points. This results in big errors by applying a wrong stiffness which differs from the neighboring undamaged elements. There was definitely a relation between the non-secant branches in the load-displacement diagram and the errors found. However, as this only occurred for some steps and the program was able to recover quite fast, this did not affect the total solution. Globally, the analysis was very stable and the results were promising.

4.4 Pavia house

4.4.1 Introduction

This part is about the analysis of the door wall of the Pavia house using continuum elements. Again, the two model approaches (CM) and (3ZCM) will be used. First the analysis is again build stepwise with first only the floor load and the lateral load (4.4.2). Later self-weight is included (4.4.3) and a mesh size study is done for both the three-zoned model as the standard continuum model. A comparison is made between the results of the continuum model and the incremental iterative approach of Nobel [2] (4.4.5).

Again, an in-depth analysis is done with the improved version of Diana FEA (4.4.6). Initial load factor reductions are investigated and the possibilities of crack openings. Further, non-secant branches are investigated and the behaviour of the piers. Finally, some possible improvements are suggested and tested (4.4.7). The results will be discussed and conclusions will be drawn to conclude this chapter (4.5).

4.4.2 3-zone Pavia house without self-weight

Here, the full house will be analysed using the sequentially linear analysis technique. In this model, the corners which are purple in Figure 4.38 have the same material properties as the middle of the piers (strength f_{tu} and fracture energy G_{f-tu}^{I}). The vertical loads (f_1 and f_2) are distributed over the floors. At the left side of the floors, two loads are applied, each with a force of 0.5 N. These loads are scaled in the SLA procedure. In the load-displacement diagrams, the load axis always shows the total horizontal load. This is the value of the load multiplier, because two loads are applied with a value of 0.5 N each.

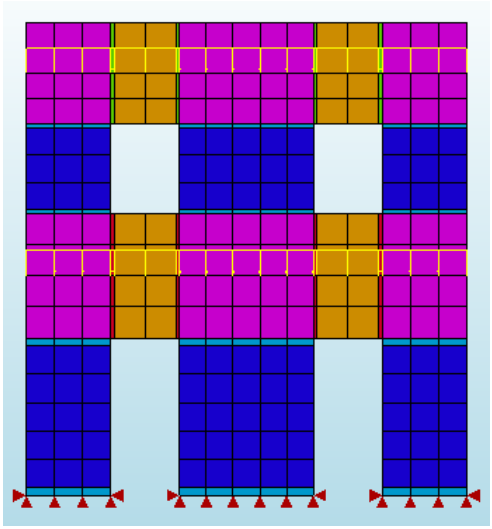

Figure 4.38; Pavia house façade model

Important to remember is that the flexural failure elements in the piers and spandrels could have a bad aspect ratio when the mesh size decreases, this can result in bad element behaviour. A smaller element size also leads to an exponential increase of the calculation time, and more analysis steps as there are more integration points to damage before the structure fails.

The vertical load does not result in a critical point in the structure, therefore no failure occurs in the building before the lateral load is applied.

The first damage occurs in the bottom of the middle pier, followed by the bottom of the right pier, both from the left side. This damage propagates in these elements until the left corner at the bottom of the left pier damages continued by the top right corner of the first pier. These damages continue to grow which result in a tilt of the house to the right. Next, the right pier of the second floor starts to crack at the left bottom followed by damages at the bottom left and top right corner of the left and middle pier of the second floor. Figure 4.40 shows analysis step 1176 in which the load is still increasing ($F = 91.2$ kN; $d = 3.4$ mm) and analysis step 2900, around the point where the maximum load is reached ($F = 118.9$ kN; $d = 8.6$ mm). After this point, the program calculates a huge drop in load in which the structure definitely has failed. Damage continues, but with a much smaller load.

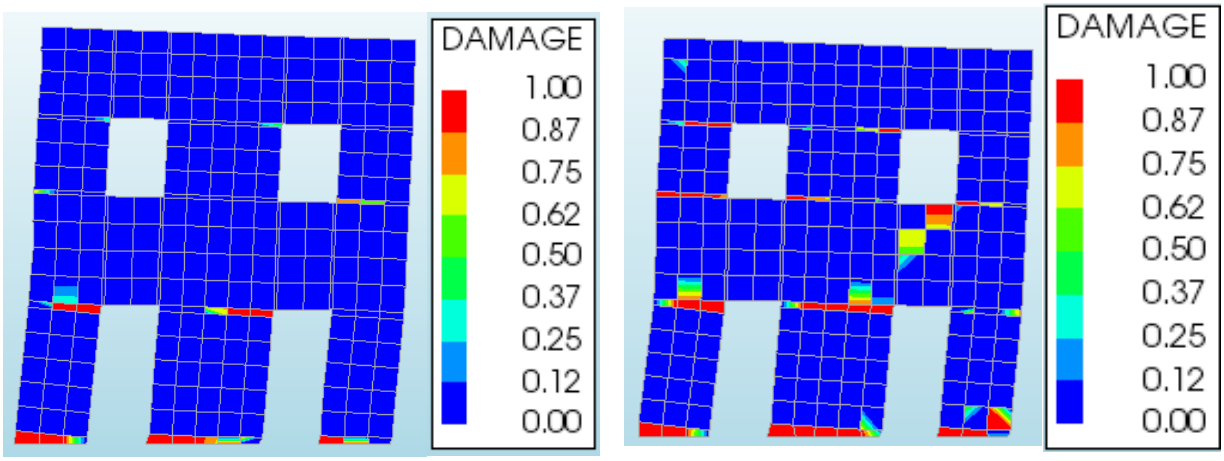

Figure 4.40; Damage - Damage step 1176 (load 91214 N) (l) and damage step 2900 (load 118930 N) (r)

The load displacement diagram of the Pavia façade can be found in Figure 4.39. Not all the 20,000 steps are shown in this figure, because the load continued to be relatively small, with unrealistic high displacements after the initial load factor had reduced. Even before the big drop after the maximum load, the structure already had three big unloadings.

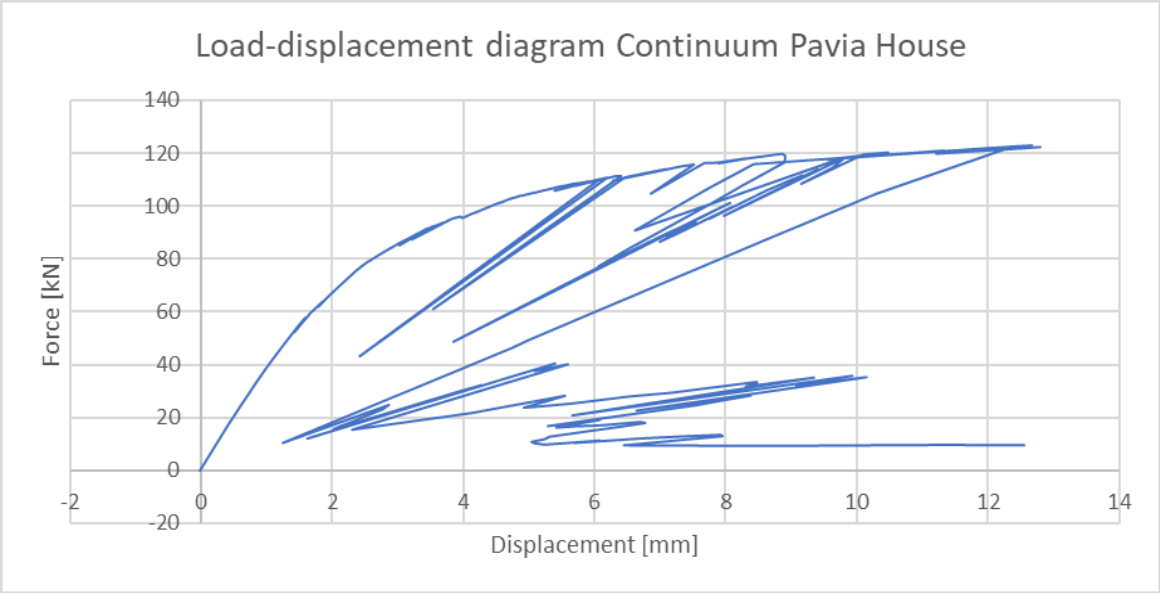

Figure 4.39; Load displacement diagram Continuum Model (20,000 steps)

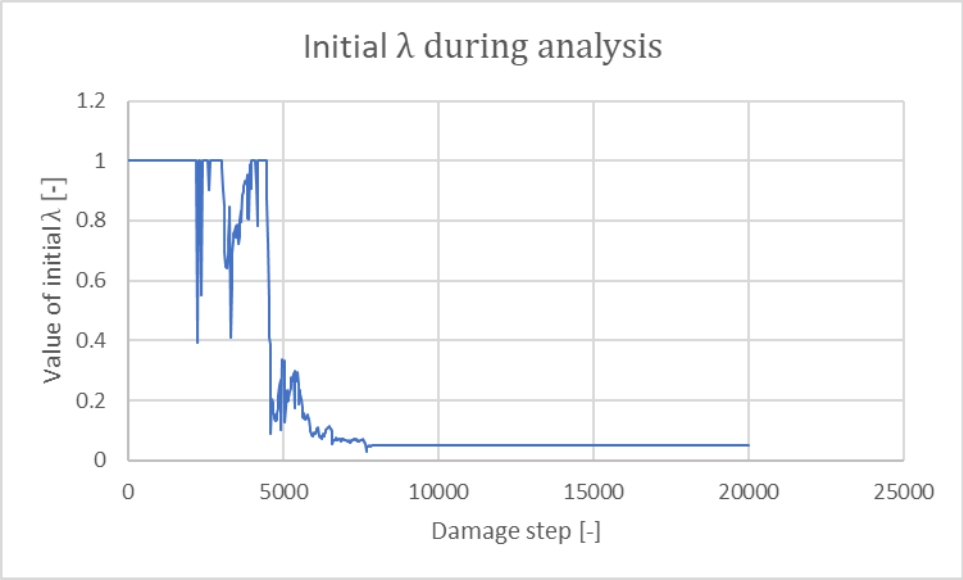

Figure 4.41; λ_{ini} during analysis; Pavia house Continuum elements no self-weight

Just after the big drop after maximum load, the damage is shown in Figure 4.42. This point corresponds with the drop of the initial load factor whereafter it cannot return to the value 1. The failure occurs when the right spandrel on the first floor is fully damaged over the height. The failure can be regarded as shear failure as the elements are damaged over the full height and the displacements are similar to vertical shearing elements.

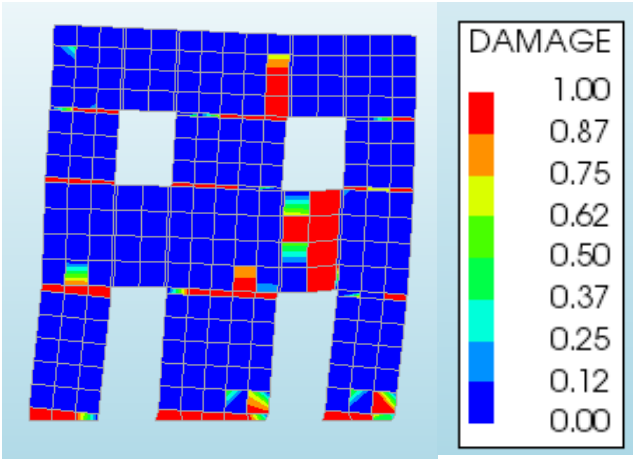

Figure 4.42; Damage - Damage step 4150 (load (90855)

4.4.3 3-zone Pavia House with self-weight, mesh sensitivity

In the next case, the Pavia house will be analysed with self-weight included.

In this case, the same thing happened as in the example with the single wall. The structure loads to a maximum load value, but instead of increased deformations and a reduced load, the structure unloads approximately along the same branch. Because the full vertical load cannot be applied anymore, the analysis prematurely stops. A possible solution can be to change the mesh size like in section 4.3.5.

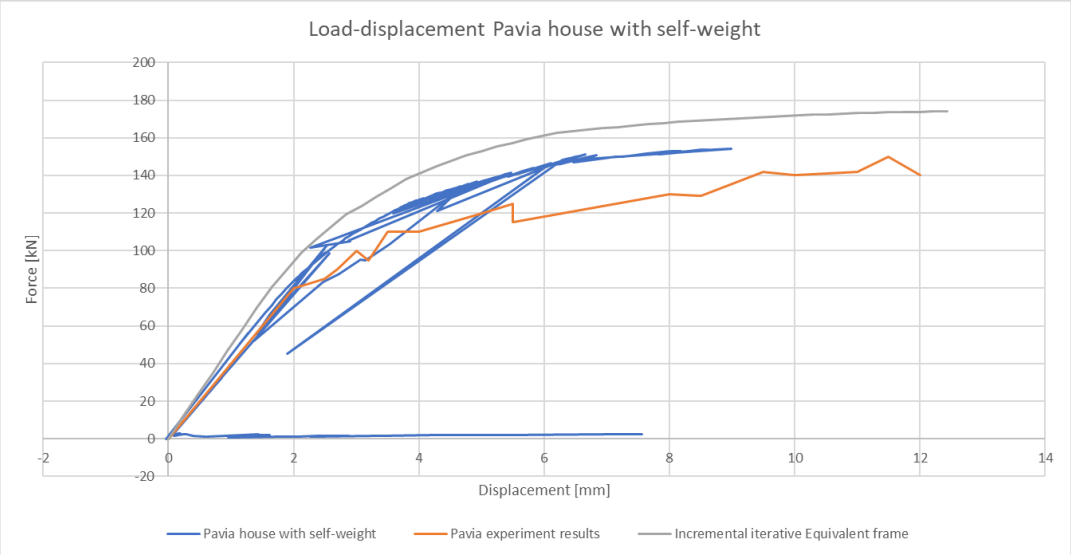

Figure 4.43; Load-displacement diagram of the Pavia house all loads included

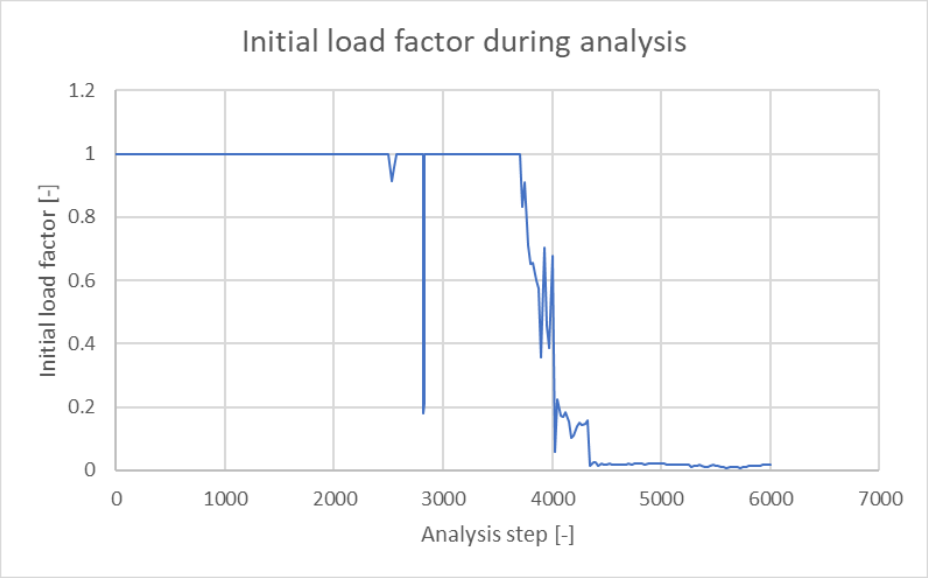

Figure 4.44; λ_{ini} during analysis standard mesh Pavia façade

First a coarse mesh is applied in which the required mesh size is doubled. The result is a very coarse mesh with two elements over the width of the pier. This means that the width is described by four integration points in width. Surprisingly, the results are still acceptable. The analysis is able to continue until the displacement has reached $d = 12$ mm. Comparing the result with the load-displacement

diagram of the experiment and the equivalent frame model of Nobel, the results are acceptable. The structure follows a different failure mechanism than in the experiment. The analysis is relatively stable as only one big load reduction occurs before failure.

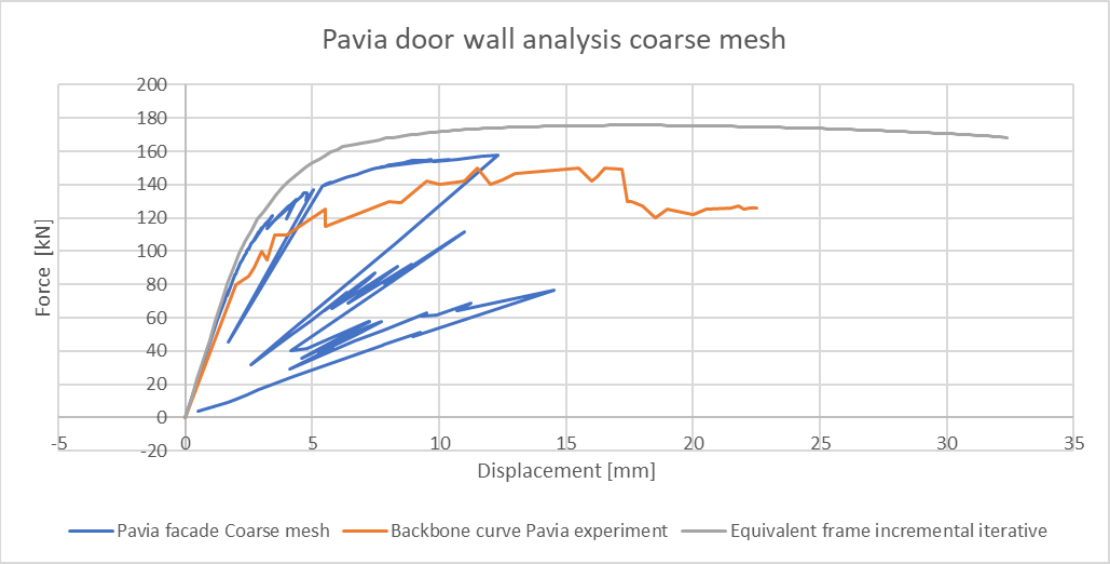

Figure 4.45; Load-displacement diagram Full house with coarse mesh

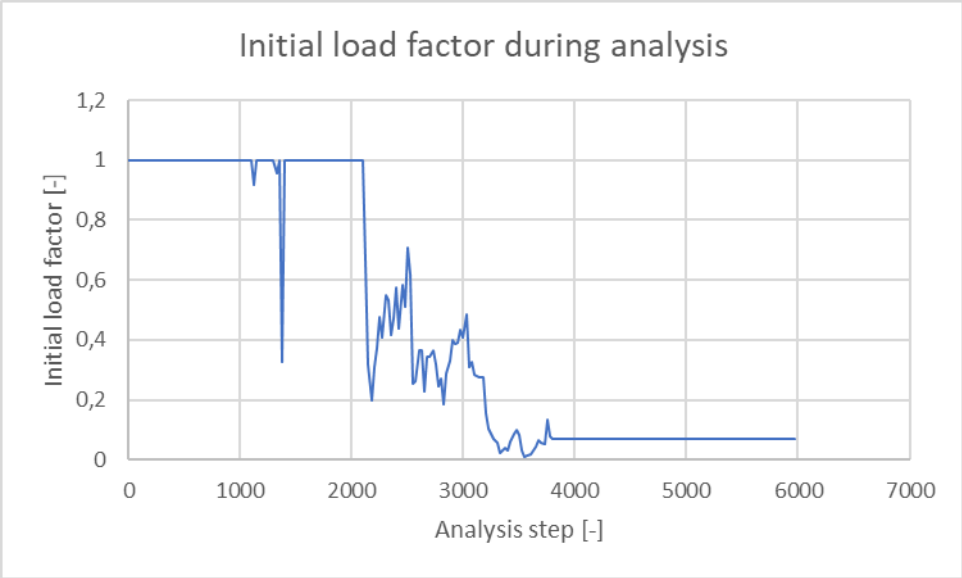

Figure 4.46; λ_{ini} during analysis; Pavia house Continuum elements coarse mesh

Now the structure is modelled by making the mesh size twice as small. The disadvantage of the three-zoned model is that in this case, the flexural zones become very shallow and long. This could lead to large aspect ratio which could influence the analsyis. This is a consequence of using rectangular elements. If the mesh size is reduced that much that the elements in the flexural zones are accurately scaled, the mesh size in the shear parts also reduces and the number of elements is far too big to make the calculation. A solution is using triangular elements for the flexural parts, this will be experimented later. Looking at the results, they still seem fair. The same failure mode occurs as for the other meshes, which is not equal to the failure mode in the experiment. The load-displacement diagram is however still accurate although the high aspect ratio.

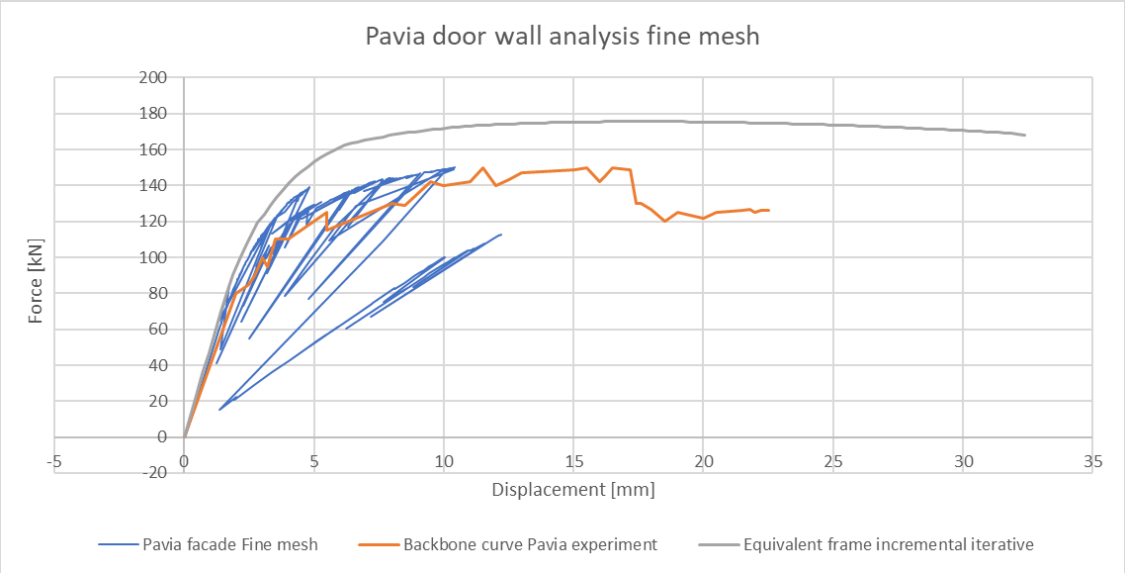

Figure 4.47; Load-displacement diagram Pavia facade fine mesh

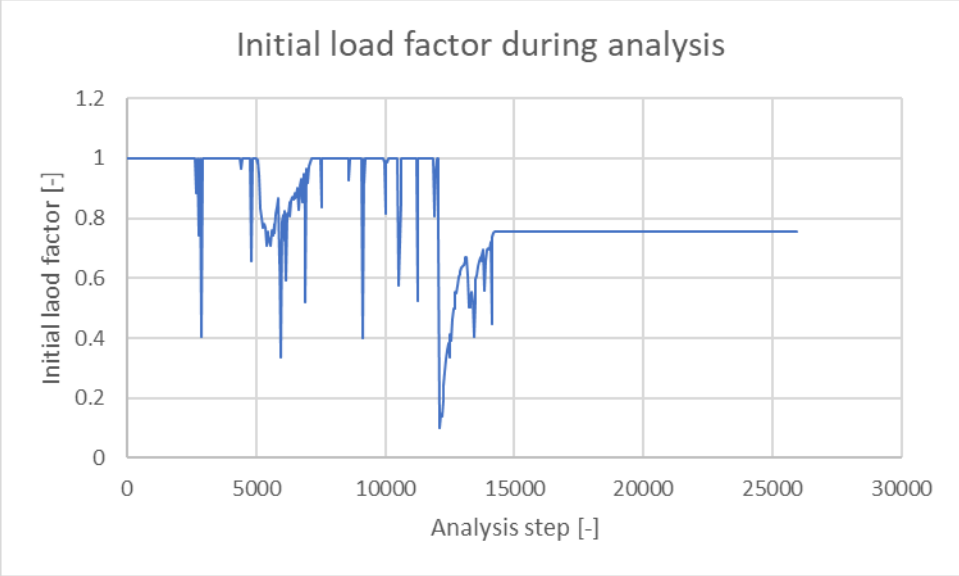

Figure 4.48; λ_{ini} during analysis fine mesh Pavia façade

4.4.4 One zone (standard) continuum model CM

In this section, the pavia façade will be modelled with the standard continuum model CM. In this model, all elements in one spandrel or pier have the same (flexural failure) properties as the tensile strength is based on the bed joint tensile strength of the masonry. This is done, because the shear strength in the 3ZCM was too high to force shear failure in the piers. Therefore all piers failed flexural, which is not in line with the experiment. Again three different meshes are made, fine, standard and coarse, with mesh sizes of $0.1\ \mathrm{m}$, $0.2\ \mathrm{m}$ and $0.4\ \mathrm{m}$. Again, the load-displacement curve is shown together with the initial load factor during the analysis. The damage in the structure is also made visible.

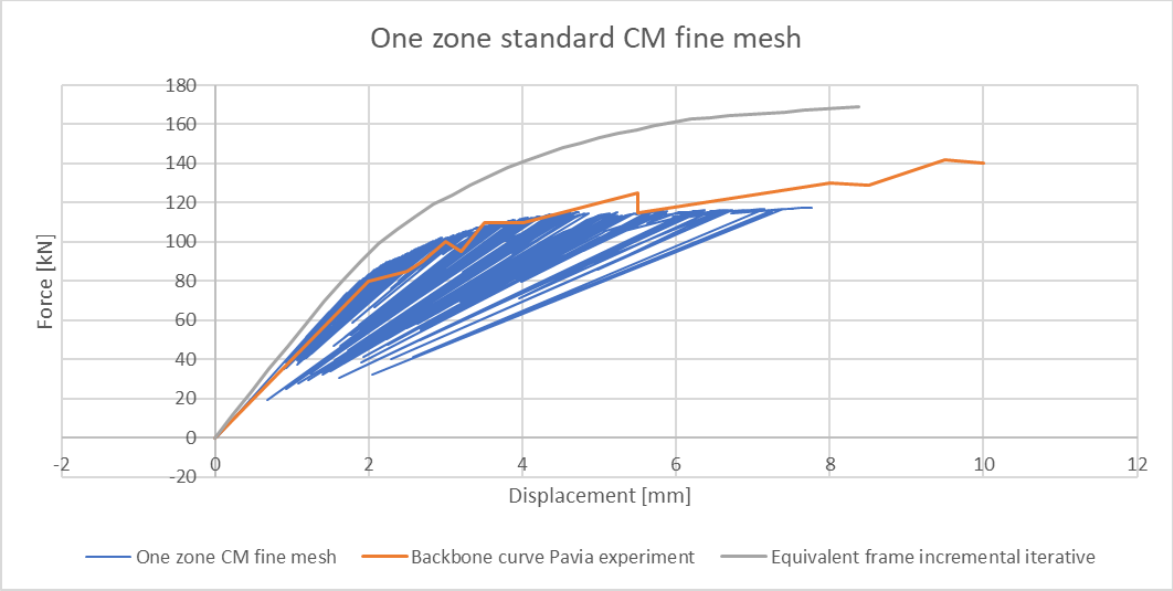

Figure 4.49; Load-displacement curve; CM fine mesh 30000 steps

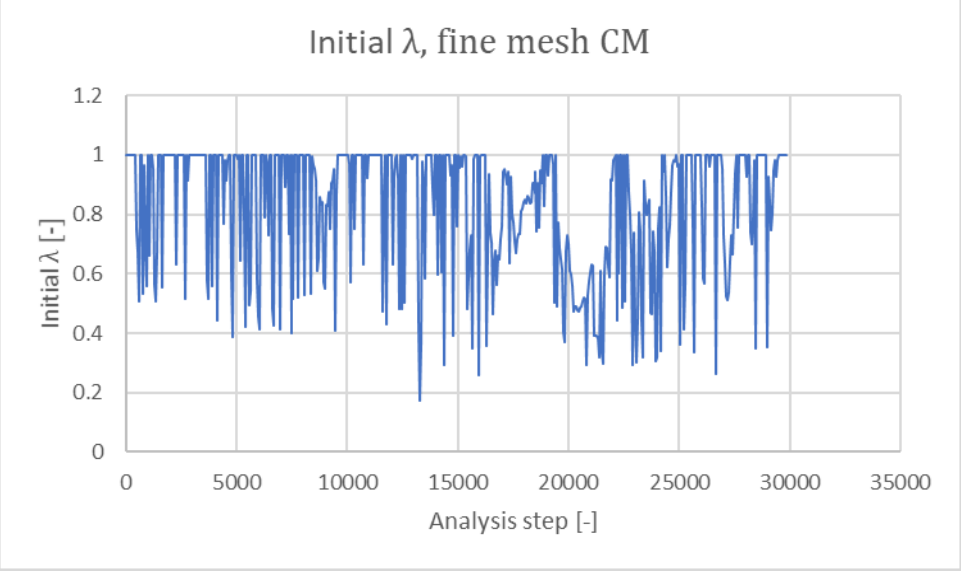

Figure 4.50; λ_{ini} during analysis fine mesh CM Pavia façade

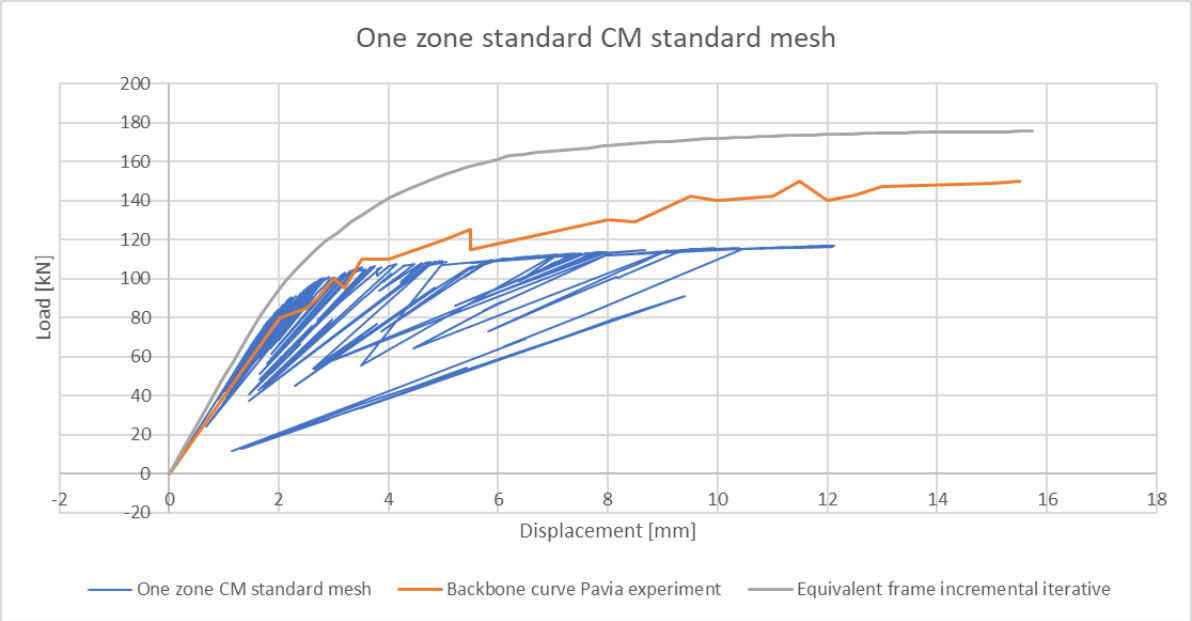

Figure 4.51; Load-displacement curve; CM standard mesh

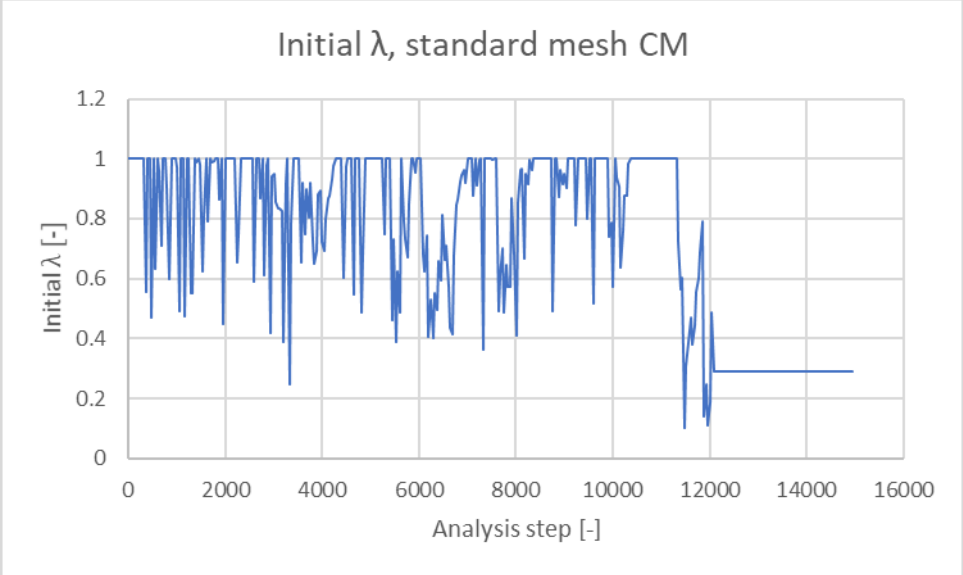

Figure 4.52; λ_{ini} during analysis standard mesh CM Pavia façade

Surprisingly, the number of initial load reduction has increased a lot compared to with the standard model. Very often, the analysis had to reduce the load to distribute the forces in the structure. Ignoring that, the load-displacement diagrams show maximum loads that are smaller than in the three-zoned continuum model analyses. As the lower flexural tensile strength is used for all sections, this was expected. Like in the case with the 3ZCM, the fine mesh uses far more analysis steps to go through the full simulation than the standard model. The coarse model uses even less steps.

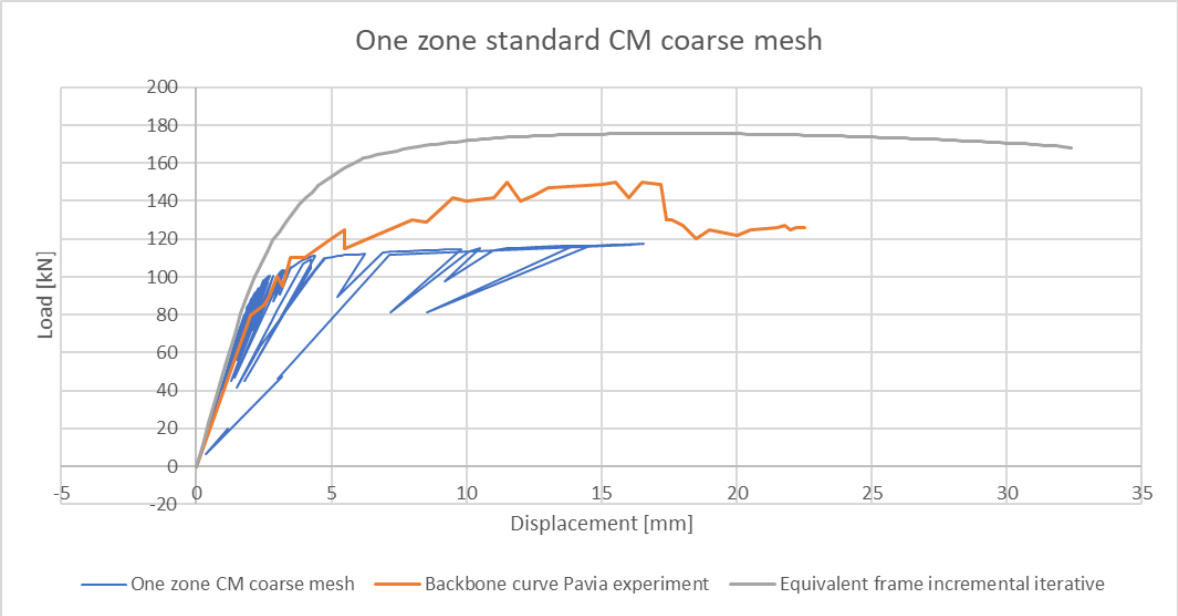

Figure 4.53; Load-displacement curve; CM coarse mesh

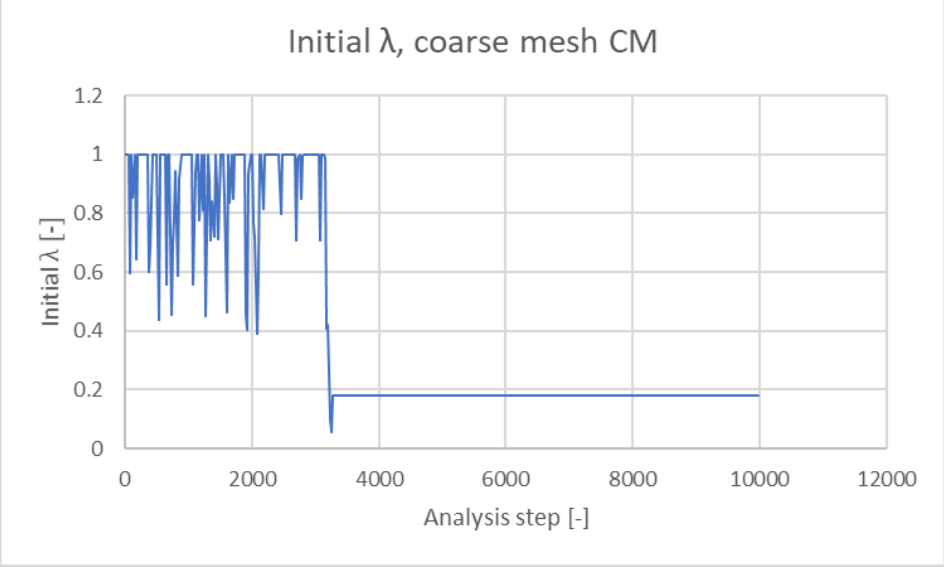

Figure 4.54; λ_{ini} during analysis coarse mesh CM Pavia façade

One important thing that can be concluded from these analyses is that there is severe unloading compared to the 3ZCM. If an analysis should be aborted for a significant reduction of the initial load factor as this indicates failure, this model would be aborted in an early stage of the analysis. An important difference is the type of failure. In the 3ZCM, the lower piers failed in rocking and the right spandrel of the first floor failed in shear. In the CM analysis at the bottom piers, the left pier fails in rocking and the middle and right pier fail because of a diagonal shear crack (Figure 4.55), the other

parts of the façade were almost not damaged in the early stages of the analysis. Only the left corner of the first floor had damage propagating from the lower right corner.

In section 4.4.5, the results of the two different model approaches will be compared with the experimental results.
In the 3ZCM, the maximum total lateral load reaches a value around $150\ \mathrm{kN}$. In the CM model it reaches a maximum value of almost $120\ \mathrm{kN}$. A significant difference. This difference is also a result of the lower strength in the shear sections of the cross-section.

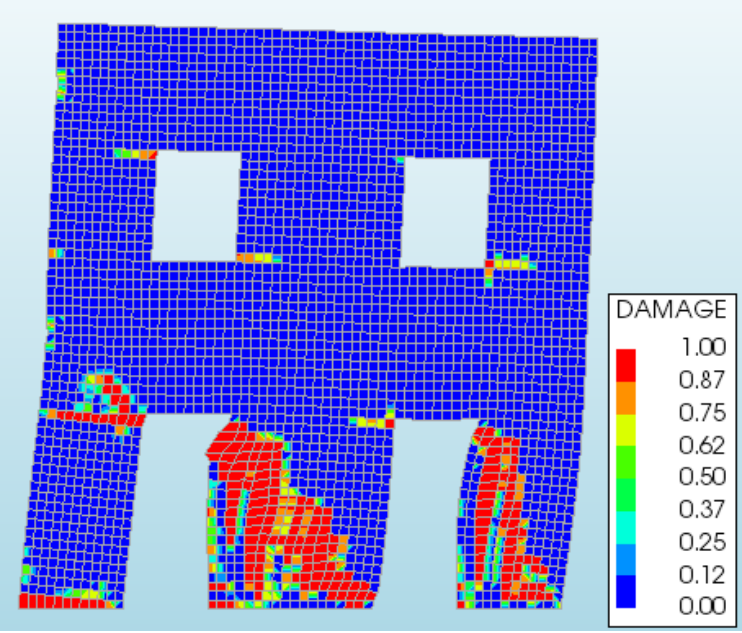

Figure 4.55; Damaged integration points CM fine mesh

4.4.5 Comparison with experiment and incremental equivalent Frame method

When comparing the results of the continuum model analysed using the sequentially linear analysis with the results from experimental data and the three-zoned continuum model used in [2] the focus will lay on the failure mode observed in all models and the maximum load versus displacement.

Comparing the failure mode of the sequentially linear analysis and the experimental data, in both situations a flexural failure mode occurs in the left pier of the bottom row. In the SLA, the middle pier of the bottom row only suffers from flexural failure, while the experimental data shows a diagonal shear crack. Later in the analysis, a shear crack also occurs in the right pier of the bottom row in the experimental data, but this is not visible because this point is not reached in the SLA due to unloading. The SLA shows in several analyses a vertical shear failure in the right spandrel of the first floor as the next developed crack. In the experiment, the shear cracks in the spandrels are horizontal and not vertical.
The three-zoned continuum model in [2] shows also flexural damage in the left and middle pier of the bottom row. Here, the shear failure in the middle and right pier of the first row is similar to the crack of the experiment.

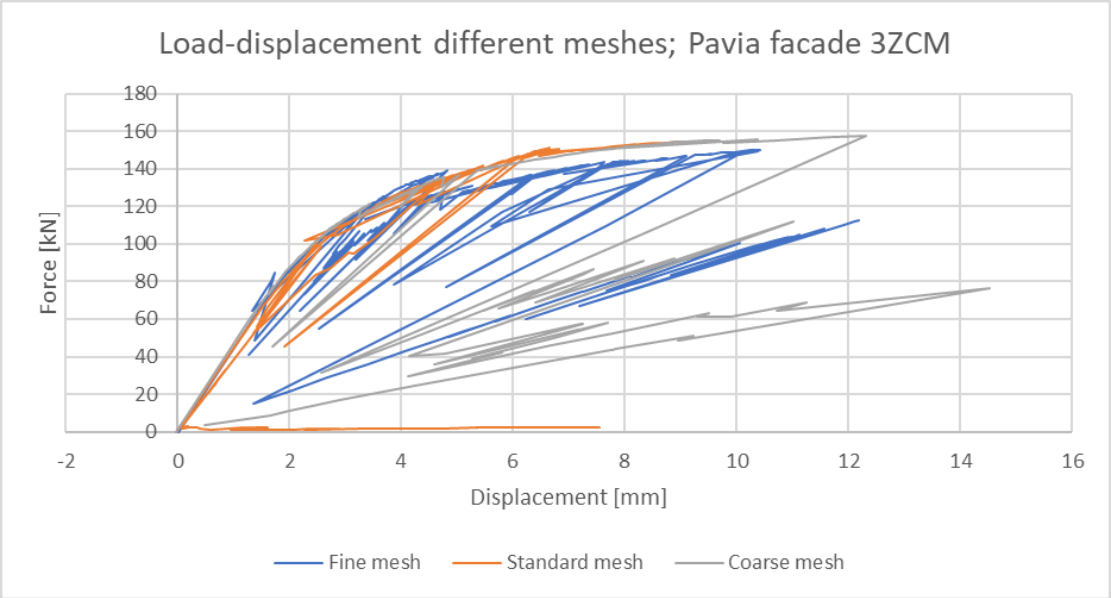

Figure 4.56; Load-displacement diagram comparison

To compare the load, the total horizontal force on the building is compared together with the displacement of the top floor for all three meshes of the continuum model. All three analyses follow the same curve. In the beginning of the analysis. The standard mesh unloads early in the analysis. The other two are able to continue. It was already shown that the analysis was quite accurate in respect of the load-displacement relation.

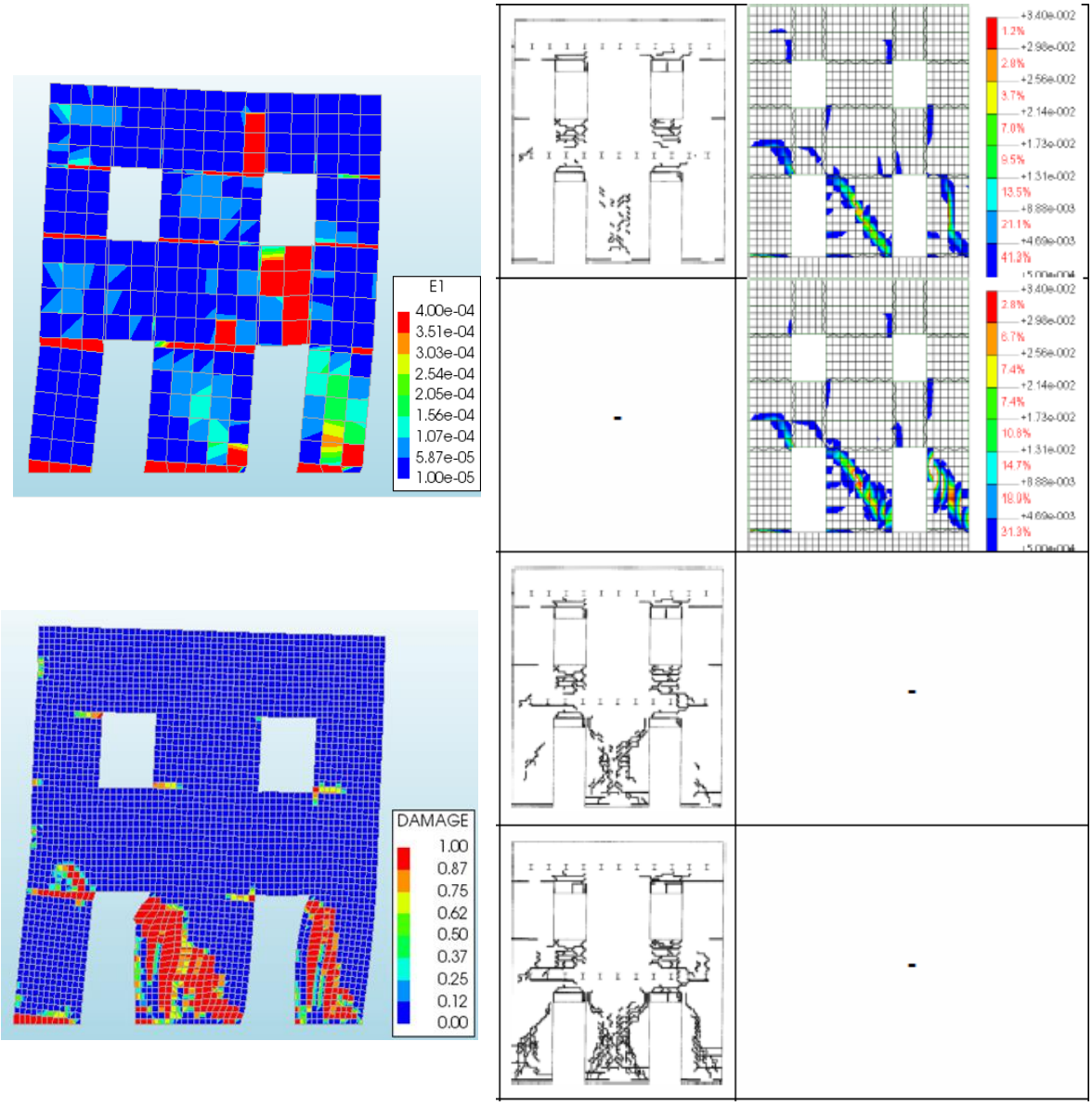

Figure 4.57; Strains 3ZCM (left top), Damage CM (left bottom), Experiment (middle) and 3-zoned model from [2]

In Figure 4.57, The models are compared with the experimental results. In terms of damage in the structure, the CM gave the best failure mode. The shear in the middle and right pier are correctly observed, the left pier starts with rocking in the experiment. In the experiment this pier showed also shear failure later. In the second floor and above, almost no damage is found excluding the damage in the corners of the windows. The 3ZCM showed vertical shear failure in the right spandrel of the first floor. The bottom piers all fail in rocking, while the experiment showed shear failure in the middle and right pier. The maximum load is approximated better in the 3ZCM. Here, it has a value around 150 kN just a little bit higher than in the experiment. The CM predicts a maximum load of almost 120 kN, which is too low. Moreover, the experiment had a cyclic loading pattern, while the analysis was just lateral. Probably, the maximum force in the experiment would be even higher when a lateral pushover analysis had been done. Concluding, the 3ZCM was not accurate in the case of the right failure mechanism, it did predict the load relatively accurate. The CM predicted the right failure mechanisms in the bottom piers. However, the total load was too conservative. In this aspect the 3ZCM performed better.

4.4.6 In-depth analysis

Like in the case with the single wall, also in this, case the model is tested again with the new Diana version. The case standard continuum model (CM) is chosen because that case gave the best results speaking about the failure mode. All elements are quadrilateral and all elements have the flexural properties based on the bed joint tensile strength of the masonry. The mesh size used has an input

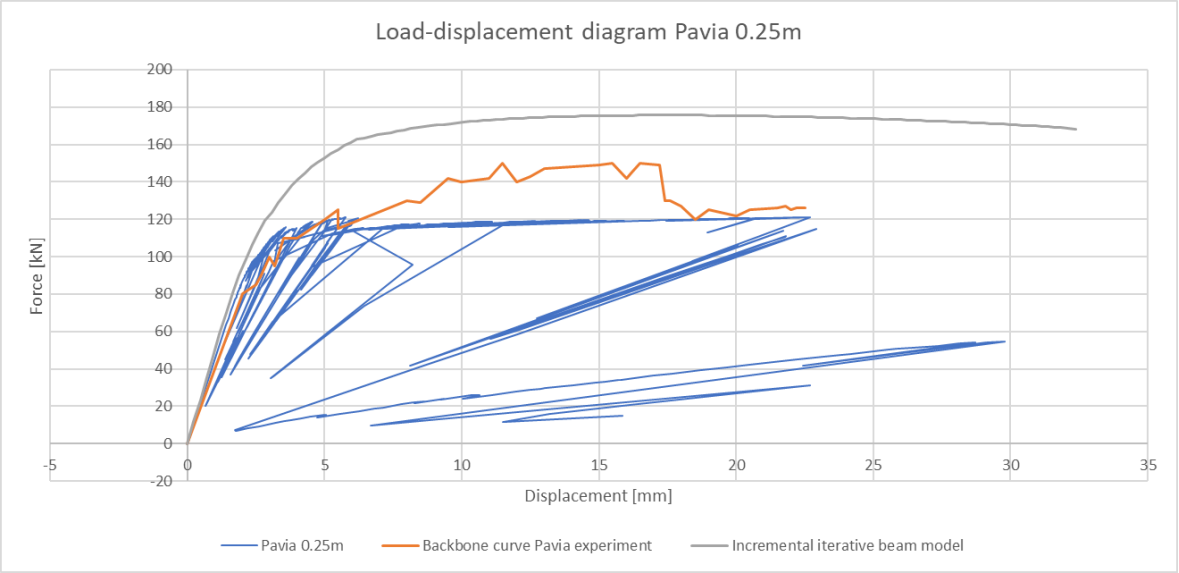

Figure 4.58; Pavia facade with 0.25m mesh in Diana 10.2

value of size $h = 0.25$ m. This results in a mesh with 9 elements in the height of the first-floor pier and 5 elements in its width. The quality of the mesh is good, with an aspect ratio almost equal to 1 and all elements approximately of the same size.

Comparing the results of the analysis with the experimental data, the approximation appears to be quite good. Concerning the lateral load versus the displacement, there is only a difference in the part between 5 mm and 17 mm. In the experiment, the load increases to 140 kN and back to 120 kN in that part, while the load in the SLA stays around 120 kN. In both cases a maximum stable deformation was found at approximately $d = 22$ mm.

When the damage pattern of the experiment is examined, the damage starts in the first-floor spandrels followed by the middle bottom pier and afterwards the left and right bottom pier. Some flexural damage occurs in the first and second floor piers, but the shear damage is more dominant. In the experiment the left bottom pier has a bottom left to top right shear pattern, the right pier a bottom right to top left shear pattern. The middle bottom pier has diagonal shear cracks in both directions.

In the SLA, the shear cracks at the bottom develop from the start even for smaller displacements ($d = 2.7$ mm) than observed in the experiment ($d = 11.4$ mm). The middle pier at bottom level shows shear damage from the bottom right to the top left corner. The right bottom pier follows the same shear behaviour as in the experiment. The left bottom pier fails flexural in the SLA. The spandrels on the first floor stay undamaged while these were damaged a lot in the experiment. Some of the smaller damages in the experiment on the second-row piers are also visible in the SLA.

Concluded, the load pattern is relatively accurately described. The SLA misses the increasing and decreasing part of the load-displacement diagram of the experiment between $d = 5$ mm and $d = 17$ mm, but approximates the structure better than the three-zoned continuum model with an incremental iterative approach in [2].

4.4.6.1 Crack openings

Like in previous cases, the initial load factor is reduced during some analysis steps (Figure 4.59). Some reductions are relatively big, with only 40% capacity left.

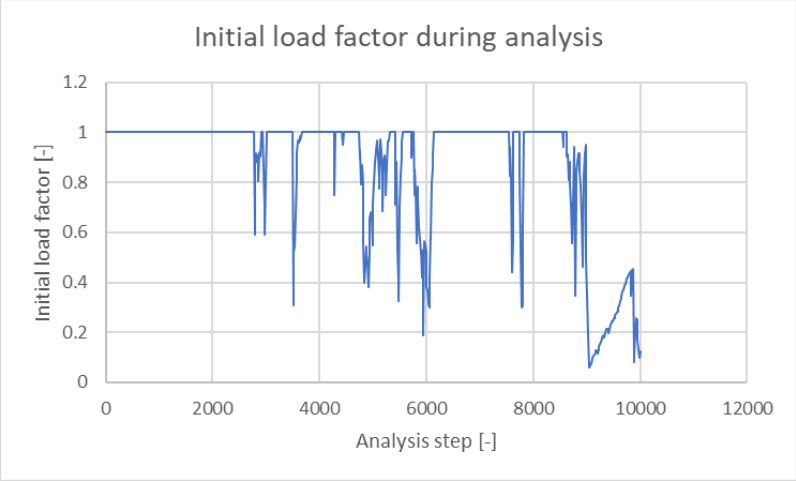

Figure 4.59; Initial load factor during the analysis. Continuum model with Diana 10.2

The integration point which is damaged when the load is reduced is investigated to find if there is a relation between the reduction and the damage. For example, a crack opening can have a relation with a load reduction as the opening of the crack results in a redistribution of forces. This can load to the structure being not able to carry the full load in the next analysis steps. The first load reduction happens at analysis step 2779. In this analysis step, the initial load factor λ_{ini} reduces from 1 to 0.39. The structure was not able to carry the vertical load and therefore only approximately 40% of the previous load case is applied to the structure. The damage in analysis step 2779 occurs in integration point 4 of element 275. To investigate this integration point, the stresses and strains of this point during the analysis are gathered. In an elastic situation, the stresses and strains in an integration point follow Hooke's law for isotropic, linear elasticity. As this model uses the plane stress approach ($\sigma_{zz} = 0$), the stress and strain tensor only consist of two axial quantities and one shear quantity. This relation can be described as:

$$\begin{bmatrix} \epsilon_{xx} \\ \epsilon_{yy} \\ \gamma_{xy} \end{bmatrix} = \frac{1}{E} \begin{bmatrix} 1 & -\nu & 0 \\ -\nu & 1 & 0 \\ 0 & 0 & 2(1+\nu) \end{bmatrix} \begin{bmatrix} \sigma_{xx} \\ \sigma_{yy} \\ \sigma_{xy} \end{bmatrix} \tag{4.4.1}$$

To make an estimate of the crack width, the elastic strain in every analysis step is estimated using the relation above and the axial stresses. This is of course an assumption, because in a sequentially linear analysis all analysis steps are linear. Strictly speaking, there is no elastic and plastic strain as all steps are linear elastic with a reduced Young's modulus. In this approach, the elastic strain is subtracted from the total strain in that analysis step to retain a fictitious crack strain:

$$\epsilon_{el} + \epsilon_{crack} = \epsilon_{total} \tag{4.4.2}$$

This fictitious crack strain is multiplied with the element size to calculate the estimated crack width in the element.

$$w_{crack} = \epsilon_{crack} * h \tag{4.4.3}$$

For element 275 integration point 4 the estimated crack width is shown in Figure 4.60.

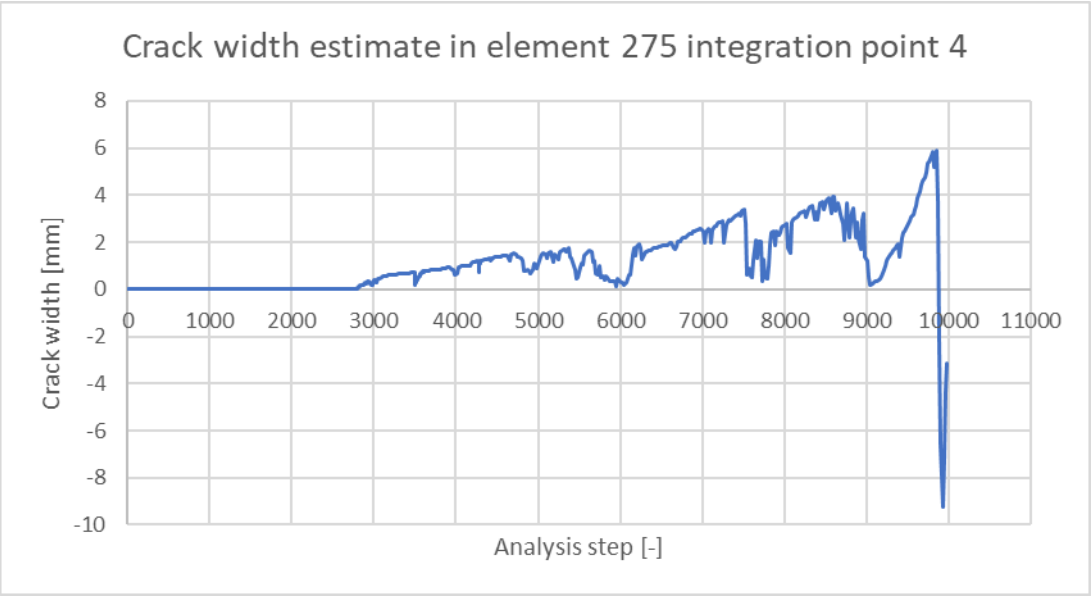

Figure 4.60; Estimated crack width during analysis of element 275 integration point 4. Crack growth after initial load reduction in step 2779

The estimated crack is negligible before step 2779. After the damage in analysis step 2779, the crack strain starts to develop. Crack initiation is found at the integration point where damage occurred during reduction of the initial load factor. The next major reduction occurs at analysis step 3500. In this step, the load reduces to 0.24 as a result of damage in element 264 integration point 1.
This is shown in Figure 4.61. Again, a crack initiates during the same analysis step the load reduces.

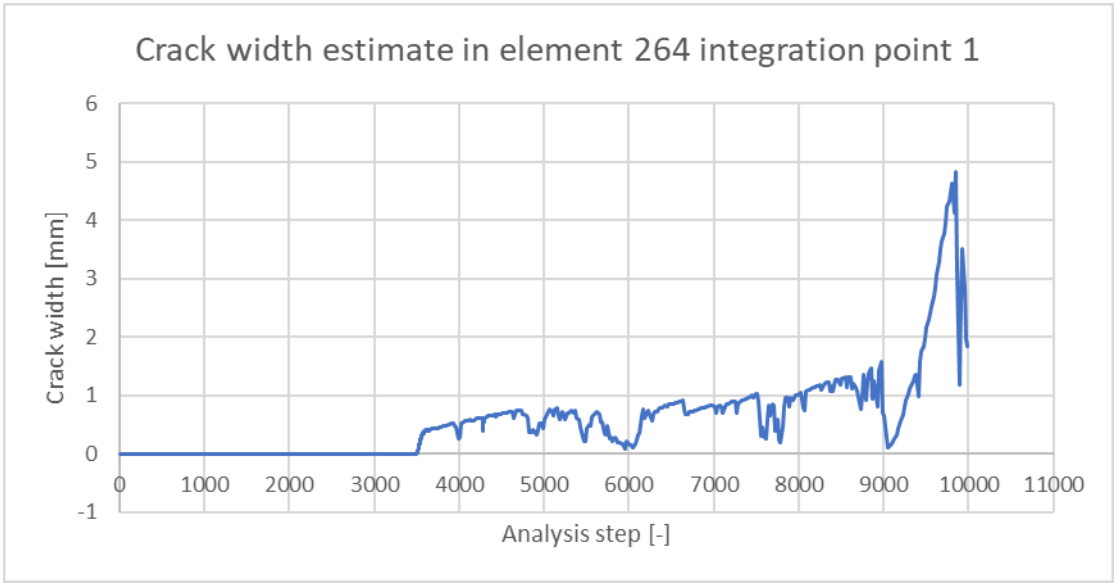

Figure 4.61; Estimated crack width during analysis of element 264 integration point 1. Crack growth occurs after the initial load factor has reduced

However, when the reduction at analysis step 4280 is examined, the crack at corresponding element 283 and integration point 2 is already present. This crack initiated at analysis step 3418 when the integration point was damaged for the first time. In this analysis step, the initial load was fully applied. This was also the case for element 290 integration point 3. The load reduces together with a damage

increment in analysis step 2937, but a crack already grew in this integration point together with the first damage occurring in analysis step 2922.
In conclusion, it is highly likely that initial load factor reductions share a relation with crack openings in the corresponding damaged integration point of the element as this is shown for several load reductions. However, in some cases, a crack had already opened and therefore this was not visible as the crack already existed. Probably, the reductions are the result of the analysis unable to cope with the abrupt change of the element due to crack opening and the associated redistributions. This however gives no explanation in the case of a load reduction when a crack has already opened, because the crack width stayed the same.

4.4.6.2 Crack closure errors

During the analysis, especially in elastoplastic part (displacements between $2.5\ \text{mm}$ and $6\ \text{mm}$) the structure unloads several times. Some of these unloading branches are not secant to the origin and are therefore investigated to see if crack closure errors occur like in the case of the single wall. Below in Figure 4.62 is a part of the load-displacement graph shown between analysis steps 1000 and 2500 and part of a line connecting the origin with the graph. The reductions are not parallel with the orange secant line between the origin and the curve as would be expected in an SLA.

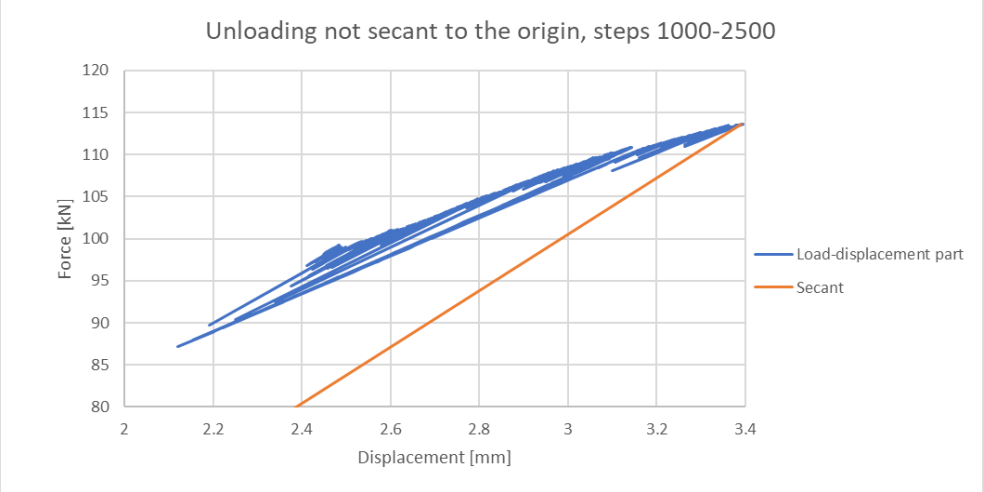

Figure 4.62; Unloading not secant to the origin in continuum model Pavia house 0.25m mesh

Four intervals of analysis steps with reductions are checked for crack closure errors: 1103-1106, 2088-2091, 2477-2480 and 2777-2780. They are shown in Figure 4.63. Interval 2777-2780 is secant to the origin, the other three are not. The same program from 4.3.7 is used to check all the integration points in these three intervals for crack closure errors. For the intervals 2088-2091, 2477-2480 and 2777-2780, no crack closure errors are found. For interval 1103-1106, a crack closure error is found between step 1104 and 1105 (reduction of load) and between steps 1105 and 1106 (increases back). The error is found in element 41 integration point 1 and integration point 3.

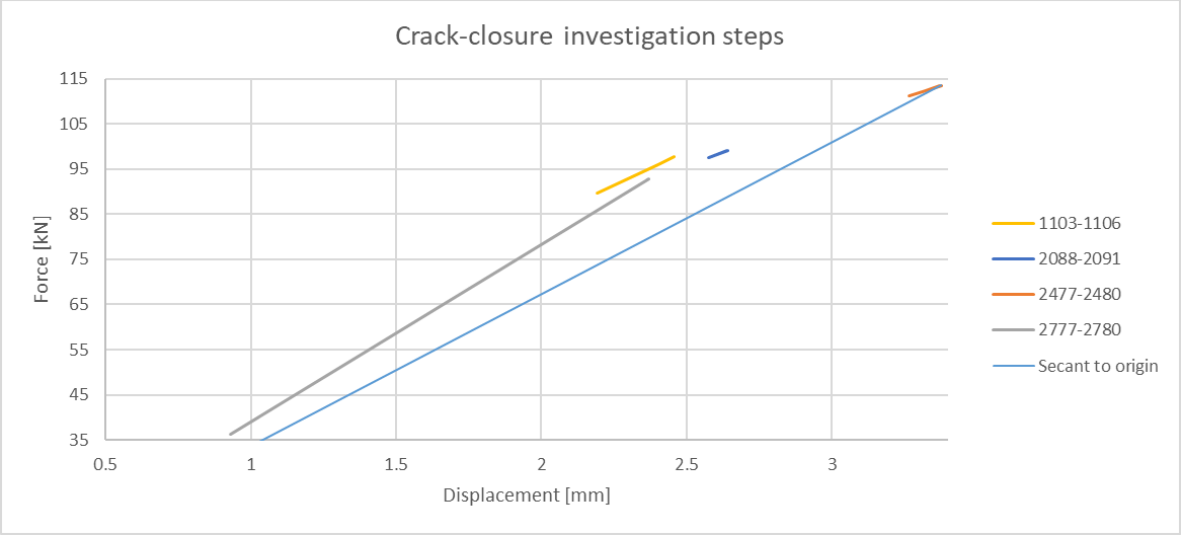

Figure 4.63; Intervals with reductions for crack closure investigation

Element 41 is the most bottom-left element of the bottom right pier. The stress-strain relation of integration point 1 is shown below. This relation very similar to the stress-strain relation of integration point 3.

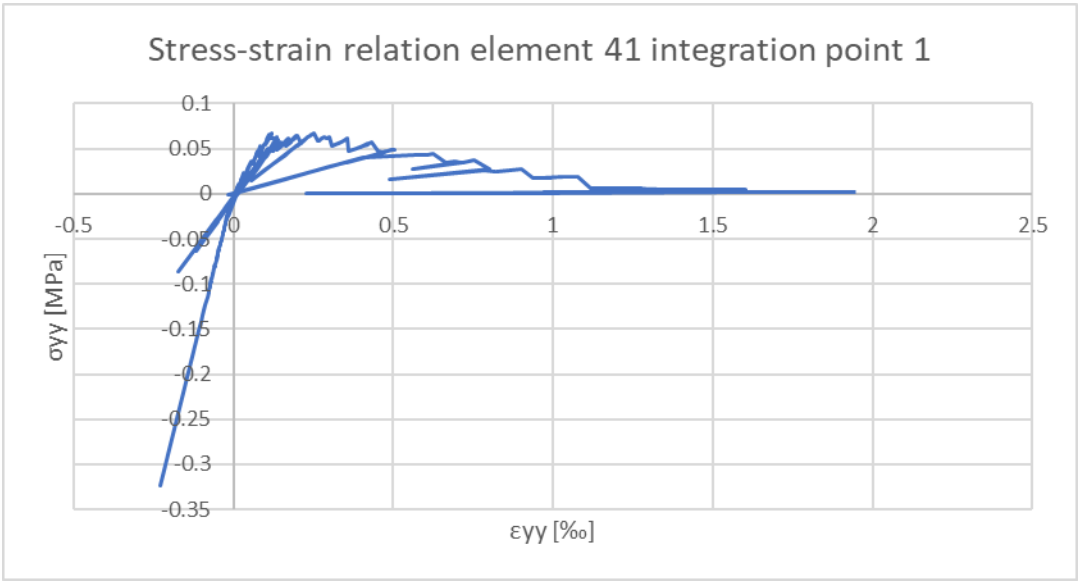

Figure 4.64; Stress-strain relation in y-direction of element 41 integration point 1 step 1-5620

The integration points are shown for the y-direction because they are sought in this coordinate system. As the principal stress always follows the biggest stress direction, negative values for a certain direction are often not visible as the principal direction rotates and other positive stresses are larger. As this element is located in the left corner in a flexural zone, the principal direction will be in the y-direction during flexural damage as the crack propagates in x-direction.

The integration point starts in compression as a result of the non-proportional load on the pier because of the self-weight and the floor load. The starting point of the stress-strain diagram has a stress $\sigma_{yy} = -0.323$ MPa and strain $\epsilon_{yy} = -0.000227$. The Young's modulus is estimated by calculating the gradient of this relation: $\hat{E}_0 = -\frac{323000}{-0.000227} = 1.423 * 10^3$ MPa. Note that the Poisson effect is not taken into account in this hand calculation. This value is close to the Young's modulus given as input for the model: $E_0 = 1.41 * 10^3$ MPa.

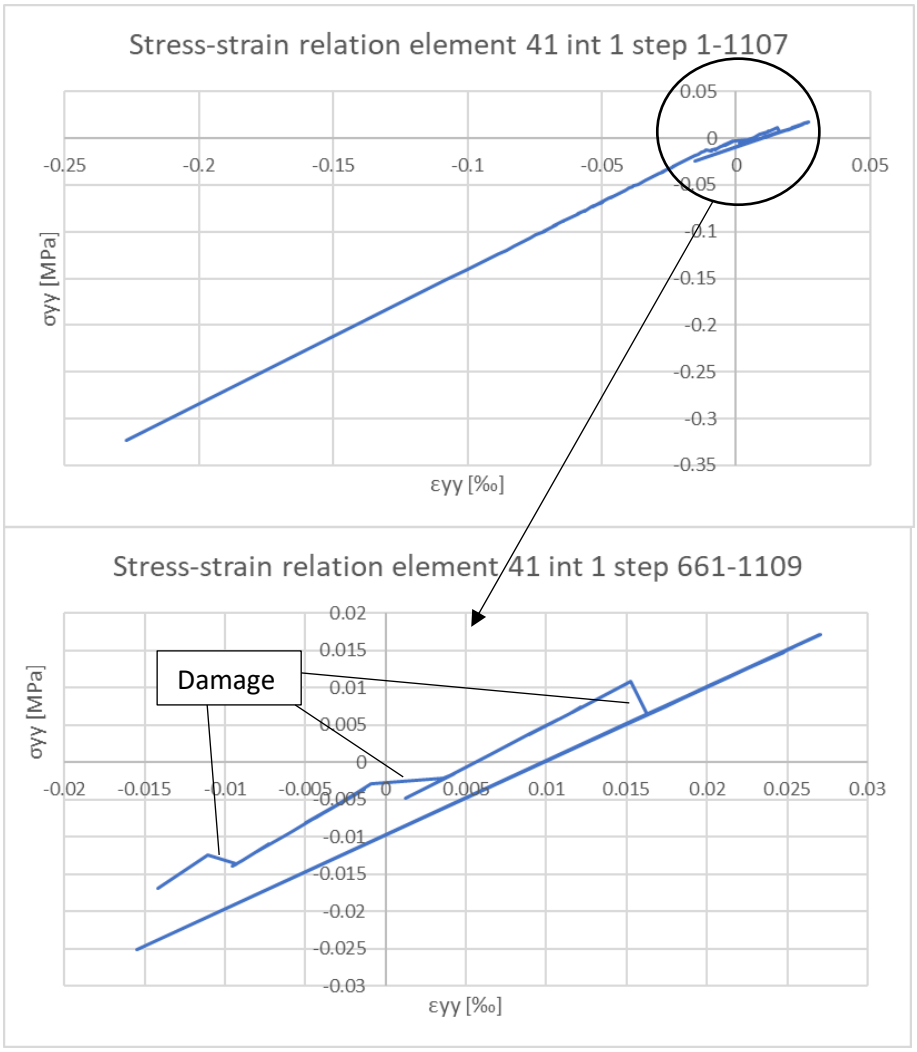

Figure 4.65; Damage and crack closure error at step 1105

Visible in Figure 4.65 is the fact that every time this integration point damages, it branches to another linear relation. Ideally, one would expect a relation like Figure 2.14, in which the unloading would be in line with the saw teeth. A possible explanation of this behaviour is that this behaviour is only possible in the case of a fixed principal direction in the integration point. In this case, a fixed crack approach is used while the principal direction changes drastically according to Figure 4.66. Globally, the unloading is in line with the expected saw tooth curve (Figure 4.64).
This principal direction is calculated by looking at the extreme values of the rotated stiffness matrix from the x, y-coordinate system to a $\bar{x}, \bar{y}$-coordinate system, $\bar{\boldsymbol{\Sigma}} = \boldsymbol{R}\boldsymbol{\Sigma}\boldsymbol{R}^T$ with:

$$\boldsymbol{\Sigma} = \begin{bmatrix} \sigma_{xx} & \sigma_{xy} \\ \sigma_{xy} & \sigma_{yy} \end{bmatrix} \quad , \quad \boldsymbol{R} = \begin{bmatrix} \cos(\alpha) & \sin(\alpha) \\ -\sin(\alpha) & \cos(\alpha) \end{bmatrix}$$

by taking the derivative of the axial stress component to the angle α and setting this to zero.

$$\frac{\partial \bar{\sigma}_{xx}}{\partial \alpha} = 0 \tag{4.4.4}$$

Elaborating this expression, these extreme values i.e. the principal values are found for an angle:

$$\tan(2\alpha) = \frac{2\sigma_{xy}}{\sigma_{xx} - \sigma_{yy}} \tag{4.4.5}$$

This angle α is also known as the principal direction θ_p [13].

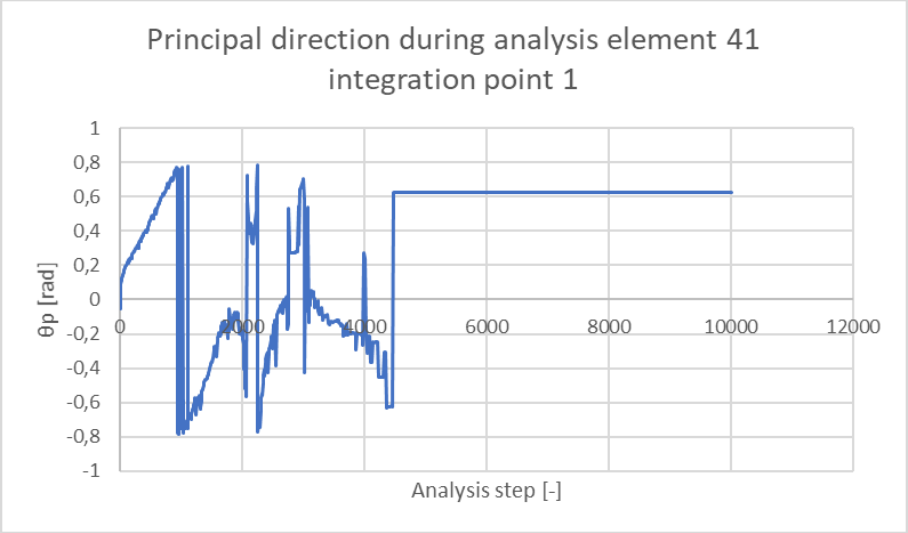

Figure 4.66; Principal direction of element 41 integration point 1 during analysis

On a global level, the strains as a result of the crack closure error at analysis step 1104 are relatively small. By taking a closer look at Figure 4.64, some big crack closure errors are detected around analysis step 3000. Below (Figure 4.67), the initial stiffness is shown together with the stiffness at the crack closure error. This illustrates the difference in strain between the real behaviour (blue line) and the behaviour in the analysis. If the initial stiffness was used as the behaviour would have been in reality, a stress of $-86750\ \mathrm{N/m^2}$ would have let to a strain of $\epsilon_0 = \frac{-86750}{1.423*10^9} = -6.097 * 10^{-5}$.The ratio between the current stress $\frac{\epsilon_{yy}}{\epsilon_0} = \frac{-6.097*10^{-5}}{-1.719*10^{-4}} = 2.8$. This is a huge difference.

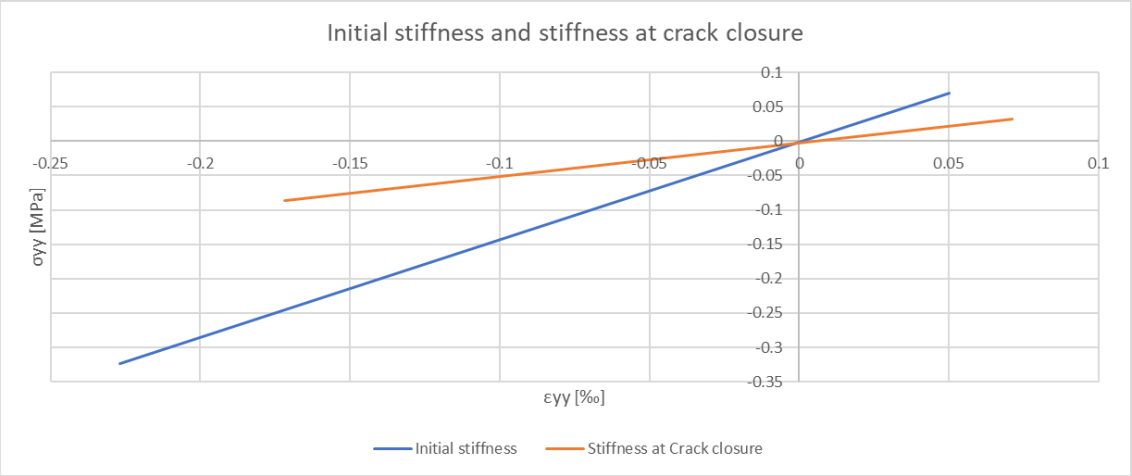

Figure 4.67; Initial stiffness and stiffness at crack closure around analysis step 3030

4.4.6.3 Toe crushing investigation

Further in the analysis, the initial vertical load is reduced often. A reason for this could be crushing of the toe of a wall. In reality when an unreinforced masonry wall fails flexural, cracks start to propagate at the heel of the wall. Because this part is damaged and loaded in tension, the remaining part of the wall has to take the vertical load. As cracks propagate, this section becomes smaller. At a certain stage, the toe of the wall starts to crush, because almost all of the vertical force is taken by a small section and the stress in this part exceeds the compressive strength. This results in toe crushing and the wall crumbles under its own weight. This behaviour can be the reason that the vertical load cannot be fully applied as this is a consequence of it.

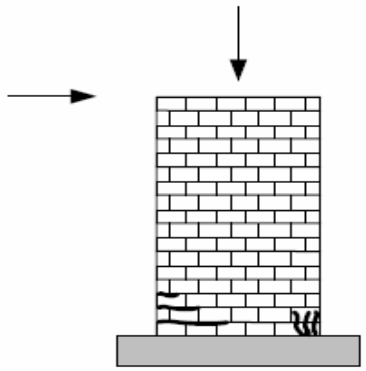

Figure 4.68; Failure mechanisms with lateral force; rocking [2]

Before the data can be analysed, some strains and stresses have to be calculated to compare them with the data.

In Figure 4.69, the constitutive relation for the tensile and compressive curve are given. The tensile curve uses a linear relation and the compressive curve a parabolic relation. Important to know is that cracking occurs for stresses larger than the plastic strain ϵ_p corresponding to the tensile strength of f_t.

The relation until that state is linear elastic and therefore, the plastic strain can be calculated by:

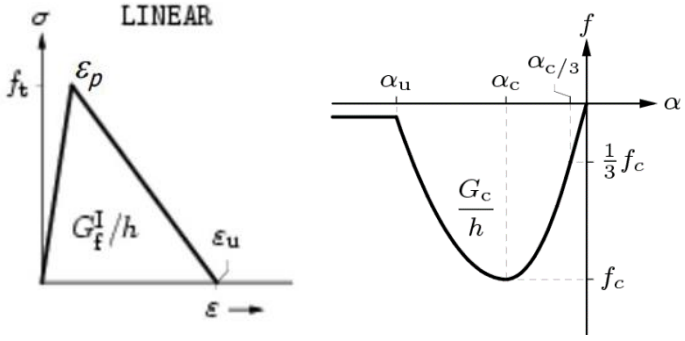

Figure 4.69; Constitutive relations. Linear tensile relation (left). Parabolic compressive relation (right) [22]

$$\epsilon_p = \frac{f_t}{E_0} \tag{4.4.6}$$

And the ultimate strain by:

$$\epsilon_u = \frac{2G_f^I}{hf_t} \tag{4.4.7}$$

For the compressive region. The maximum compressive stress f_c is reached at strain α_c. This strain is calculated as:

$$\alpha_c = \frac{5}{3}\frac{f_c}{E_0} = 5\alpha_{c/3} \tag{4.4.8}$$

The ultimate compressive strain at which softening is completed can be calculated as:

$$\alpha_u = \alpha_c - \frac{3}{2}\frac{G_c}{hf_c} \tag{4.4.9}$$

The calculated parameters are shown in Table 4.5. Only the parameters independent of the mesh size h are shown. The dependence of the mesh size is a characteristic of a smeared crack approach.

Table 4.5; Stresses, strains and parameters of the constitutive relations

Parameter	E_0 [MPa]	f_t [MPa]	f_c [MPa]	ϵ_p [−]	α_c [−]
Value	1410	0.04	−3.0	$2.84 * 10^{-5}$	$-3.55 * 10^{-3}$

The damage, strains and stresses will be given for five different analysis steps. These steps are $16, 421, 2776, 5326$ and 8611. The place in the load-displacement curve at those steps is shown in Figure 4.70.

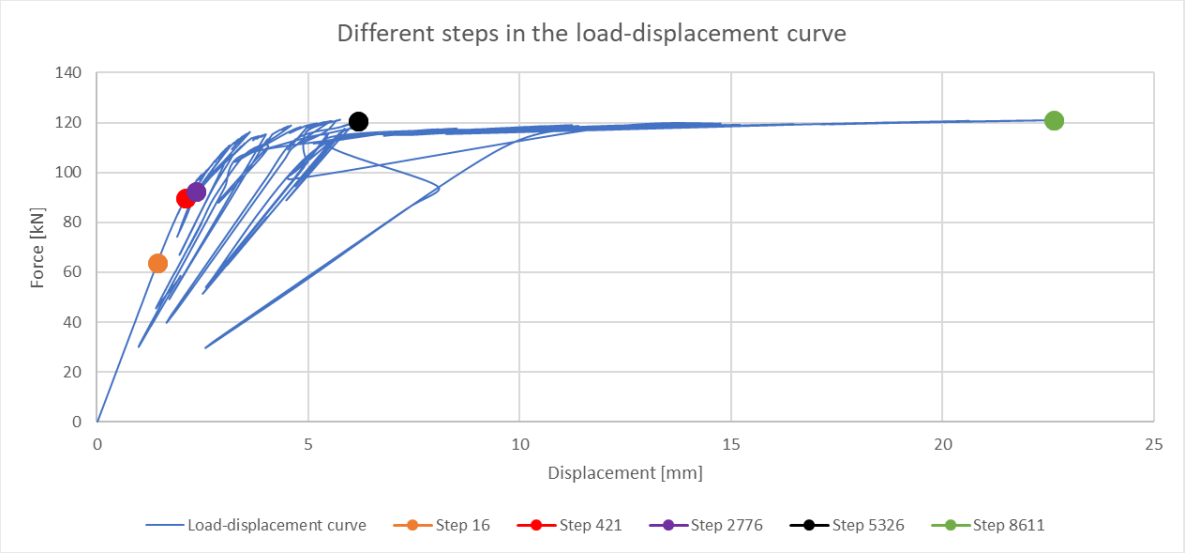

Figure 4.70; Location of the analysis steps in the load-displacement curve

To investigate the phenomenon of toe crushing, the bottom row of all three piers is investigated. For every pier, the vertical strains and stresses in the integration points of the lowest row of elements are monitored during the analysis. First the left pier is analysed.
The elements inspected are 137 up to and including 141. In the analysis, the first load reduction is in analysis step 2785.

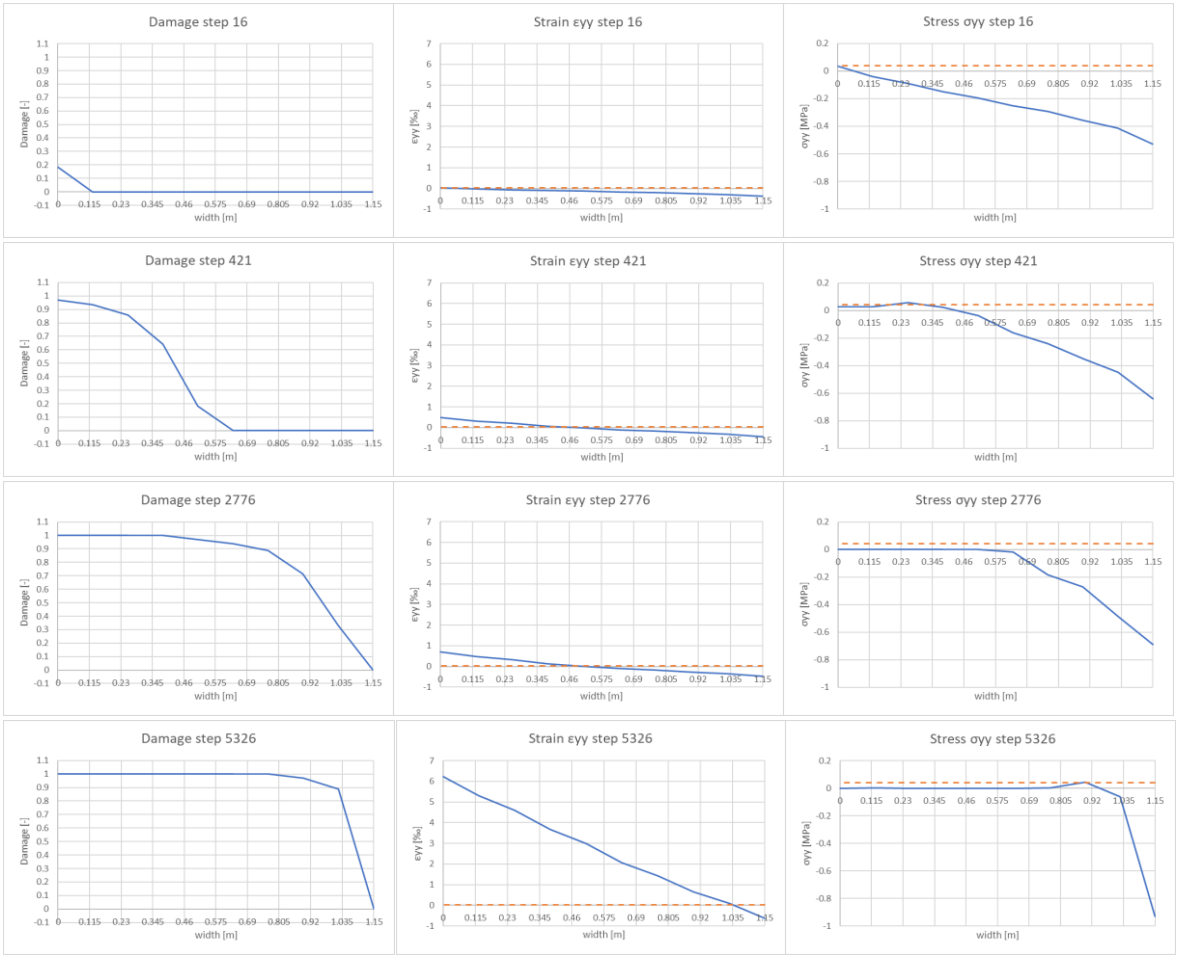

Figure 4.71; From left to right, damage, strain ϵ_{yy} and stress σ_{yy} over the bottom row of the left pier. From top to bottom analysis steps: 16, 421, 2776 *and* 5326.

In Figure 4.71 an overview is given of the damage, strain ϵ_{yy} and stress σ_{yy} over the bottom row of the left pier. Four steps in the analysis are chosen, namely steps: 16, 421, 2776 and 5326. Step 16 is at the start of the analysis, in step 421 the damage has propagated, but the structure can carry the vertical load. In step 2776 The load vertical has already reduced and in step 5326 the structure is failing.
In step 16, the behaviour is almost linear elastic. There is some damage in the left side of the pier. The stresses are almost compressive over the whole area, except the left part, which is in tension. In analysis step 421, a large part of the pier is damaged. A crack has developed from the left as strains are above the crack strain. At the left side of the pier, the cross-section is almost fully damaged, therefore no stresses can be taken in that part. The neutral point shifts to the right compared to step 16.

Step 2776 shows that the damage occurs almost everywhere in the cross-section. Only the integration point far to the right is still undamaged, all the other integration points are almost fully damaged. The neutral point has shifted more to the right and the compressive stresses have increased. In step 5326, Almost all integration points are loaded in tension. The strains have increased much. The part which can take the compressive forces has reduced to a very small band on the right side. The vertical load cannot be fully applied in this stage.

Figure 4.72 and Figure 4.73 show the damage and principal stress-strain relation of element 141 integration point 2. This element is located at the left side of this pier. Damage builds up in the early stages of the analysis and the principal stress-strain relation follows the saw-tooth law accurately.

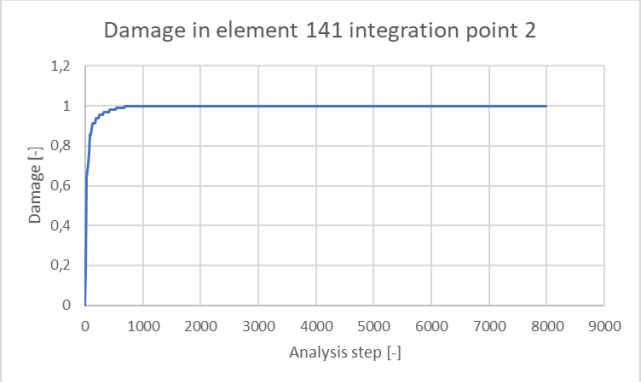

Figure 4.72; Damage in element 141 integration point 2

In conclusion, the damage, strains and stresses in the bottom row of the left pier clearly show the expected behaviour concerning rocking of a wall. Cracks propagated from the tensile side and the neutral point shifted to the compressive side. During the analysis, this process continued until almost the whole cross-section was cracked with tensile strains. A small part remained intact and still takes some compressive stresses, as the area is very small, the left pier has almost no vertical load carrying capacity left. Toe crushing can however not be concluded as the compressive strain in the integration points in compression do not reach strains belonging to the post-peak parts of the parabola. The strains are not even close as the post-peak part is reached with strains smaller than -3.55 ‰.

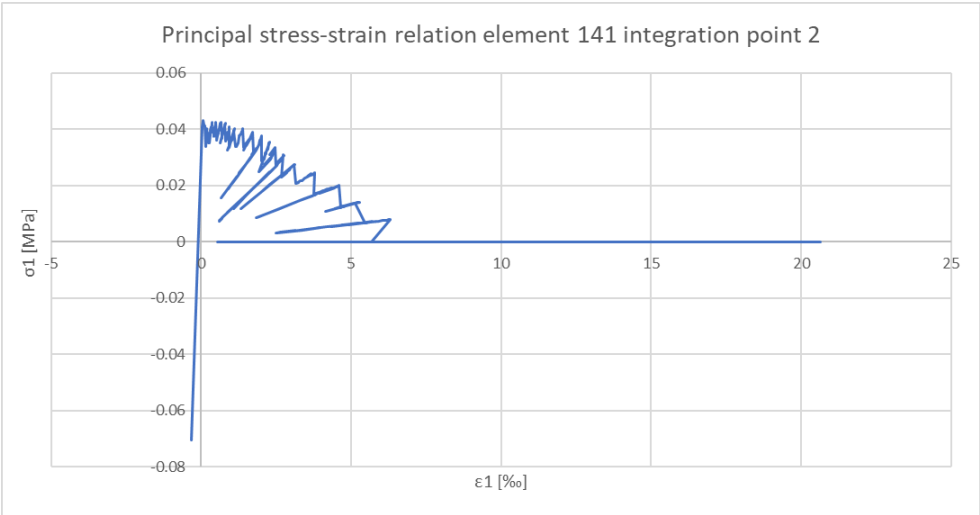

Figure 4.73; Principal stress-strain relation of element 141 integration point 2

For the middle pier, the overview of damage, strain and stress is given in Figure 4.74.

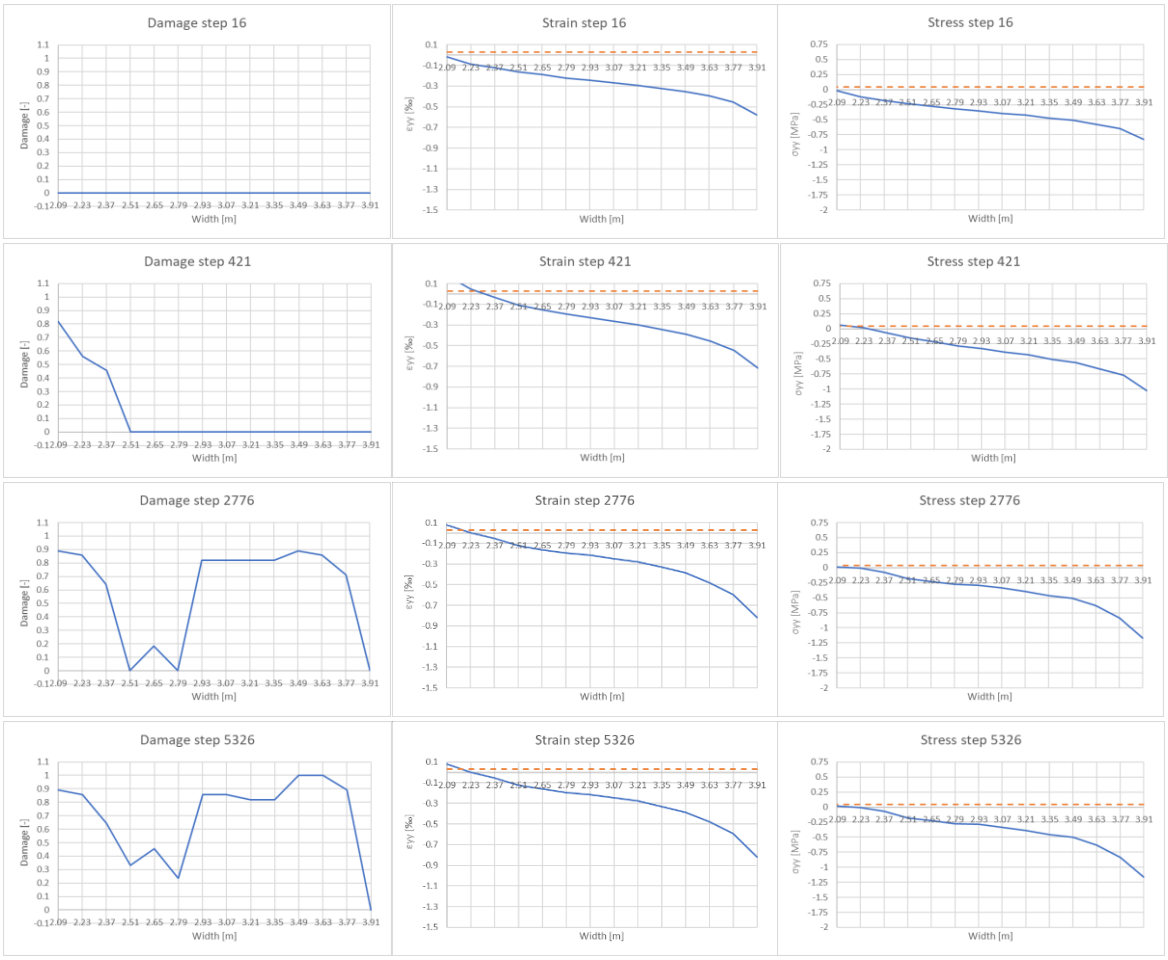

Figure 4.74; From left to right, damage, strain ϵ_{yy} and stress σ_{yy} over the bottom row of the middle pier. From top to bottom analysis steps: 16, 421, 2776 *and* 5326.

Here, the damage develops differently. Again, cracks start to grow from the left side of the pier early in the analysis. However, tensile damage is also occurring right of the center of the middle pier. This damage is propagating in a different direction then the yy-direction as the stresses σ_{yy} in those integration points are in compression. This damage is a result of the shear failure mode propagating in the middle pier. This shear crack develops at that location. Again, the vertical stresses in crack do not exceed the tensile strength of 0.4 MPa. Toe crushing is not reached, as the compressive strain is far below the plastic compressive strain.

Figure 4.75 shows the damage, strains and stresses in the bottom row of the right pier.

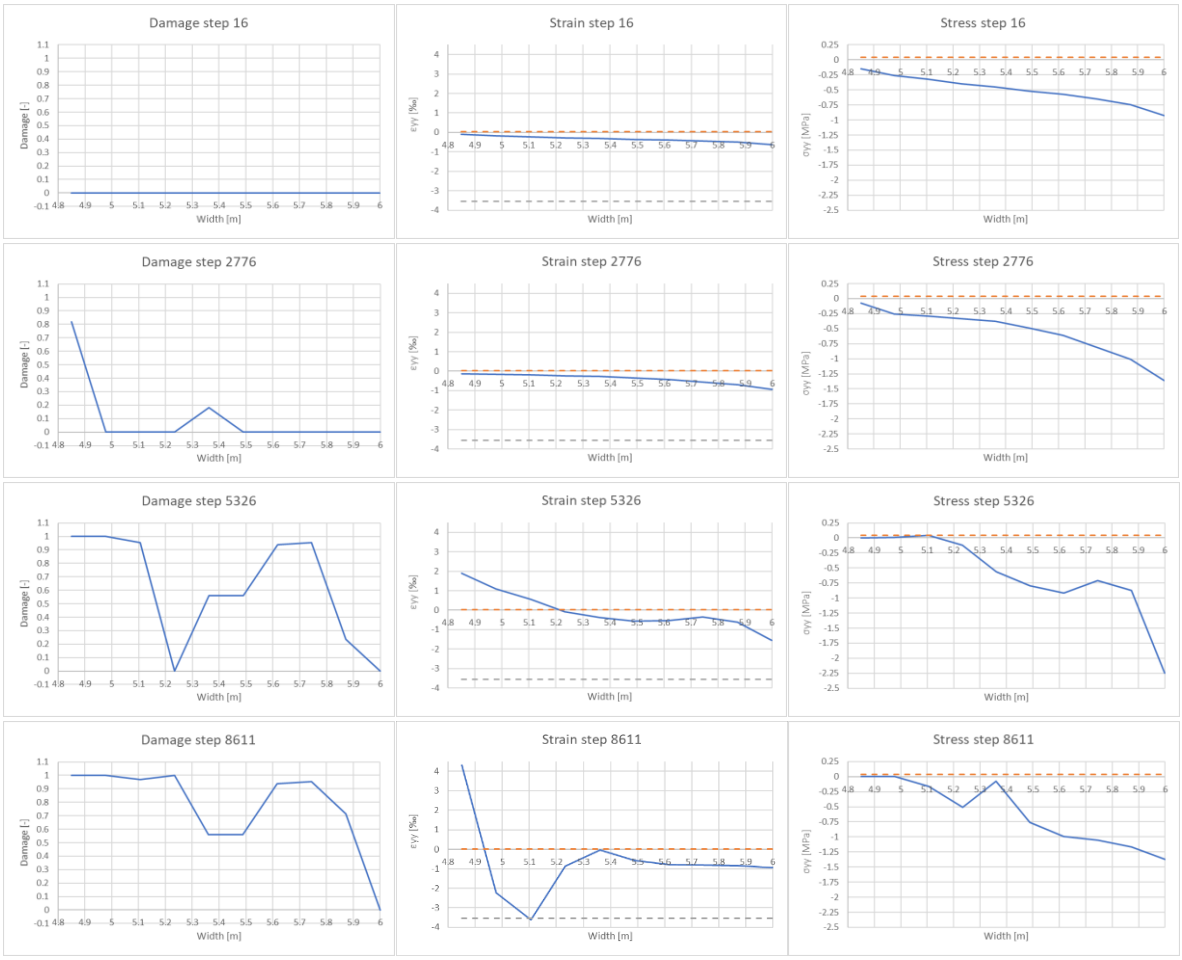

Figure 4.75; From left to right, damage, strain ϵ_{yy} and stress σ_{yy} over the bottom row of the right pier. From top to bottom analysis steps: 16, 2776, 5326 and 8611

The right pier shows similar behaviour as the middle pier. From the left, tensile cracks propagate belonging to a rocking failure mechanism. Right from the center, damage occurs because of diagonal shear failure in the pier. The tensile stresses do not exceed the tensile strength of the material.
The compressive strain limit for the maximum compressive strength is reached in step 8611 for element 42 integration point 3. By checking the principal stress-strain relation for this integration point, the reason why the strains reach this limit is because of a crack closure error, which incorrectly increased the strain. The stiffness is damaged and because this damaged stiffness is kept in compression, the strains are too large.

4.4.7 Possible improvements

In this section, the different suggested improvements of the continuum element model will be explained and discussed. It debates different model approaches.

4.4.7.1 Three zones triangular sections

In this model, the small elements at the ends of the piers and spandrels are modelled with small triangular elements. These elements are chosen because a finer mesh in the ends of the piers and spandrels is advised compared to the middle of the piers. Quadrilateral elements will have a bad aspect ratio which could give unreliable results or a too fine mesh which increases the calculation time dramatically. Again, two approaches in material parameters are done. In the first approach, the ends of the piers and spandrels are modelled with the bed joint tensile strength and fracture energy belonging to rocking of the wall, while the middle is modelled with the maximum shear strength and fracture energy belonging to shear failure. In the second approach, the whole piers and spandrels have the bed joint tensile strength and fracture energy as strength parameters.

Below in Figure 4.76, the load-displacement curve is given for the first approach. The maximum load is very similar to the experimental value. The analysis is however not very stable, because the initial load factor drops very often (Figure 4.77). The maximum displacement is around $d = 13$ mm.

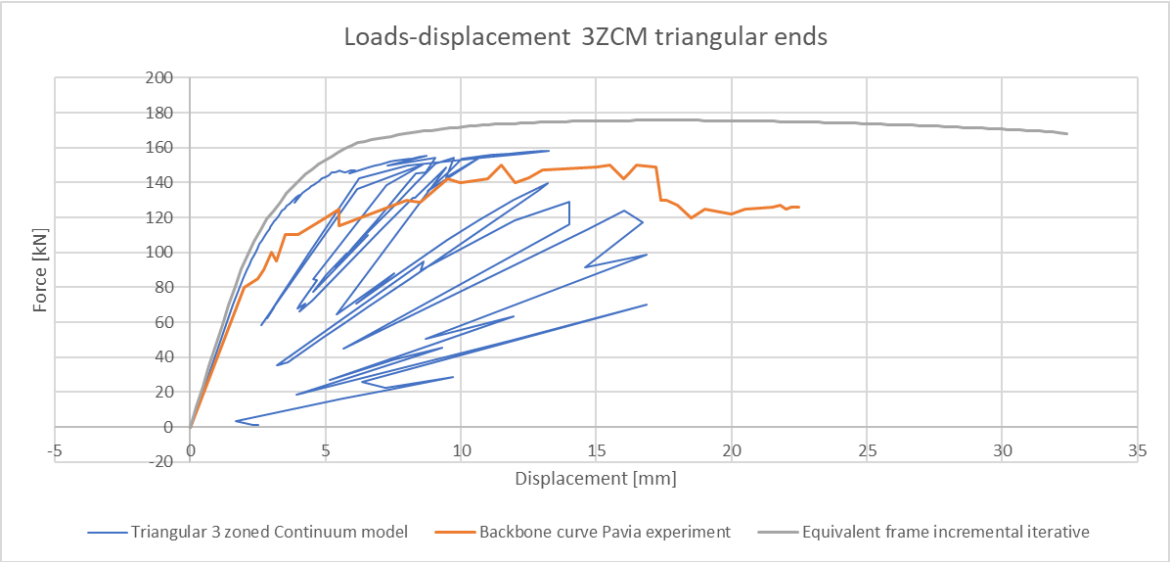

Figure 4.76; Triangular elements at the ends, 3-zoned continuum model

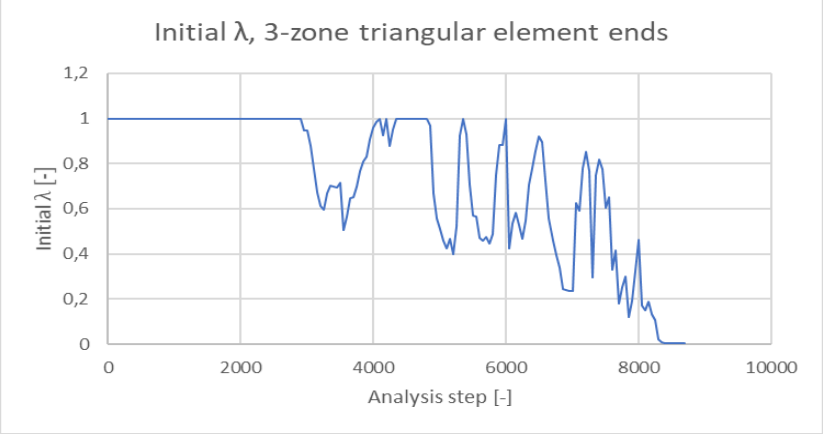

Figure 4.77; λ_{ini} during analysis, 3-zoned model triangular element ends

The failure mode is similar to the other three-zone models. The bottom piers fail in flexural failure, while the right spandrels fail in shear. After this, the right pier at bottom level also develops shear damage. This damage develops vertical in this model, instead of diagonal in the experiment.

The results of the second approach are shown in Figure 4.78. The analysis continuous until the end of the experiment and even further while being able to carry the full load, although the initial load reduces often. The unloading branches happen when the initial load factor reduces. The failure mode of this model is flexural failure in the left pier of the bottom row and shear failure in the middle and right pier. This is the similar to the experiment. In general, the triangular elements did not improve the results. The failure modes were similar as were the load-displacement diagrams. Only the second approach stood out as it reached relatively large displacements.

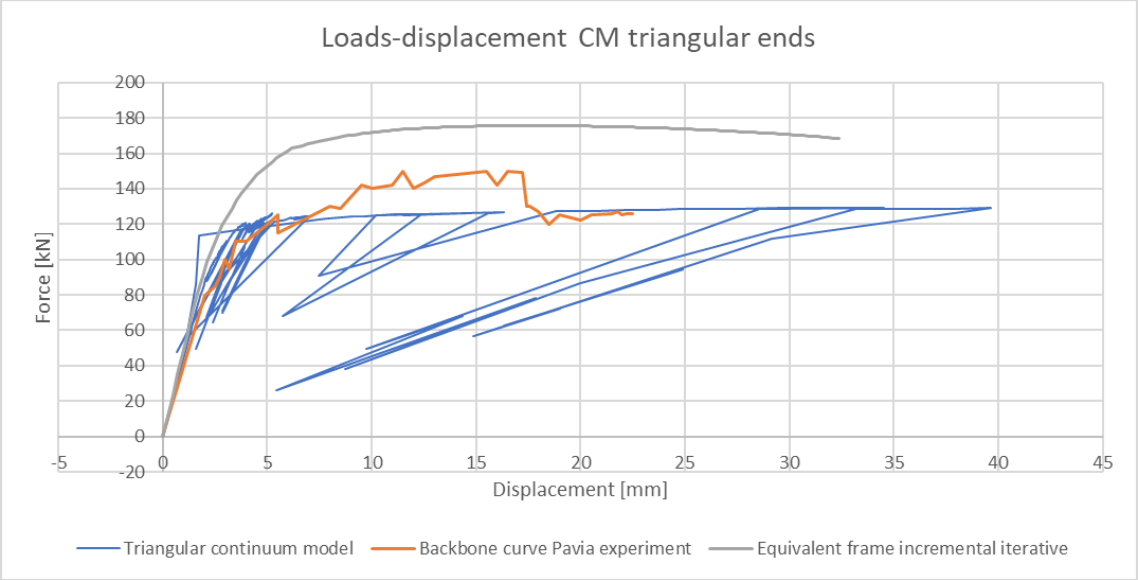

Figure 4.78; Load-displacement diagram triangular ends, flexible parameters

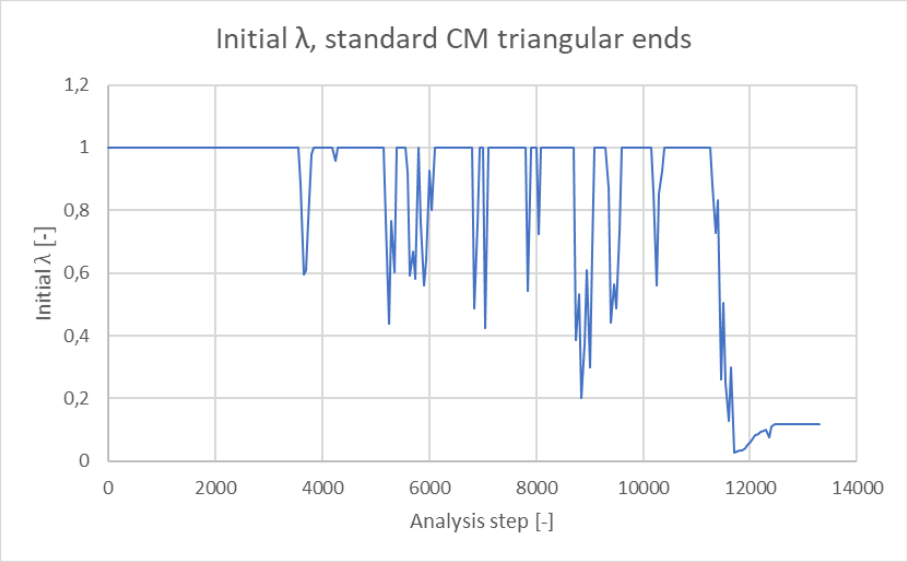

Figure 4.79; λ_{ini} during analysis, triangular element ends, flexible parameters

4.4.7.2 Variation in tensile shear strength

It is peculiar to see that in the continuum model, the best results come from the model which should be less accurate. The three-zoned approach is used to make a distinction between the flexural failure at the ends and the shear failure over the height in an unreinforced masonry wall. Unwillingly, this model results in a different failure mode namely dominating flexural failure instead of shear failure. The previous approximation in which the flexural strength of the wall is chosen for all sections is not fully correct as the shear strength of a wall is higher. Therefore, it is expected that the maximum load should be higher, as the strength is higher in reality. An uncertain value is the reference tensile strength f_{tu}. This factor was not given in the Pavia experiment and is estimated: $f_{tu} = 0.14\ \mathrm{MPa}$.

This is based on the relation of this parameter with the brittle shearing failure mode [2]. In the experiment, this failure mode happened for a displacement $d = 11.4\ \mathrm{mm}$. A rapid decrease in force was observed in the three-zoned continuum model of Nobel with this value for f_{tu}. As this value is empirically chosen and not based on a solid explanation, it is advisable to perform a parameter sensitivity study on this factor. Especially because this factor has a big influence on the shear failure mode, which was not present in the piers for the 3ZCM.

Four different model configurations are used in this study, shown below in Figure 4.80.

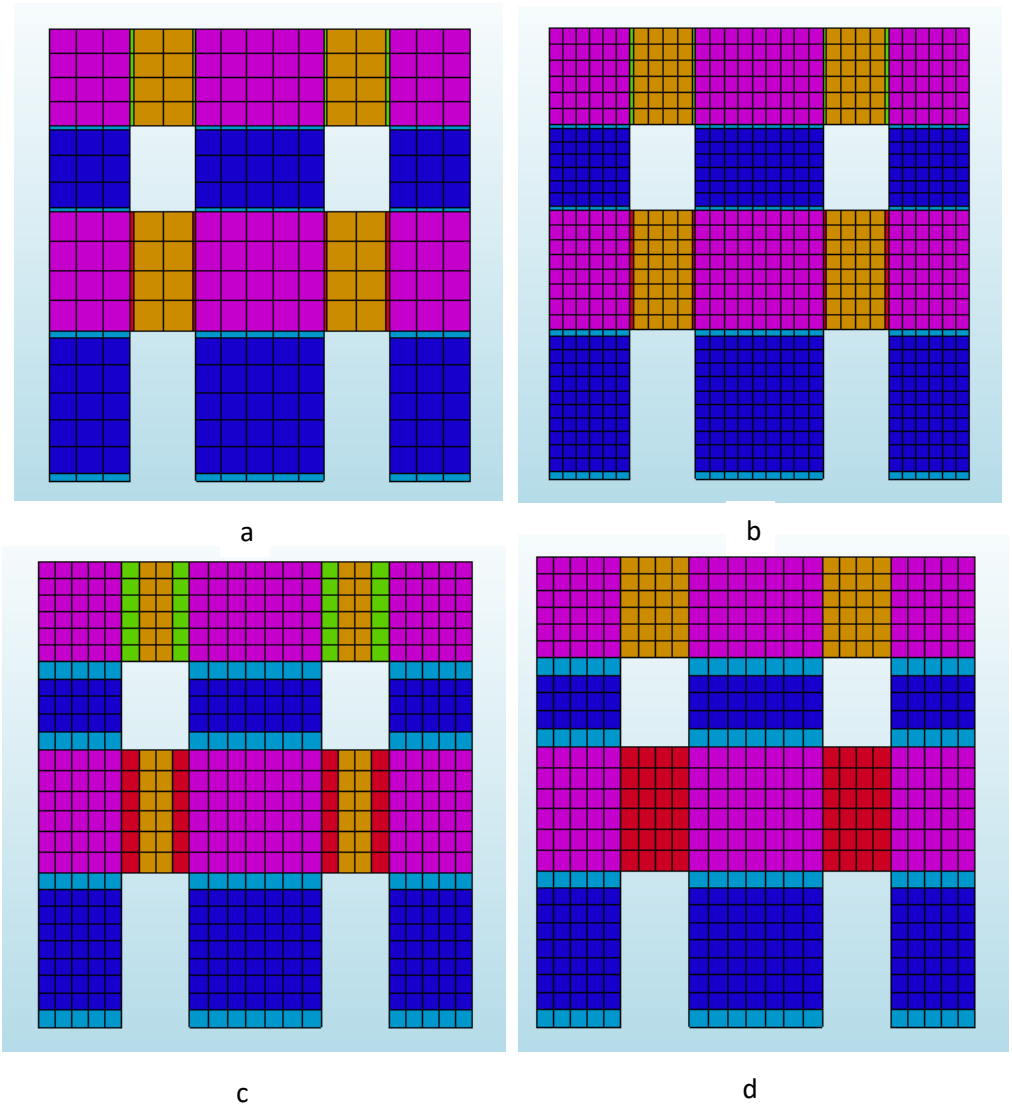

Figure 4.80; Four models to investigate the influence of the shear strength. From left to right, top to bottom: (a) Original Pavia model; (b) Sophisticated Pavia model; (c) Aspect ratio = 1 pier and spandrels; (d) Aspect ratio = 1, only the piers reduced

Model a uses the same mesh as the original Pavia model from chapter 4.4. Model b uses a finer mesh. The reason is to improve the aspect ratio of the element, while maintaining the ratio of that one twentieth of the total height of a pier is the height of the flexural zone. The difficult tradeoff in this model is that a finer mesh increases the number of elements greatly, which also increases the number of integration points. In an SLA, this means that the time for each analysis step will increase because of the greater number of elements slows the calculation, while also the number of analysis steps increases because more integration points need to be damaged to collapse the structure. A finer mesh in the flexural zones will also result in a finer mesh in the shear zones. Otherwise long oddly shaped triangular elements are needed to connect the nodes which are also not accurate.
Model c uses the model of chapter 4.4.6 which relatively accurately described the failure pattern. The strength of the elements is manually augmented after the mesh is generated. Model d is equal to model c with the only difference that the tensile strength is only augmented in the piers, while the spandrels still have the joint tensile strength. This model is used because in model c, the vertical load could not be applied without damage in the spandrels as a result of the self-weight due to the lower properties. The flexural strength of the spandrels is estimated much higher (six to eight times higher), than for the piers. As the damage should be a result of the lateral load and not the vertical load, this model offers a solution. As the real structure has lintels above the openings in the wall, this assumption is just. The advantage of model c and d is that the aspect ratio of the elements is very good. A downside is that especially in the spandrels, the flexural zone is large compared to the shear zone. However, a finer mesh will result in calculation times that takes many hours, which is not practical. For all models, five different values for f_{tu} are chosen: 0.04 MPa, 0.06 MPa, 0.08 MPa, 0.11 MPa and 0.14 MPa.

To analyze the results, an overview is given of the load-deformation curve. The curve is shown as long as the vertical load can be fully applied. Steps in which the structure is unloaded are also present, but only if the structure was able to take the full load later in the analysis. The failure pattern is also investigated to see if the structure fails flexural or in shear.

Model a

This model starts with damage at the bottom of the spandrels as a result of bending of the spandrels by the vertical load (floors and self-weight). Damage occurs because of the lower strength of the spandrels. The damage is followed by vertical shear in the right spandrels and shear in the middle and right pier and flexural damage in the left pier. The same behaviour is found for $f_{tu} = 0.06$ MPa and $f_{tu} = 0.08$ MPa. Interesting to see is the fact that the left corner at floor 1 and the top left corner start to damage diagonally. Damage starts from the bottom right corner of this element, similar to the experiment.
The results of $f_{tu} = 0.11$ MPa and $f_{tu} = 0.14$ MPa are different as only the right bottom pier fails in shear in a later stage, after the right spandrels have failed and the other piers fail flexural. The main damage occurs because of vertical shear in the right spandrels. Similar to the results of the original 3ZCM model as the same parameters are used. As expected, the maximum load increased as the strength was higher, although this influence was limited. The big difference was the failure pattern. For low strengths, the middle and right pier failed in shear and the left pier flexural. This is more accurate than for higher values in which the right spandrels fail in vertical shear. Low values of the shear strength result in damage because of the vertical weight on the spandrels. This is not wanted nor realistic as the structure would be designed to carry the vertical load.

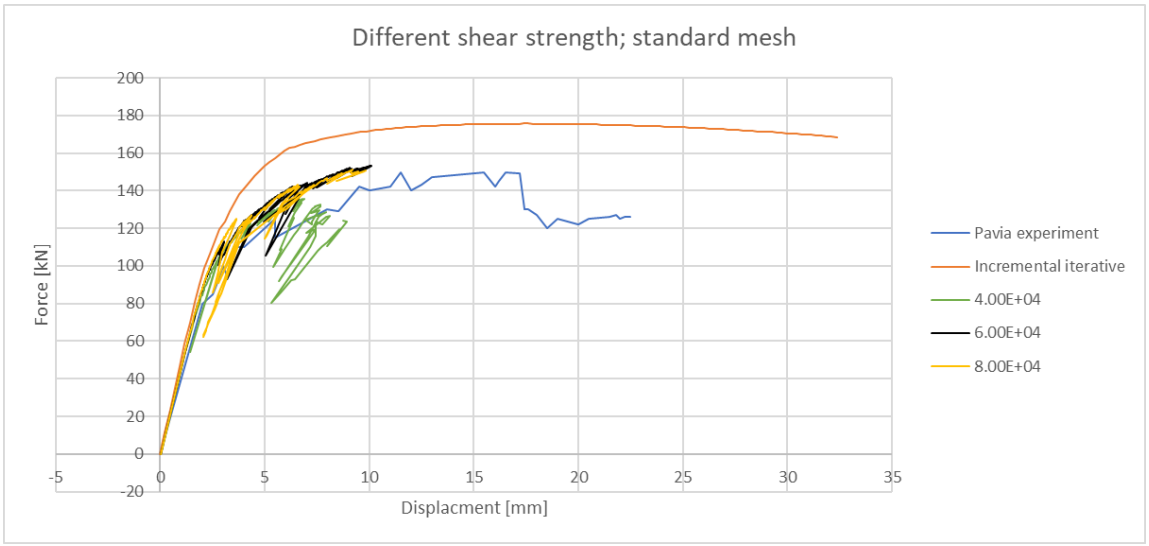

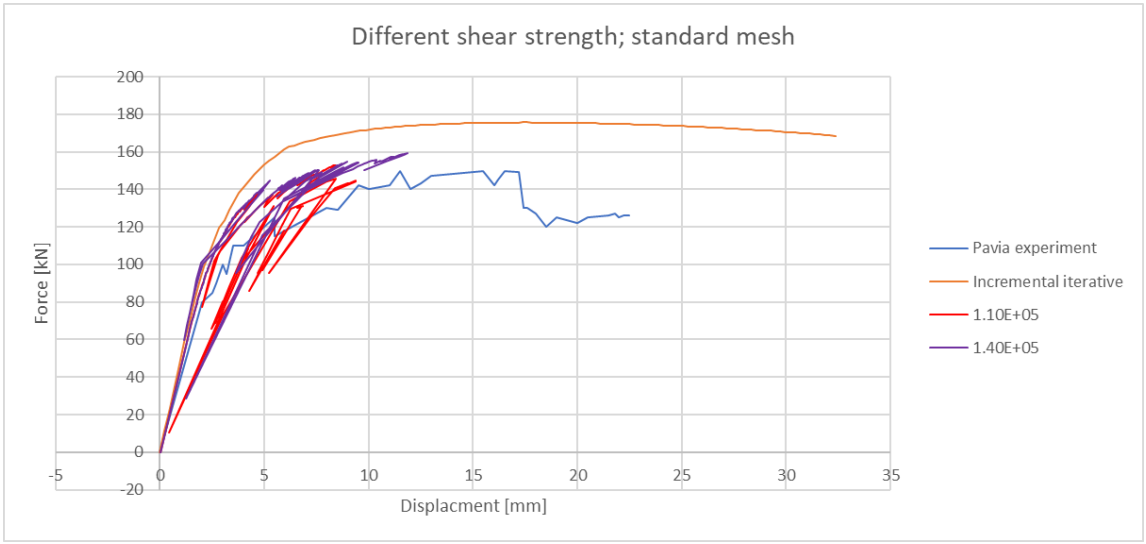

Figure 4.81; a: Different shear strengths for the original Pavia facade model, legend values are in $[Pa]$.

Model b

During the analysis with $f_{tu} = 0.04$ MPa, it is not possible to apply the full vertical load. The analyses with $f_{tu} = 0.08$ MPa and $f_{tu} = 0.11$ MPa fail almost immediately after the vertical load is partly applied. The model of $f_{tu} = 0.08$ MPa starts with bending damage in the spandrels because of the low strength in this region. Later, the right spandrel at the first floor fails and the second-floor spandrel at the right cracks, followed by shear damage in the middle and right pier of the bottom floor. $f_{tu} = 0.14$ MPa shows similar behaviour as in the previous analysis, i.e. shear failure in the right spandrels and flexural damage in the piers.

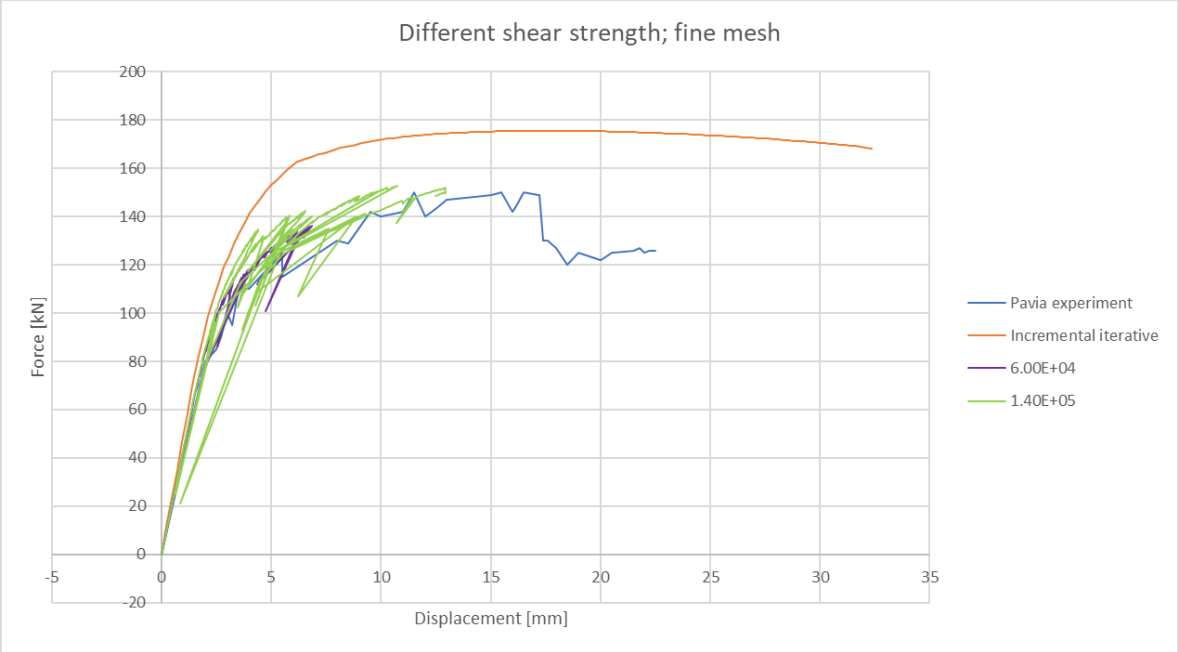

Figure 4.82; b: Different shear strengths. Pavia model with finer mesh, legend values are in $[Pa]$.

In conclusion, the finer mesh resulted in the fact that three of the five analyses failed as a result of the vertical force. Oddly, the analysis with $f_{tu} = 0.06$ MPa could be executed, while two analyses with higher strengths could not. The failure pattern was wrong for both analyses, with too weak spandrels for the first, and a shear strength that is too high for the second.

Model c

For $f_{tu} = 0.04$ MPa, the vertical force cannot be fully applied. For $f_{tu} = 0.06$ MPa, $f_{tu} = 0.08$ MPa and $f_{tu} = 0.11$ MPa the results are similar to the original Pavia model (modal a). The spandrels are too weak in the first two models which result in severe damage at those locations followed by shear in the middle and right pier. The model with $f_{tu} = 0.14$ MPa has piers that are too strong, which result in flexural damage only. Important to see is that the displacements have increased for this model. The results could be better if the spandrels were uncoupled from the variating shear strength. This would mean that the spandrels would not fail in bending and shear in the center as happened in the previous analyses because of the reduced shear properties. Therefore, model d is made.

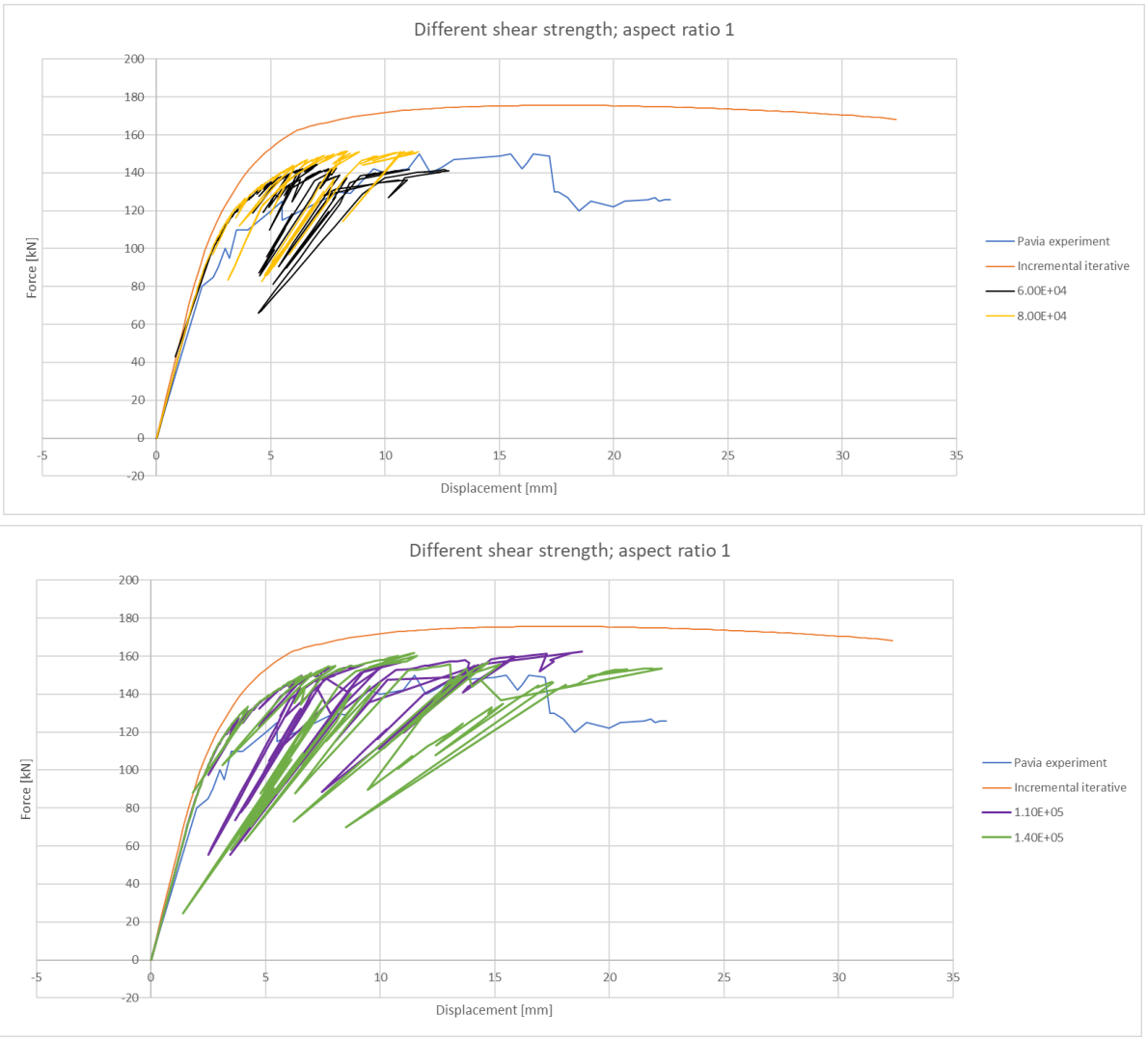

Figure 4.83; c: Lower shear strength model of Pavia facade with aspect ratio equal to 1, legend values are in $[Pa]$.

Model d

In the final model, the full spandrels have the same properties as in their ends. This to avoid damage in the first analysis steps and too early vertical shear failure because of the vertical load. Important to see is that the analyses with $f_{tu} = 0.04$ MPa and $f_{tu} = 0.08$ MPa are very stable. There are almost no initial load reductions and the SLA characteristic reductions are clearly visible. With increasing strength in the spandrels, the damage focusses on diagonal shear in the middle and right pier. Again, the left corner of the first floor starts to crack. The left bottom pier fails flexural. Not surprising, a higher shear strength results in a higher maximum load. The higher the shear strength, the later shear occurs in the piers. For $f_{tu} = 0.14$ MPa, there is no shear in the piers (only the pier most to the right at the end of the analysis) and the failure is dominated by flexural damage in the piers. As the ends of the piers are more damaged, the structure cannot carry the vertical load and the initial load factor reduces very often.

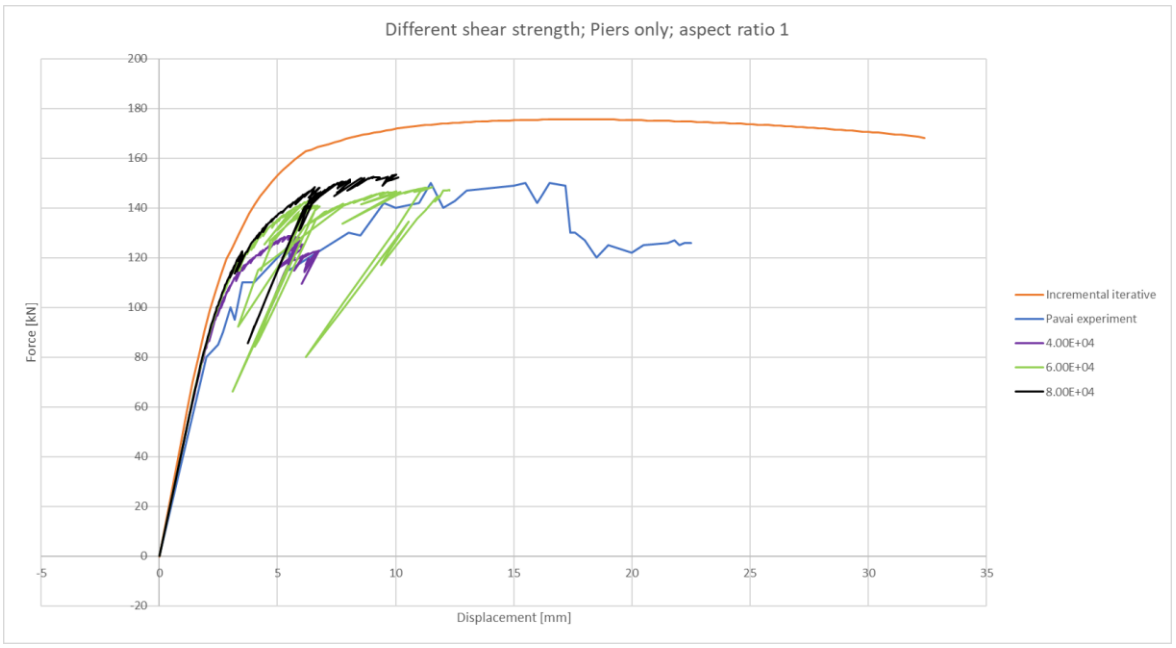

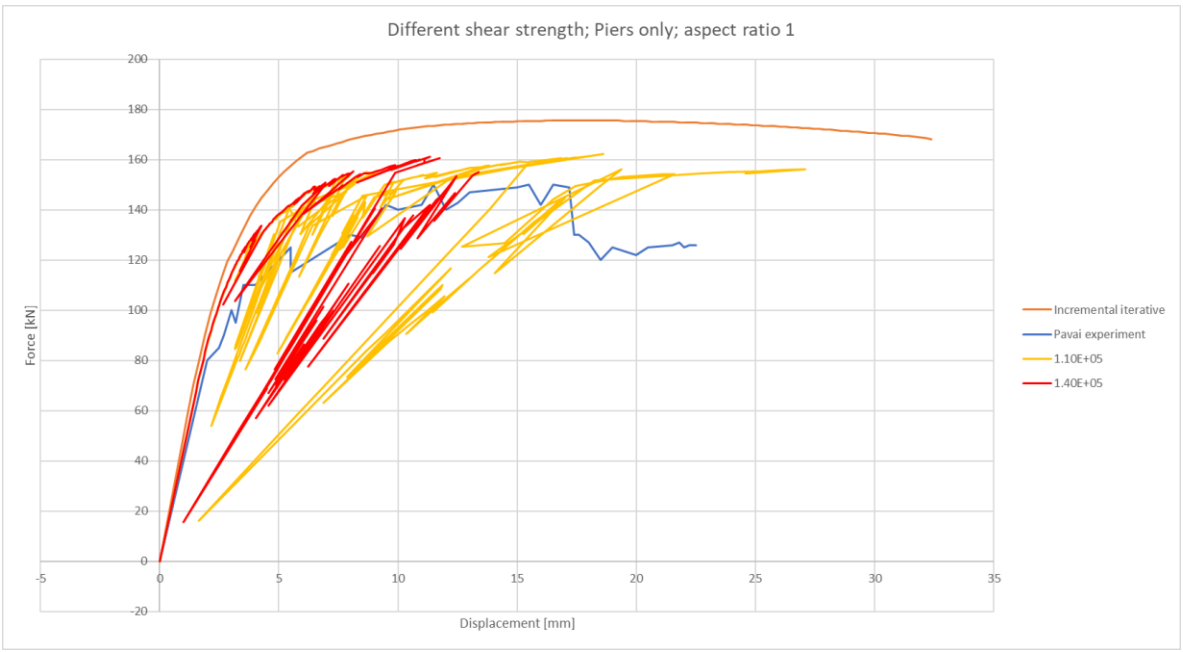

Figure 4.84; d: Lower shear strength model of Pavia facade, aspect ratio =1 and only piers are reduced, legend values are in $[Pa]$.

In Figure 4.85, the damage pattern is given for analysis step 5941 in the model with $f_{tu} = 0.08\,\mathrm{MPa}$. Shear diagonals are progressing in the middle pier as in the left corner of the first floor. Also, a vertical, slightly diagonal crack propagates in the right pier of the first floor.

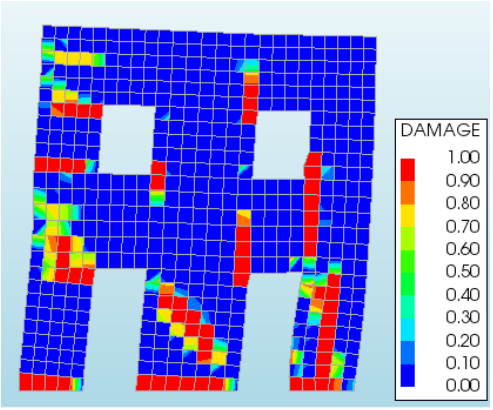

Figure 4.85; Damage pattern in the Pavia facade for $f_{tu} = 0.08\ MPa$. Analysis step 5941

In conclusion, in model a, b and c the strength of the spandrels and the piers were both reduced as a result of the reduced shear strength. This resulted for low shear strengths in the right failure pattern in the piers, but damage in the spandrels as a result of the vertical load. For high values, the piers were too strong which resulted in an incorrect failure pattern. Especially in the fine mesh, the analysis could not continue because of the first situation as the vertical load could not be applied. Model d offered a good trade-off. This model had a good aspect ratio and the spandrels were not influenced by the decreasing shear strength. This resulted in a stable analysis, especially for the value: $f_{tu} = 0.08\,\mathrm{MPa}$. This value gave a stable analysis with almost no reductions in load, the failure pattern was among one of the most accurate, with shear failure in the piers. The result came very close to the experimental data of the Pavia experiment. It was somewhat higher, which can be explained by the fact that the Pavia experiment included cyclic testing of the house. With a cyclic load, a lower load is needed to fail the structure. The maximum displacement of the house was $d = 10.04\,\mathrm{mm}$, which is only halve of the maximum displacement in reality. Another important thing that can be concluded is that a relation seems to exist between the failure pattern and the reductions of the initial load factor. With higher f_{tu}, the piers failed in rocking failure which consist of severe damages along the top and bottom of the piers, while for lower f_{tu} the shear failure was more dominant, which also included damage over the bottom of the piers as visible in Figure 4.85, but not at the top. For higher f_{tu} and flexural failure, the load reductions are more severe for all four models, with reductions to values were almost no load was left. As with flexural failure, a larger part of the bottom and top of the piers is damaged, it is more difficult to apply the vertical load as the strength of those elements is reduced. The load has to reduce more often to redistribute the load resulting in a less stable analysis. Especially the fact that the top of the middle and right pier does not damage over the width contributes to this mechanism as the load can still be transferred vertically to the remaining undamaged part of the bottom row.

4.5 Conclusion

In this chapter, several analyses are done on a continuum model of the Pavia house. First, the three-zoned approach (3ZCM) of Nobel [2] is used and a standard approach (CM) in which the bed joint tensile strength is used in all piers and spandrels of the model. Although the single wall performed best by using the three-zoned approach, the Pavia façade showed a different result. In the three-zoned approach, the piers started to fail flexural together with shear failure in the right first floor spandrel. In the standard approach, shear failure occurred in the middle and right pier of the first floor together with flexural failure in the left pier. In reality the façade failed with shear failure in all three piers, in the middle pier in two diagonal directions. In terms of maximum load, the standard CM model estimated the maximum load below the experimental value. The lateral load increased to $120\ \mathrm{kN}$ at a displacement of $3.5\ \mathrm{mm}$ which was similar to the results of the experiment. In the simulation, the load stayed constant until the structure failed at a displacement of approximately $22\ \mathrm{mm}$. In the experiment, the façade also failed at a displacement of $22\ \mathrm{mm}$, but the load increased to $150\ \mathrm{kN}$ and decreased back to $120\ \mathrm{kN}$. The 3ZCM estimated the load somewhat higher than in the experiment $(160\ \mathrm{kN})$, which can be explained by the fact that the experiment used cyclic loading instead of a pushover load. The displacements were smaller for the 3ZCM, most analyses reached a maximum displacement around $10\ \mathrm{mm}$.

During the analysis, the initial load factor reduced to values between 0.4 and 0.6 or even lower. These reductions are quite severe, although the program was able to recover relatively quick from those reductions. A relation was sought between the reductions of the initial load factor and crack propagation in the integration point that was damaged. An approximation was used in which the current strain in an integration point was split in an elastic part using the stress, Poisson's ratio and the initial stiffness and a remaining plastic part. This plastic part was multiplied with the element length to estimate a crack width. This method showed an increase in crack width in the analysis step after the load factor had reduced. For example, in element 275 integration point 4, the crack width began to increase after the initial load was reduced in this integration point in the previous step. This behaviour was also found for other integration points which were damaged in the same analysis step as the initial load factor reduction. In some cases, a crack started to grow after this reduction, while in other cases a crack had already grown and no increased crack width was found. More importantly, the damage, strain and stress over the width of the bottom row of the bottom left pier was investigated. In this overview, it became clear that the tensile damage and crack opening from the left pier shifted the neutral line to the right. Further in the analysis, more integration points were damaged as the crack propagated. As a result of this, the vertical load in this pier was carried by a decreasing part of the pier. The compressive stresses in this part grew. At a certain moment, the pier was not able to transfer the vertical load as only one integration point over the entire width was still undamaged. The left pier had no vertical load capacity left as the area over which the compressive load was transferred was very small. The phenomenon toe crushing was not found as the compressive strains were far below the strains corresponding to post-peak behaviour in the compressive material relation.

In the analysis, many non-secant branches were found, especially in the elastoplastic region of the load-displacement curve. These intervals are checked for crack-closure errors in which the stress and strain reversal from tension to compression or vice versa happens with a reduced stiffness. In reality, a tensile damaged cross-section would have a recovered stiffness back to the initial value when loaded in compression due to crack closure, making it possible to transfer compressive stresses through the section. As these errors can result in unrealistic high strains, it is important to get an overview. Three non-secant branches were investigated and one secant branch for confirmation, where no crack closure error was found. From the three investigated non-secant branches, only for the interval in analysis step 1103-1106 crack closure errors were found in the left most element of the bottom row

of the right pier in analysis steps 1104-1105 and in steps 1105-1106. By looking at the stresses and strain in that analysis step one can conclude that the error is relatively small as the strains are not that big in this analysis step. By looking at the stress-strain relation in Figure 4.64 another error was found around analysis step 3000. This error was more severe as the integration point was further damaged making the difference between the current stiffness and the initial stiffness larger. A hand calculation was made to estimate the ratio between the current strain and the strain expected in reality. The current strain was a factor 2.8 larger. In the bottom of the right pier, a large crack closure error was found which resulted in a compressive strain close to the plastic limit. The fact that non-secant branches exist is however not only the result of crack closure errors. This is supported by the fact that for the other two investigated intervals, no crack closure errors were found. The fact that a non-proportional loading method is used also results in non-secant branches. Although these branches are disturbing as they give false results, there is no indication that they have a big influence in the global result in this analysis in the Diana 10.2 version. This version showed improved results in not-secant branches which were present together with negative displacements in the previous version.

A parameter sensitivity study was done on the reference tensile strength f_{tu}, the parameter that describes the shear behaviour of the mid-sections of the piers and spandrels. Four different models were made and for each model, five different values for f_{tu} were implemented. Upon decreasing the value for f_{tu}, the piers started to fail in shear, which described the failure pattern of the experiment better. Model d offered the best results in combination with the shear strength of the piers reduced to $f_{tu} = 0.08$ MPa. Model d used the bed joint tensile strength for the full spandrels as the lower f_{tu} in the spandrels would mean that the spandrels were not able to carry the floor load.

This analysis was very stable with only a few reductions and estimated the maximum load just a bit higher than the experimental data. Unfortunately, the analysis stopped for a displacement of 10 mm, which is half the distance of the experiment. It was found that the flexural failure modes in all piers corresponding to higher values for f_{tu}, resulted in a more unstable analysis as both the bottom row and top row of the piers were damaged. Vertical forces were reduced to low values very often. With lower values for f_{tu}, the damage was more similar to the experiment, but also the vertical load could be carried easier as horizontal damage did not occur at the top of the middle and right pier. The vertical force could still be transferred.

In general, the original 3ZCM showed an acceptable load-displacement diagram but had the wrong failure mechanism. In this experiment, a reduced value for $f_{tu} = 0.08$ MPa gave better results in terms of the failure mechanism and stability of the analysis. Unfortunately, the analysis aborted at a displacement of 10 mm, because the vertical load could not be carried by the structure anymore.

5. Fiber beam model with SLA

5.1 Introduction

In this chapter, the door wall of the Pavia house is modelled with beam elements according to the equivalent frame method. A sequentially linear analysis is performed to model the failure mode of the structure. The equivalent frame method could increase the speed of the analysis because the structure is simplified with beam elements, while the accuracy should not be reduced much compared with the continuum elements. This chapter will contain several parts. After the general parameters, elements and dimensions of the model are explained (5.2), a short introduction with a simple three-point bending test is performed to test the new element (5.3). Then the fibre flexural model (FFM) of Willem Nobel is used to do an incremental iterative finite element analysis. This model is then made applicable for a sequentially linear analysis. The results of the SLA will be compared with the incremental iterative analysis results. Both the standard one zone equivalent frame (1ZEF) which is the FFM as the three-zoned equivalent frame model (3ZEF) are used (5.4). Again, an in-depth analysis is performed on initial load factor reductions and non-secant branches (5.5). Later several improvements are suggested (5.6): Mesh sensitivity, increased integration points over the width, a model that can only fail in tension, a proportional loading scheme for which the vertical load is used to prestress the structure, a parameter sensitivity study on fracture energy and an increased number of saw teeth. Finally, the reaction forces and internal bending moments in the piers are examined (5.7) and conclusions are drawn (5.8).
Again, important to notice is that for all the damage plots given, the damage in this version of Diana can be tensile or compressive. No distinction is made in the plots. As the tensile strength of the material used is much lower as the compressive strength, almost all damage visible in the plots is tensile damage. The damage is defined as: $D = 1 - \frac{E_{current}}{E_{initial}}$.

5.2 General information and parameters

Beam elements are used to model the façade in this chapter. New developments in the Diana software make it possible to do a sequentially linear analysis on a beam element model.
The piers and spandrels in the façade will be modelled by flexible beam elements, while the corners will be stiff. Failure is therefore occurring in the beams and spandrels. The dimensions of the different parts of the beam model are shown in Figure 5.1 and Table 5.1. The beam elements are all rectangular in cross-section. The width (D) is the in-plane dimension of the rectangular cross-section while the thickness (t) is the out-of-plane dimension of the rectangular cross-section.

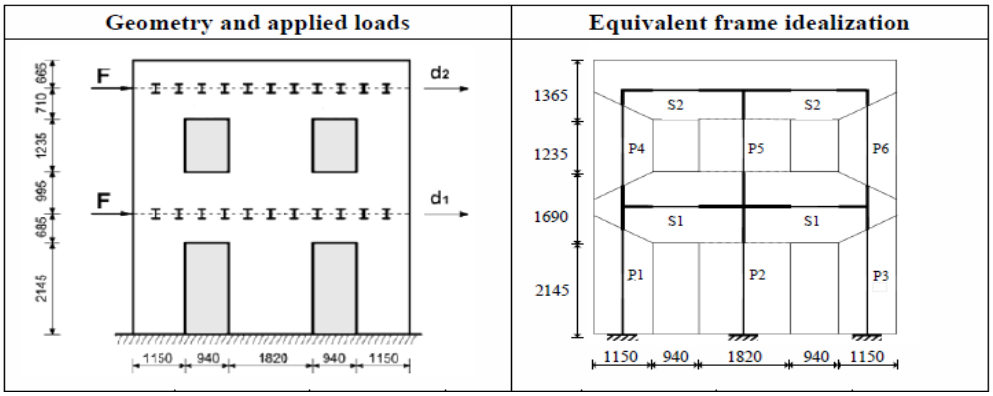

Figure 5.1; Geometry of the door façade [2]

Table 5.1; Dimensions of the beam element model

Pier Label	D	t	l_{ver}	l_{hor}
	[mm]	[mm]	[mm]	[mm]
P1, P3	1150	250	2477	–
P2	1820	250	2145	–
P4, P6	1150	250	1899	–
P5	1820	250	1235	–
S1	1680	250	–	940
S2	1375	250	–	940
CF1	900	250	1026	575
MF1	900	250	1690	1820
CF2	1150	250	350.5	575
MF2	1820	250	682.5	1820

The beam element used is CL9BE. This curved class-III beam element has three nodes and is a 2-dimensional element. The degrees of freedom in the nodes are the two displacements u_x and u_y and the rotation ϕ_z. As the elements have three nodes, the interpolation polynomials are quadratic. They are defined in the local ξ, η-coordinate system along the beam axis (ξ-axis):

$$u_x(\xi) = a_0 + a_1\xi + a_2\xi^2 \quad (5.2.1a)$$
$$u_y(\xi) = b_0 + b_1\xi + b_2\xi^2 \quad (5.2.1b)$$
$$\phi_z(\xi) = c_0 + c_1\xi + c_2\xi^2 \quad (5.2.1c)$$

As the strains are the derivatives of the displacements. The strains vary linearly along the center line of the beam. Again, the different parts of the façade will have their own strength parameters. The parameters are shown below in Table 5.2:

Table 5.2; Parameters of the beam element model

		Piers	Spandrel f1	Spandrel f2	Corners
E_0	[MPa]	$1.41 * 10^3$	$1.41 * 10^3$	$1.41 * 10^3$	$2.0 * 10^8$
ν_0	[−]	0.2	0.2	0.2	0
ρ	[kg/m^3]	1800	1800	1800	1600
f_t	[MPa]	0.04	0.32	0.26	–
$G_{f,t}$	[N/m]	5.0	20.0	20.0	–
f_c	[MPa]	3.0	3.0	3.0	–
$G_{f,c}$	[N/m]	$1.0 * 10^4$	$1.0 * 10^4$	$1.0 * 10^4$	–

The three piers at the bottom floor are connected to the foundation with clamped supports, no rotations or deformations are allowed. For the non-proportional load, the self-weight of the structure is included together with a distributed load $f_1 = 20700$ N/m on the first floor and $f_2 = 19800$ N/m on the second floor which represents the weight of the floor carried by this part.

5.3 Beam model introduction – Three-Point bend test

Like in the case with continuum elements when a wall was tested first. In this case, a simple three-point bending test is performed to validate if the elements are able to describe the behaviour and the results are acceptable.
The beam has a length of $2.05\ \mathrm{m}$. The cross-section has a width of $0.12\ \mathrm{m}$ and a height of $0.15\ \mathrm{m}$. At the point load, a notch is applied. At that section, the beam has a height of $0.09\ \mathrm{m}$.
Other properties are the Young's modulus $E = 1.6 * 10^{10}\ \mathrm{N/m^2}$, Poisson's ratio $\nu = 0.15$, the mass density $\rho = 2.5 * 10^{3}\ \mathrm{kg/m^3}$, tensile strength $f_t = 3.78\ \mathrm{Mpa}$ and the fracture energy $G_f = 300\ \mathrm{N/m}$. Again, the shear modulus is one hundred times smaller than the Young's modulus and the p-factor of the saw-tooth law is: $p = 0.1$. Only the elements of the notch are modeled with a tensile strength. The other elements are linear elastic. The size of the notch is from $x = 1.0\ \mathrm{m}$ until $x = 1.05\ \mathrm{m}$. The notch is modeled with 8 elements, the other parts have 50 elements each. Eleven integration points are used over the width, two over the length of an element.

The results are shown in Figure 5.2. The maximum displacement is around $2.5\ \mathrm{mm}$. The plastic behaviour shows increasing displacements for a slightly increasing force. At a displacement of approximately $2.5\ \mathrm{mm}$, the force drops and the displacements also reduce a bit. There is some snap-back behaviour which the program describes without any problems. The initial load factor stays 1 for the entire analysis. Therefore, this analysis is very stable. This is also the reason why the analysis ends before the force has decreased totally. The remaining force at the end of the analysis is the self-weight on the structure.

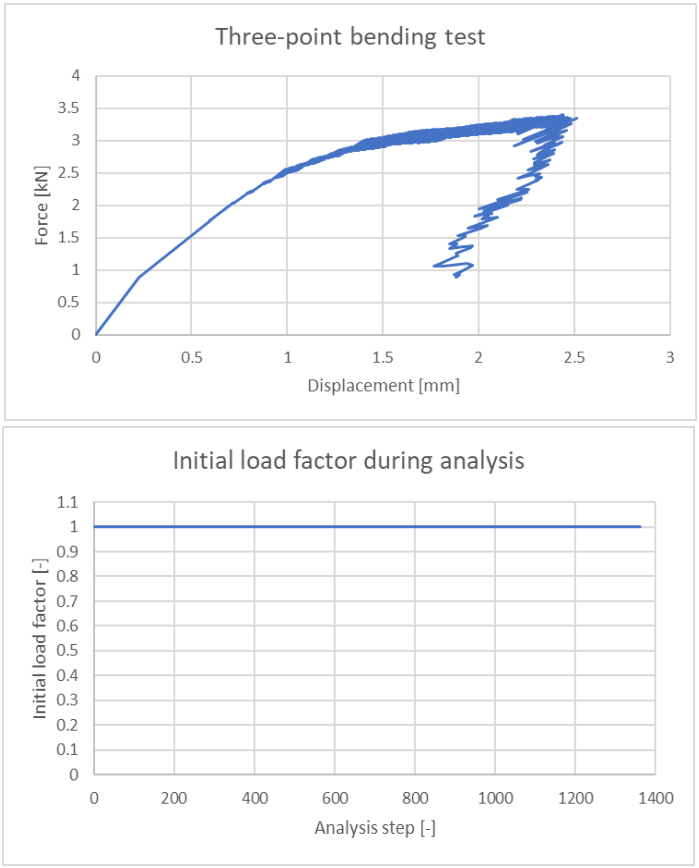

Figure 5.2; Above the load-displacement diagram of the three-point bending test. Below, the initial load factor during the analysis

The estimated plastic lower limit based on a full cross-section with height $h = 0.15\ \mathrm{m}$ can be determined from the elastic moment distribution. The bending moment at $x = \frac{1}{2}l$ can be determined by:

$$M_{\frac{1}{2}l} = \frac{1}{8}ql^2 + \frac{1}{4}Fl \tag{5.3.1}$$

with

$$q = \rho * g * b * h \quad ; \quad g = 9.81\ \mathrm{m/s^2} \tag{5.3.2}$$

Parameter q is the distributed load over the cross-section from the self-weight. The moment at which cracking occurs can be determined by:

$$M_{cr} = f_t W_{zz} \tag{5.3.3}$$

with

$$W_{zz} = \frac{1}{6}bh^2 \tag{5.3.4}$$

Using $(5.3.1)$ the force F at which the first crack occurs can be determined. This gives $F_{cr} = 2867\ \mathrm{N}$ and is a lower limit for the plastic limit.

An upper limit can be calculated by assuming a plastic hinge in the center of the cross-section with plastic moment M_p. Then the equation of virtual work of the work by the forces and moments can be used to calculate an upper limit [21]:

$$\delta W = \sum F_i \delta u_i + \sum M_j \delta \theta_j = 0 \tag{5.3.5}$$

Using:

$$M_p = \frac{bd^2}{4} f_t \tag{5.3.6}$$

Gives:

$$F_p = \frac{4M_p}{l} - ql \tag{5.3.7}$$

This gives an upper limit of $F_p = 4074\ \mathrm{N}$. In Figure 5.2, the maximum force is between these limits. Although, it should be said that the cross-section is somewhat weaker because of the notch.

5.4 Pavia house - First analyses with One zone and Three zone model

The fibre flexural model is shown below in Figure 5.3. The same mesh is applied as in [2].The spandrels are modelled with 8 beam elements, the outer piers with 24 beam elements, the middle piers with 10 beam elements and the corners with 15 elements. In this model the load is applied by loading the fictitious bar at the left with a proportional horizontal load of $1\ \mathrm{N}$ in the sequentially linear analysis and a proportional displacement in the incremental iterative approach. Different amounts of integration points have been used in the analysis. Later an overview will be given in which the results with different integration points are compared. Eleven integration points are used in the result further in this chapter. The 11 integration points are distributed over the thickness to increase the precision. Two rows are used over the length. Nobel [2] does not uses his three-zone approach in his fibre flexural model. All the piers and spandrels have the bed joint tensile strength f_{jt} as tensile strength.

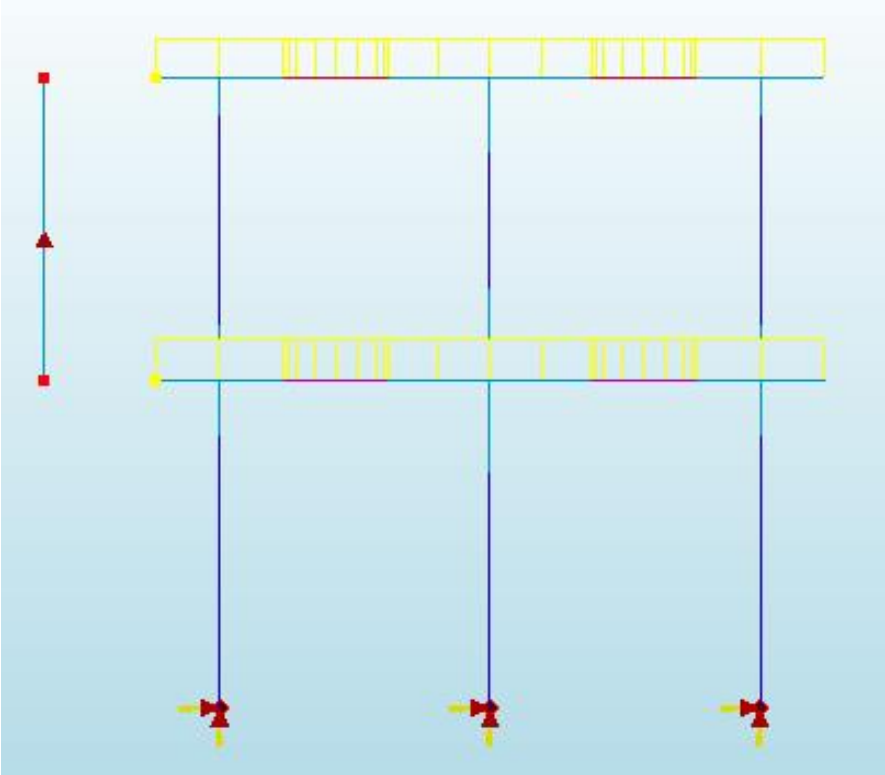

Figure 5.3; Fibre flexural model used in [2]

The load-displacement curves of both this analysis and the incremental iterative analysis are shown in Figure 5.4. The results are very different for the same model. While the incremental approach has a slight increase in load bearing capacity when plasticity is initiated, and keeps a sort of constant maximum load for large deformations, the sequentially linear analysis reaches a higher maximum load, but immediately unloads 75% of the maximum load afterwards. Afterwards, the deformations can increase but with a low load and reduced vertical weight.

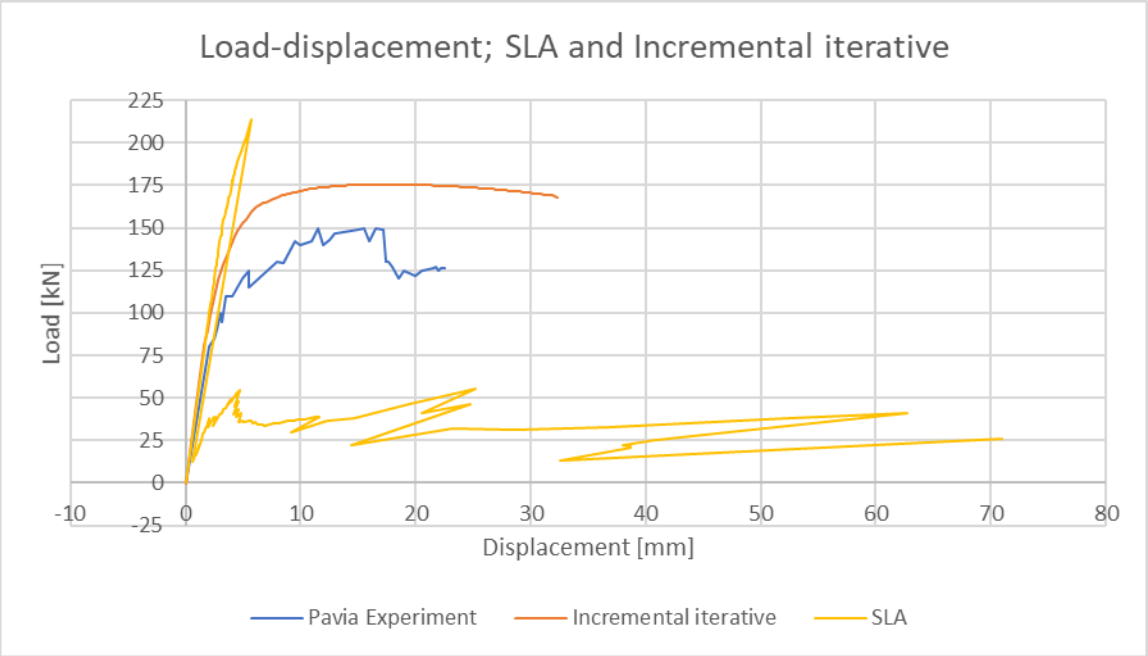

Figure 5.4; Load-displacement diagram SLA and Incremental iterative analysis of the original fibre flexural model

The value of the initial load multiplier is shown in Figure 5.5. At step 986, the maximum non-proportional load cannot be born by the structure. This step coincides with the peak load in Figure 5.4. After this step, the load is not recovered and the structure can already be regarded as failed.

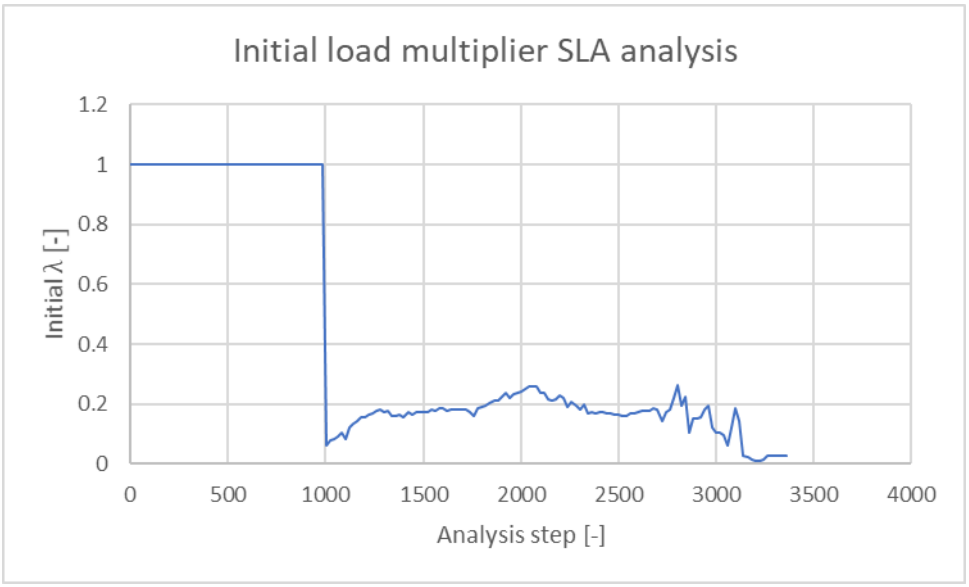

Figure 5.5; Initial load multiplier SLA analysis original beam model

The highest strains in the piers first develop at the top of pier P1. When the maximum load is reached, the damage develops at the bottom of pier P3 (element 39), which eventually reaches a state where the element deforms intensively, which is unrealistic. Element 39 has three nodes and bends double in its middle node after the peak load. An attempt to resolve this by using a finer mesh did not work. For all attempts with the one zone equivalent frame (1ZEF) somewhere locally an element misbehaved like in Figure 5.6, which ruined the analysis. Therefore, this model is not used anymore and the three-zoned approach (3ZEF) is used. In this model the distinction will be made in flexural parts and shear parts.

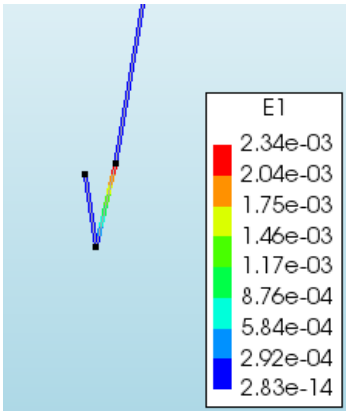

Figure 5.6; Unrealistic deformation of element 39

With the three-zoned approach, the analysis is able to continue a bit longer. Below in Figure 5.7, the damage in the structure is shown after failure. The damage starts from the beginning of the analysis in the left pier. This pier starts in compression in the first analysis steps as a result of the vertical load, but as the lateral load increases, the left end of the pier is loaded in tension and damage rapidly propagates. Not only the left pier damages, also the middle pier and the right pier. Especially the right pier starts to bend to the right. At this stage, the full load can still be applied. As the left pier is fully damaged, the right spandrel on the first floor starts to bend as is visible in the figure. The connections between the flexural parts of the spandrels and the shear part of the spandrel are damaged the most. These are elements 208 and 214. At this stage the initial load factor reduces and is not able to recover. The analysis continues and slowly the upper spandrel on the right side starts to bend. When this element is kinked the analysis ends.

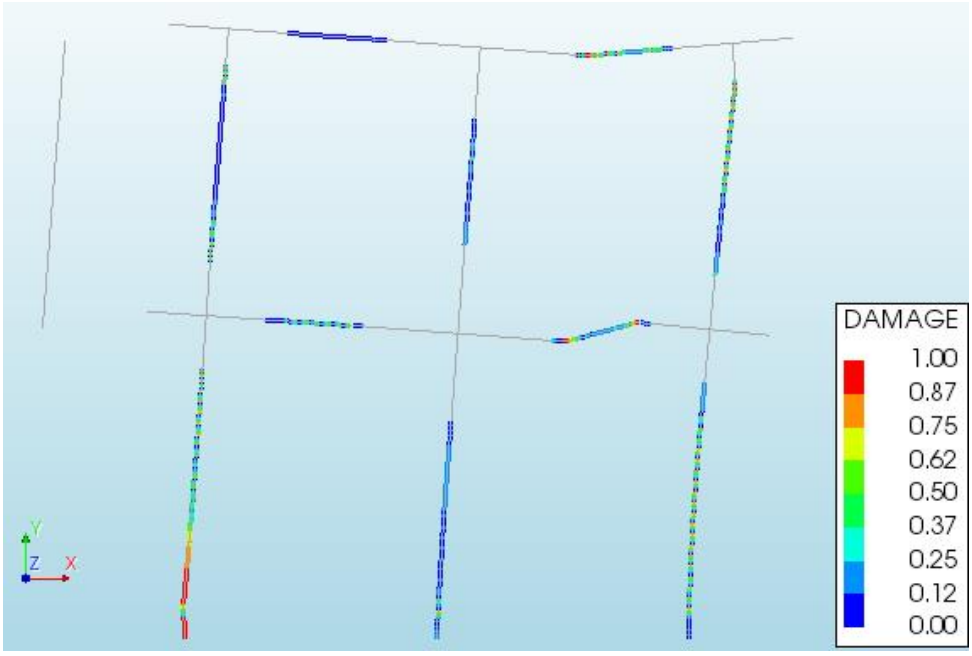

Figure 5.7; Damage in the left pier, right first floor spandrel and top right spandrel for the three-zoned beam model

The next analyses will have a finer mesh with respectively a requested element length of $0.2\ \mathrm{m}$, $0.1\ \mathrm{m}$ and $0.05\ \mathrm{m}$. This as an attempt to prevent the analysis from failing in an early stage.
The results can be found in Figure 5.8 together with the results of the incremental iterative approach and the experimental data.
For the element length of $0.2\ \mathrm{m}$, $0.1\ \mathrm{m}$, the results of these models are almost equal to the incremental iterative approach until a deformation of $5\ \mathrm{mm}$. A finer mesh leads to a somewhat higher peak load. After the deformation of $5\ \mathrm{mm}$, the load reduces and the structure is only able to resist an average of 60% of the initial load. The failure mode consists large shear deformation in the right first floor spandrel together with bending failure in the top floor spandrel and left bottom pier. Decreasing the mesh size is no effective way to achieve better results as the result were similar before the initial load factor reduced.

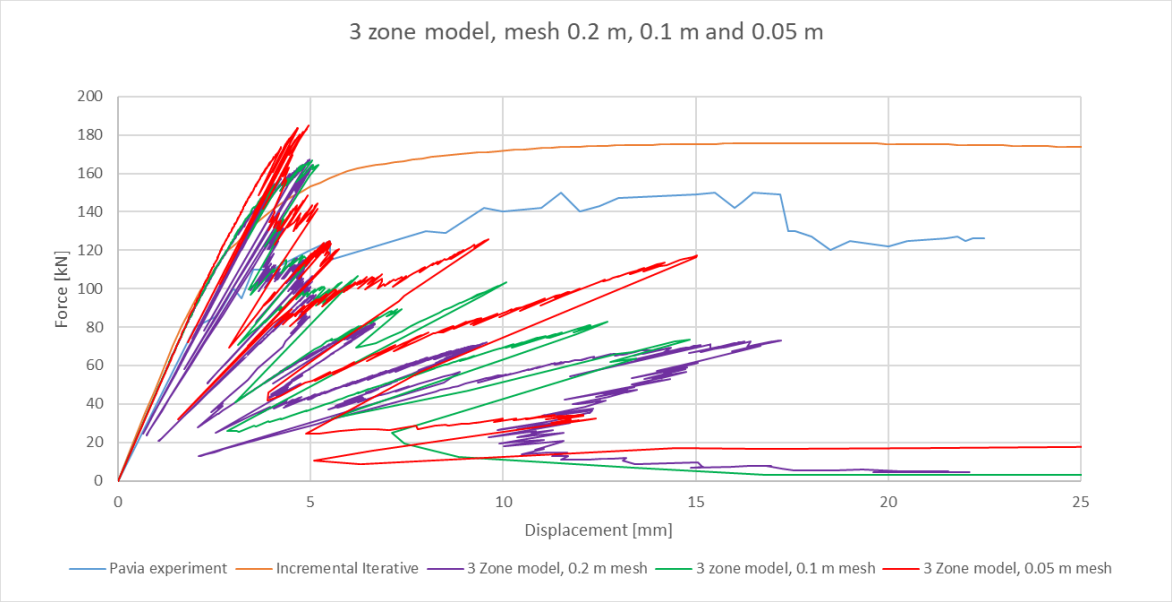

Figure 5.8; 3-Zone model, mesh of 0.2 m, 0.1 m and 0.05 m

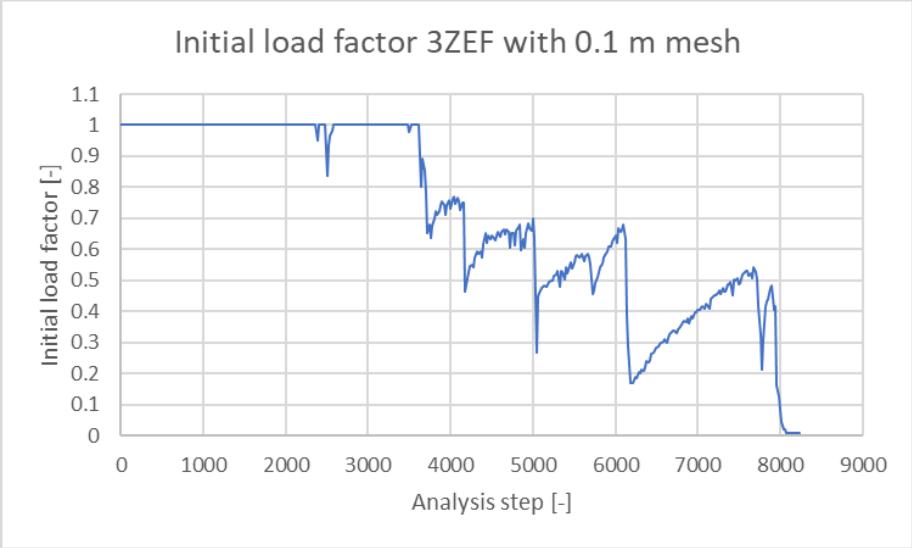

Figure 5.9; Initial load factor during analysis for 3ZEF with a mesh size of 0.1 m

When the number of integration points is changed over the width, there is no clear difference. Every analysis fails after reaching the peak load. Again, the load-displacement relation shows very brittle behaviour. It is not possible to carry more load and increase the displacements, because the vertical load cannot be applied. Maximum displacements with full vertical load are $5\ \mathrm{mm}$ for all three analyses. Because eleven integration points over the width is the most accurate version mathematically speaking, this is adapted in all the analyses further in this chapter. For more information about the integration schemes of the Simpson rule, the Diana manual can be consulted [22].

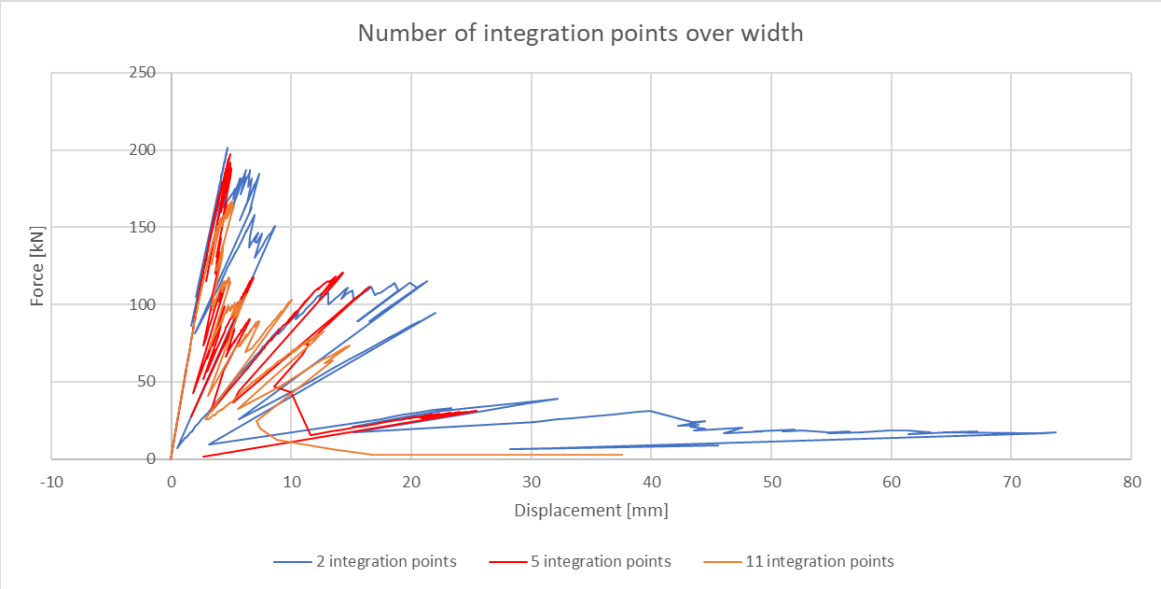

Figure 5.10; Variation in the number of integration points over the width

5.5 In-depth analysis

5.5.1 Initial load factor reductions

Like in the case with plane stress elements, the initial load factor λ_{ini} has some large drops while the structure cannot necessarily be defined as failed. As an example, the initial load factor during the analysis of the beam element analysis with a 3-zone model and 0.1 m mesh is given in Figure 5.11. From this figure can be seen that in between analysis step 2000 and 2556 the initial load factor drops several times but recovers again to a unit value. This opens a debate about whether the structure should be regarded as failed or not. Looking beyond that debate, the reason why this happens in the first place is investigated in this section.

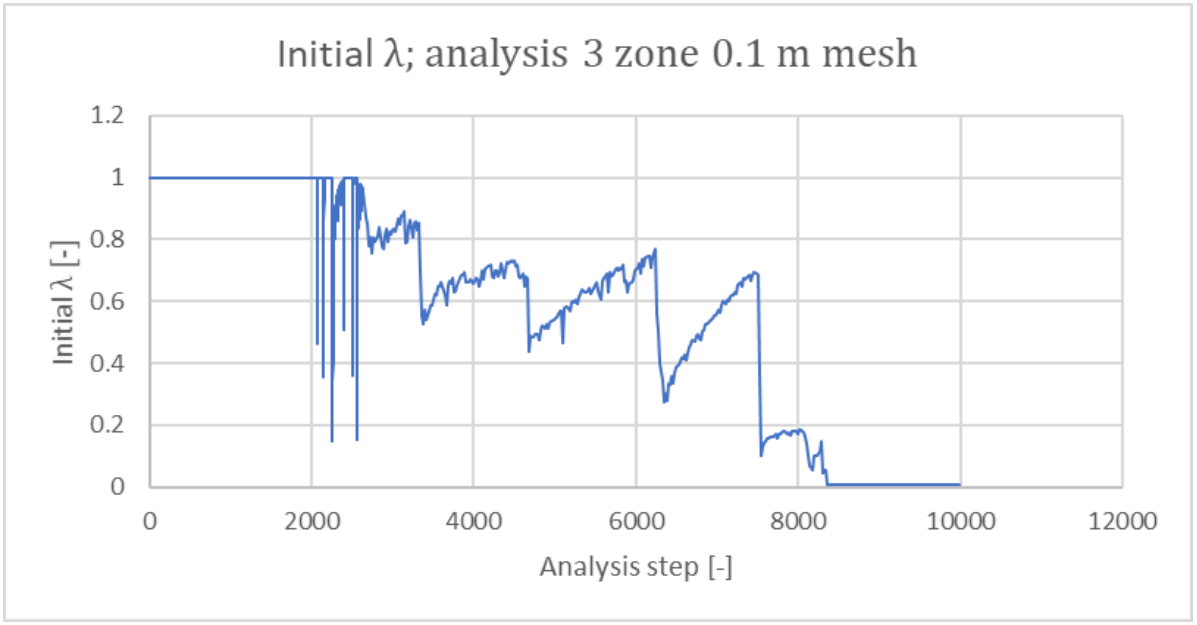

Figure 5.11; λ_{ini} during analysis: Beam model 3 zones, $0.1\ m$ mesh

In section 0, it is explained that there are in general two ways of reducing the load when the full initial non-proportional load cannot be reached. The initial load itself can be reduced and the proportional load is zero in that analysis step, or the previous load case can be scaled with an additional load factor. The latter was preferred because this resulted in a similar stress-strain ratio in the material while the first method would load the structure in a different way, in this case only vertically. This would lead to a different stress distribution and therefore a different type of failure as one would expect.
As expected, the reduction between the current vertical load and the previous vertical load one step before is equal to the reduction of the initial load factor. For example, in step 2071, the initial load factor has reduced from 1 to 0.464401. The reduction of the horizontal load is from $167.968\ \mathrm{kN}$ in step 2070 to $78.005\ \mathrm{kN}$ in step 2071, which is the same ratio.

First, the output file in which the logging of the analysis is saved is used. In all steps where the initial load factor reduces between step 2000 and 2556, the damage propagates in element 208 and 214. Until step 2396, the big reductions happen while damage propagates in element 208. From step 2396 until step 2556, the reductions are mostly because of damage in element 214. Elements 208 and 214 are found in the right spandrel of the first floor. Figure 5.12 shows this spandrel. The corresponding nodes of the element are colored red. The middle node of the element will provide results for the current element only, because the nodes at the end of an element are shared with the neighboring element. These nodes are node 421 for element 208 and node 427 for element 214.

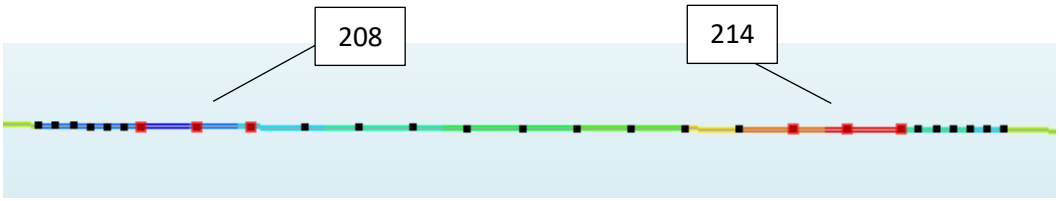

Figure 5.12; Element 208 and 214 in the right spandrel of the first floor

To get a better understanding of the behaviour of these elements, the relations between the stresses and the strains in these elements are examined. First the principal strains in the element are investigated. However, as the model is two dimensional. The stresses and strains in the third dimension are zero by definition. It is expected that the stress in the local axial direction (σ_{xx}) will be larger than the normal stresses over the height of the cross-section (σ_{yy}) as this stress is zero by definition in the fibre beam approach. For the principal stresses, there will be a non-zero value for the stresses σ_1 and σ_3 because of Poisson's ratio and the fact that the principal stresses can rotate. As there is always a zero valued principal stress perpendicular to the façade, the result will be that the first principal stress σ_1, which is also the largest, will be tensile, the second principal stress σ_2 will be zero and the third σ_3 will be compressive and therefore negative. When the stresses in an element change, the direction of the principal stresses will change. To take a closer look at crack closure behaviour, the axial stresses give a better view as they are fixed. However, the Cauchy stress tensor is defined in the initial coordinate system, which means that differences may arise when a member rotates substantially.

From step 3402, the stress state switches from tensile to compressive in many integration points like element here in element 208. In Figure 5.13, the stress-strain relation is given for integration point 1. Only once in 20 analysis steps the results were reported to reduce calculation time and memory. After some time, the stress and strain changes sign from tension to compression. However, the stiffness in this integration point was already reduced fully. This results in a compression stiffness which is incorrect. The strains become too large because of the reduced stiffness which leads to incorrect displacements for that analysis step.

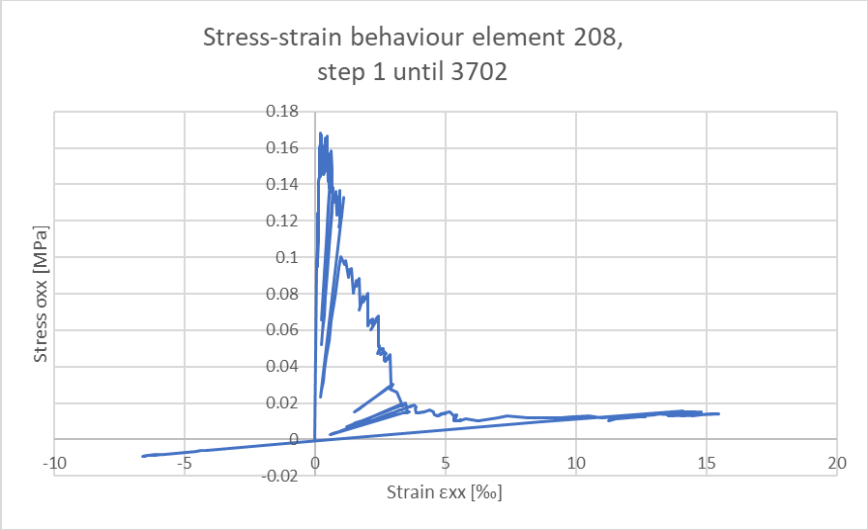

Figure 5.13; Stress-strain behaviour in element 208 integration point 1, Tension to compression

5.5.1.1 Damage, strain and stress distribution over the width

In Figure 5.14, the damage, strain and stress are shown for analysis steps 1, 16, 421, 2551 and 3706 for element 46. These results will be discussed on the next page.

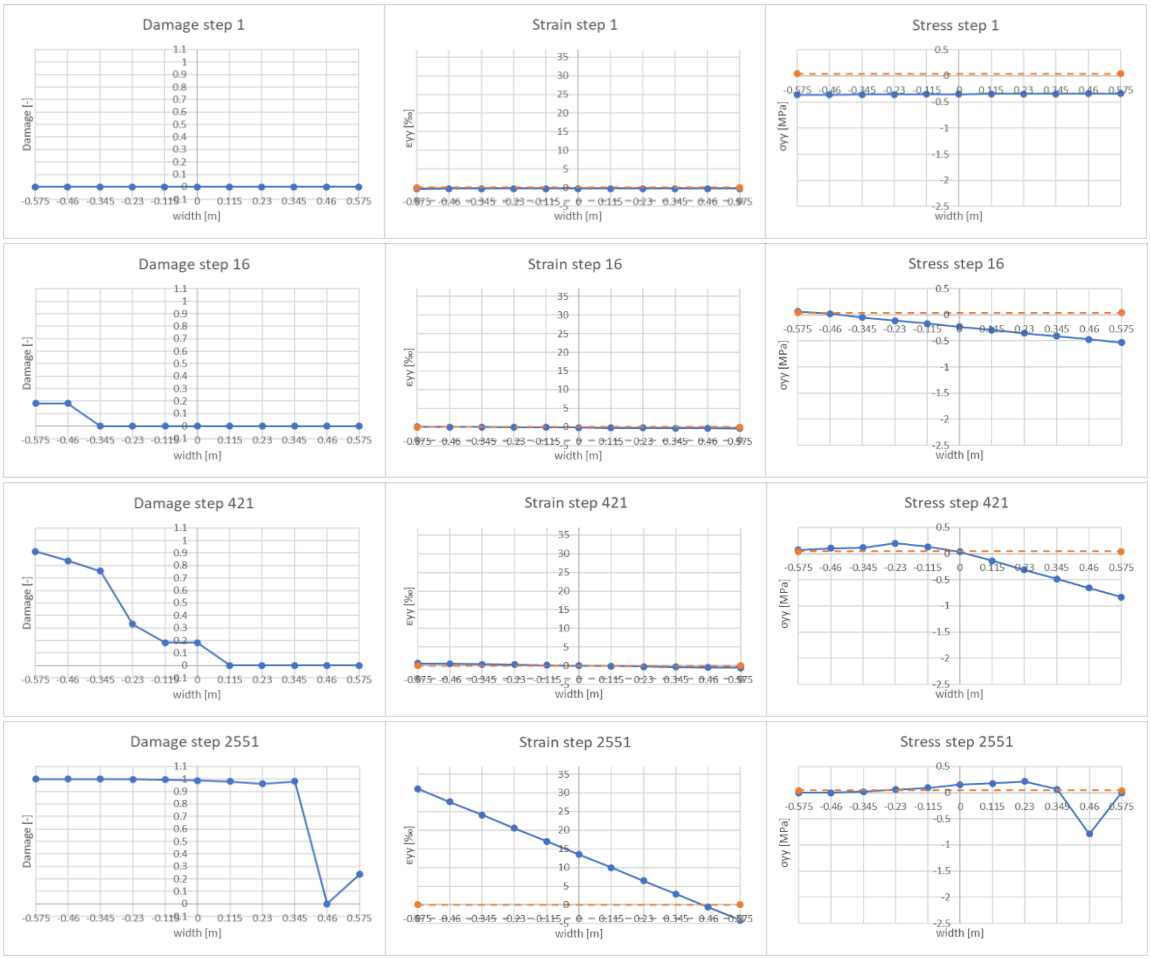

Figure 5.14; Damage, strain ϵ_{yy} and stress σ_{yy} in element 46, analysis steps: 1, 16, 421, 2551, 3706

The location of the different steps in the load-displacement curve is shown in Figure 5.16.

In the first analysis step, only the weight is applied. Therefore, the element has a constant compressive stress over its width. In the next steps, the proportional load is applied and the relation is linear elastic in most integration points. Element 46 is one of the first elements which is damaged and therefore some damage has propagated at the tension side. Because the tensile strength is far lower than the compressive strength, the damage propagates from that side through the cross-section. In step 421, the damage has propagated further. Strangely, the tensile strength is exceeded in many integration points in this analysis step. The tensile strength of element 46, $f_t = 0.04$ MPa, the stress in integration point 15, $\sigma_{yy} = 0.196$ MPa. The principal stress is even higher:

$\sigma_1 = 0.249$ MPa, more than six times the tensile strength. By looking at the other analysis steps, the tensile strength is also exceeded in different integration points.

In step 2551, a large part of the section is damaged. Because the weight of the top floor still has to be transferred through the cross-section, the compressive stress has a high peak value at the compressive side, especially because the undamaged cross-section is very small. Also, because the cross-section is almost fully damaged at the tension side and the stiffness is reduced, there is almost no tensile stress transferred in that region. The strains in the cross-section stay linear during the whole analysis. Comparing the strains in the later steps, with the first steps, it is evident that a large crack has occurred

at that side. Because almost the whole cross-section is damaged and the strains are far above the plastic limit, All the stresses have to be transferred through a small area of the cross-section. Looking at the compressive stresses and strains, the post peak value at the compressive constitutive relation is not reached, because the strains are far below α_c.

Table 5.3; Stresses, strains and parameters of the constitutive relations

Parameter	E_0 [MPa]	f_t [MPa]	f_c [MPa]	ϵ_p [−]	α_c [−]
Value piers	1410	0.04	−3.0	$2.84 * 10^{-5}$	$-3.55 * 10^{-3}$
Value spandrel (208)	1410	0.14	−3.0	$9.929 * 10^{-5}$	$-3.55 * 10^{-3}$

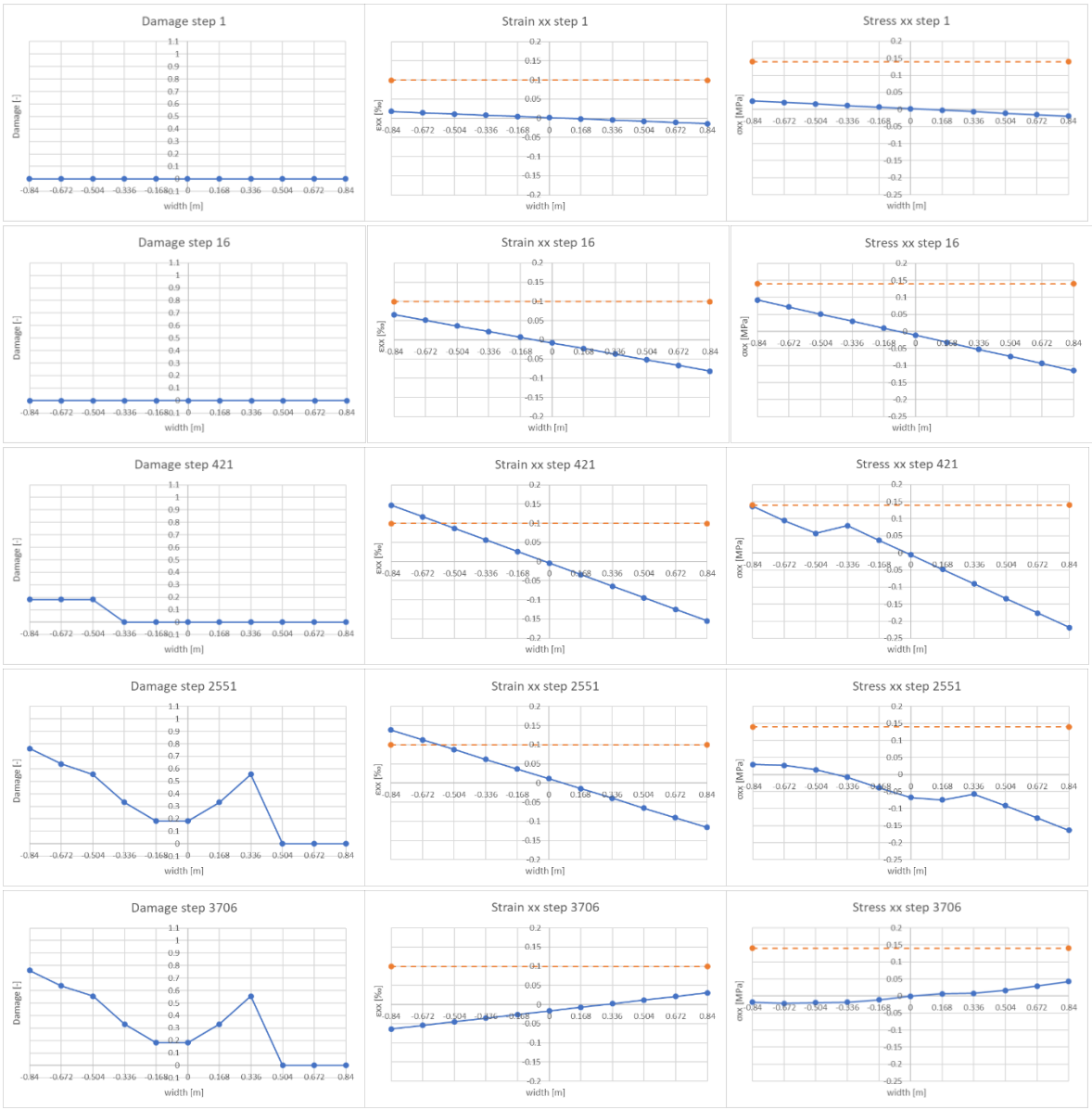

Figure 5.15; Damage, strain ϵ_{xx} and stress σ_{xx} in element 208, analysis steps: 1, 16, 421, 2551 and 3706

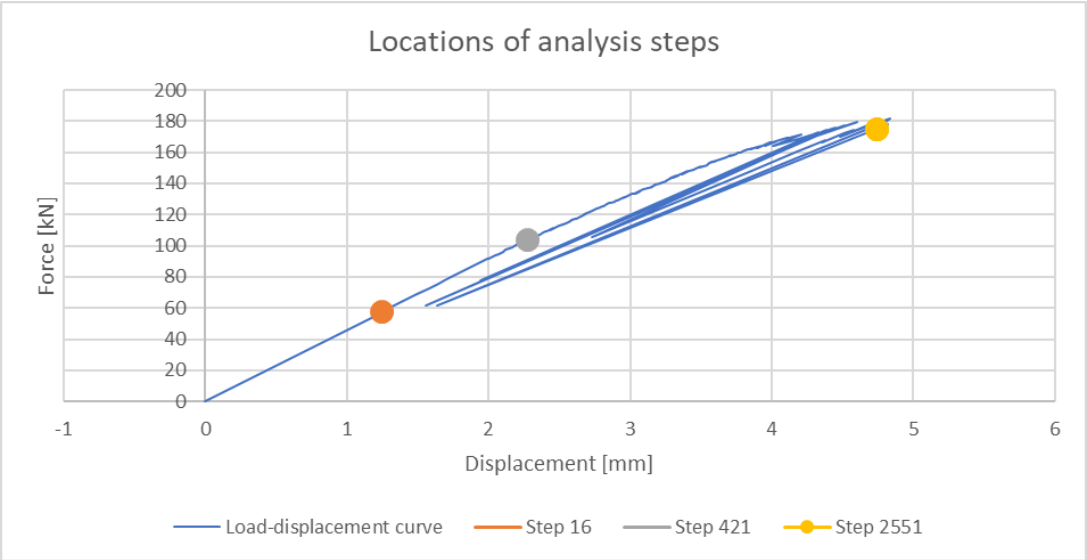

Figure 5.16; Location of analysis steps 16, 421 and 2551 in load-displacement curve

Figure 5.15 shows the damage, strain and stress in element 208 at analysis step 1, 16, 421, 2551 and 3706. Again, the stress-strain distribution is linear in the beginning. Because this element is situated in a spandrel, the element is already bended in the first analysis step under the self-weight of the building. Interesting to see is the damage accumulating in integration point 19. This is the fourth integration point from the right. The damage starts to grow from analysis step 2041. Here, the full vertical load is applied and the structure and this point is just before (30 steps) the vertical load cannot be applied anymore. The strain is linear over the cross-section and the stress somewhat linear with plasticity at the tensile end. However, a tensile failure occurs in integration point 19 while this point is loaded in compression in the global coordinate system ($\sigma_{xx} = -0.1324$ MPa). The principal stresses in that integration points are $\sigma_1 = 0.1537$ MPa and $\sigma_3 = -0.2861$ MPa. The damage is propagating in this integration point, while there are other neighboring integration points with higher principal stresses. Like integration point 17, $\sigma_1 = 0.2922$ MPa and integratiron point 18, $\sigma_1 = 0.2628$ MPa. Again, these stresses are far above the tensile strength ($f_t = 0.14$ MPa). An overview of the same behaviour for the analysis steps before load reductions in which neighboring integration points have higher stresses is given in Table 5.4.

Table 5.4; Principal stress σ_1 in the integration points before load reductions. Higher stresses in neighboring integration points. Stresses are given in $[Pa]$. Damaged integration point is marked in red.

steps	2070	2145	2257	2505	2556
Dam. IP	208 int 9	208 int 10	208 int 11	214 int 13	214 int 12
intp	σ_1 [Pa]	σ_1 [Pa]	σ_1 [Pa]	σ_1 [Pa]	σ_1 [Pa]
1	1.37E+05	1.34E+05	1.35E+05	6.91E+04	6.76E+04
2	1.69E+05	1.68E+05	1.36E+05	8.52E+04	8.31E+04
3	1.65E+05	1.65E+05	1.65E+05	1.09E+05	1.06E+05
4	2.06E+05	2.09E+05	2.00E+05	2.45E+05	2.36E+05
5	2.87E+05	2.39E+05	2.74E+05	2.79E+05	2.68E+05
6	2.97E+05	3.04E+05	3.48E+05	2.73E+05	2.62E+05
7	2.64E+05	2.70E+05	3.09E+05	2.77E+05	2.65E+05
8	1.99E+05	2.02E+05	2.31E+05	2.46E+05	2.34E+05
9	1.54E+05	1.80E+05	1.64E+05	2.21E+05	2.10E+05
10	1.20E+05	1.54E+05	1.40E+05	2.03E+05	1.92E+05
11	9.63E+04	1.24E+05	1.54E+05	1.85E+05	1.75E+05
12	1.52E+05	1.44E+05	1.35E+05	1.23E+05	1.54E+05
13	1.85E+05	1.77E+05	1.66E+05	1.54E+05	1.32E+05
14	1.87E+05	1.78E+05	1.71E+05	1.74E+05	1.54E+05
15	2.51E+05	2.38E+05	2.36E+05	2.27E+05	2.54E+05
16	2.47E+05	2.82E+05	2.85E+05	2.58E+05	2.88E+05
17	2.70E+05	3.06E+05	3.13E+05	3.04E+05	2.75E+05
18	2.43E+05	2.74E+05	2.81E+05	2.52E+05	2.79E+05
19	2.25E+05	2.07E+05	2.13E+05	2.24E+05	2.03E+05
20	1.07E+05	1.25E+05	1.34E+05	2.04E+05	1.90E+05
21	8.65E+04	1.01E+05	1.09E+05	1.88E+05	1.78E+05
22	7.17E+04	8.29E+04	9.04E+04	1.74E+05	1.67E+05

Looking at the principal stresses and strains, they have a linear relation before the first damage at step 2041. After this step, the principal stress increases to a value of 0.2436 MPa. This while, the tensile criterion is set on 0.14 MPa. It is possible that the principal tensile strength is somewhat higher than the tensile strength criterion as a result of the way the saw tooth relation is constructed. As explained in section 2.3.3, the softening curve is shifted up and down with a factor p. The maximum strength becomes somewhat higher. An increase like in this example is however not because of that reason. After three steps, the stress-strain relation becomes linear again with a different stiffness. The tangent of this linear relation is higher than it was before the damage. This means that the structure has a higher stiffness after the damage in this integration point, which contradicts the effect of the damage. When the value of the modulus of elasticity is calculated, this does not coincide with the given value. The given value of the modulus of elasticity: $E_0 = 1.410 * 10^3$ MPa.
Taking into account Poisson's ratio. The modulus of elasticity can be calculated with the constitutive relations:

$$\begin{bmatrix}\epsilon_1\\ \epsilon_2\\ \epsilon_3\end{bmatrix} = \frac{1}{E_0}\begin{bmatrix}1 & -\nu & -\nu\\ -\nu & 1 & -\nu\\ -\nu & -\nu & 1\end{bmatrix}\begin{bmatrix}\sigma_1\\ \sigma_2\\ \sigma_3\end{bmatrix} \tag{5.5.1}$$

Because all principal stresses and strains are available from the calculation and the model used is two dimensional. The modulus of elasticity can be calculated with two equations.

$$E_1 = \frac{\sigma_1 - \nu\sigma_3}{\epsilon_1} \tag{5.5.2a}$$

$$E_3 = \frac{\sigma_3 - \nu\sigma_1}{\epsilon_3} \tag{5.5.2b}$$

For the first equation, the modulus of elasticity has a value of approximately:
$E_1 \approx 1.225 * 10^3$ MPa. For the second equation, the average is approximately:
$E_3 \approx 1.191 * 10^3$ MPa.

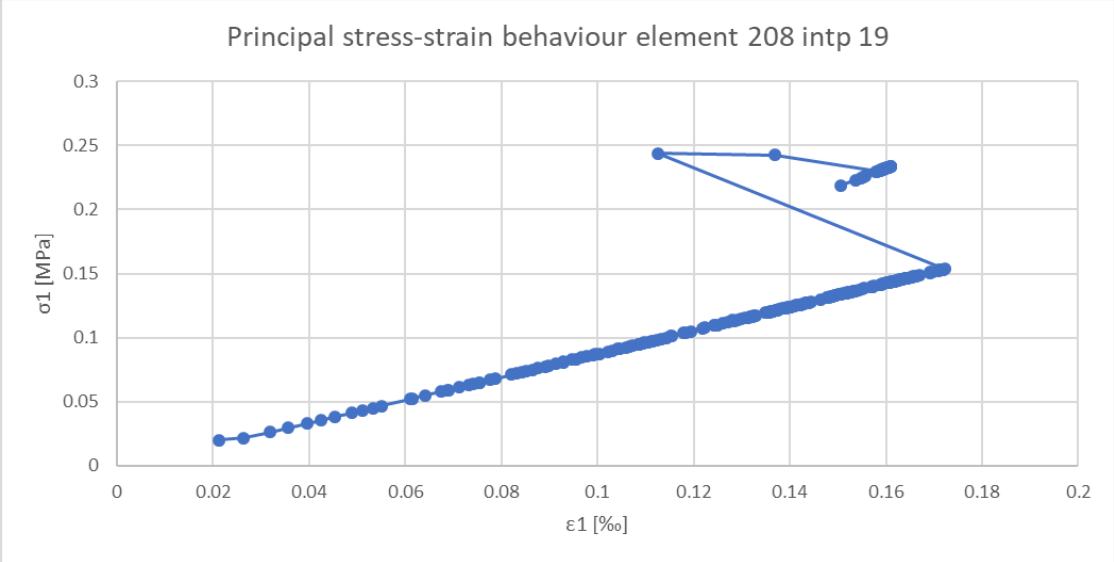

Figure 5.17; Principal stress-strain behaviour element 208 integration point 19. Steps 1-2070

In the Diana model, the decrease of the Poisson's ratio upon damage from equation (2.3.16) is not yet included. When an integration point is damaged, the Poisson's ratio is set to zero.
When the stiffness is calculated from for the damaged integration point in Figure 5.17. The stiffness can be calculated with Poisson's ratio set to zero:
$E_1 \approx 1.451 * 10^3$ MPa and $E_3 = 1.261 * 10^3$ MPa. This explains for a part, why the stiffness seems to increase as the linear relation becomes steeper. However, both values are not accurate for the undamaged and damaged cross-section.
Analysis step 3706 shows that the cracks in this spandrel have closed. There are compressive strains visible. The stress in this part is however still very small as the integration points were damaged in tension. The reduced stiffness remains when the load in the integration point is reversed from tension to compression. This is an example of a crack closure error as in reality, the material would have the initial stiffness upon load reversal.

The damage, vertical strain ϵ_{yy} and vertical stress σ_{yy} distribution over the width of the bottom row of the other piers will examined in this part. Below in Figure 5.18 the distribution for the middle pier is given and in Figure 5.19, the distribution for the right pier.

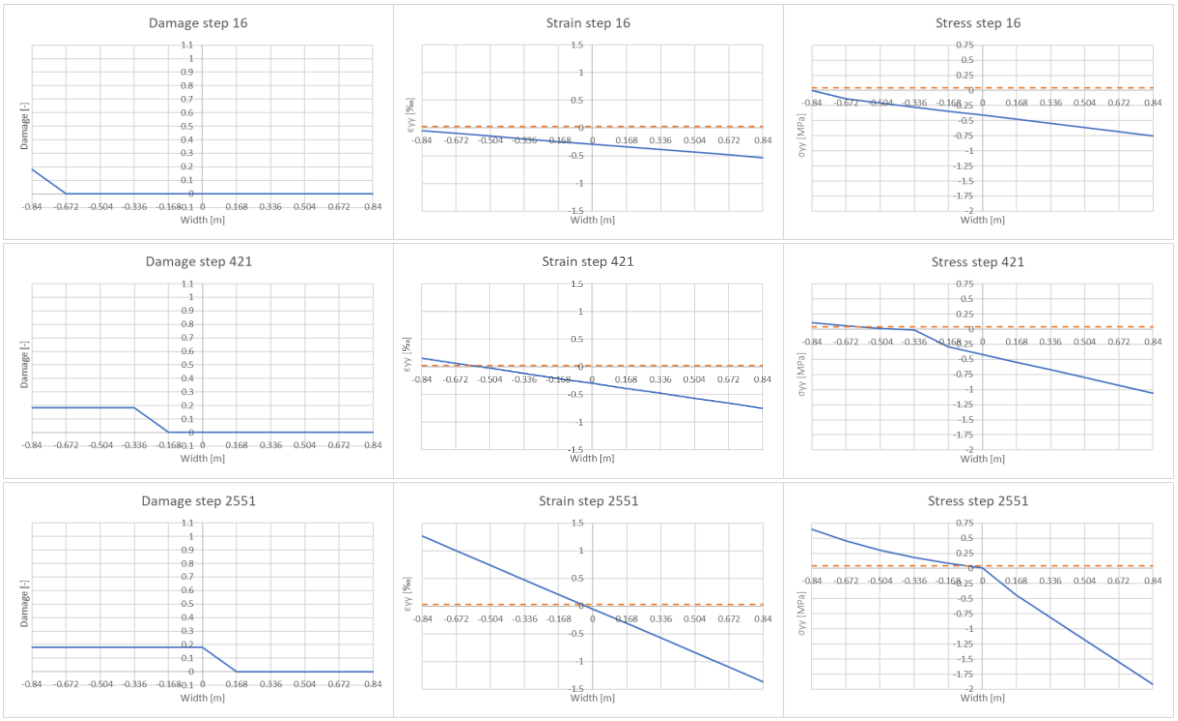

Figure 5.18; Damage, ϵ_{yy} and σ_{yy} of the bottom row of the middle pier for analysis steps 16, 421 and 2551

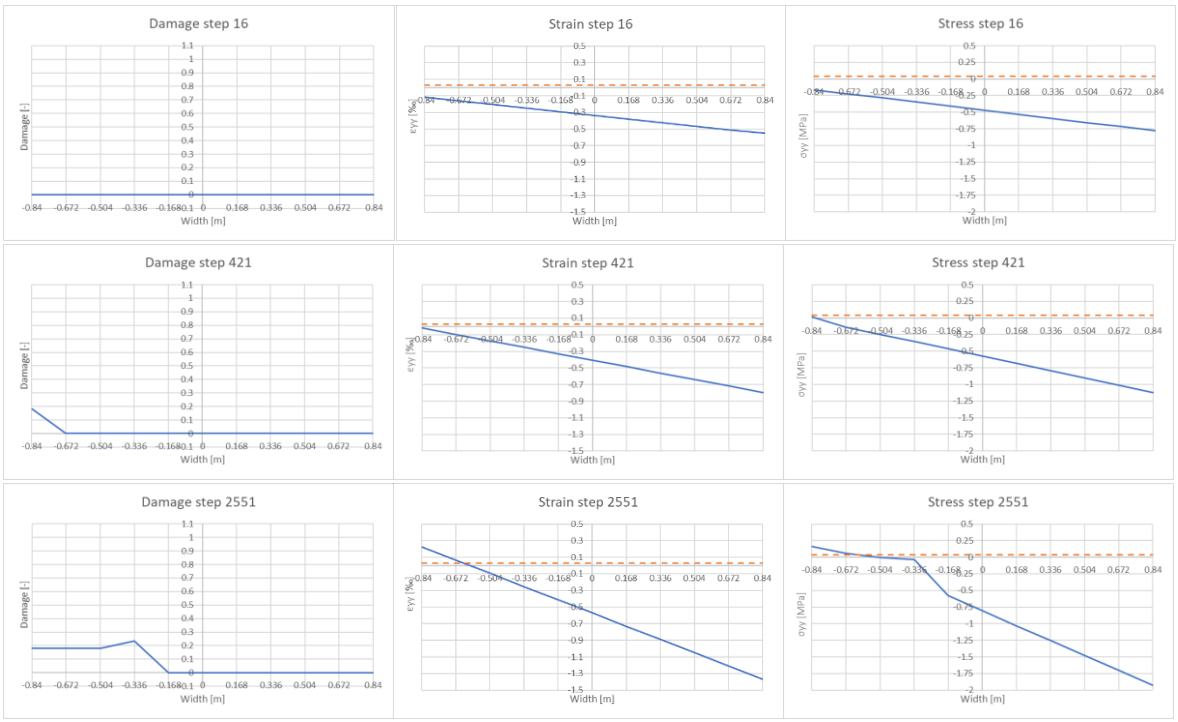

Figure 5.19; Damage, ϵ_{yy} and σ_{yy} of the bottom row of the right pier for analysis steps 16, 421 and 2551

The location of the different analysis steps is shown in Figure 5.16. Again, the stresses exceed the strength of the material. Concluding: For all three piers, the occurring damage confirms the expectations that the piers will crack at the left side. This is similar to the continuum model. As the beam model can only fail in bending and not in shear, the expected shear failure visible in the beam model is not present here. For the piers, the tensile stresses exceed the tensile strength of the material in the global and principal directions. The reason for this is the high shear stress in the cross-section. This high shear stress rotates the principal direction while the governing crack direction is along the axis of the element. With a fixed crack approach, the principal stresses grow and can be larger than the stresses in neighboring elements, as the fixed crack coordinate system has the boundary for the strength of the material. As a result of this for the spandrel, damage propagated in an element which did not have the highest stress in the spandrel. This resulted in an incorrect damage pattern and disturbs the analysis. For all piers, toe crushing did not happen as the strains were far below α_c meaning that the stresses and strains were still before the maximum compressive strength.

5.5.1.2 Crack openings

Because the current version of Diana does not include crack width calculations for a sequentially linear procedure, this has to be estimated from the strain and known parameters like in the continuum model.

Because a smeared crack model is used, the cracks are not predefined and can occur everywhere in the mesh. When the tensile stress exceeds the tensile strength, a crack occurs perpendicular to this direction. The crack is influenced by different factors, like the tensile strength f_t of the material and the fracture energy G_f. In a smeared case like this, the crack band width h is also of importance. This is the length over which the crack is smeared out. This length is for example influenced by element type and element size.

In this case, the tension softening curve is linear which gives the relations shown in Figure 5.20. Of course, this stress-strain relation is approximated with the saw-tooth relation during the analysis.

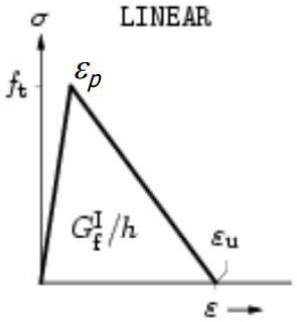

Figure 5.20; Fracture energy and ultimate strain, smeared crack model [22]

From this figure, the relations of yield strain ϵ_p and the ultimate strain ϵ_u, and other material parameters can be derived:

$$\epsilon_p = \frac{f_t}{E_0} \tag{5.5.3}$$

As the gradient of the elastic branch is the initial modulus of elasticity E_0. And for the ultimate strain:

$$\epsilon_u = \frac{2G_f^I}{hf_t} \tag{5.5.4}$$

An important parameter is the fracture energy divided by the crack band width G_f^I/h , which can be seen as the fracture energy available in the element, i.e. the area under the linear tension softening curve. The crack band width h is dependent on the element type. For linear two-dimensional elements, this width is $h = \sqrt{2A}$, for higher order two-dimensional elements $h = \sqrt{A}$. With A, the area of the element. For a beam element its default is the length of the element calculated as $h = V/\bar{A}$. The volume of the element divided by the average cross-sectional area [22].

When the plastic strain is reached, cracks will occur and therefore the strain can be formulated by adding an elastic component and a plastic or crack component.

$$\epsilon = \epsilon^{el} + \epsilon^{cr} \tag{5.5.5}$$

In this formulation, the elastic part is determined by Hooke's law:

$$\epsilon^{el} = \frac{\sigma}{E_0} \tag{5.5.6}$$

The initial elasticity E_0 is used, because the reduction in elasticity in the sequentially linear analysis is already included in the stress σ which is influenced by the current modulus of elasticity. In the continuum model, stresses in both directions had to be used to take into account the Poisson effect. In the case of beam element CL9BE, this is not necessary because the stresses in y-direction and z-direction are set to 0 by definition for the used element [3]. Only the axial stress in the length of the element remains. When the damage is fully developed i.e. equal to 1, the stress in the material will be reduced to zero. Therefore, the elastic strain in the material will also disappear. All strains left are only determined by the crack strain ϵ^{cr}. This crack strain can be described as a function of the crack opening displacement w and the crack band width described above h.

$$\epsilon^{cr} = \frac{w}{h} \tag{5.5.7}$$

In the finite element results, the crack opening can be estimated by calculating the elastic strain from the stress, subtracting this from the total strain and multiply the answer with the crack band width.
In x-direction, this gives:

$$w_{xx} = \left(\epsilon_{xx} - \frac{\sigma_{xx}}{E_0}\right) * h \tag{5.5.8}$$

Of course, this is an approximation only to give an indication of the crack opening. In a sequentially linear analysis, the structure is unloaded and reloaded every analysis step making all the steps linear elastic, hence the name sequentially linear analysis.

Examining the graph of Figure 5.11, the first reductions occur in the intervals step 2071 till 2075, 2146 till 2165, 2258 till 2404 and 2506 till 2517. The next reduction starts at step 2557 and the structure is hereafter not able to recover.

Looking at the output file, the damage in step 2071 till 2075 develops in integration point 9 of element 208. The left side of the right spandrel on the first floor. In the top graph of Figure 5.21, the steps until step 2070 are shown. The integration point is undamaged, which results in a linear stress-strain relation. At step 2070, first damage occurs and the integration point is damaged with $d = 0.1821$. At step 2071, the non-proportional load cannot be applied fully. Therefore, the load is reduced. A reduction till $46{,}44\%$ of the previous analysis step is needed, visible in the second graph of Figure 5.21. In this analysis step, again integration point 9 of element 208 is damaged, after this step $d = 0.3317$. Next, the load is increased in 5 analysis steps until the initial load multiplier λ_{ini} has reached a value of 1. In these steps, integration point 9 is still damaged every step. When $\lambda_{ini} = 1$ in

step 2076, the damage $d = 0.7062$. The second graph of Figure 5.21 shows this reloading in the almost horizontal part.
Interesting to see is the increase of the principal stress σ_1 between steps 2070 and 2071.
The tensile limit is reached in analysis step 2070 and the load factor reduces in step 2071 to 0.4644. However, the principal stress increases from $\sigma_{1,2070} = 0.1537$ MPa to $\sigma_{1,2071} = 0.2002$ MPa. The tensile limit; $f_t = 0.14$ MPa. The fact that the principal stress is higher than the stress limit can be explained in the way the saw-tooth relation is build. By adding the p-factor times the tensile strength, the tensile stress can be higher than the strength. This does however, not explain the difference between $ft = 0.14$ MPa and $\sigma_{1,2071} = 0.2002$ MPa, which is a result of the fixed crack approach as explained in the previous chapter.

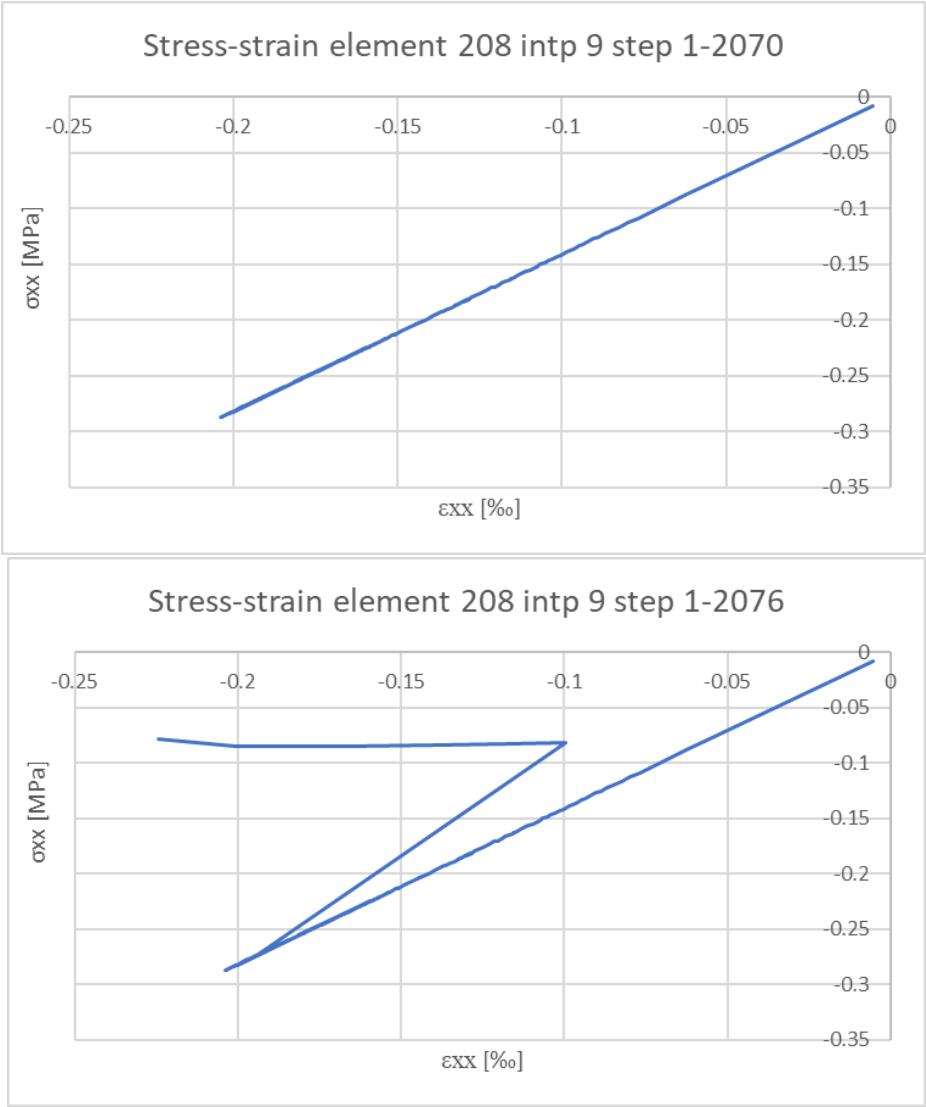

Figure 5.21; Stress-strain relation in element 208 integration point 9. Elastic in step 1-2070. Load reduction and reloading between step 2071 and 2075

The crack width is estimated by applying (5.5.8) on the data. The principal direction is however differently orientated. In the global coordinate system, integration point 9 is in compression while the first principal stress violates the tensile criterion in the principal directions.
In theory, this angle can be found with:

$$\tan(2\theta_p) = \frac{2\tau_{xy}}{\sigma_{xx} - \sigma_{yy}} \tag{5.5.9}$$

Element CL9BE does not have an axial stress in the direction perpendicular to its axis as a result of the fibre beam formulation. Therefore equation $(5.5.9)$ cannot be used.
Because the model uses a fixed crack approach, the crack will be fixed in direction. The principal stresses can however change every analysis step. Therefore, giving a crack width on the basis of the principal direction will not be accurate because of the change in direction. Calculating a width in the uniaxial direction of an integration point will also not be accurate, because some integration points will be in compression, which will give a negative crack width, while the damage is tensile. However, this gives an idea of the increasing fictitious crack strain compared with the fictitious elastic strain.

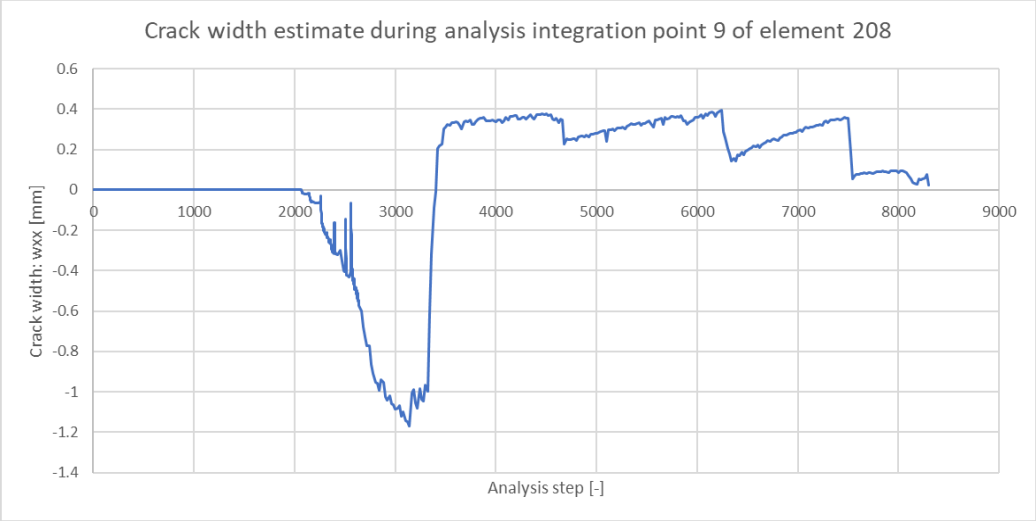

Figure 5.22; Crack width estimate during analysis element 208 integration point 9

Interesting to see is that the first small jump from negligibly small $w = -3.00 * 10^{-9}$ m to $w = -4.387 * 10^{-6}$ m happens in analysis step 2071. When the initial load factor is reduced, a crack rapidly starts to grow in integration point 9 of element 208.
The change from negative to positive is because of the crack closure reported earlier. This is however far after the vertical load cannot be applied fully.

The same story can be written for analysis steps 2146 till 2165. In step 2145 the first damage in integration point 10 of element 208 occurs. In analysis step 2146, the load reduces to 35.97%. This is recovered in step 2166, but meanwhile the element is damaged to $d = 0.8457$. Other integration points and elements are also damaged during these steps. Again, the graphs (Figure 5.23) show an elastic relation between analysis step 1 and 2144. Unloading after damage has occurred (step 2145) and reloading with an increasing strain for an almost constant stress.

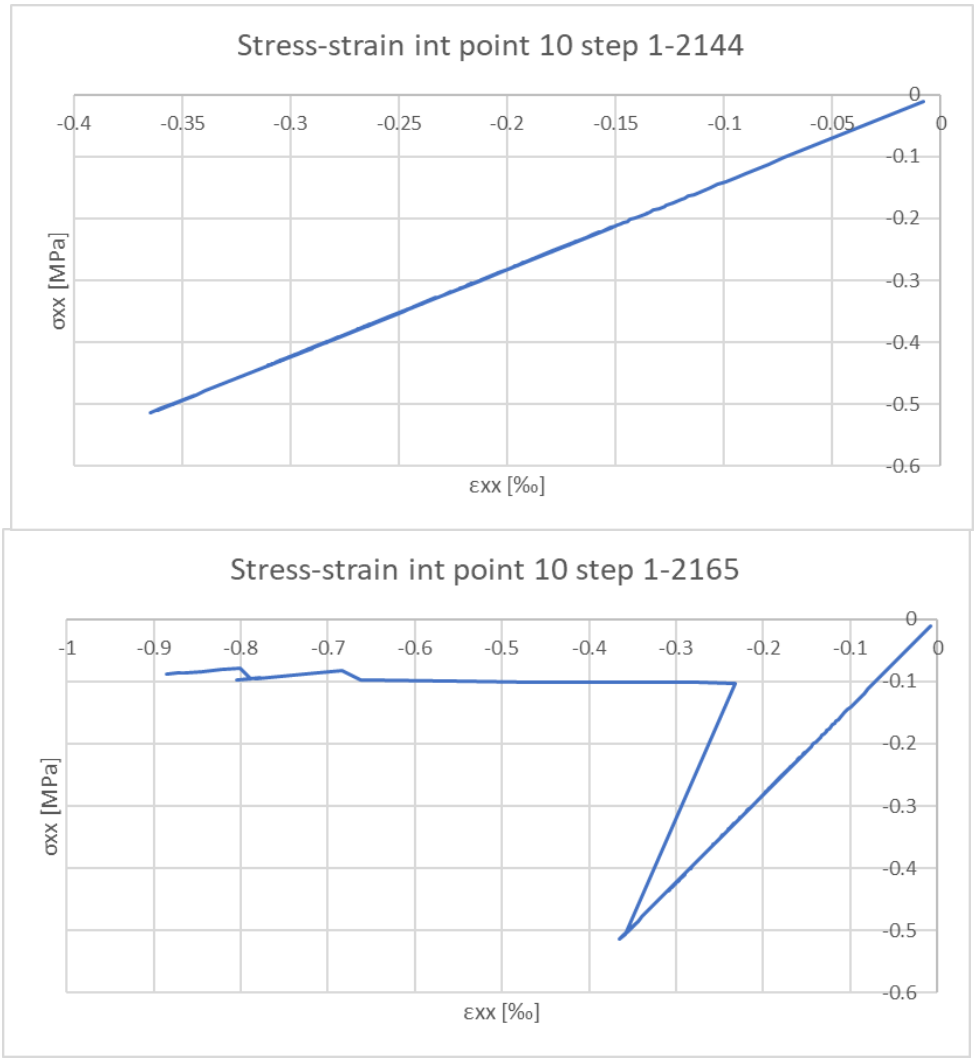

Figure 5.23; Stress-strain relation in element 208 integration point 10. Elastic in step 1-2144. Load reduction and reloading between step 2145 and 2165

The load reduction between step 2258 and 2404 is initiated with successive steps of damage in element 208 integration point 11. The reduction between analysis step 2506 and 2517 is initiated with damage in element 214 integration point 13.

Below (Figure 5.24) an overview is given for the damage cracks in integration points 9, 10 and 11 of element 208. For all three points, the crack opens after the initial load factor reduces and at the same time a damage increment occurs in the corresponding integration point. There appears to be a relation between the opening of a crack and the reduction of the initial load factor. Like explained before, the opening of a crack will result in a redistribution of the forces in the structure. In all cases, where an integration point is damaged and the non-proportional load is reduced, a crack opens in the step after the damage. The load is lower and as it cannot be fully applied on the cracked cross-section. The load redistributes in the next analysis step and the full vertical load can be applied again.
Important to notice is that cracks open when the initial load factor is reduced, but the opposite is not necessarily true. Crack openings are also observed while the initial load can be fully applied in the next analysis steps. As the vertical non-proportional load is also applied on the spandrels which bend, the opening of cracks here could also result in an initial load reduction because the force has to be redistributed in the spandrels.

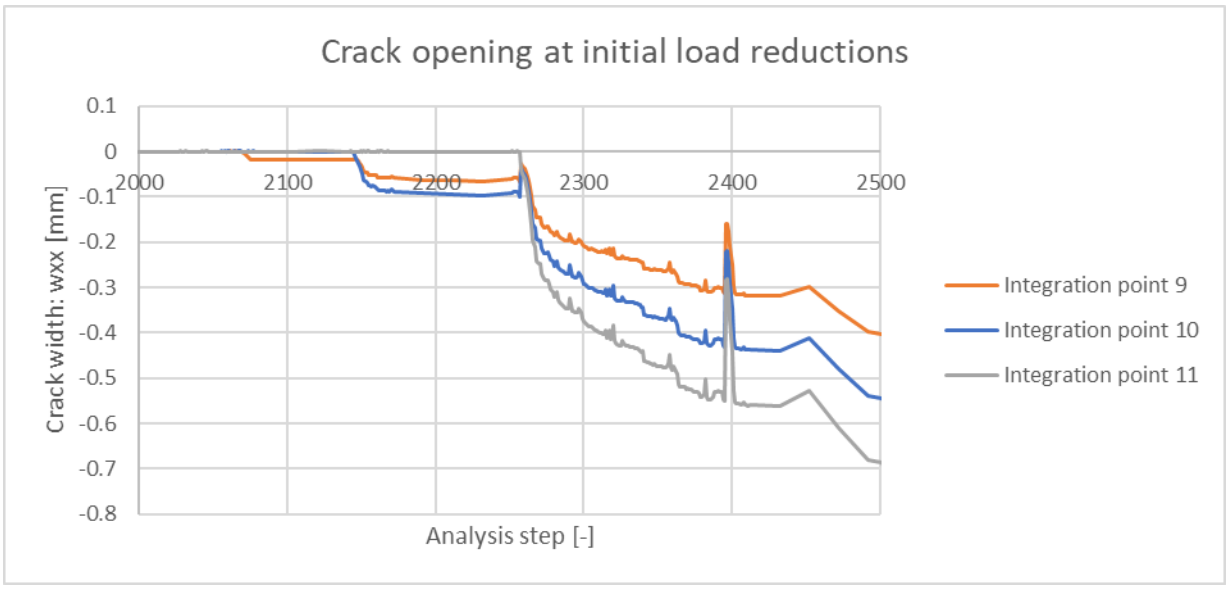

Figure 5.24; Crack opening for different integration points of element 208. Cracks open at the time the initial load factor reduces. Damage increases in the corresponding integration point

5.5.2 Crack closure problems

Stress changes from compression to tension and vice versa occur often during the analysis. Sometimes even early in the analysis, especially in the nodes which are close to the center of the cross-section. An example is given in the case of integration point 6 of element 208. In the beginning of the analysis, this integration point is loaded in compression speaking in terms of the axial component (σ_{xx}). In analysis step 433, this integration point is loaded in tension. This is not problematic because this integration point is undamaged in that step and therefore, the original tensile stiffness is used. In section 5.5.1.1 it was shown how the strain distribution changes during the analysis. For example, a sections damages at the tensile side and therefore the neutral point in terms of strain shifts more to the compressive side. Some points which were compressive first, will become tensile after this shift. Another example is in the case of a load reversal. For element 208, the strain distribution was reversed during the analysis because of large displacements. When as a result of this, stresses also change from compression to tension and vice versa a crack closure problem can occur. This will happen when the integration points which change from tension to compression or compression to tension were already damaged before this change. An example is given for integration point 9 of element 208. The relation between the strain ϵ_{xx} and the stress σ_{xx} is shown in Figure 5.25.

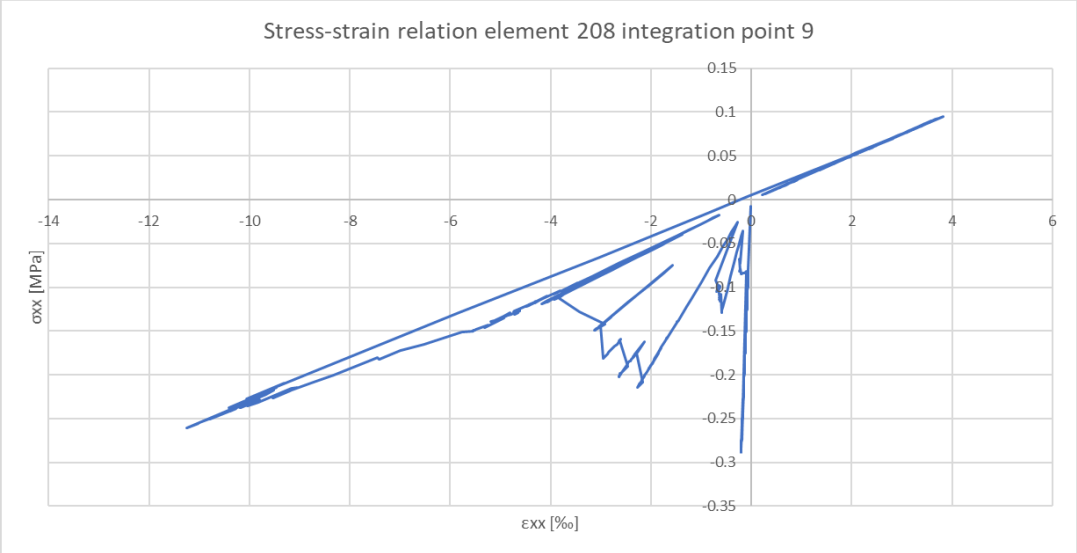

Figure 5.25; Stress-strain relation in element 208 integration point 9. Crack closure problem.

This integration point is loaded in compression in the first part of the analysis. The integration point is damaged by tensile stresses following the output file of the analysis. After analysis step 3382, the stress varies from compressive to tensile. However, as the stiffness is already reduced, the tensile stress is calculated with a reduced stiffness.

In reality this crack would close and therefore should be able to transfer compressive stresses. The tensile stiffness of the integration point should therefore be higher than the reduced version used here.

5.5.3 Integration point stress-strains during analysis

Not all integration points give the smooth stress-strain relations that where determined beforehand in the saw-tooth law. Previously shown was the relation in Figure 5.13 in which the saw-tooth law was very clear. Integration point 11 of element 208 shows this relation less clear. This is the because of big load reductions and sudden high damage propagation in this integration point.

First, a high peak value for the compressive stress in this integration point is reached. This point is at analysis step 2258 just before the step in which the initial load factor has a big reduction. In the next analysis steps, the damage in this integration point increases from no damage to 90.2% damage. The fact that this reduction takes place in 12 analysis steps, results in the large, almost instant change in stiffness for this integration point from relatively stiff to very weak. Later in the analysis a crack closure error occurs. Although this change in stiffness is very rapid and abrupt, the results in stress-strain behaviour are according to the theory implemented in the method. Therefore, this behaviour is expected. In the next example, this is less clear. Integration point 6 is examined, again by looking at the stress-strain behaviour during the analysis for the axial direction.

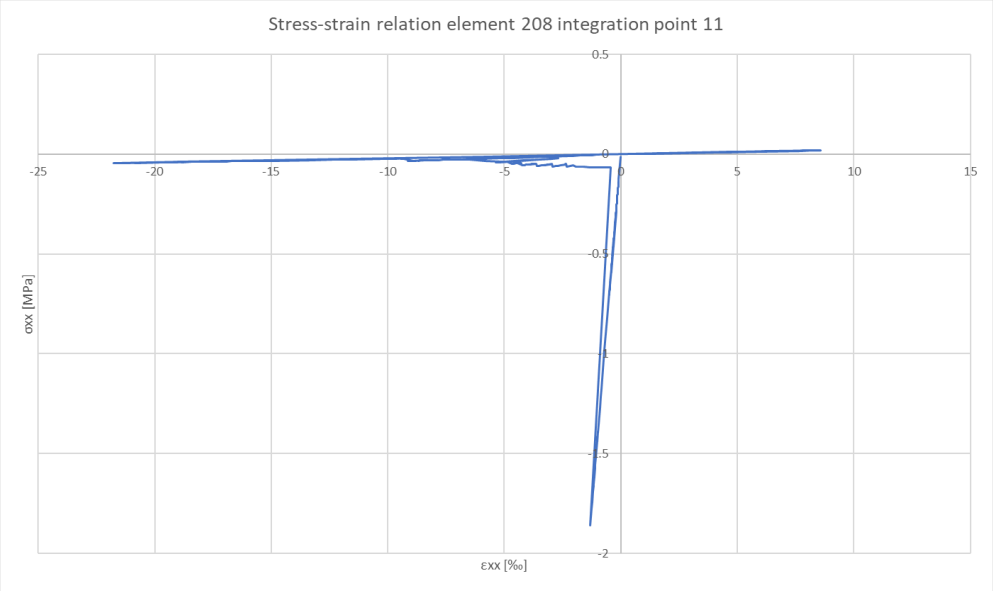

Figure 5.26; Stress-strain relation in element 208 integration point 11

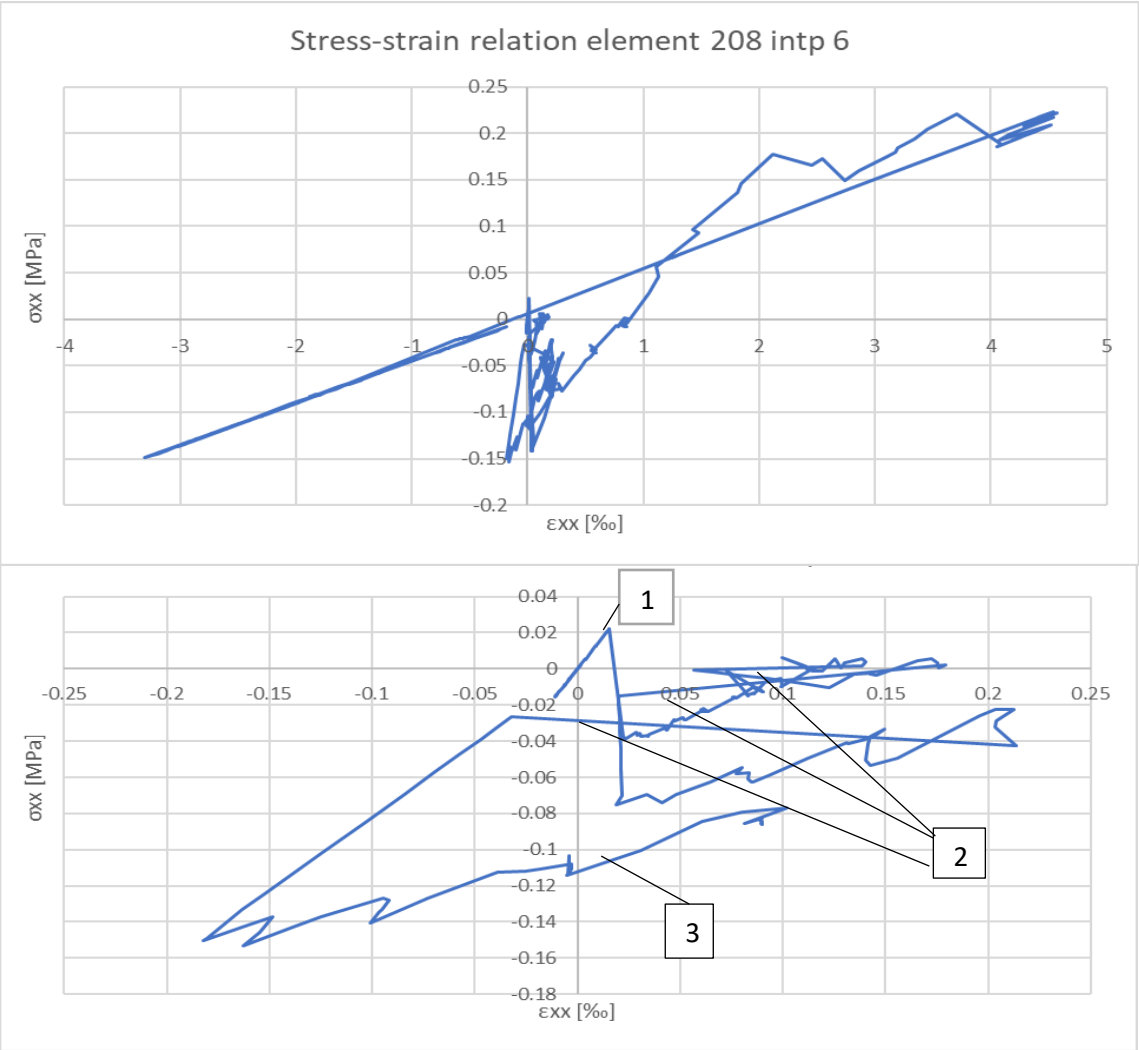

Figure 5.27; Stress-strain behaviour, element 208 integration point 6. Top figure shows whole analysis, bottom figure until analysis step 2312

The point 1 refers to the step where the first damage occurs. This damage results in a crack in this integration point. The principal tensile direction is parallel to the axial direction but has a different angle. This integration point is located at the center in the width of the element.
The parts indicated with 2 are the parts in which the initial load factor reduces. This is visible by the big decrease in loads. Because the principal direction in this element change often, these decreases are not secant to the origin. The part at point 3 is a load increase after a load reduction. Again, this is not secant to the origin. The principal stresses and strains also give a disturbed stress-strain relation.

5.6 Improvement techniques

Two approaches have been done at this point. The model with continuum elements and the model with beam elements. The differences between the results of those approaches will be summarized here based on several properties.

The first property is the ability to simulate the experimental load-displacement curve as accurate as possible. With respect to the maximum load, the continuum model was far more accurate than the beam model. The continuum element model had maximum load values between $120\ \mathrm{kN}$ and $160\ \mathrm{kN}$, the most stable analysis was found with a maximum displacement of $10\ \mathrm{mm}$ and a maximum load of $150\ \mathrm{kN}$. The experimental data had a peak load of $150\ \mathrm{kN}$, but the largest part of the curve was around $120\ \mathrm{kN}$. On the other hand, the experimental curve was made based on the outer bound of the cyclic loading results, while the simulation is based on a push over analysis. Therefore, it should be expected that the maximum load of the push over analysis is somewhat higher as in general buildings fail with a lower maximum load in a cyclic experiment compared with a pushover load.

The beam element model is at this stage not able to give an accurate description of the load-displacement behaviour of the structure. The maximum load achieved while the initial non-proportional load is applied is at a displacement of $5\ \mathrm{mm}$. In this stage, the structure is still in the elastic-plastic region of the load displacement diagram. At this stage the right spandrel on the first-floor damages rapidly which results in a big reduction of the initial load. After this, the structure is only able to carry 80% of the initial load. Peak values of the horizontal load are higher compared with the continuum model. The beam model reaches peak loads of $180\ \mathrm{kN}$ or even $200\ \mathrm{kN}$.

With respect to the robustness of the method, the number of times the initial load factor was not reached is taken into account. Comparing this, the standard continuum model showed more reductions than the beam model for most analyses. This was especially the case when the mesh became smaller. The model was however able to redistribute the forces and recover the full initial load. The beam model had a different pattern. It had a long part in which the full initial load was applied until a critical damage point was reached. After this point the initial load was only recovered a few times before the structure finally failed. On the other hand, as the beam model did not reach the region of large displacements, it could be that the model would suffer from load reductions in that stage as well. As most reduction in the continuum model happened in the elastoplastic region, which is just reached in the beam model.

As the beam model was still in the elastic-plastic part at this stage and not in the plastic part like in the continuum model simulation, the continuum model is able to keep the full initial load further in the analysis, although with more reductions for finer meshes. With the increased parameters and mesh type for the continuum model, the analysis became very stable and the load was maintained with just some small reductions until a deformation of $10\ \mathrm{mm}$.

Another thing that happened often in the continuum models and was almost not present in the beam models was unloading which was not secant to the origin with the old version of Diana FEA. For the old version, negative displacements were found for the continuum model, which disturbed the load-displacements relation. This is greatly reduced in the analyses done with the new version to a level where it only happens a few times, without much influence in the global result.

In terms of failure mode, the continuum model was more accurate. The most important failure mode in reality was of course the shear failure in the piers. The continuum model was able to describe this behaviour rather precise for the middle and right pier. Shear interfaces cannot yet be implemented in a sequentially linear analysis and therefore, the beam elements where only able to fail in bending. As expected, this led to a higher maximum load.
The failure mode in the beam element case was tensile failure in the left bottom pier, combined with bending failure in the right spandrel of the first floor followed by bending failure of the right spandrel of the second floor. From Figure 5.18 and Figure 5.19 it was visible that the middle and right pier do not damage that much at the support.
In the next paragraph, several improvements are suggested to increase the precision of the model.

5.6.1 Only tensile failure

As masonry is relatively weak in tension compared to compression, it can be assumed that the damage will mostly occur because of reaching the tensile strength of the material. Expected is that only in the case of large load redistribution, the structure will start to fail in compression. As this behaviour is expected post-peak, an assumption could be made by fictitiously increasing the compressive strength of the material, demanding the structure to fail in tension. With this assumption, crack-closure errors which are present in SLA are not totally evaded, because although no compressive failure is allowed, the modulus of elasticity is still reduced for the compressive behaviour. The compressive parabolic constitutive relation is changed in a linear elastic constitutive relation. No compressive strength is given and therefore the structure cannot fail in compression and will be infinitely linear elastic. The third principal stress is shown for the structure in the contour plot below for analysis step 2441. The step with a maximum lateral load. This contour plot shows that the maximum compressive strength is only violated in the infinitely rigid corners. Therefore, the structure is not likely to fail in compression, which supports the assumption to simplify the constitutive model with a linear tensile failure relation and an infinite linear elastic compressive relation.

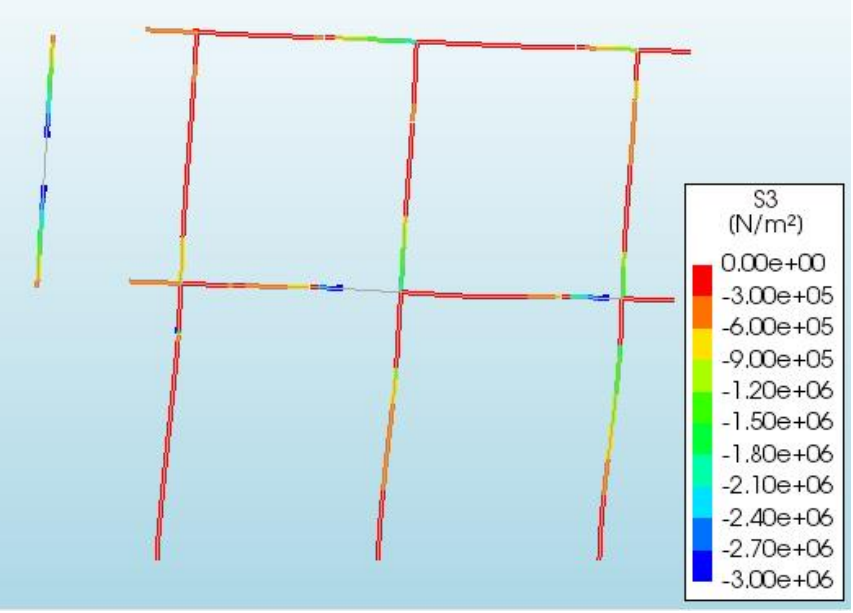

Figure 5.28; Third principal stress with at the analysis step with maximum lateral load

When the analysis is repeated with this simplified constitutive law. It is possible for the program to retain the full initial load after the first peak (Figure 5.30).

The first part of the analysis until the peak load is identical to the default model, after the peak load the load is reduced as the structure is not able to carry the full load. In this part, roughly analysis step 2500 until 6700, the same damage occurs as in the default model, i.e. major damage in the right first spandrel followed by bending in the right second-floor spandrel. There is a small difference as the severe deformations in the right first floor spandrel in the default model were developing both on the left and right side (element 208 and element 214) while in the tensile failure model, the deformations are on the right side of the spandrel in element 214 only (Figure 5.31).

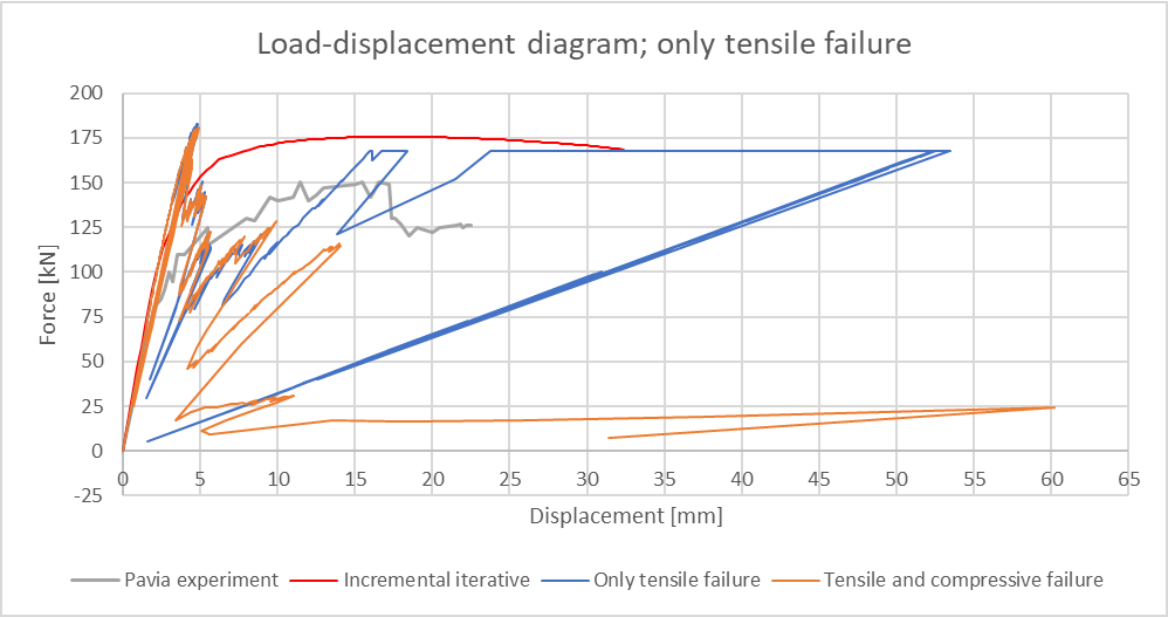

Figure 5.29; Load-displacement diagram. Pavia facade with linear elastic compression and the default model

After these damages and deformations have occurred, the structure is able to retain the full vertical load. This happens at a deformation $d = 15.95\ \text{mm}$. At this stage, the deformations are increasing while the lateral load stays constant; $F = 167.675\ \text{kN}$. The failure pattern stays the same until a deformation $d = 52.29\ \text{mm}$. At this stage, the load again reduces and the left piers slowly start to bend as the left first floor corner starts to rotate counterclockwise until the left bottom pier breaks.

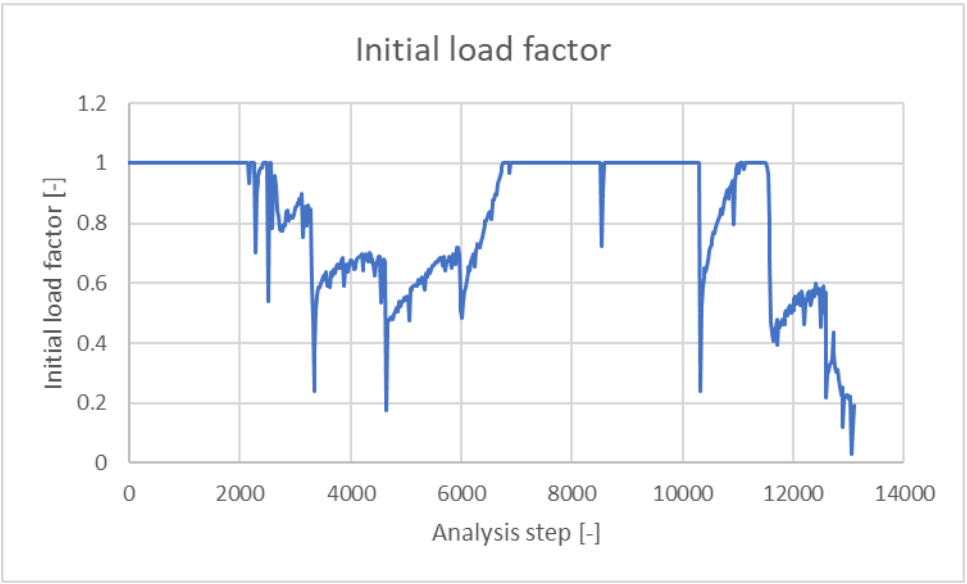

Figure 5.30; Initial load factor for infinite linear elastic compression

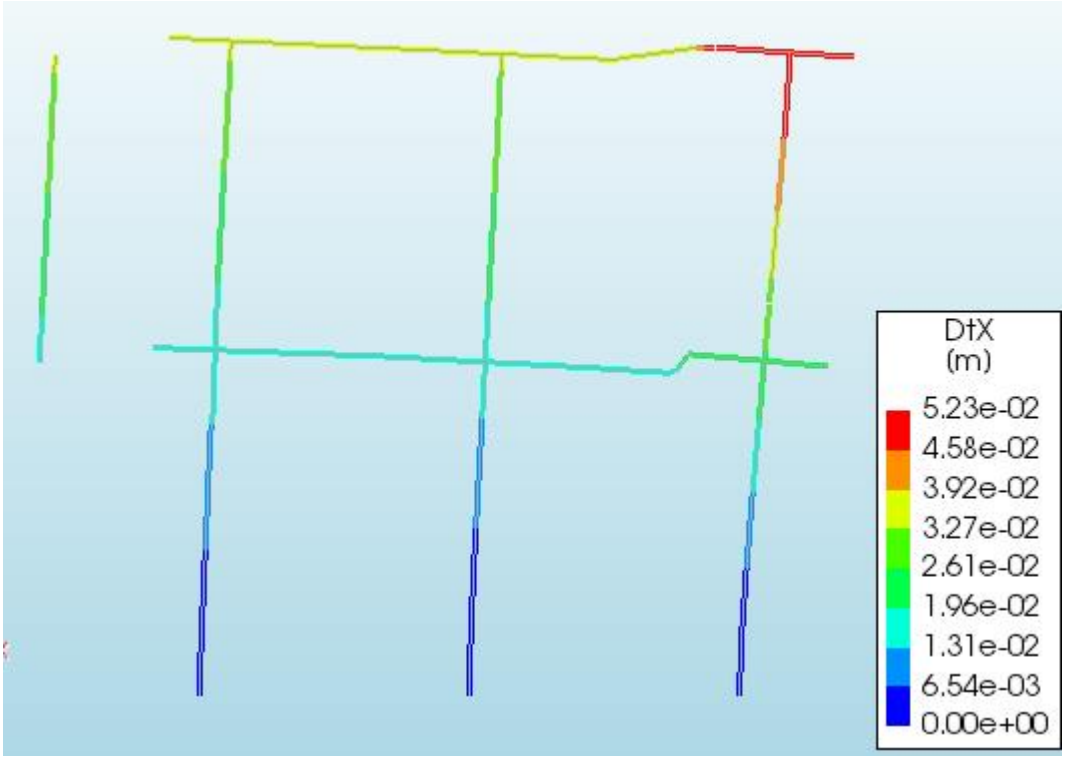

Figure 5.31; Stable analysis step 11501. Large displacements while the spandrels are already severely damaged

The simplification of the constitutive model has not resulted in a more stable analysis as the initial load factor still reduced after the peak load was reached. This part of the analysis was very similar to the default model. Changes appeared after the right first-floor spandrel and the right second floor spandrel were severely deformed. In the default analysis, the structure would fail entirely while in this case, the structure was able to recover to the full non-proportional load from which the deformations could increase. From the peak load, the stresses concentrate in the right first floor spandrel. When the spandrel deforms severely, this section unloads and the stress concentration is shifted to left edge of the right second floor spandrel. This part is bending until the stress concentration shifts to the right edge of this spandrel and the middle pier first floor pier. Every time a part fails, the stresses shift to another part, which takes over the load and the damaged part is able to unload. The question is whether this is realistic or not as the large deformations in the beam model are prevented by the floors and the height of the spandrels. Therefore, this behaviour is not likely. Also, by looking back at the previous observations. By making the material infinitely strong in compression, the vertical load is easier to bear as the piers have infinite compression strength. Therefore, the failure of the piers by vertical compressive strengths is evaded. The reason that no violation of the compressive strength was noticed in Figure 5.28 does not mean that this does not influence the analysis. First the vertical non-proportional load is applied, when this is not possible, most likely because of a violation of the compressive criterion in the piers, the full previous analysis step is scaled and failure can occur in a different part of the structure.

5.6.2 Proportional with prestress

This is an approach which tries to reduce the difficulty of the non-proportional approach by making some assumptions.

The non-proportional load is skipped and a prestress, which would be the resulting stresses of the non-proportional load is applied to the piers. This prestress is applied by increasing the tensile strength of the section. This approach is developed by Belletti et al. [23]. First, an overview is given of the relative vertical reaction force in the supports during the analysis (Figure 5.32). In analysis step 1, only the vertical load is applied. The vertical force in the right and left pier is equal and the vertical reaction force in the middle pier is almost twice the value of the other piers. The relative vertical reaction force in the different piers changes during the analysis. As the lateral load increases, the compression in the left pier changes in tension. This results in an increase of the compressive force in the right pier as the total sum of the forces should remain the constant.

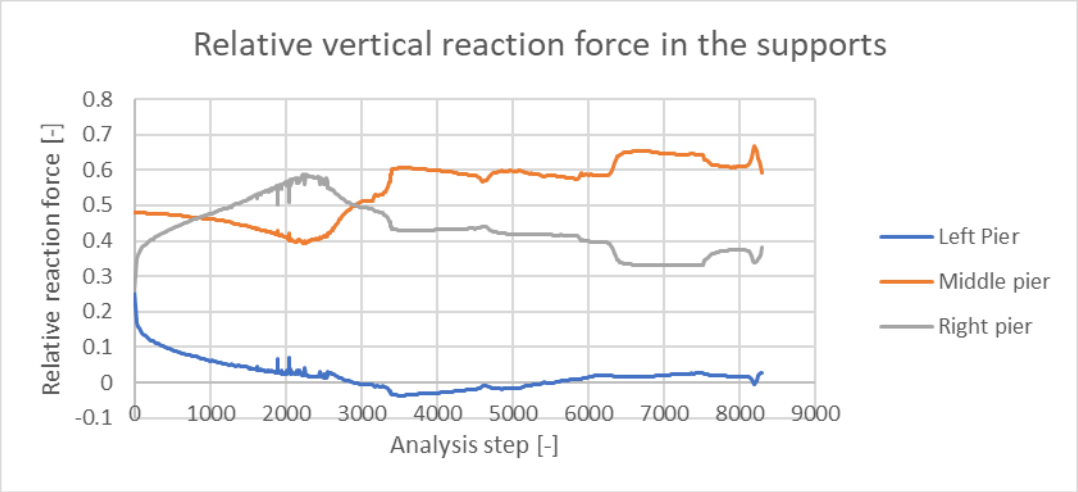

Figure 5.32; Vertical reaction force in the piers during the analysis

In a first attempt, the forces in the piers after the first load are used to calculate the corresponding vertical stresses in the piers by dividing the vertical forces by the cross-section, shown in Table 5.5.

Table 5.5; Stress in the piers, analysis step 1

1st analysis step:	R_v [N]	A [m^2]	σ_{yy} [N/m^2]
Pier 1	-100744.7	0.2875	-350416.483
Pier 2	-185653.7	0.4625	-401413.315
Pier 3	-100744.7	0.2875	-350416.483

These stresses are added to the tensile capacity of the sections. For example, the end of a pier, first had a tensile strength $f_t = 0.04$ MPa. This tensile strength is increased with the compressive stress as a result of the vertical load of the structure. The strength of pier 1 becomes:
$f_{t,pre} = 0.390$ MPa. Note that the different piers now have different tensile strengths as the prestress is different for every pier.

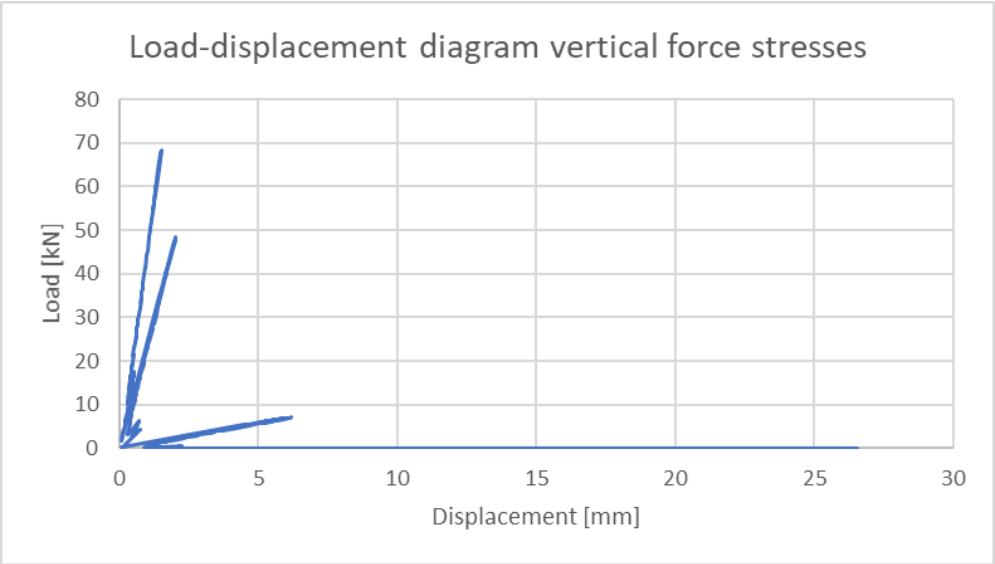

Figure 5.33; Load-displacement diagram. Vertical reaction force stresses of the first analysis step are used as prestress

Visible in Figure 5.33 are three peaks. These peaks correspond with the failure in the three piers. In the first peak, the left pier damages and fails. Next, the middle pier takes the most stress and fails followed by the third peak. The results are poor and this can be explained by the fact that the compressive stress from the initial load is assumed constant during the full analysis, while Figure 5.32 clearly shows the change in the reaction forces. In this approach, when the left pier is damaged, it is still assumed that a prestress force of the initial load is applied there, while in reality this compressive force is redistributed to the other piers increasing their strength. This effect is neglected in this approach [1].

An improvement is suggested by taking an average value of the reaction force during the analysis and transfer this average force into a stress which is used as a prestress for the piers. The result is shown in Figure 5.34.

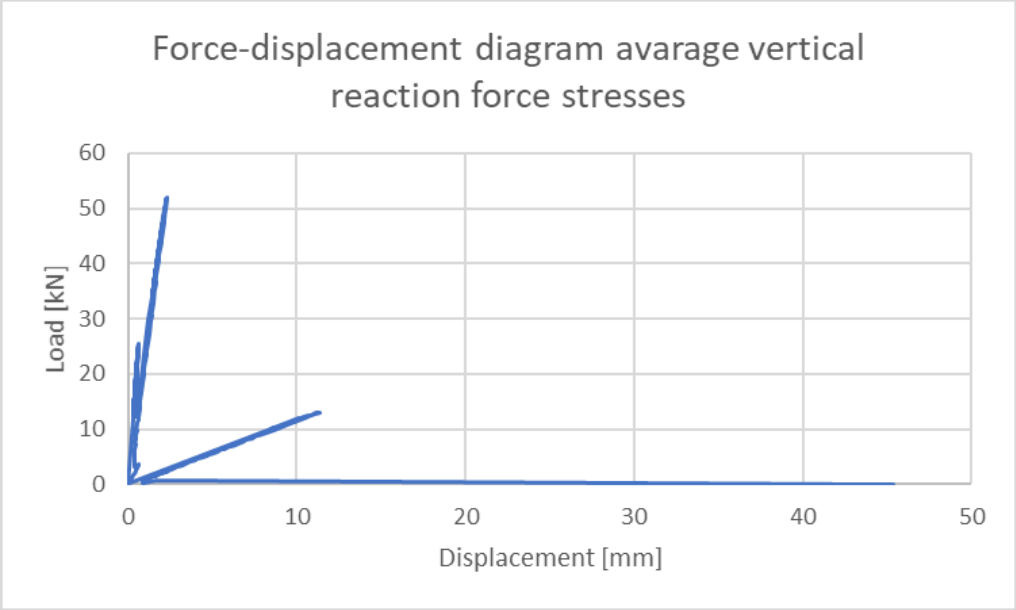

Figure 5.34; Force-displacement diagram. Average vertical reaction force stresses are used as prestress

Again, three peaks are visible. This time the first peak is smaller than before as the average vertical reaction force in the left pier is very small. The force in that pier is sometimes even tensile. This results in a lower capacity of this pier. The capacity of the second pier is somewhat higher and the capacity of the third pier has increased much. Both are because of a higher vertical reaction force in these piers. Shown in Figure 5.35 is the behaviour of the first pier. Typical SLA behaviour is observed for this pier.

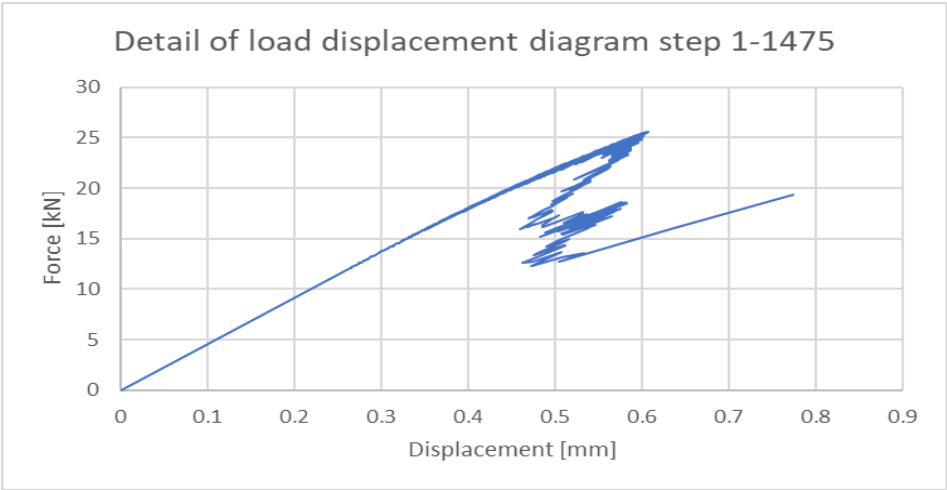

Figure 5.35; Overview of step 1-1475 of the load-displacement diagram using the average stresses of the vertical reaction forces. Typical SLA behaviour is visible.

Like in the previous case, the structure does not fail as a system, but more as three separate piers. In conclusion this method evades the problem of the reduction of the initial load factor but is not an applicable solution to the problem as the structure cannot be seen as a system, but more as three separate piers, which is not a correct representation. The assumption included in this method that the compressive stresses in the piers as a result of the vertical load stay approximately equal during the analysis is poor and not valid in this case as the loads change during the analysis. This was shown in Figure 5.32.

5.6.3 Increasing the fracture energy

The next variation will be an increase in crack energy. The standard value for the crack energy was $G_{f-tu}^{I} = 20\ \mathrm{N/m}$ for the parts with shear failure, $G_{f-jt}^{I} = 5\ \mathrm{N/m}$ for the parts in flexural failiure and $G_{f-m} = 10000\ \mathrm{N/m}$ for the compressive fracture energy. These values will be increased with the following factors: 10, 100, 1000 and 10^6. Below are the results of the different analyses.

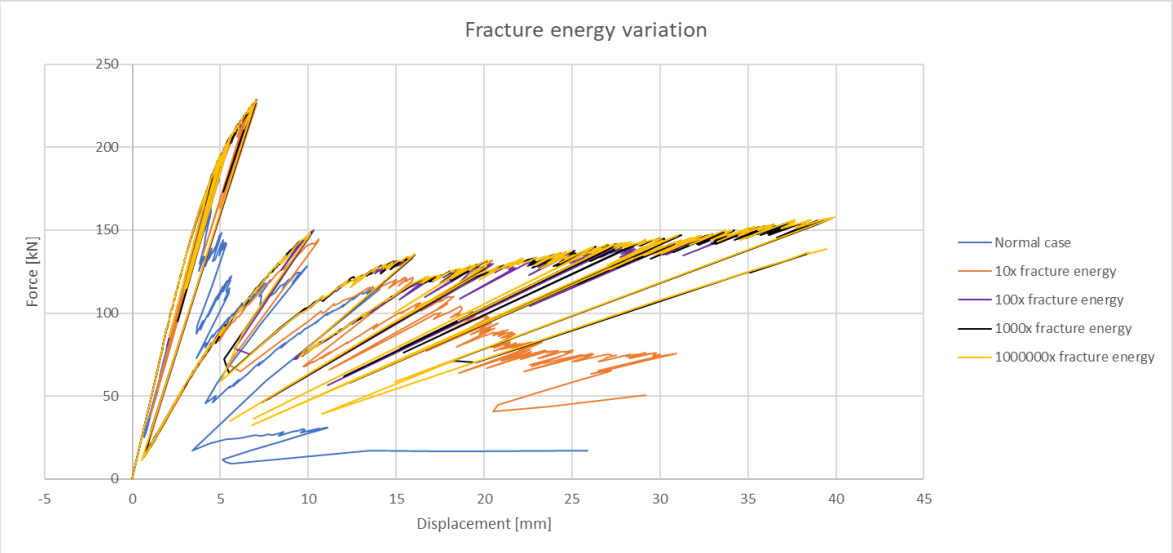

Figure 5.36; Variation in crack energy for the three-zoned beam model

As expected from theory, the peak load is higher when the fracture energy increases. The maximum peak value is already reached for a multiplication factor of 10, the peak load does not increase for higher multiplication factors. After the peak load, all analyses showed a large reduction of the load as a result of the initial load factor reduction. The differences in fracture energy appeared after the attempt to increase the load back to an initial load factor of 1. The higher the fracture energy, a larger part of the load is retained. With a higher fracture energy, the structure can dissipate more energy. However, a limit is reached for a fracture energy multiplication factor of 100. When a higher multiplication factor is chosen, the load does not increase.

In conclusion, the increase in fracture energy resulted in a higher peak load but was not useful in maintaining an initial load factor of 1 after the peak load. Differences were visible in post-peak behaviour as a higher part of the load was retained when the fracture energy was higher. However, a limit was reached for a multiplication factor of 100.

5.6.4 Increasing the number of saw teeth

The next possibility to increase the accuracy of the solution is increasing the number of saw teeth. To accomplish this, the p-factor (2.3.3) is reduced from the original value; $p = 0.1$. The two new values are $p = 0.05$ and $p = 0.025$. The algorithm used to make the saw-tooth law has the result that the reductions will be large in the early stages and small at the end. In the default case with a p-factor of 0.1, the first damage increment reduces the stiffness with 18%, where the last while the last step reduces the stiffness with 0.02%. The standard p-factor of 0.1 has 31 saw-teeth.
An increased number of saw-teeth can make the calculation more precise as the damage propagates in smaller steps. On the other hand, the calculation time will increase, because more steps are needed for the same damage to occur.

The result is shown in Figure 5.37. All three cases show a similar behaviour, after the elastic part the elastoplastic part starts with already many initial load factor reductions. The load is not able to recover fully and the analysis continues with increasing and decreasing initial load factors which makes the load-displacement curve look irregular. From literature [1] it is known that 30 saw-teeth is in general accurate enough. Results of this chapter confirm this as the result is not improving.

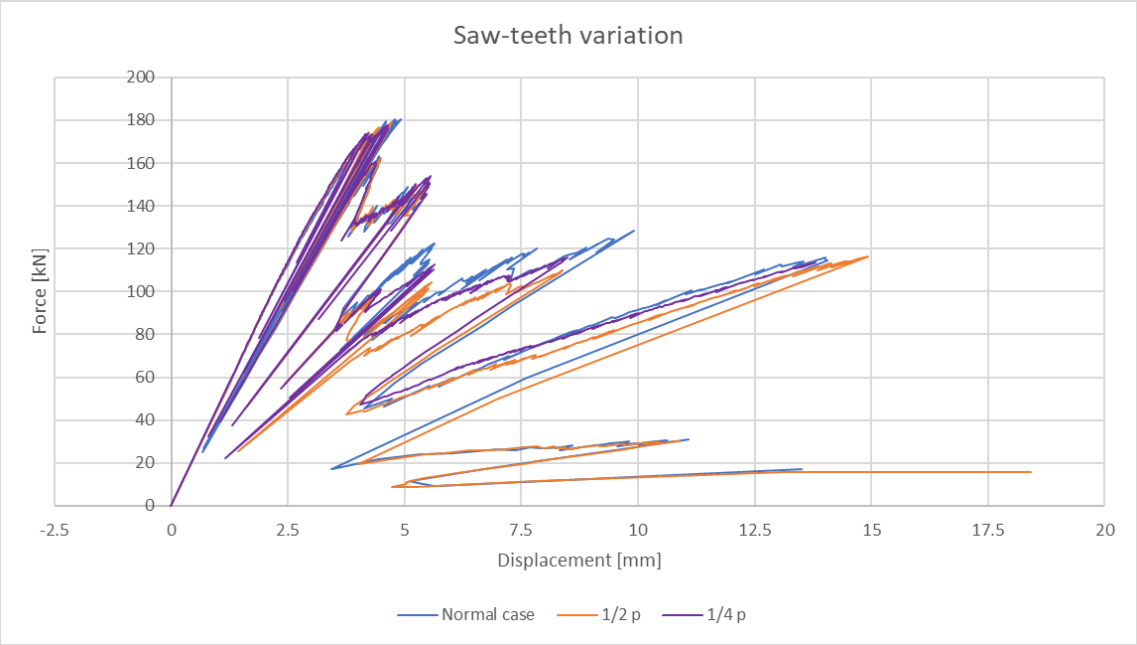

Figure 5.37; Variation in the number of saw-teeth for the three-zoned beam model

5.7 Bending moment distribution in beam model

5.7.1 Horizontal and vertical reaction force

Earlier in 5.6.2, an overview was given of the horizontal reaction forces during the analysis. These forces were shown relative to the total vertical force as there were analysis steps in which the total load reduction factor was reduced. In this part it became clear that the left pier initially took a part of the vertical force. This part decreased rapidly as a result of the damage in this pier. Because of this, the other piers contributed more. It would be interesting to look at the distribution of the horizontal reaction force as well. The bending moments between the piers and the bending moments internally could provide interesting information on how the structure resists the load.

Below (Figure 5.38), an overview is given of the relative vertical reaction force in the three piers and the horizontal reaction force. The relative reaction force is calculated by dividing the reaction force in a pier by the sum of the reaction forces of all three piers.

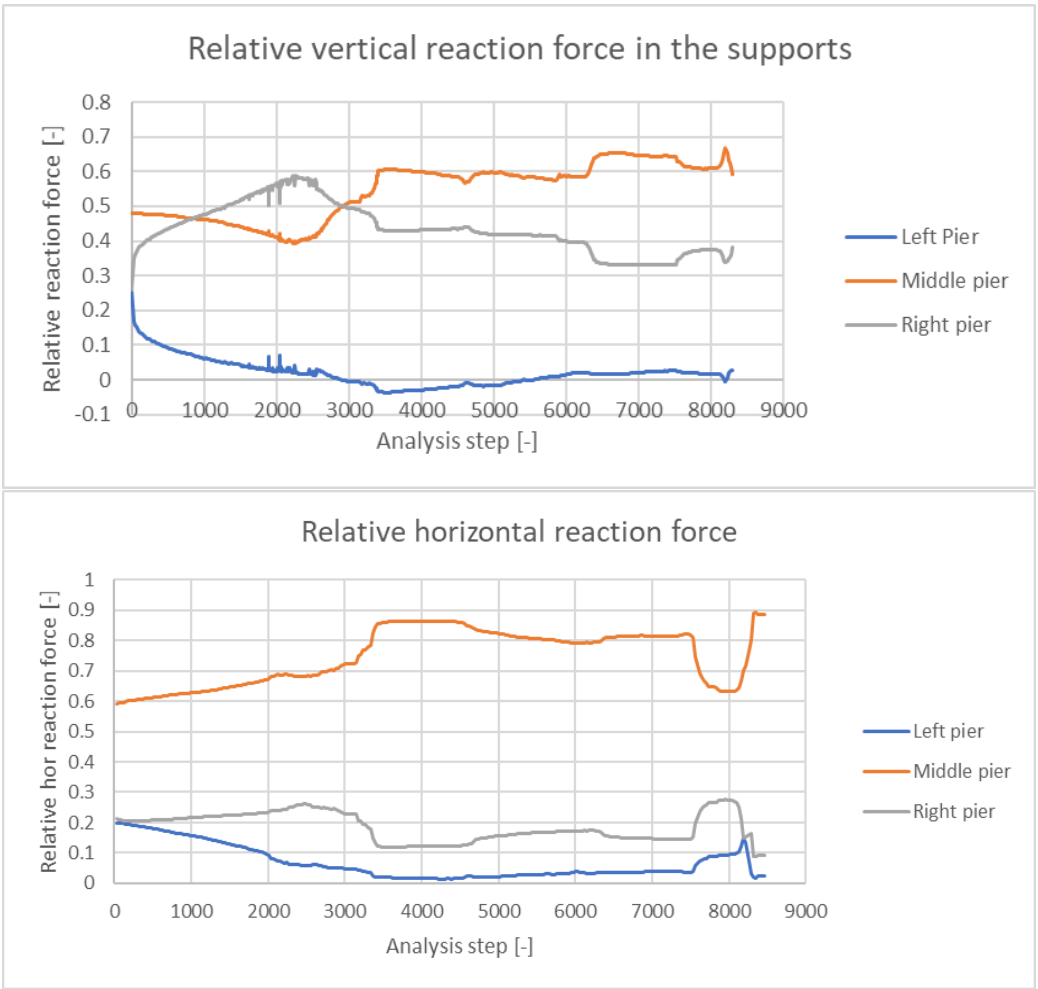

Figure 5.38; Relative vertical (top) and horizontal (bottom) reaction force in the supports

Like in the case of the vertical load, also for the horizontal load, the contribution of the left pier reduces during the analysis. This because severe damage propagates fast in this pier from the start of the analysis. Where for the vertical load, the right pier took most from the left pier. For the horizontal load, the middle and right pier both take a part. Around step 3200, an increase is visible for the middle pier, while a sudden decrease is visible for the right pier. In these steps, the right spandrel deforms severely.

The middle pier cannot transfer forces to the right pier through the first-floor right spandrel and therefore the force in the support increases for the middle pier. From the same line of reasoning it can be concluded that the force decreases in the right pier support.

5.7.2 Bending moments in the supports

The lateral load is applied at both floors. Therefore, it is expected that a counterclockwise moment will occur in all three supports. Because the middle pier is wider, the support of this pier will most likely have the largest bending moment.

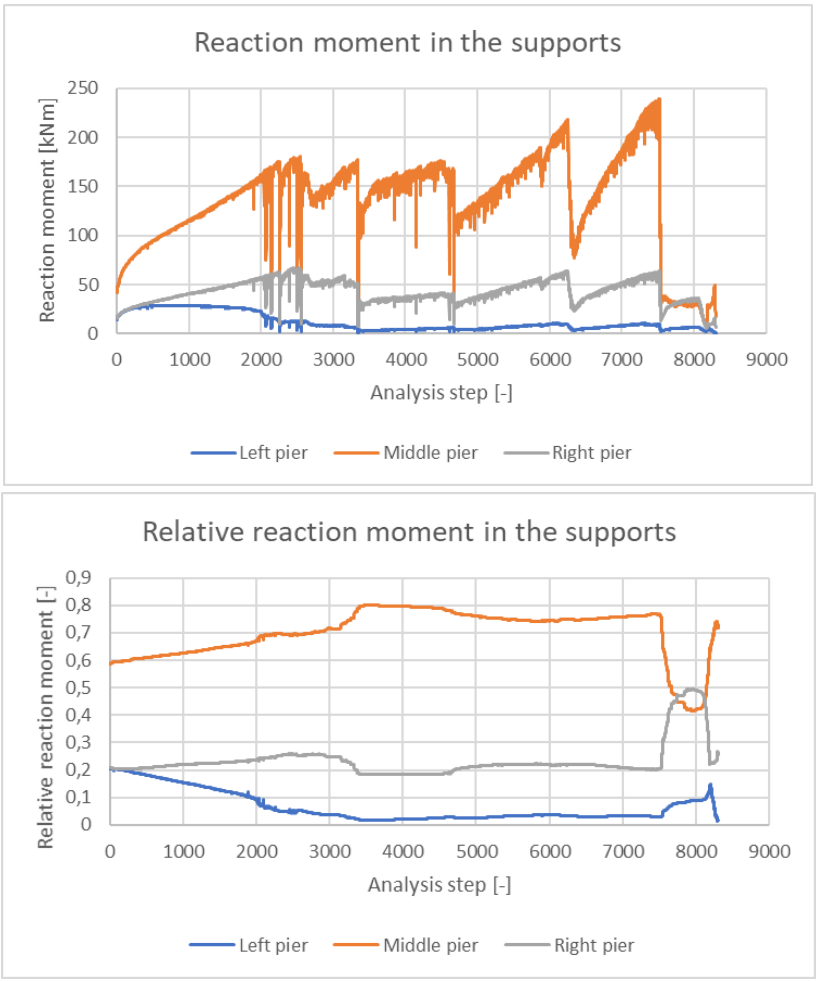

Figure 5.39; Reaction moment of the three supports of the piers (up). Relative contribution of each pier (down)

Figure 5.39 indeed shows that this is correct. The middle pier takes 60% of the total bending moment and this increases during the analysis. The contribution of the left pier again decreases because of the damage that propagates in this pier. Before the structure fails, the maximum bending moment of the middle pier is around 178 kNm.

5.7.3 Internal normal forces and shear forces

Below, the normal forces and shear forces in the structure are shown at analysis step 2551. This analysis step has the largest force on the structure while applying the full vertical non-proportional load. These results can be compared with the result of Nobel for a displacement of 5 mm. Figure 5.41 shows the default 3ZEF model. Figure 5.42 and Figure 5.43 are the results of the only tensile failure model of section 5.6.1. The results at analysis step 2551 are the same for those models. This was expected as the load-displacement curve was similar until this point (Figure 5.29). Important to see in these graphs are the shear forces in the piers. For the middle pier for example, a quick hand calculation shows that the shear strength should be exceeded if shear failure was possible.

The shear force in the middle pier $Q_y = -123$ kN. The cross-sectional area of this pier is $1.820 * 0.25 = 0.455$ m^2. This gives a shear force $\tau = \frac{123*10^3}{0.455*10^6} = 0.270$ MPa. The shear strength of this pier $f_{tu} = 0.14$ MPa. For the right pier, the shear strength would also be exceeded.

The right pier has a shear force of $Q_y = -60.1$ kN and a cross-sectional area $A = 1.15 * 0.25 = 0.2875$ m^2. The shear force will be: $\tau = \frac{60.1*10^3}{0.2875*10^6} = 0.209$ MPa > 0.14 MPa.

In the right first-floor spandrel: $Q_y = 81.3$ kN. The cross-sectional area $A = 0.94 * 0.25 = 0.235$ m^2. The shear force: $\tau = \frac{81.3*10^3}{0.235*10^6} = 0.235$ MPa > 0.14 MPa.

Comparing the shear forces with the model of Nobel in Figure 5.40, it appears the forces are very similar. The shear forces in the spandrels are in both models around 80 kN. Only the middle and right pier of the bottom row are somewhat different as Nobel has a shear force of 105 kN in the middle pier and 52.2 kN in the right pier and this model has a shear force of 123 kN in the middle pier and 60.1 kN in the right pier. The differences are small especially considering that in the FFM of Nobel, the flexural elements are not used and only the shear strength. The 3ZEF uses the strength of the bed joint tensile strength at the ends of the piers and spandrels.

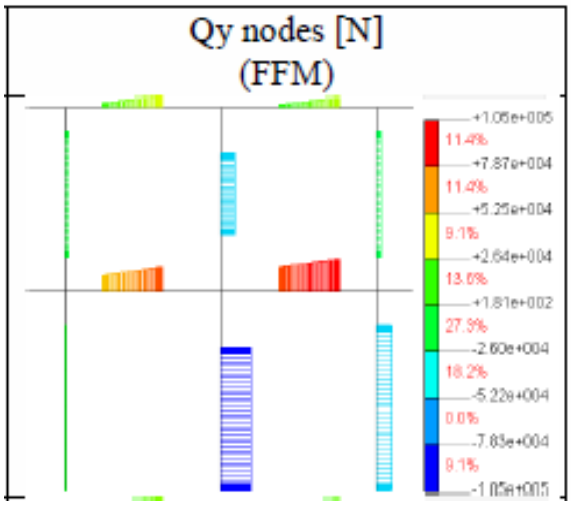

Figure 5.40; Shear forces in the FFM of Nobel, $d = 5.76$ mm. [2]

The reduction in strength of the right pier of the bottom row in the analysis with only tensile failure follows from Figure 5.43, these forces are transferred to the middle pier. The right first floor spandrel cannot transfer the forces anymore.

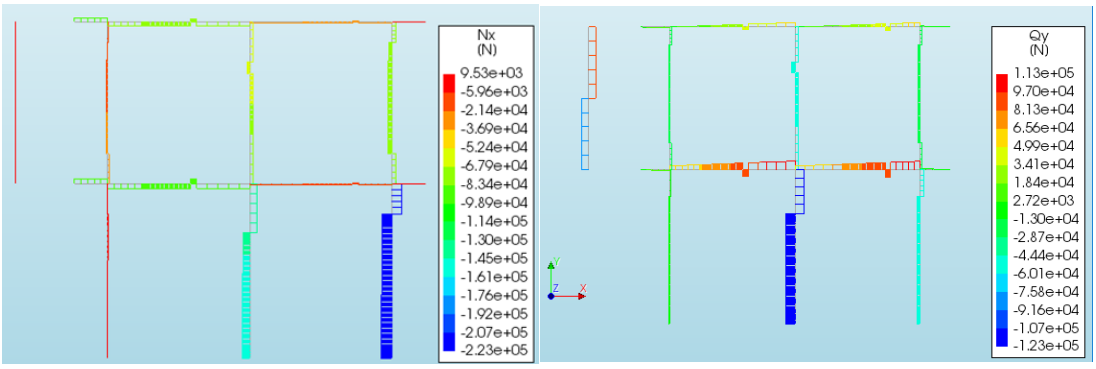

Figure 5.41; 3ZEF, analysis step 2551. Normal and shear forces

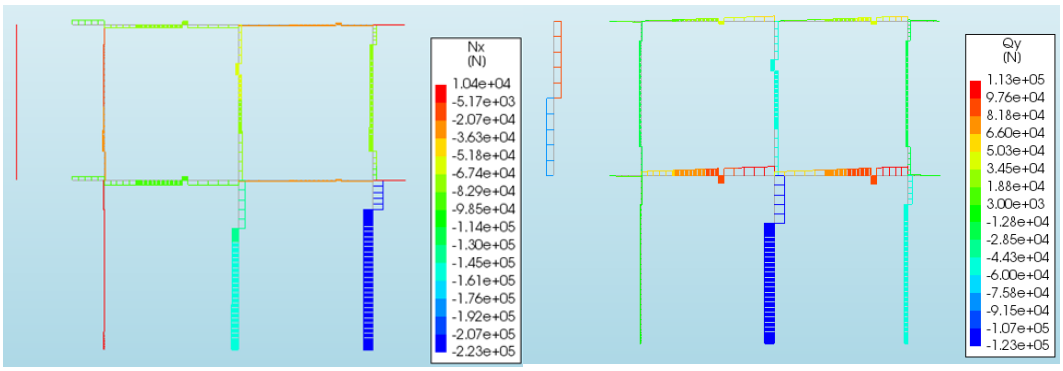

Figure 5.42; Linear compressive analysis, analysis step 2551. Normal and shear forces

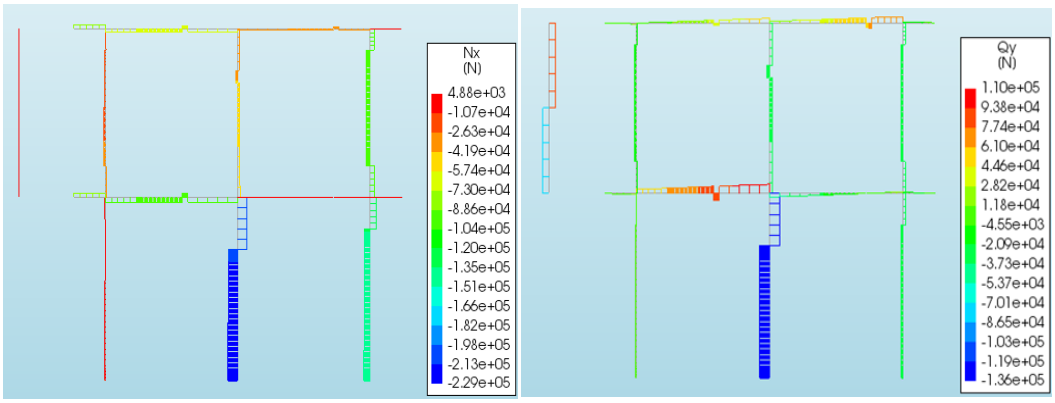

Figure 5.43; Linear compressive analysis, analysis step 6801. Normal and shear forces

5.7.4 Internal bending moments

A first attempt to extract the internal bending moments from the analysis was done by adding a command in the analysis file to register them. This failed however for every non-supported node, because this function is not yet implemented in the program. All bending moments except the three of the supports were of the order 10^{-10} Nm, which is practically zero.
This problem is solved by making an approximation of the internal bending moment from the axial stress in the element. A MATLAB program is developed, the full code is shown in Appendix B. A summary will be presented here.

Every beam element has two rows of eleven integration points over its width. The width of the element is $w_l = w_r = 1.15$ m for the left and right pier and $w_m = 1.82$ m for the middle pier.
For every analysis step, the stress distribution over the width of the element can be determined. By taking the axial stresses σ_{yy} in the integration points as output from the analysis and distribute them over the width of the element. The width of the element is divided in ten parts with eleven nodes.

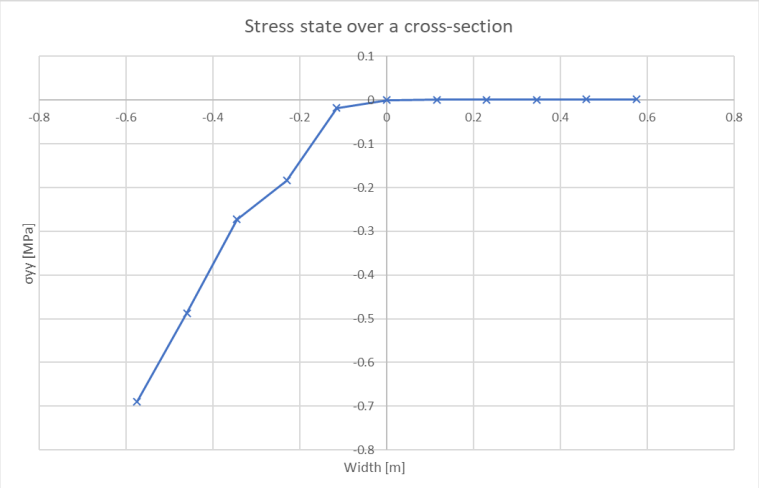

Figure 5.44; Stress state σ_{yy} over the cross-section of an element. Stresses in the integration points are used

In chapter 2.2.1 the Timoshenko beam theory was derived. In this chapter, the bending moment in the cross-section was derived from the axial stress-distribution [11].
Equation (2.2.7) was derived which holds this relation. This relation is repeated below for the axis of the element in the y-direction.
The bending moment in a cross-section can be determined by taking the axial stress in a cross-section, multiplying this with the distance from the central line and integrating it over the area of the cross-section.

$$M = \int dM = \int \sigma_{yy} y dA \tag{5.7.1}$$

There is however no closed form analytical expression for the distribution of the axial stresses as the data comes from a numerical finite element analysis which approximates the results. Therefore, a numerical approximation is needed. The trapezoidal rule is used to approximate the integral of (5.7.1) in a numerical approach using a Riemann sum.

Figure 5.45 shows this approach in practice. The stresses over the width of the cross-section are divided in small trapezoids between the estimated integration point locations. They are assumed to be spread with a constant interval over the width of the cross-section. Because the distance y in (5.7.1) is independent of the area of the cross-section in this approximation, this can be excluded from the integral. The area of every trapezoid can be calculated by applying the general formula:

$$\int \sigma_{yy} dA = \frac{1}{2} h(b_1 + b_2) t \tag{5.7.2}$$

in which h is the height of the trapezoid, i.e. the distance between the two parallel sides, t is the thickness in the other direction and b_1 and b_2 are the lengths of the parallel sides.
In this example, the distance h between the parallel sides is the length of the interval over the width. This is the estimated distance between the integration points. The width of the cross-section of the left pier $w_l = 1.15$ m. Divided over eleven nodes, the length of the interval is $h = \frac{w_l}{10} = 0.115$ m.
The lengths b_1 and b_2 are the stresses in the integration points.

Figure 5.45; Trapezoidal rule to numerically integrate the axial stress

The distance y in $(5.7.1)$ is the distance between the center of gravity of the trapezoid and the center of the cross-section. The center of gravity of the trapezoid is approximated as if it was a rectangle, i.e. halfway the interval $(\frac{1}{2}h)$. This approximation is better the more the trapezoids are shaped like a rectangular. If the trapezoid become triangular like in the interval $[-0.23; -0.115]$ the center of gravity is more at a distance $\frac{1}{3}h$ from the longest side and the approximation becomes less accurate. In Figure 5.45, the green dots represent the approximated center of gravity on the x-axis of the corresponding trapezoidal.

In an algorithm, the approximation of the bending moment in the cross-section can be described as:

$$M = \sum_{i=1}^{10} \frac{1}{2}(x_{i+1} - x_i)\left(\sigma_{yy,i} + \sigma_{yy,i+1}\right) * -\frac{1}{2}(x_i + x_{i+1})t \qquad (5.7.3)$$

in which x_i is the coordinate of the integration points on the x-axis. The fact that the distance is negative is a consequence of the chosen coordinate system in which a clockwise rotation is regarded negative. The program uses this equation to estimate the bending moments in the beams of all three piers. The results are stored in a matrix in which every row represents the data from an integration point and every column is an analysis step. The first column consists of the estimated y-coordinates of the rows of integration points. In general, several assumptions are made. For example, the locations of the integration points over the width are estimated. Errors in these distances influence the lever

arms of the bending moments and are linear errors. Errors of the order; $O(h)$. Also, the assumption is done to approach the stress pattern with a set of trapezoids. This assumption is however quite accurate as the stress pattern itself is calculated in eleven integration points, which is quite accurate. Like mentioned before, the assumption to estimate the center of gravity of a trapezoid at $\frac{1}{2}h$ is a good assumption when the trapezoids are more rectangular like $(b_1 \approx b_2)$, than triangular.
To make an estimation of the error, the bending moments at the supports are compared with the bending moments in the lowest integration points. Also, an in theory more accurate approach is used in which the center of gravity of the trapezoid is determined precise. The equation is for the center of gravity is changed in:

$$x_c = \frac{h}{3}\frac{b+2a}{b+a} \tag{5.7.4}$$

with b the long parallel side of the trapezoid. Implemented in the equation:

$$M = \sum_{i=1}^{10} \frac{1}{2}(x_{i+1} - x_i)\left(\sigma_{yy,i} + \sigma_{yy,i+1}\right) * \frac{1}{3}(x_{i+1} + x_i) * \frac{2\sigma_{yy,i+1} + \sigma_{yy,i}}{\sigma_{yy,i+1} + \sigma_{yy,i}} * t \tag{5.7.5}$$

The estimated error is shown in the following figures:

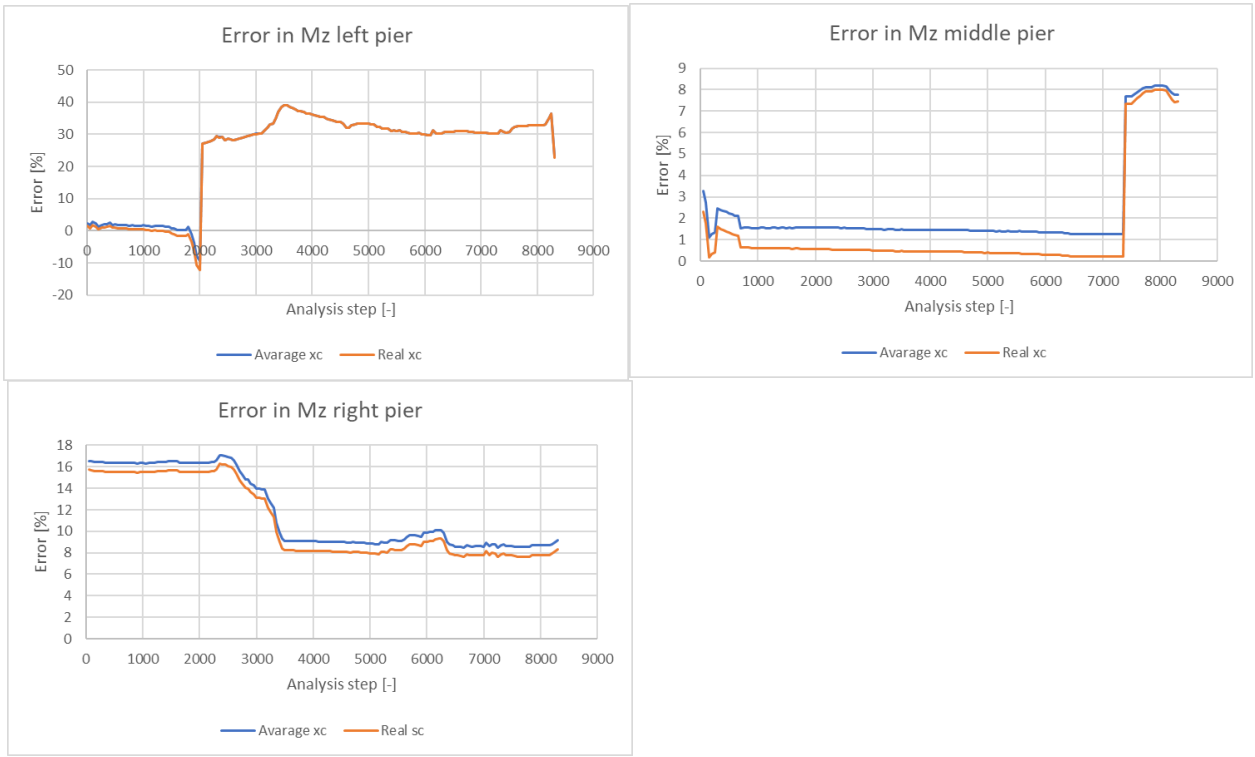

Figure 5.46; Estimated error of the bending moments in the supports

The error is calculated as the ratio of the approximated bending moment over the nodal bending moment:

$$\epsilon = 1 - \frac{\hat{M}_z}{M_{z,nod}} \tag{5.7.6}$$

Note that the lowest row of integration points is not at the same location as the lowest node. Therefore, the nodal value is expected to be even higher than the bending moment in the lowest row of integration points. Following this, even for a perfect approximation, a small positive error is expected beforehand. The error in the left pier becomes very big after analysis step 2000. A possible explanation is the total damage of the cross-section except the rightest integration point. This results in a strange stress-state with almost zero values for the other integration points, while the rightest integration point has a huge stress. As the pier damaged, the arm of the bending moment has reduced in reality as the support is badly damaged. In this model, the bending moment is still calculated from the center line as if the support was still intact. This leads to big errors.
For the other piers, the error is very small. It is also visible that the method with the real center of gravity is more accurate than the method with the average center of gravity. Although the differences are not that big.

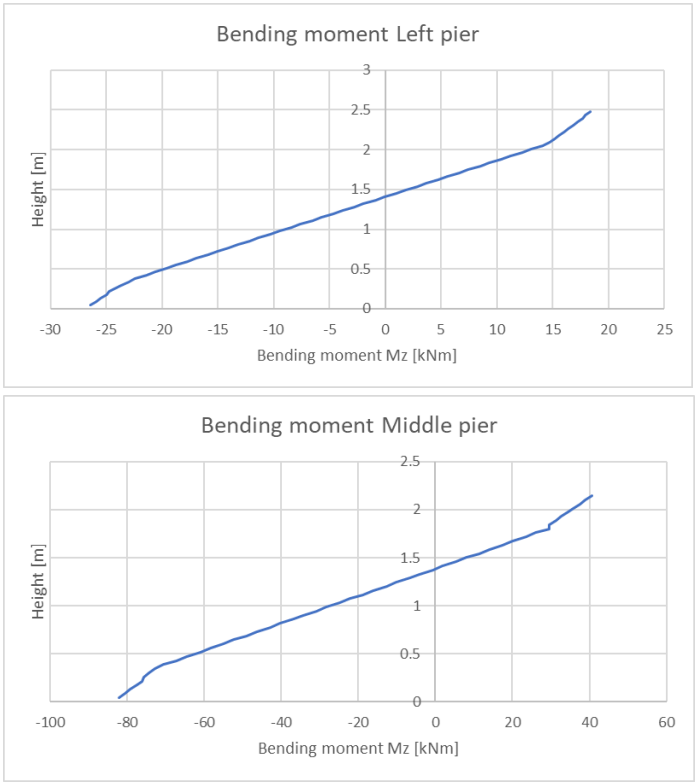

Figure 5.47; Bending moment M_z in left and middle pier over the height. Analysis step 301

Figure 5.47 shows the bending moment over the height of the left and middle pier. As expected, a counter clockwise bending moment at the bottom and a clockwise bending moment at the top of the pier. At the toe of the middle pier, the bending moment is estimated at $M_z = 82.2\ \mathrm{kNm}$.
An animation is made to show the change in bending moments during the analysis. The shape stays more or less the same for the entire analysis before failure. Only the values change with respect to the lateral load.

Comparing the magnitude of the bending moments in this analysis with the results found by Nobel for his beam model the magnitude is result is in the same order. Figure 5.48 shows the magnitude of the bending moments and axial forces in the members at a displacement of 5 mm. At this moment, the bending moment in the middle pier is around $1.22 * 10^8$ Nmm. In the beam model with SLA, the bending moment fluctuates in the analysis steps between $1.2 * 10^5$ Nm and $1.5 * 10^5$ Nm. There is however still a small bending moment in the left pier, while this is not the case in the model of Nobel. The bending moment for the right pier is more difficult to read from his results. It is approximately $6.59 * 10^7$ Nmm. In the SLA, it is around $5.0 * 10^4$ Nm. This is somewhat lower, but in the SLA, the left pier also contributes to the resisting bending moment which explains this.

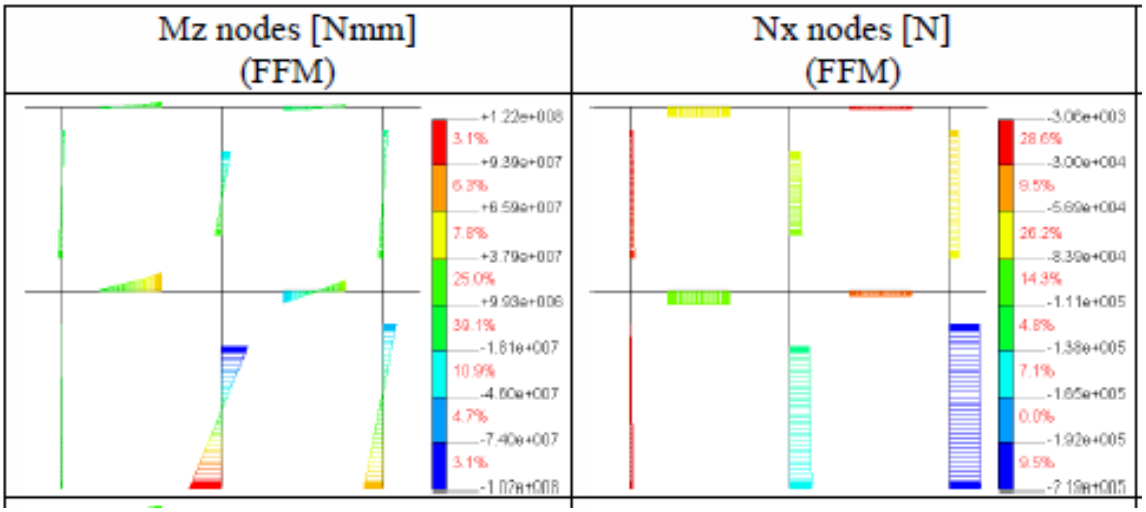

Figure 5.48; Bending moments and axial forces in the members at a displacement of 5 mm [2]

Considering the axial forces in the structure, the model of Nobel has a relatively small tensile force in the left pier, a force around $1.50 * 10^5$ N in the middle pier and a force of $2.19 * 10^5$ N in the right pier. In the sequentially linear analysis, the force in the left pier is still compressive but also relatively small and almost neglectable. The force in the middle pier is around $1.5 * 10^5$ N and the right pier has a vertical axial force of $2.2 * 10^5$ N. This is very close to the results of Nobel. The displacement of 5 mm is around analysis step 2000 (Figure 5.49).

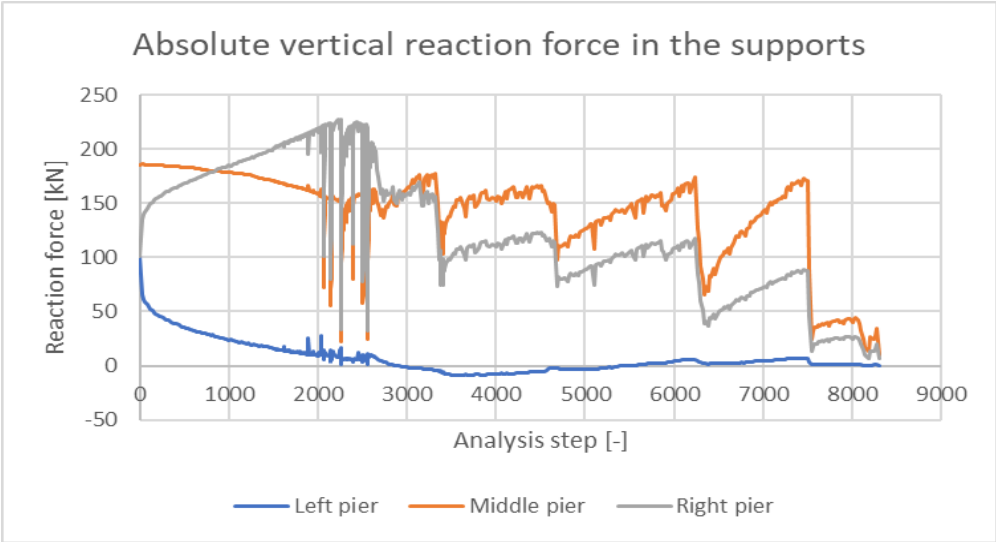

Figure 5.49; Absolute vertical reaction force in the piers

5.8 Conclusion

With the implementation of the sequentially linear analysis for beam element models, it was possible to use the equivalent frame approach combined with a sequentially linear analysis. First, two different approaches were tried. Both approaches used the same types of models from Nobel's research. The first model only used the bed joint tensile strength for of the piers and spandrels of the structure for those elements. The results of this model were very poor as local failure early on prevented the analysis to continue. The three-zoned approach was used in which the ends of the elements had properties based on the bed joint tensile strength of the masonry and the center of the piers and spandrels the maximum tensile strength of the masonry, which corresponds with shear failure. With this model it was possible to perform the analysis without local defects. Although the analysis was able to continue for a long time, the initial load factor was reduced early in the analysis. At this stage, the displacement of the second floor was only $5\ \mathrm{mm}$. The mesh size and the number of integration points were changed, but this did not improve the results.

An analysis was done to investigate why the initial load factor reduced early in the analysis. First the damage, strain and stress in the integration points at the bottom of the left pier were investigated. It was found that the tensile strength of the elements was validated in several integration points for both the axial direction of the element as the principal direction. Even a fully damaged integration point was able to reach high stresses. This was however a result of the fixed crack approach used in this model in combination with high shear forces. Stresses are able to build in the global and principal direction as the tensile strength criterion is defined in the fixed cracked coordinate system. This can have a negative effect as tensile damage started to propagate in an integration point in the center of the element as a result of this. For element 208, a stress-strain relation was found in which the stiffness seemed to increase after damage as a result of the Poisson's ratio which is set to zero when the integration point is damaged. By calculating the modulus of elasticity from the stresses, there was however a deviation from the input value.

Secondly, an indication was found that an initial load factor reduction shares a relation with the opening of a crack in an element. The strain was divided in a fictitious elastic strain and a fictitious plastic strain. When an initial load factor reduction occurred, the fictitious plastic strain in the corresponding integration point started to grow in the next analysis step. This was shown for several integration points. A possible theory is that the redistribution of the forces because of the damage in the integration point results in a stage where the full vertical load cannot be applied. This crack opening was often found in the spandrels, again in element 208. As the vertical load is also applied on the spandrels this is also of influence there. A relation between crack closure errors and the reduction of the initial load factor was investigated and it was concluded that there is none. Crack closure errors occurred in the analysis and resulted in odd results for some analysis steps but did not have a negative effect on the analysis. Significant errors were found far after load reduction.

Several improvement techniques were tried to make sure that the model would continue the analysis with a full initial load factor for a longer time. The most interesting technique was changing the parabolic constitutive relation of the compressive behaviour with an infinite linear elastic relation. With this method, the analysis was able to continue for a long time. The behaviour was however not realistic because the compressive strength of the piers was overestimated.

Another possible improvement used the approach by Belletti et al. [23], which includes prestressing the structure with the stresses resulting from the non-proportional load. With this approach, the structure responded not as one system, but as three piers failing consecutive. Also, the assumptions implemented in this approach that the stresses as a result of the non-proportional load do not change during the analysis is not valid in this case.

Other possible improvements included increasing the fracture energy of the material, which showed a higher energy dissipation for a higher fracture energy. The initial load factor was however still reduced and not retained. Also, increasing the number of saw-teeth was not effective. The results were almost similar concluding that the used number of saw-teeth was accurate enough.
At the end of this chapter, reaction forces of the model were evaluated together with the internal bending moments in the piers. From the vertical reaction forces could be concluded that the contribution of the left pier to carry the vertical non-proportional load disappears early in the analysis. This force is taken by the right pier. The contribution for the horizontal reaction force of the left pier also reduces. This force is mainly redistributed to the middle pier.
Looking at the shear forces, the results were very similar to the shear forces in the FFM model of Nobel. When the shear stresses as a result of the shear forces were calculated, they appeared to be far above the shear strength. This was checked for the middle pier, right pier and right first floor spandrel. For example, in the middle pier, the stress $\tau = 0.270\ \mathrm{MPa}$ while the strength is $f_{tu} = 0.14\ \mathrm{MPa}$. As the beam model can only fail in tension along its length, shear damage cannot initiate. By looking at the continuum model and the experimental data, shear failure is the most important failure mode in the structure. Shear strength criteria are therefore essential in this model to give a good approximation.
The middle pier takes the largest bending moment as it has the largest width. The bending moment of the left pier is reduced during the analysis as a result of the damaged cross-section.
A MATLAB program is written to approximate the internal bending moments in the piers as this is not yet implemented in the new Diana FEA version for beam elements in a sequentially linear analysis.
The MATLAB program uses a numerical approximation to calculate the integral of the stresses over the cross-section. A trapezoidal rule is used combined with a Riemann sum. The results are very accurate for the right and middle pier, and for the left pier until analysis step 2000. Comparing the results with the bending moments and axial force in the model of Nobel, the results are similar. Only the contribution of the bending moment of the right pier is larger in the model of Nobel and the bending moment of the left pier is nil. While in the SLA, the left pier is still able to contribute to the total bending moment. This contribution is not accurate as a large arm is assumed in the approximation which is not present anymore as a result of the damage.

6. Conclusions

The goal of this research was to study how the sequentially linear analysis could be used to model an unreinforced masonry structure. To investigate this, two approaches have been used to simulate the façade of the cyclic experiment at the University of Pavia in Italy, a continuum model and the equivalent frame method, for both categories a standard uniform approach is used and a three-zoned approach.

6.1 Standard (uniform) model - Three-zoned approach

The three-zoned approach showed better results for both models. For the continuum model, only the rocking failure mechanism was visible in the first analyses with the three-zoned approach. With a parameter sensitivity check for the maximum tensile strength f_{tu} it was shown that a tensile strength of $0.08\ \mathrm{MPa}$ in the piers results in an accurate failure pattern for the piers similar to that of the experiment. This failure pattern is a combination of rocking in the left pier and shear failure in the middle and right pier of the first floor. The middle and right pier have some rocking damage at the heel of the wall. Keeping in mind that the load was cyclic in the experiment, mirroring the damage as a result of load reversal in the model would give a very accurate representation of the damage and failure mode in the experiment, diagonal shear in both outer piers and diagonal shear in both directions of the middle pier. The damage in the top of the spandrels which was visible in the experiment was not present in the model. This damage initiated at the start of the experiment and occurred mostly in these regions because there was no vertical stress applied here as these regions were above the floor and the joint shear strength was therefore less than in other parts of the wall [19]. The three-zoned approach resulted in the correct material strength at the right place as the bed joint tensile strength was used in the rocking failure mode at the ends and the maximum tensile strength in the shear failure mode in the middle of the element. This was not the case for the standard uniform model. For the beam models, the uniform model suffered from local unstable elements. As the focus laid on the three-zoned model, this was not investigated further and only the three-zoned model was used in the rest of the investigation.

6.2 Continuum element model- Beam element model

At this stage, the three-zoned continuum model performs better than the beam element model.
The 3ZCM is able to give an accurate description of the load-displacement diagram of the experiment until a deformation of $10\ \mathrm{mm}$ and a force of $150\ \mathrm{kN}$. This is somewhat higher than the experimental values, which can be explained by the difference in load application. The results of section 4.4.7.2 showed for all models that a shear failure mode resulted in a more stable analysis than a rocking failure mode as the initial load factor was less constant and had larger drops for the latter. In rocking, cracks start to grow horizontally over the wall, also reducing the vertical load carrying capacity in an SLA, resulting in initial load factor drops. As shear damage initiates from the center, this failure mode is less sensitive to load factor drops as the sides are still undamaged.
The beam model was not able to reach displacements larger than $5\ \mathrm{mm}$, just in the elastoplastic part of the load-displacement curve. At this stage the vertical load could not be carried and the analysis could not continue. A parameter sensitivity check was performed for the mesh size, number of saw-teeth, fracture energy and the number of integration points over the width. It was concluded that these values were not affecting the analysis results and were accurate enough. The reaction forces on the structure and the internal bending moments in the piers were monitored and compared with the

incremental iterative results. It was concluded that the forces were almost identical. The bending moment distribution was similar. The bending moments were somewhat higher in the left pier and lower in the right pier in the SLA. In terms of load distribution, the incremental iterative approach and the SLA were similar. With a hand calculation it was verified that the shear stresses in middle and right pier and the spandrels are higher than the maximum strength f_{tu}. As the beam elements can only fail in bending, the shear failure which was observed in the continuum model was not present here.

6.3 SLA-performance

The SLA performed very good in the continuum models as it was able to accurately describe the load-displacement curve of the experiment. In the end, the number of initial load reductions was limited. The stress-strain relations showed that the saw-tooth law was followed accurately and that the ultimate strain was reached in multiple integration points. The SLA was able to retain the initial load in most cases after initial load reductions. The damage-strain-stress overviews showed accurate damage propagation in the piers. The parabolic constitutive law was not tested as this stage was not reached in the analyses performed in this investigation. In the beam model, the analysis aborted early, while an incremental iterative approach was able to reach displacements of $25\ \mathrm{mm}$ and a maximum load of $175\ \mathrm{kN}$. An in-depth analysis was performed and several important results were found:

i. For the beam element approach, it was found that the principal stress in several integration points exceeded the strength of the material. This was a result of the implemented fixed crack model. The high shear stresses in this structure rotated the crack coordinate system from the beam axis. As the strength criterion is set in this direction and the coordinate system is fixed, the principal stresses are able to build when the principal direction rotates from the crack coordinate system, exceeding the tensile strength. Following this, other integration points with lower stresses were damaged which resulted in damage in wrong integration points. This disturbs the analysis and is a reason why the initial load factor could not be applied as the strength of these integration points is reduced severely. A rotating crack approach would help. It can be confirmed by looking at the stresses and strains in the fixed crack coordinate system that the saw-tooth law is followed accurately.
ii. The modulus of elasticity was calculated from the principal stresses and strains and a small deviation from the initial value was found for the beam element model. This was also the case for undamaged integration points. This was correct in the continuum model. It is not investigated why this happens for the beam model.
iii. There is a relation between an initial load factor reduction and the opening of a crack in the corresponding integration point that damages at an initial load factor reduction. This occurred in the continuum model and the beam model. A possible explanation is that cracks initiate a redistribution of stresses which result in a temporary vertical load reduction. This behaviour was only observed at some crack openings. To understand this properly, this should be investigated further.
iv. Crack closure errors were present in both models and can result in non-secant branches in the load-displacement curve. This did not lead to big errors in the early stages of the analysis. However, when post-peak behaviour is reached, this can result in large errors.

The results of this thesis confirm the potential of the SLA to accurately approximate the behaviour of an unreinforced masonry structure as it was possible to run a stable analysis with accurate results for the continuum model. The beam model analysis gave accurate results in terms of forces and bending moments similar to the results of an incremental iterative approach but aborted in an early stage. New developments in a rotating crack approach and shear interfaces will result in a more stable analysis as the right failure behaviour will be followed.

7. Recommendations

Some recommendations for future investigations are listed below in order of importance:

i. The fixed crack approach resulted in difficulties for this model as shear stresses were able to build far above the tensile strength which resulted in incorrect damage propagation. A rotating crack formulation could prevent this. With this implementation, it should be possible to describe the post-peak behaviour of the structure and hopefully come close to the experimental data and fulfill the potential of this modeling technique to reduce the computational effort while keeping the result accurate.

ii. As the equivalent frame approach uses beam elements only, the only possible failure mode is failure in bending. With respect to that, it would be interesting to see further developments in the direction of shear interfaces in the piers and spandrels of the beam model. As it was demonstrated that the shear stresses are above the maximum shear strength, this failure mode will definitely be active in the middle and right pier and the spandrels. The thought is that these shear interfaces will result in a different failure mode for the beam element which will possibly result in a more stable analysis, as shear failure in the piers gave more stable results in the case of a continuum model.

iii. The relation between the reductions of the initial load factor and the opening of a crack in the corresponding integration points which was observed should be investigated further. The opening of a crack results in a redistribution of the forces which could result in a temporary drop of the initial load factor. The precise mechanism behind this and why this occurs with some cracks while it did not happen with others is still unknown.

iv. SLA could be implemented for three-dimensional beam or shell elements to investigate the behaviour of unreinforced masonry buildings further in a full three-dimensional model. This is not possible at this stage. In this model, the behaviour of floors should be investigated thoroughly as they have an important function in connecting the walls and transferring forces together with the out of plane bending behaviour of the floors themselves. A modelling approach to make an appropriate equivalent frame model from a three-dimensional building will also be a challenge.

v. In this analysis, the effect of lintels on the structure was neglected. In the experiment, the openings in the wall have lintels. The lintels will prevent a vertical crack in the spandrels and could therefore be added to the finite element model to make it more complete.

References

[1] A. V. v. d. Graaf, "Sequentially linear analysis for simulating brittle failure," Delft, 2017.

[2] W. L. Nobel, "A Fibre Flexure - Lumped Shear Model for Masonry Structures," Delft University of Technology, Delft, 2017.

[3] D. C. Ferreira, "Project: Fibre models for beam and shell elements," Diana FEA, Delft, 2015.

[4] R. Kist and M. a. d. Brugh, "Vijf vragen over Gronings gas die je nooit hebt durven stellen," NRC, 18 February 2015. [Online]. Available: https://www.nrc.nl/nieuws/2015/02/18/vijf-vragen-over-gronings-gas-die-je-nooit-hebt-durven-stellen-a1497642. [Accessed 5 October 2017].

[5] H. Ekker, "100.000 mensen met aardbevingsschade in Groningen," NOS, 4 September 2016. [Online]. Available: https://nos.nl/artikel/2129869-100-000-mensen-met-aardbevingsschade-in-groningen.html. [Accessed 5 October 2017].

[6] J. G. Rots, J. Blaauwendraad and P. B. Lourenço, "Two approaches for the analysis of masonry structures: micro and macro-modeling," Heron, Delft, 1995.

[7] G. Sarangapani, B. V. Venkatarama Reddy and K. S. Jagadish, "Brick-Mortar Bond and Masonry Compressive Strength," American Society of Civil Engineers (ASCE), Reston, Virginia, 2005.

[8] U. Andreaus, "Failure Criteria for Masonry Panels under In-Plane Loading," Journal of Structural Engineering, 1996.

[9] M. J. DeJong, M. A. Hendriks and J. G. Rots, "Sequentially linear analysis of fracture under non-proportional loading," Elsevier, 2008.

[10] G. Magenes and G. M. Calvi, "In-plane Seismic Response of Brick Masonry Walls," Earthquake Engineering and Structural Dynamics, Pavia, 1997.

[11] A. Simone, An Introduction to the Analysis of Slender Structures, Delft, Zuid-Holland: Delft University of Technology, 2011.

[12] G. N. Wells, The Finite Element Method: An Introduction, Delft: University of Cambridge and Delft University of Technology, 2009.

[13] R. de Borst and L. J. Sluys, Computational Methods in Non-linear Solid Mechanics, Delft: Delft University of Technology, 2015.

[14] J. G. Rots, "Sequentially linear continuum model for concrete fracture," Faculty of Architecture, Delft University of Technology, Delft, 2001.

[15] M. Pari, J. G. Rots and M. A. Hendriks, "Non-proportional loading for 3-D stress situations in Sequentially Linear Analysis," Delft University of Technology, Delft, 2018.

[16] J. Eliáš, "Generalization of load-unload and force-release sequentially linear methods," International Journal of damage Mechanics, Brno, 2015.

[17] J. Eliáš, P. Frantík and M. Vořechovský, "Improved sequentially linear solution procedure," Elsevier, Brno, 2010.

[18] G. Magenes and A. Della Fontana, "Simplified Non-linear Seismic Analysis of Masonry Buildings," University of Pavia, Pavia, 1998.

[19] G. Magenes, G. M. Calvi and G. R. Kingsley, "Seismic Testing of a Full-Scale, Two-Story Masonry Building: Test Procedure and Measured Experimental Response," University of Pavia, Pavia, 1995.

[20] J. Manie, "User's Manual - Release 10.2," Diana Finite Element Analysis, 15 September 2017. [Online]. Available: https://dianafea.com/manuals/d102/Diana.html. [Accessed 31 October 2017].

[21] A. C. Vrouwenvelder, The plastic behaviour and the calculation of beams and frames subjected to bending, Delft: Delft University of Technology, 2003.

[22] "DIANA 9.4 User's Manual section 6.2.2. Tensile Behavior," Diana FEA, 2010. [Online]. Available: https://dianafea.com/manuals/d94/MatLib/node75.html. [Accessed 23 January 2018].

[23] B. Belletti, M. J. DeJong, A. V. van de Graaf, M. A. Hendriks and J. G. Rots, "“Sequentially linear analysis” for the response prediction by pushover analysis of URM buildings subjected to seismic loads," *Proceedings of ANIDIS2009,* 2009.

[24] J. Kraus, "Sequentially linear modelling of combined tension/compression failure in masonry structures," Delft University of Technology, Delft, 2014.

[25] L. Ning, L. Zhongxian and X. Lili, "A fiber-section model based Timoshenko beam element using shear-bending interdependent shape function," Earthquake Engineering and Engineering Vibration, 2013.

[26] C. R. Goyal, "Uncertainty Quantification in Non-linear Seismic Wave Propagation," Carleton University, Ottawa, 2017.

[27] R. T. Mullapudi and A. S. Ayoub, "Fiber Beam Element Formulation Using the Softened Membrane Model," Aci Structural Journal, Houston, 2009.

[28] J. G. Rots, Structureal Masonry: An Experimental/Numerical Basis for Practical Design Rules, R. N. J.G. Rots TNO Building and Construction Research, Ed., Rotterdam: A.A.Balkema/Rotterdam/Brookfield, 1997.

Appendices

Appendix A

Matlab program to find crack closure errors:

```
clc
close all

a=Stressstrain;
b=Damage;

nelements=538;
nintp=4;
steps=4;
nsteelelements = 0;

Datad=zeros((nelements-nsteelelements)*nintp,1+4*steps);
k=1;

% Damage part

for k = 1:nintp
    s=k;
    for l=1:length(b)
        if k == 1
            if b(l,2) == 1 && b(l,3)>=0
                Datad(s,1)=b(l,3);
                s=s+nintp;
                if s >(nelements-nsteelelements)*nintp
                    break
                end
            else
            end
        else
%             if k==2
              if b(l,1) == k
                  if b(l,3)>=0
                      disp(l);
                  else
                      Datad(s,1)=b(l,2);
                      s=s+nintp;
                      if s>(nelements-nsteelelements)*nintp
                          break
                      end
                  end
              end
%             else
%                 if b(l,1) == k && (b(l-1,1)==k-1)
%                     Datad(s,1)=b(l,2);
%                     s=s+nintp;
%                     if s>(nelements-nsteelelements)*nintp
%                         break
%                     end
%                 end
%             end
        end
    end
```

```
end

Data=zeros(nelements*nintp,1+4*steps);
Data=Datad;

% Stress-strain part

for k = 2:1:nintp
    s=k;
    for l=1:1:length(a)
        if a(l,1) == k
            if s <= nintp*nelements
                Data(s,2)=a(l,2);
                Data(s,3)=a(l,3);
                Data(s,4)=a(l,5);
                Data(s,5)=a(l,6);
                s=s+nintp;
            elseif s>nintp*nelements && s<= 2*nintp*nelements
                Data(s-nintp*nelements,2+steps)=a(l,2);
                Data(s-nintp*nelements,3+steps)=a(l,3);
                Data(s-nintp*nelements,4+steps)=a(l,5);
                Data(s-nintp*nelements,5+steps)=a(l,6);
                s=s+nintp;
            elseif s>2*nintp*nelements && s<=3*nintp*nelements
                Data(s-2*nintp*nelements,2+2*steps)=a(l,2);
                Data(s-2*nintp*nelements,3+2*steps)=a(l,3);
                Data(s-2*nintp*nelements,4+2*steps)=a(l,5);
                Data(s-2*nintp*nelements,5+2*steps)=a(l,6);
                s=s+nintp;
            elseif s>3*nintp*nelements
                Data(s-3*nintp*nelements,2+3*steps)=a(l,2);
                Data(s-3*nintp*nelements,3+3*steps)=a(l,3);
                Data(s-3*nintp*nelements,4+3*steps)=a(l,5);
                Data(s-3*nintp*nelements,5+3*steps)=a(l,6);
                s=s+nintp;
            end
        end
    end
end
f=0;
s=1;
for i = 8:length(a)
    if a(i,2)>-1 && a(i,2)<1
        f=f+1;
        f=mod(f,nintp);
        if f==1
            if s <= nintp*nelements
                Data(s,2)=a(i,2);
                Data(s,3)=a(i,3);
                Data(s,4)=a(i,5);
                Data(s,5)=a(i,6);
                s=s+nintp;
            elseif s>nintp*nelements && s<= 2*nintp*nelements
                Data(s-nintp*nelements,2+steps)=a(i,2);
                Data(s-nintp*nelements,3+steps)=a(i,3);
                Data(s-nintp*nelements,4+steps)=a(i,5);
                Data(s-nintp*nelements,5+steps)=a(i,6);
                s=s+nintp;
            elseif s>2*nintp*nelements && s<=3*nintp*nelements
                Data(s-2*nintp*nelements,2+2*steps)=a(i,2);
                Data(s-2*nintp*nelements,3+2*steps)=a(i,3);
```

```
                Data(s-2*nintp*nelements,4+2*steps)=a(i,5);
                Data(s-2*nintp*nelements,5+2*steps)=a(i,6);
                s=s+nintp;
            elseif s>3*nintp*nelements
                Data(s-3*nintp*nelements,2+3*steps)=a(i,2);
                Data(s-3*nintp*nelements,3+3*steps)=a(i,3);
                Data(s-3*nintp*nelements,4+3*steps)=a(i,5);
                Data(s-3*nintp*nelements,5+3*steps)=a(i,6);
                s=s+nintp;
            end
        end
    end
end


% search for Crack closure faults

for l = 1:length(Data)
    ep=0; si=0;
    if (Data(l,2) < 0 && Data (l,6) > 0) || (Data(l,2) > 0 && Data (l,6) <
0) || (Data(l,3) < 0 && Data (l,7) > 0) || (Data(l,3) > 0 && Data (l,7) < 0)
        if (Data(l,4) < 0 && Data (l,8) > 0) || (Data(l,4) > 0 && Data (l,8)
< 0) || (Data(l,5) < 0 && Data (l,9) > 0) || (Data(l,5) > 0 && Data (l,9) <
0)
            if Data(l,1)>0
                disp(l);  disp('step  1103-1104');  disp('Crack  closure  in
element');       disp(ceil(l/nintp));       disp('integration       point');
disp(mod(l,nintp));
            end
        end
    end
    if (Data(l,2+4) < 0 && Data (l,6+4) > 0) || (Data(l,2+4) > 0 && Data
(l,6+4) < 0) || (Data(l,3+4) < 0 && Data (l,7+4) > 0) || (Data(l,3+4) > 0 &&
Data (l,7+4) < 0)
        if (Data(l,4+4) < 0 && Data (l,8+4) > 0) || (Data(l,4+4) > 0 && Data
(l,8+4) < 0) || (Data(l,5+4) < 0 && Data (l,9+4) > 0) || (Data(l,5+4) > 0 &&
Data (l,9+4) < 0)
            if Data(l,1)>0
                disp(l);  disp('step  1104-1105');  disp('Crack  closure  in
element');       disp(ceil(l/nintp));       disp('integration       point');
disp(mod(l,nintp));
            end
        end
    end
    if (Data(l,2+8) < 0 && Data (l,6+8) > 0) || (Data(l,2+8) > 0 && Data
(l,6+8) < 0) || (Data(l,3+8) < 0 && Data (l,7+8) > 0) || (Data(l,3+8) > 0 &&
Data (l,7+8) < 0)
        if (Data(l,4+8) < 0 && Data (l,8+8) > 0) || (Data(l,4+8) > 0 && Data
(l,8+8) < 0) || (Data(l,5+8) < 0 && Data (l,9+8) > 0) || (Data(l,5+8) > 0 &&
Data (l,9+8) < 0)
            if Data(l,1)>0
            disp(l);  disp('step  1105-1106');  disp('Crack  closure  in
element');       disp(ceil(l/nintp));       disp('integration       point');
disp(mod(l,nintp));
            end
        end
    end
end
```

Appendix B

Matlab program to calculate the moments in the piers:

```
clc
close all

a=Stressstrainleft;
b=Stressstrainmiddle;
c=Stressstrainright;

nelementsl=29;          %elements in left pier
nelementsm=25;          %elements in middle pier
nelementsr=29;          %elements in right pier
nintp=22;               %number of integration point
widthl=1.15;            %width of left pier
widthm=1.82;            %width of middle pier
widthr=1.15;            %width of right pier
heightl=2.477;          %height of left pier
heightm=2.145;          %height of middle pier
heightr=2.477;          %height of right pier
thickness=0.25;         %thickness of the facade
lelementsstart=18;      %lowest element of left pier
melementsstart=47;      %lowest element of middle pier
relementsstart=72;      %lowest element of right pier

%Left pier

lines=zeros(100,2);
lines(1,1)=1;
lines(1,2)=1;

Data=zeros(nelementsl*nintp,5);

k=30;
s=2;

for k=30:1:length(a)
    if a(k,3) > 10
        lines(s,1)=k;
        lines(s,2)=a(k,3);
        s=s+1;
    end
end
lines(length(lines)+1,1)=length(a);

% Stress-strain part

k=1;
s=1;

seq1=1:nintp;
seq1=repmat(seq1,1,nelementsl);
seq1=seq1';

seq2=-widthl/2:widthl/(nintp/2-1):widthl/2;
```

```
seq2=repmat(seq2,1,nelementsl*2);
seq2=seq2';

Momentsl=zeros(nelementsl*2,length(lines));
o=2;
d=1;
for d=1:length(lines)-1
    Data=zeros(nelementsl*nintp,5);
    for k = 1:1:nintp
        s=k;
        for p=lines(d,1):1:lines(d+1,1)
            if a(p,2) == k
                    Data(s,4)=a(p,4);
                    s=s+nintp;
            end
        end
    end
    Data(:,2)=seq1;
    Data(:,3)=seq2;
    %calculating moments
    for m = 1:nintp/2:length(Data)
        for n=0:nintp/2-2
            Data(m+n,5)=(1/2*(Data(m+n,4)+Data(m+n+1,4))*(Data(m+n+1,3)-
Data(m+n,3))*(Data(m+n+1,3)+Data(m+n,3))/2)*thickness;
        end
        Data(m+n+1,5)=sum(Data(m:m+n,5));
    end
    Momentsl(1:nelementsl*2,o)=Data(nintp/2:nintp/2:end,5);
    o=o+1;
end
Momentsl(:,1)=flipud((1:nelementsl*2)'*heightl/(nelementsl*2));
Momentsl=sortrows(Momentsl,1);

%Middle pier

lines=zeros(100,2);
lines(1,1)=1;
lines(1,2)=1;

Data=zeros(nelementsm*nintp,5);

k=30;
s=2;

for k=30:1:length(b)
    if b(k,3) > 10
        lines(s,1)=k;
        lines(s,2)=b(k,3);
        s=s+1;
    end
end
lines(length(lines)+1,1)=length(b);

% Stress-strain part

k=1;
s=1;

seq1=1:nintp;
seq1=repmat(seq1,1,nelementsm);
```

```
seq1=seq1';

seq2=-widthm/2:widthm/(nintp/2-1):widthm/2;
seq2=repmat(seq2,1,nelementsm*2);
seq2=seq2';

Momentsm=zeros(nelementsm*2,length(lines));
o=2;
d=1;
for d=1:length(lines)-1
    Data=zeros(nelementsm*nintp,5);
    for k = 1:1:nintp
        s=k;
        for p=lines(d,1):1:lines(d+1,1)
            if b(p,2) == k
                    Data(s,4)=b(p,4);
                    s=s+nintp;
            end
        end
    end
    Data(:,2)=seq1;
    Data(:,3)=seq2;
    %calculating moments
    for m = 1:nintp/2:length(Data)
        for n=0:nintp/2-2
            Data(m+n,5)=(1/2*(Data(m+n,4)+Data(m+n+1,4))*(Data(m+n+1,3)-
Data(m+n,3))*(Data(m+n+1,3)+Data(m+n,3))/2)*thickness;
        end
        Data(m+n+1,5)=sum(Data(m:m+n,5));
    end
    Momentsm(1:nelementsm*2,o)=Data(nintp/2:nintp/2:end,5);
    o=o+1;
end
Momentsm(:,1)=flipud((1:nelementsm*2)'*heightm/(nelementsm*2));
Momentsm=sortrows(Momentsm,1);

%Right pier

lines=zeros(100,2);
lines(1,1)=1;
lines(1,2)=1;

Data=zeros(nelementsr*nintp,5);

k=30;
s=2;

for k=30:1:length(c)
    if c(k,3) > 10
        lines(s,1)=k;
        lines(s,2)=c(k,3);
        s=s+1;
    end
end
lines(length(lines)+1,1)=length(c);

% Stress-strain part

k=1;
s=1;
```

```
seq1=1:nintp;
seq1=repmat(seq1,1,nelementsr);
seq1=seq1';

seq2=-widthr/2:widthr/(nintp/2-1):widthr/2;
seq2=repmat(seq2,1,nelementsr*2);
seq2=seq2';

Momentsr=zeros(nelementsr*2,length(lines));
o=2;
d=1;
for d=1:length(lines)-1
    Data=zeros(nelementsr*nintp,5);
    for k = 1:1:nintp
        s=k;
        for p=lines(d,1):1:lines(d+1,1)
            if c(p,2) == k
                    Data(s,4)=c(p,4);
                    s=s+nintp;
            end
        end
    end
    Data(:,2)=seq1;
    Data(:,3)=seq2;
    %calculating moments
    for m = 1:nintp/2:length(Data)
        for n=0:nintp/2-2
            Data(m+n,5)=(1/2*(Data(m+n,4)+Data(m+n+1,4))*(Data(m+n+1,3)-
Data(m+n,3))*(Data(m+n+1,3)+Data(m+n,3))/2)*thickness;
        end
        Data(m+n+1,5)=sum(Data(m:m+n,5));
    end
    Momentsr(1:nelementsr*2,o)=Data(nintp/2:nintp/2:end,5);
    o=o+1;
end
Momentsr(:,1)=flipud((1:nelementsr*2)'*heightr/(nelementsr*2));
Momentsr=sortrows(Momentsr,1);

%Animation left pier

y=Momentsl(:,1);
line([0 0],[0 heightl])
for t=2:length(Momentsl)
    x=Momentsl(:,t);
    plot(x,y)
    hold on
    line([0 0],[0 heightl],'Color','black')
    xlim([-30000 30000])
    ylim([0 heightl])
    hold off
    drawnow
    pause(0.1)
end

%Animation middle pier

y=Momentsm(:,1);
line([0 0],[0 heightm])
for t=2:length(Momentsm)
```

```
    x=Momentsm(:,t);
    plot(x,y)
    hold on
    line([0 0],[0 heightm],'Color','black')
    xlim([-250000 100000])
    ylim([0 heightm])
    hold off
    drawnow
    pause(0.1)
end


%Animation right pier

y=Momentsr(:,1);
line([0 0],[0 heightr])
for t=2:length(Momentsr)
    x=Momentsr(:,t);
    plot(x,y)
    hold on
    line([0 0],[0 heightr],'Color','black')
    xlim([-80000 60000])
    ylim([0 heightr])
    hold off
    drawnow
    pause(0.1)
end
```

Appendix C

The meshes below belong chapter 3. Modelling strategies. The requested mesh size h is used for the mesh size of the piers.

Wall h=0.1 m

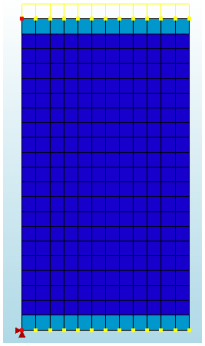

Wall h=0.05 m

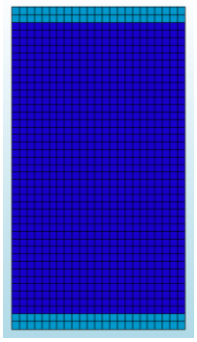

Wall h=0.2 m

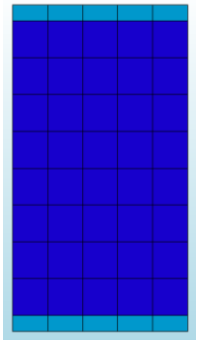

3ZCM h=0.4 m

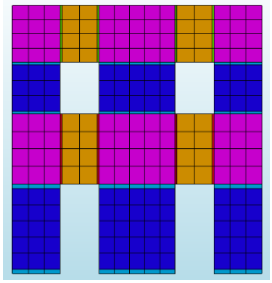

3ZCM h=0.8 m

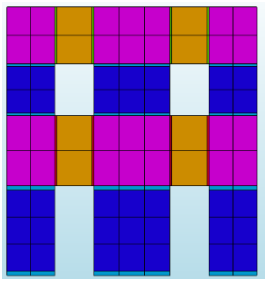

CM h=0.2 m

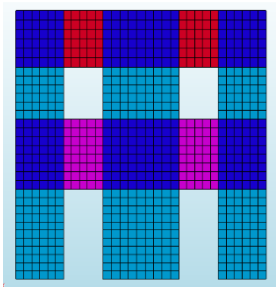

CM h=0.1 m

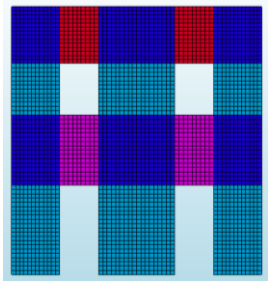

CM h=0.4 m

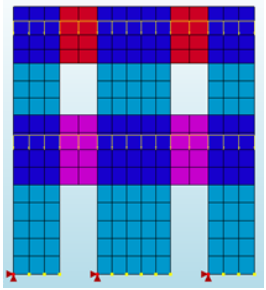

CM h=0.25 m

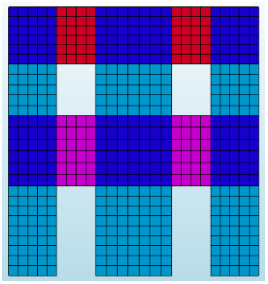

Triangular h=0.2 m

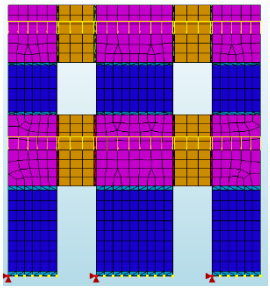

Model b h=0.2 m

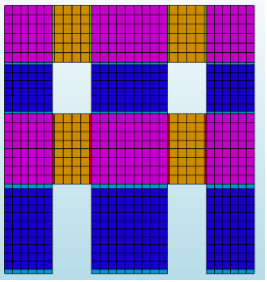

Model d h=0.25 m

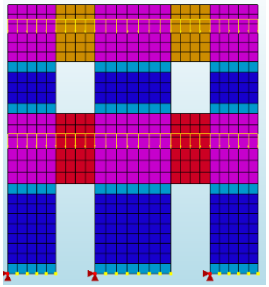

1ZEF Nobel (FF

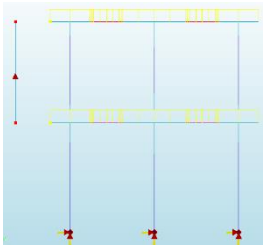

3ZEF h=0.1 m

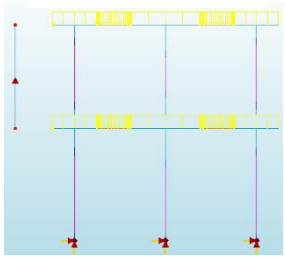

Other different meshes for the sensitivity analysis are made by changing the requested mesh size h to the size mentioned in the section.